Investigating anharmonic effects in condensed matter systems

This dissertation is submitted for the degree of
Doctor of Philosophy

Joseph Charles Alfred Prentice
St. Edmund's College
University of Cambridge

September 2017

For Laura

Preface

This dissertation presents work carried out between October 2014 and September 2017 in the Theory of Condensed Matter Group at the Cavendish Laboratory in the University of Cambridge, under the supervision of Professor Richard Needs. Several sections of this dissertation include work that has either been published or is being prepared for publication. The relevant sections and the related publications are:

- Chapter **3**: J. C. A. Prentice and R. J. Needs, *Using forces to accelerate first-principles anharmonic vibrational calculations*, Physical Review Materials **1**, 023801, 2017
- Chapter **4**: J. C. A. Prentice, B. Monserrat and R. J. Needs, *First-principles study of the dynamic Jahn-Teller distortion of the neutral vacancy in diamond*, Physical Review B **95**, 014108, 2017
- Chapter **5**: J. C. A. Prentice, N. C. Bristowe and R. J. Needs, *First-principles anharmonic study of phase transitions in* $BaTiO_3$, in preparation

This dissertation is a result of my own work and includes nothing that is the outcome of work done in collaboration except as declared in the Preface and specified in the text. This dissertation is not substantially the same as any that I have submitted, or is being concurrently submitted, for a degree or diploma or other qualification at the University of Cambridge or any other university or similar institution, except as declared in the Preface and specified in the text. I further state that no substantial part of my dissertation has already been submitted, or is being concurrently submitted for any such degree, diploma or other qualification at the University of Cambridge or any other university or similar institution, except as declared in the Preface and specified in the text. This dissertation does not exceed the word limit of 60,000 words.

Joseph Charles Alfred Prentice
Cambridge, September 2017

Abstract

This thesis presents work done on the calculation of the effects of anharmonic nuclear motion on the properties of solid materials from first principles. Such anharmonic effects can be significant in many cases. A vibrational self-consistent field (VSCF) method is used as the basis for these calculations, which is then improved and applied to a variety of solid state systems.

Firstly, work done to improve the efficiency of the VSCF method is presented. The standard VSCF method involves using density functional theory (DFT) to map the Born-Oppenheimer (BO) energy surface that the nuclei move in, a computationally expensive process. It is shown that the accurate forces available in plane-wave basis DFT can be used to help map the BO surface more accurately and reduce the computational cost. This improved VSCF+f method is tested on molecular and solid hydrogen, as well as lithium and zirconium, and is found to give a speed-up of up to 40%.

The VSCF method is then applied to two different systems of physical interest. It is first applied to the case of the neutral vacancy in diamond, in order to resolve a known discrepancy between harmonic *ab initio* calculations and experiment – the former predict a static Jahn-Teller distortion, whilst the latter leads to a dynamic Jahn-Teller effect. By including anharmonic corrections to the energy and nuclear wavefunction, we show that the inclusion of these effects results in agreement between first-principles calculations and experiment for the first time.

Lastly, the VSCF method is applied to barium titanate, a prototypical ferroelectric material which undergoes a series of phase transitions from around 400 K downwards. The nature of these phase transitions is still unclear, and understanding them is an active area of research. We describe the physics of the phase transitions of barium titanate, including both anharmonicity and the effect of polarisation caused by long wavelength vibrations, to help understand the important physics from first principles.

Acknowledgements

Firstly, I would like to thank my supervisor, Professor Richard Needs, as well as Dr. Bartomeu Monserrat, for their support, attention and help with guiding the work presented in this thesis, which has been invaluable. I would also like to thank Dr. Nick Bristowe at the University of Kent for his help and support with the work on barium titanate. Thanks are also due to my various office-mates, Jonathan Lloyd-Williams, Nicholas Worth and Tom Whitehead, for their help and support (especially on coding-related issues), as well as to the rest of the TCM group for making TCM such a welcoming and friendly place in which to do research. Rob Baldock, Edgar Engel, Gareth Conduit, Andrew Morris and Joseph Nelson all deserve particular thanks for this, as does our computer officer Michael Rutter, for guiding us all through the wonderful world of computers, and the various group administrators throughout my time in TCM. My housemates and St. Edmund's College also deserve thanks for making Cambridge a wonderful place in which to live and work, along with acquaintances from many other colleges. I would also like to acknowledge my funding from the EPSRC, which has allowed me to conduct this research. My parents, Debbie and Barrie, my brother, Sam, and all the rest of my family and friends deserve many thanks for their love and support. Finally, I would especially like to thank my fiancée, Laura Clash, for always being there and supporting me throughout.

Contents

Part I

Introduction and Background

Chapter 1

Introduction

1.1 Quantum mechanics, condensed matter and computers

Every once in a while, every field of human study, including the sciences, undergoes a paradigm shift, through which its most basic tenets are completely revolutionised, resulting in a completely new understanding of the field [1]. Physics experienced not one, but two of these paradigm shifts in the early twentieth century, completely overturning our understanding of space, time and matter in the relatively short space of time between Einstein's *annus mirabilis* in 1905 [2–5], and Dirac's discovery of his eponymous equation in 1928 [6]. The result was the emergence of the twin pillars that modern physics stands on – quantum mechanics and general relativity. Despite many fundamental inconsistencies between the two, each theory is spectacularly successful in its own domain, with quantum mechanics dominating at the atomic scale and general relativity governing at planetary scales or higher. Using these two theories, humanity's technological capabilities and fundamental understanding of the universe has advanced at an unprecedented rate.

A physicist with a reductionist viewpoint could say that these two theories are indeed all we need, leaving only the application of these theories to all possible systems and observation of the results – to paraphrase Ernest Rutherford, everything else is simply 'stamp-collecting'. However, this ignores the fact that applying the basic equations of either quantum mechanics or general relativity to anything much beyond the simplest systems rapidly becomes unmanageable from an analytical stand-point. The largest field of physics today – condensed matter physics – in the most general terms revolves around studying many interacting particles, an utterly impossible task to do directly using basic quantum mechanics. A system containing many particles is not only insurmountably difficult to analyse using elementary physical equations, but also often exhibits new and interesting behaviours due to the interaction of these particles, as discussed in Anderson's famous paper, *More is different* [7]. This richness of behaviour, along with its broad scope and myriad technological and scientific applications, is what has made condensed matter the immense field of study that it currently is, including significant overlap with the fields of chemistry, materials science and biophysics. The work presented in this thesis focuses on studying condensed matter systems of scientific and technological importance, as well as the methods used to approach these problems.

To be able to study such systems and accurately predict their properties, it is usually necessary to make approximations or assumptions to make a solution to the problem

possible. Well-known approximations in the field of condensed matter include the Born-Oppenheimer [8] and harmonic [9] approximations, both of which will be discussed in more detail later in this thesis. Approximations allow us to simplify the problem, at the cost of some accuracy, providing greater insight into the true underlying physics. Sometimes this will result in the problem becoming analytically soluble, but more often the simplified problem will still require solving numerically – although this will generally be more tractable than the original problem.

Solving physical problems numerically has a long history, but the advent of computers has resulted in such numerical approaches becoming much more routine. A computational approach to a physical problem allows accurate numerical solutions much faster than would be possible by hand, as long as the problem can be coded into a suitable algorithm and one has access to a sufficiently powerful computer. The computational power available to the average physicist has grown exponentially over the past few decades, in accordance with the well-known Moore's Law [10], which states that the number of transistors in an integrated circuit doubles roughly every two years. This massive increase in computational power has allowed computational condensed matter physicists to tackle larger and more complex problems than ever before, and use more accurate approximations than was previously possible.

A particular example of a condensed matter problem that requires both appropriate approximations and computational approaches is the treatment of atomic motion in condensed matter. This is an important effect in many situations, and thus requires careful and accurate study. Thanks to increased computing power as well as methodological advances, assumptions and methods typically used to treat the motion of the nuclei in condensed matter can be replaced with more accurate ones. This thesis focuses on developing and applying these new more accurate methods to systems of quantum mechanical interest, where previously neglected quantum mechanical effects are vital in understanding their behaviour.

1.2 Outline of thesis

This thesis is arranged into three broad sections: the theoretical background to the work presented, method development, and finally applications to systems of interest in condensed matter. Chapters 3 to 5 each have an associated appendix, containing supplementary material.

Chapter 2 describes the main theoretical foundations on which the rest of this work rests. It outlines the many-body problem within condensed matter physics, the use of the Born-Oppenheimer approximation and density functional theory (DFT) to tackle the electronic part of this problem, and finally both harmonic and anharmonic methods to deal with the motion of the nuclei, including the vibrational self-consistent field (VSCF) method on which the bulk of this thesis is based.

Chapter 3 presents work that develops the basic VSCF method, showing how the accuracy and efficiency of the VSCF method can be improved by including force data from DFT calculations. The improved method is demonstrated through applications to several different condensed matter systems, and the results are compared to those obtained using the basic VSCF method.

Chapter 4 focuses on the neutral vacancy point defect in diamond, and specifically on the structure of the lattice around the defect. The VSCF method is applied to obtain a good description of the vibrational wavefunction, allowing the dynamic Jahn-Teller effect around the vacancy to be described from first principles, resolving a long-standing discrepancy between theory and experiment.

Chapter 5 focuses on the prototypical ferroelectric material barium titanate ($BaTiO_3$), and the series of phase transitions it undergoes. The VSCF method is again applied, with modifications to include the effect of the macroscopic polarisation created by long wavelength vibrations, to obtain a description of the vibrational wavefunction of the system. Analysing the results of these calculations provides the initial steps towards the first truly first-principles description of the phase transitions of $BaTiO_3$.

Finally, in Chapter 6 the results of the work are briefly summarised and potential directions for future work are discussed.

Chapter 2

Theoretical Background

Throughout this chapter, and indeed throughout this thesis, Hartree atomic units (a.u.) are used unless otherwise specified. In these units, the reduced Planck constant, the magnitude of the electronic charge, the rest mass of the electron and the permittivity of free space multiplied by 4π are all set equal to one:

$$\hbar = |e| = m_e = 4\pi\varepsilon_0 = 1 \ . \tag{2.1}$$

2.1 The many-body problem

2.1.1 The many-body Schrödinger equation

In theory, to completely understand the static properties of a non-relativistic quantum mechanical system, one simply needs to write down the appropriate Hamiltonian $\hat{\mathrm{H}}$ for the system and use it to solve the time-independent Schrödinger equation, $\hat{\mathrm{H}}\Psi = E\Psi$, for the energy eigenvalues E and the overall wavefunction of the system Ψ. If we work in the position representation, the wavefunction is given by $\Psi(\mathbf{r}_1, \mathbf{r}_2, ...)$, where the $\mathbf{r}_i$ represent the positions of the particles making up the system [11, 12]. From Ψ we can work out the expectation value of any observable represented by an operator $\hat{\mathrm{O}}$ by simply calculating [11]

$$\langle\Psi|\,\hat{\mathrm{O}}\,|\Psi\rangle = \int \Psi^* \hat{\mathrm{O}}\Psi \ \mathrm{d}^3\mathbf{r}_1 \mathrm{d}^3\mathbf{r}_2 ... \ . \tag{2.2}$$

Formally at least, this procedure allows us to predict the properties of any and all quantum mechanical systems, up to the point where relativistic effects become important [13].

However, for systems of more than two particles, the Schrödinger equation is no longer exactly solvable, so it must be solved numerically. For very small systems, exact numerical solutions can be found, but for systems of more than a few particles, the Schrödinger equation becomes entirely intractable, even for the best modern-day computers [12]. This results from the increasing dimension of the problem – if there are N particles, there must be $3N$ variables defining the state of the system – $r_{a,i}$, where a labels the Cartesian directions and i runs from 1 to N. This makes the problem $3N$-dimensional, significantly increasing the complexity of the problem as the system increases in size [14]. The sheer scale of this problem in most realistic systems of interest in condensed matter physics means that approximations to simplify the problem are necessary.

Before we can start to make such approximations, however, we need the general Hamiltonian of a condensed matter system, including the motions of its constituent

electrons and nuclei and their interactions. Neglecting relativistic and magnetic effects (such as the spin-orbit interaction) for the time being, the Hamiltonian can be written as

$$\begin{aligned}\hat{\mathrm{H}} &= \hat{\mathrm{T}}_{\mathrm{e}} + \hat{\mathrm{T}}_{\mathrm{n}} + \hat{\mathrm{V}}_{\text{e-e}} + \hat{\mathrm{V}}_{\text{n-n}} + \hat{\mathrm{V}}_{\text{e-n}} \qquad (2.3)\\ &= -\sum_i \frac{1}{2}\nabla_i^2 - \sum_\alpha \frac{1}{2m_\alpha}\nabla_\alpha^2 + \sum_i \sum_{j\neq i} \frac{1}{2|\mathbf{r}_i - \mathbf{r}_j|} + \sum_\alpha \sum_{\beta\neq\alpha} \frac{Z_\alpha Z_\beta}{2|\mathbf{R}_\alpha - \mathbf{R}_\beta|} - \sum_{i,\alpha} \frac{Z_\alpha}{|\mathbf{r}_i - \mathbf{R}_\alpha|}\ ,\end{aligned}$$

where i, j run over all electrons and α, β run over all nuclei. $\mathbf{r}_i$ and $\mathbf{R}_\alpha$ represent the position of the ith electron and αth nucleus respectively, whilst m_α and Z_α are the mass and atomic number of the αth nucleus respectively. The terms represent, in order, the electronic kinetic energy, the nuclear kinetic energy, the electron-electron Coulomb interaction, the nucleus-nucleus Coulomb interaction, and the electron-nucleus Coulomb interaction.

2.1.2 The Born-Oppenheimer approximation

The Hamiltonian defined by equation (2.3) includes the motion of both the nuclei and the electrons. The three potential terms, $\hat{\mathrm{V}}_{e-e}, \hat{\mathrm{V}}_{n-n}$ and $\hat{\mathrm{V}}_{e-n}$ are of similar size, only differing by factors of atomic numbers, but the mass of the electrons is smaller than that of the nuclei by a factor of the order of $m_p/m_e \simeq 1836$. This implies that the electrons move much faster than the nuclei, and are able to react to any motion of the nuclei essentially instantaneously. This suggests that it should be possible to simplify the Schrödinger equation of the problem by separating out the electronic and nuclear motion, solving the electronic problem with the nuclei fixed in place. This assumption is known as the *Born-Oppenheimer approximation* [8], and is a vital part of many calculations in condensed matter systems.

Mathematically, the Born-Oppenheimer approximation can be described as follows. We make the approximation, as mentioned above, that the nuclei can be treated as fixed point charges, allowing us to initially neglect the nuclear kinetic energy and obtain the

electronic Schrödinger equation:

$$\begin{aligned}\hat{\mathrm{H}}_{\mathrm{elec}}\phi_n(\{\mathbf{r}_k\};\{\mathbf{R}_\gamma\}) = \Bigg(&-\sum_i \frac{1}{2}\nabla_i^2 - \sum_\alpha \frac{1}{2m_\alpha}\nabla_\alpha^2 + \sum_i \sum_{j\neq i} \frac{1}{2|\mathbf{r}_i - \mathbf{r}_j|} \\ &+ \sum_\alpha \sum_{\beta\neq\alpha} \frac{Z_\alpha Z_\beta}{2|\mathbf{R}_\alpha - \mathbf{R}_\beta|} - \sum_i \sum_\alpha \frac{Z_\alpha}{|\mathbf{r}_i - \mathbf{R}_\alpha|} \Bigg) \phi_n(\{\mathbf{r}_k\};\{\mathbf{R}_\gamma\}) \\ &= E_{\mathrm{el}}^{(n)}(\{\mathbf{R}_\gamma\})\phi_n(\{\mathbf{r}_k\};\{\mathbf{R}_\gamma\}) \ .\end{aligned} \tag{2.4}$$

Here $\phi_n(\{\mathbf{r}_k\};\{\mathbf{R}_\gamma\})$ is the nth eigenfunction of the electronic Hamiltonian, with energy $E_{\mathrm{el}}^{(n)}(\{\mathbf{R}_\gamma\})$, parametrised by the fixed set of nuclear positions $\{\mathbf{R}_\gamma\}$. $\{\mathbf{r}_k\}$ represents the set of all electronic positions. The nuclear-nuclear term in the Hamiltonian is simply a constant as the positions of the nuclei are fixed.

The electronic eigenfunctions $\phi_n(\{\mathbf{r}_k\};\{\mathbf{R}_\gamma\})$ constitute a complete basis of the electronic problem, and thus we can expand any function of the electronic co-ordinates $\{\mathbf{r}_k\}$ in terms of them, including the lth eigenfunction of the total Hamiltonian shown in equation (2.3):

$$\psi_l(\{\mathbf{r}_k\};\{\mathbf{R}_\gamma\}) = \sum_n \chi_{ln}(\{\mathbf{R}_\gamma\})\phi_n(\{\mathbf{r}_k\};\{\mathbf{R}_\gamma\}) \ . \tag{2.5}$$

$\chi_{ln}(\{\mathbf{R}_\gamma\})$ are the expansion coefficients, which depend on the nuclear positions. If we now apply the total Hamiltonian of equation (2.3) to the expanded wavefunction of equation (2.5), we obtain

$$\begin{aligned}\sum_n \left[-\sum_\alpha \frac{1}{2m_\alpha}\nabla_\alpha^2 + E_{\mathrm{elec}}^{(n)}(\{\mathbf{R}_\gamma\}) \right] &\chi_{ln}(\{\mathbf{R}_\gamma\})\phi_n(\{\mathbf{r}_k\};\{\mathbf{R}_\gamma\}) \\ &= E_l \sum_n \chi_{ln}(\{\mathbf{R}_\gamma\})\phi_n(\{\mathbf{r}_k\};\{\mathbf{R}_\gamma\}) \ .\end{aligned} \tag{2.6}$$

E_l is the total energy of the lth eigenstate of the overall Hamiltonian. From now on we drop the explicit dependences on $\{\mathbf{r}_k\}$ and $\{\mathbf{R}_\gamma\}$ for brevity.

Taking the inner product of equation (2.6) with ϕ_m results in the summation over n disappearing in all terms but the first, the nuclear kinetic energy, due to the orthonormality of the electronic eigenfunctions ϕ_n. This gives

$$\sum_n \left[-\sum_\alpha \frac{1}{2m_\alpha} \int \prod_i d\mathbf{r}_i \phi_m^* \nabla_\alpha^2 (\chi_{ln}\phi_n) \right] + E_{\mathrm{elec}}^{(m)}\chi_{lm} = E_l\chi_{lm} \ . \tag{2.7}$$

Applying the product rule $\nabla^2(fg) = f\nabla^2 g + g\nabla^2 f + 2(\nabla f)\cdot(\nabla g)$ to the first term and again using the orthonormality of the ϕ_n gives

$$-\sum_n \sum_\alpha \frac{1}{2m_\alpha}\left[\chi_{lm}\int\prod_i d\mathbf{r}_i\phi_m^*\nabla_\alpha^2\phi_n + 2(\nabla_\alpha\chi_{lm})\cdot\int\prod_i d\mathbf{r}_i\phi_m^*(\nabla_\alpha\phi_n)\right] \tag{2.8}$$
$$+\left[-\sum_\alpha \frac{1}{2m_\alpha}\nabla_\alpha^2 + E_{\text{elec}}^{(m)}\right]\chi_{lm} = E_l\chi_{lm}\ .$$

We can now assume that, due to the much greater speed of the electrons compared to the nuclei, changes to the nuclear positions only affect the electronic state adiabatically – that is, smooth changes in the nuclear positions will not cause transitions between different ϕ_n, according to the adiabatic principle [15, 16]. This eliminates all the non-diagonal terms in the sum, i.e. those where $n \neq m$. The diagonal terms remaining in the first summation over α can also be neglected. The expectation value of ∇_α is exactly zero, as it is proportional to the derivative of a constant, the total density of electrons, whilst the expectation value of $\frac{1}{2m_\alpha}\nabla_\alpha^2$ is of the same magnitude as the electronic kinetic energy multiplied by $\frac{1}{m_\alpha}$, which is negligible compared to the other energies involved. This leaves us with the final nuclear Schrödinger equation:

$$\left[-\sum_\alpha \frac{1}{2m_\alpha}\nabla_\alpha^2 + E_{\text{elec}}^{(m)}\right]\chi_{lm} = \hat{\text{H}}_{\text{vib}}\chi_{lm} = E_l\chi_{lm}\ . \tag{2.9}$$

The eigenvalue $E_{\text{elec}}^{(m)}$ for a given configuration of nuclei, obtained from the solution of the electronic equation (equation (2.4)), defines the potential energy surface that the nuclei move in [17]. This is known as the *Born-Oppenheimer (BO) surface*. Although in general any electronic state could be used to define the BO surface, in this work we will only consider the electronic ground state, where $m = 0$.

By utilising the Born-Oppenheimer approximation, we have been able to simplify the problem presented by the full Schrödinger equation by splitting it into two parts – the electronic and nuclear motion. The electronic Schrödinger equation, equation (2.4), is solved first, followed by the nuclear/vibrational equation, equation (2.9), using a suitable expression for the BO surface. In the remainder of this section and all of the next, we will discuss methods for solving the electronic problem, before finally discussing methods of solving the vibrational problem in the final section of this chapter.

2.1.3 Determining the electronic wavefunction

The variational principle

Before tackling the general N-electron problem, it is useful to first consider a system that contains only a single electron, meaning that the electron-electron interaction term in equation (2.4) can be ignored. We can solve the electronic Schrödinger equation of this system to obtain single-particle wavefunctions $\psi_i(\mathbf{x}) = \phi_i(\mathbf{r})\xi_i(\sigma)$. Here, $\xi_i(\sigma)$ is the spin part of the wavefunction, dependent on the electronic spin σ, whilst $\phi_i(\mathbf{r})$ is the spatial part. $\mathbf{x}$ is a collective vector of the space and spin co-ordinates $(\mathbf{r}, \sigma)$.

If we now want to consider a system with N electrons instead of one, our problem becomes harder. The introduction of the electron-electron interaction means that the N-body eigenfunctions of the electronic Hamiltonian cannot be found exactly in general, so we must instead turn to approximate approaches to find the electronic ground state. Of particular use here is the theorem known as the variational principle [17]. This states that, given a Hamiltonian $\hat{\mathrm{H}}$ and a wavefunction $\tilde{\Psi}$ (not necessarily an eigenfunction of the Hamiltonian), the expectation value of the Hamiltonian over this wavefunction gives an upper bound to the ground state energy of the system. Mathematically in bra-ket notation:

$$\langle \tilde{\Psi} | \hat{\mathrm{H}} | \tilde{\Psi} \rangle \geq E_0 \ , \tag{2.10}$$

where E_0 is the ground state energy, and it is assumed that $\tilde{\Psi}$ is normalised. The equality holds if $\tilde{\Psi}$ is exactly the ground state wavefunction $\tilde{\Psi}_0$.

The variational principle implies that, given a set of trial wavefunctions obtained by some procedure, the linear combination of these trial wavefunctions that minimises the expectation value of the Hamiltonian gives an estimate of the ground state energy. It also provides an approximation to the true ground state wavefunction, although equation (2.10) implies that first order errors in the wavefunction give second order errors in the ground state energy. This means that a good estimate of E_0 can be obtained from wavefunctions that are significantly different to the true ground state wavefunction.

Hartree products

In order to use the variational principle to get a good estimate of the ground state energy, we need to use an appropriate set of trial wavefunctions. A potential choice could be a

simple product of single-particle wavefunctions, known as a *Hartree product* [17]:

$$\Psi_{\text{Hartree}}(\mathbf{x}_1, \mathbf{x}_2, \ldots, \mathbf{x}_N) = \psi_i(\mathbf{x}_1)\psi_j(\mathbf{x}_2)\ldots\psi_k(\mathbf{x}_3) \ . \tag{2.11}$$

Different trial wavefunctions are given by different values for the integers $i, j, \ldots, k$.

Whilst the Hartree product has the advantage of being simple, it does not include the correlation between the electrons due to the electron-electron interaction term. More importantly, however, it does not take into account the indistinguishability of electrons, which has implications for the form of the wavefunction.

Exchange symmetry

A many-body wavefunction of a set of fundamentally indistinguishable particles, such as electrons, should possess exchange symmetry. This means that, if two electrons are swapped over, the electronic probability density, which is proportional to the modulus of the wavefunction squared, should remain precisely the same, as the two particles are absolutely identical. Mathematically, this means that particle exchange can only change the phase of the wavefunction:

$$\Psi(\mathbf{x}_1, \ldots, \mathbf{x}_j, \ldots, \mathbf{x}_i, \ldots, \mathbf{x}_N) = e^{i\alpha}\Psi(\mathbf{x}_1, \ldots, \mathbf{x}_i, \ldots, \mathbf{x}_j, \ldots, \mathbf{x}_N) \ . \tag{2.12}$$

If we exchange the particles for a second time, we obtain a second phase factor, giving

$$\Psi(\mathbf{x}_1, \ldots, \mathbf{x}_i, \ldots, \mathbf{x}_j, \ldots, \mathbf{x}_N) = e^{i2\alpha}\Psi(\mathbf{x}_1, \ldots, \mathbf{x}_i, \ldots, \mathbf{x}_j, \ldots, \mathbf{x}_N) \ . \tag{2.13}$$

This implies that the change in phase $\alpha = 0$ or π, i.e. the wavefunction after exchange is either equal to or -1 times the original wavefunction [11]:

$$\Psi(\mathbf{x}_1, \ldots, \mathbf{x}_j, \ldots, \mathbf{x}_i, \ldots, \mathbf{x}_N) = \pm\Psi(\mathbf{x}_1, \ldots, \mathbf{x}_i, \ldots, \mathbf{x}_j, \ldots, \mathbf{x}_N) \ . \tag{2.14}$$

Taking the positive solution gives an exchange symmetric wavefunction, whilst the negative solution gives an exchange antisymmetric wavefunction. Particles which have symmetric wavefunctions are known as bosons, and those with antisymmetric wavefunctions are known as fermions. The spin-statistics theorem states that particles with integer values of spin are bosons, whilst those with half-integer values of spin are fermions [18]. Electrons are spin-$\frac{1}{2}$ particles, and are therefore fermions, meaning they have a wavefunction that is antisymmetric under exchange.

A consequence of the requirement of exchange antisymmetry is the Pauli exclusion principle for fermions. This states that two fermions cannot occupy the same quantum state. If two fermions occupying the same state were exchanged, the total wavefunction would remain the same. However, the total wavefunction must also change its sign when two fermions are exchanged. The only way for these two requirements to be consistent is if the total wavefunction is zero – that is, the probability of an overall state containing two fermions sharing a quantum state is zero.

Slater determinants

The Hartree product as defined in equation (2.11) is symmetric under exchange, unlike the true N-electron wavefunction. To fix this problem and take exchange symmetry into account correctly, we need a new set of trial wavefunctions that are antisymmetric under exchange. A convenient way of enforcing this antisymmetry on the trial wavefunctions is to use *Slater determinants* [17, 19]. These express the wavefunction as a determinant of single particle states:

$$\Psi_{\text{Slater}}(\mathbf{x}_1, \mathbf{x}_2, \ldots, \mathbf{x}_N) = \frac{1}{\sqrt{N!}} \begin{vmatrix} \psi_1(\mathbf{x}_1) & \psi_2(\mathbf{x}_1) & \cdots & \psi_N(\mathbf{x}_1) \\ \psi_1(\mathbf{x}_2) & \psi_2(\mathbf{x}_2) & \cdots & \psi_N(\mathbf{x}_2) \\ \vdots & \vdots & \ddots & \vdots \\ \psi_1(\mathbf{x}_N) & \psi_2(\mathbf{x}_N) & \ldots & \psi_N(\mathbf{x}_N) \end{vmatrix} . \tag{2.15}$$

$\frac{1}{\sqrt{N!}}$ is a normalisation factor. Exchanging two particles amounts to swapping two rows of the determinant, which changes the overall sign, as required.

The exchange-correlation hole

A consequence of the presence of exchange antisymmetry (as well as the Coulomb repulsion between particles in the case of electrons) is the existence of the *exchange-correlation hole*. This concept arises from the fact that the presence of an electron reduces the probability of other electrons being nearby, due to both exchange and correlation effects. We can express this in terms of the pair density

$$n(\mathbf{x}, \mathbf{x}') = N(N-1) \int \prod_{i=3}^{N} d\mathbf{x}_i |\Psi(\mathbf{x}, \mathbf{x}', \mathbf{x}_3, \ldots, \mathbf{x}_N)|^2 . \tag{2.16}$$

The single-particle density is

$$n(\mathbf{x}) = N \int \prod_{i=2}^{N} d\mathbf{x}_i |\Psi(\mathbf{x}, \mathbf{x}_2, \ldots, \mathbf{x}_N)|^2 \ . \tag{2.17}$$

For two non-interacting classical particles, the pair density is simply the product of the individual single-particle densities, $n(\mathbf{x}, \mathbf{x}') = n(\mathbf{x})n(\mathbf{x}')$, but for interacting quantum mechanical particles we expect a correction due to exchange-correlation effects, leading us to write

$$n(\mathbf{x}, \mathbf{x}') = n(\mathbf{x})n(\mathbf{x}') + n(\mathbf{x})n_{\mathrm{xc}}(\mathbf{x}, \mathbf{x}') \ . \tag{2.18}$$

$n_{\mathrm{xc}}(\mathbf{x}, \mathbf{x}')$ is the exchange-correlation hole density.

As the wavefunction is assumed to be normalised to 1, equations (2.16) and (2.17) lead directly to the expressions

$$\int d\mathbf{x} d\mathbf{x}' n(\mathbf{x}, \mathbf{x}') = N(N-1) \tag{2.19}$$

$$\int d\mathbf{x} n(\mathbf{x}) = N \ . \tag{2.20}$$

Substituting (2.18) into (2.19) and applying (2.20) leads us finally to the exchange-correlation hole sum rule:

$$\int d\mathbf{x}' n_{\mathrm{xc}}(\mathbf{x}, \mathbf{x}') = -1 \ . \tag{2.21}$$

The Hartree-Fock method

Using a Slater determinant as the trial wavefunction, we can now calculate the expectation value of the electronic Hamiltonian in equation (2.4), before minimising this expectation value with respect to the single-particle states. This is known as the Hartree-Fock method [17]. Splitting $\mathbf{x}$ into its component parts $(\mathbf{r}, \sigma)$ and neglecting the constant nucleus-nucleus interaction term, we obtain the expectation value of the Hamiltonian as:

$$\begin{aligned} \langle \hat{\mathrm{H}}_{\mathrm{elec}} \rangle = & \sum_{i,\sigma} \int d\mathbf{r} \psi_i^*(\mathbf{r}, \sigma) \left(-\frac{1}{2}\nabla^2 - \sum_{\alpha} \frac{Z_\alpha}{|\mathbf{r} - \mathbf{R}_\alpha|} \right) \psi_i(\mathbf{r}, \sigma) \\ & + \sum_{i,j} \sum_{\sigma,\rho} \int d\mathbf{r} d\mathbf{r}' \frac{|\psi_i(\mathbf{r}, \sigma)|^2 |\psi_j(\mathbf{r}', \rho)|^2}{2|\mathbf{r} - \mathbf{r}'|} \\ & - \sum_{i,j} \sum_{\sigma,\rho} \int d\mathbf{r} d\mathbf{r}' \frac{\psi_i^*(\mathbf{r}, \sigma) \psi_j^*(\mathbf{r}', \rho) \psi_i(\mathbf{r}', \rho) \psi_j(\mathbf{r}, \sigma)}{2|\mathbf{r} - \mathbf{r}'|} \ . \end{aligned} \tag{2.22}$$

The first term includes all the terms in the Hamiltonian that depend on only one electron, so only includes one integral over $\mathbf{r}$ and one summation each over spin (σ) and single-particle states (i). The second and third terms are known as the direct and exchange terms respectively. They involve the interaction between two electrons, and therefore include double the number of summations and integrals. The direct interaction can be interpreted as simply the Coulomb repulsion of the two electrons, as $|\psi_i(\mathbf{r},\sigma)|^2$ represents the electron probability density. The exchange interaction, however, has no classical analogue, and arises from the correlation of the motion of electrons with parallel spin, due to the antisymmetry of the Slater determinant and the Pauli exclusion principle. Although terms where $i = j$ do not exist in the Hamiltonian, they are included here for ease of notation, as the $i = j$ terms in the direct and exchange integrals in equation (2.22) cancel.

We can now minimise equation (2.22) by varying the single-particle states, subject to the constraint that they remain orthonormal, which leads directly to the Hartree-Fock integro-differential equation [17]:

$$\left(-\frac{1}{2}\nabla^2 - \sum_\alpha \frac{Z_\alpha}{|\mathbf{r}-\mathbf{R}_\alpha|}\right)\psi_i(\mathbf{r},\sigma) + \sum_{j,\rho}\int d\mathbf{r}'\frac{|\psi_j(\mathbf{r}',\rho)|^2}{|\mathbf{r}-\mathbf{r}'|}\psi_i(\mathbf{r},\sigma) - \sum_{j,\rho}\int d\mathbf{r}'\frac{\psi_j^*(\mathbf{r}',\rho)\psi_i(\mathbf{r}',\rho)}{|\mathbf{r}-\mathbf{r}'|}\psi_j(\mathbf{r},\sigma) = \epsilon_i\psi_i(\mathbf{r},\sigma)\ . \tag{2.23}$$

ϵ_i is the energy eigenvalue of the single-electron state ψ_i.

As the integrals used to calculate the potentials in equation (2.23) involve the single-particle states, the Hartree-Fock equation can only be solved iteratively in a self-consistent manner. Starting with an initial guess at the form of the $\psi_i(\mathbf{r},\sigma)$, we calculate the direct and exchange integrals and solve the equation to obtain a new set of $\psi_i(\mathbf{r},\sigma)$. The process is then repeated with the new single-particle states until self-consistency is reached, i.e. the input states and the output states for an iteration are equal to within some tolerance. Once this has been achieved, we can construct the ground state wave-function from the N states with the lowest energies. The energy of this ground state is given by

$$E_0^{(\mathrm{HF})} = \sum_i \epsilon_i - \sum_{i,j}\sum_{\sigma,\rho}\int d\mathbf{r}d\mathbf{r}'\frac{|\psi_i(\mathbf{r},\sigma)|^2|\psi_j(\mathbf{r}',\rho)|^2}{2|\mathbf{r}-\mathbf{r}'|} + \sum_{i,j}\sum_{\sigma,\rho}\int d\mathbf{r}d\mathbf{r}'\frac{\psi_i^*(\mathbf{r},\sigma)\psi_j^*(\mathbf{r}',\rho)\psi_i(\mathbf{r}',\rho)\psi_j(\mathbf{r},\sigma)}{2|\mathbf{r}-\mathbf{r}'|}\ . \tag{2.24}$$

The Hartree-Fock approximation includes the effect of exchange in its solution of the electronic problem, but has the major flaw that it does not take the correlation between electrons fully into account. The motion of electrons with opposite spins will be correlated in the exact solution, but within the Hartree-Fock approximation, correlation of electrons with opposite spins is not considered at all [17]. A number of ways of dealing with this issue have been devised. One method is to view the difference between the Hartree-Fock Hamiltonian and the exact Hamiltonian as a perturbation to the Hartree-Fock Hamiltonian, and treat it with Møller-Plesset perturbation theory [20]. Alternatively, it can be seen that the wavefunctions of the eigenstates of the exact N-electron Hamiltonian can be written as a linear combination of a complete set of N-electron Slater determinants, instead of simply including one Slater determinant as in the Hartree-Fock method. Exact diagonalisation can then be used to find the ground and excited states, a method known as *configuration interaction* (CI) [17]. However, the number of determinants increases exponentially with the number of electrons, meaning that calculations involving all possible determinants (full CI) are limited at present to around twenty electrons, using the most advanced full CI quantum Monte Carlo (QMC) methods [21–23]. The number of Slater determinants can be reduced by only including single or double excitations, or both (SCI, DCI and SDCI respectively), but such truncated CI calculations lose the property of size consistency – in a system consisting of two non-interacting parts, truncated CI calculations of the total energy are not simply the sum of the truncated CI energies of the parts. A third possibility is to use the *coupled cluster* (CC) method [24], which uses an expansion in terms of Slater determinants in the form of an exponential wavefunction ansatz, which guarantees size consistency. This expansion is also often truncated to include up to single, double, triple, and further excitations.

All the post-Hartree-Fock methods mentioned above scale badly with system size, meaning that only small systems can be feasibly studied. In order to make progress with larger systems of the kind that often occur in condensed matter physics, an alternative approach is needed, that can deal with large systems whilst still providing accurate results.

2.2 Density functional theory

2.2.1 Historical background

In order to calculate the ground state properties of systems larger than a few atoms, we need a new method that can calculate at least some properties to an acceptable degree of accuracy. *Density functional theory* (DFT), which was initially proposed in 1964-5 by Kohn, Hohenberg and Sham [25, 26], and led to Kohn being awarded the 1998 Nobel Prize in Chemistry, provides just such a method. Since the 1980s, the number of publications per year on the topic of DFT has continually increased, with a particularly dramatic growth occurring after 1990 and continuing to the present day. Well over 15000 publications on the topic have been published per year in recent times, making DFT the most popular method for calculating electronic structure today [27]. It is based on the simple idea that, instead of using the $3N$-dimensional wavefunction to characterise the state of the system, we can use the 3-dimensional electron density, $n(\mathbf{r})$, to uniquely identify the state, which drastically reduces the size and complexity of the problem [28].

The idea of using the density instead of the wavefunction had been considered before 1964 – Thomas-Fermi (TF) theory, formulated in 1927, was the first use of electron density to characterise a system [29–31]. In TF theory, the electrons are treated as independent, only interacting via the electrostatic interaction, and the kinetic energy is taken to be that of a gas of non-interacting electrons with density $n(\mathbf{r})$, i.e. $T_0[n(\mathbf{r})] = \frac{3}{10}(3\pi^2)^{\frac{2}{3}} \int d\mathbf{r}[n(\mathbf{r})]$. Minimising the total energy functional, using these approximations and with particle number held constant, gives the Thomas-Fermi equation [12]:

$$\frac{1}{2}(3\pi^2 n(\mathbf{r}))^{\frac{2}{3}} + \int d\mathbf{r}' \frac{n(\mathbf{r}')}{|\mathbf{r} - \mathbf{r}'|} + V_{\text{ext}}(\mathbf{r}) + \mu = 0 \ . \tag{2.25}$$

However, the approximations involved in TF theory are quite significant and lead to many serious problems. TF theory incorrectly predicts that the electronic charge density decays as r^{-6} far from the nucleus, instead of exponentially, and also lacks any atomic shell structure, meaning it cannot reproduce the periodicity of many properties with atomic number seen in the periodic table [27]. It also cannot describe binding in molecules or solids [12, 31, 32]. In order to improve on this state of affairs and obtain reasonable results, DFT splits up the total energy functional in a different way to TF theory, and makes different approximations.

2.2.2 The Hohenberg-Kohn theorems

The use of the electronic density instead of the wavefunction to characterise the state of the system, the bedrock of DFT, is justified by the two Hohenberg-Kohn (HK) theorems, first demonstrated by their namesakes, and later more extensively proved by Levy [25, 33]. These theorems state that: [14]

1. the energy, wavefunction and other properties of the ground state are uniquely determined by the electron density, and

2. that the density that minimises the energy, expressed as a functional of the electron density, is the true electron density of the ground state.

In principle, these results allow us to find the ground state density and energy by varying the density until we reach a minimum of the energy functional. Before going any further, we will briefly look at these theorems on a more mathematical basis.

The first Hohenberg-Kohn theorem

The ground state density at a point $\mathbf{r}$ is defined as

$$n_0(\mathbf{r}) = N \sum_{\sigma} \sum_{\sigma_2,\sigma_3,\ldots,\sigma_N} \int \prod_{i=2}^{N} d\mathbf{r}_i |\Psi_0(\mathbf{r}, \mathbf{r}_2, \ldots, \mathbf{r}_N)|^2 \ , \tag{2.26}$$

and the Hamiltonian is taken to be of the general form

$$\hat{\mathrm{H}} = -\frac{1}{2} \sum_i \nabla_i^2 + \sum_i \sum_{j \neq i} \frac{1}{2|\mathbf{r}_i - \mathbf{r}_j|} + \sum_i V_{\mathrm{ext}}(\mathbf{r}_i) \ . \tag{2.27}$$

Here, Ψ_0 is the ground state wavefunction, and $V_{\mathrm{ext}}(\mathbf{r})$ is an external potential. In the case of the electronic Hamiltonian, the three terms in equation (2.27) correspond to $\hat{\mathrm{T}}_{\mathrm{e}}$, $\hat{\mathrm{V}}_{\text{e-e}}$ and $\hat{\mathrm{V}}_{\text{e-n}}$ from equation (2.3), respectively.

To prove the first HK theorem, we need to show that there is a one-to-one correspondence between the Hamiltonian of the system (up to a constant) and its ground state density. As the rest of the Hamiltonian is fixed, this implies that external potentials $V_{\mathrm{ext}}(\mathbf{r})$ that differ by more than a constant must lead to different ground state densities. To begin, we assume that there *are* two Hamiltonians, $\hat{\mathrm{H}}_1$ and $\hat{\mathrm{H}}_2$, differing by more than a constant, that produce the same ground state density, $n_0(\mathbf{r})$. The external potentials are $V_{\mathrm{ext}}^{(1)}(\mathbf{r})$ and $V_{\mathrm{ext}}^{(2)}(\mathbf{r})$ respectively. These two Hamiltonians must have different ground

state wavefunctions $\Psi_0^{(1)} = \Psi_0^{(1)}(\mathbf{r}_1, \ldots, \mathbf{r}_N)$ and $\Psi_0^{(2)} = \Psi_0^{(2)}(\mathbf{r}_1, \ldots, \mathbf{r}_N)$, with energies $E_0^{(1)}$ and $E_0^{(2)}$ respectively. $\Psi_0^{(1)}$ cannot be the ground state (or even an eigenfunction) of $\hat{\mathrm{H}}_2$, as if it were (that is, $\hat{\mathrm{H}}_2\Psi_0^{(1)} = E'\Psi_0^{(1)}$), we would obtain:

$$(\hat{\mathrm{H}}_1 - \hat{\mathrm{H}}_2)\Psi_0^{(1)} = (E_0^{(1)} - E')\Psi_0^{(1)} \ . \tag{2.28}$$

This implies that $\hat{\mathrm{H}}_1 - \hat{\mathrm{H}}_2$ is simply a constant, contradicting our initial assumption. The same argument applies for $\Psi_0^{(2)}$ and $\hat{\mathrm{H}}_1$, showing that $\Psi_0^{(1)}$ and $\Psi_0^{(2)}$ must be different.

We can then apply the variational principle, as expressed in equation (2.10), to the expectation value of $\hat{\mathrm{H}}_1$ in the state $\Psi_0^{(2)}$:

$$\begin{aligned} E_0^{(1)} < \int \prod_i d\mathbf{r}_i \Psi_0^{(2)*} \hat{\mathrm{H}}_1 \Psi_0^{(2)} &= \int \prod_i d\mathbf{r}_i \left[\Psi_0^{(2)*} \hat{\mathrm{H}}_2 \Psi_0^{(2)} + \Psi_0^{(2)*} (\hat{\mathrm{H}}_1 - \hat{\mathrm{H}}_2) \Psi_0^{(2)} \right] \\ &= E_0^{(2)} + \int d\mathbf{r} \left(V_{\mathrm{ext}}^{(1)}(\mathbf{r}) - V_{\mathrm{ext}}^{(2)}(\mathbf{r}) \right) n_0(\mathbf{r}) \ . \end{aligned} \tag{2.29}$$

The strict inequality holds because $\Psi_0^{(2)}$ is not the ground state of $\hat{\mathrm{H}}_1$. If we do the same for the expectation value of $\hat{\mathrm{H}}_2$ in the state $\Psi_0^{(1)}$, we get a similar result:

$$E_0^{(2)} < E_0^{(1)} + \int d\mathbf{r} \left(V_{\mathrm{ext}}^{(2)}(\mathbf{r}) - V_{\mathrm{ext}}^{(1)}(\mathbf{r}) \right) n_0(\mathbf{r}) \ . \tag{2.30}$$

Because the ground state density is assumed to be the same for both wavefunctions, adding inequalities (2.29) and (2.30) results in the integral term cancelling, to give

$$E_0^{(1)} + E_0^{(2)} < E_0^{(2)} + E_0^{(1)} \ . \tag{2.31}$$

This is clearly contradictory, thus proving that our initial assumption must have been incorrect, and that there is a one-to-one correspondence between the Hamiltonian of the system (up to a constant) and its ground state density [25]. As the density uniquely determines the Hamiltonian, and the Hamiltonian defines the wavefunctions and thus the properties of the system, this proves that all properties of the system are uniquely determined by the ground state electron density.

The second Hohenberg-Kohn theorem

Thanks to the first HK theorem, we know the energy of the system is defined by the ground state density, meaning the energy of the system can be written as a functional of the density $n(\mathbf{r})$:

$$E[n(\mathbf{r})] = F[n(\mathbf{r})] + V[n(\mathbf{r})] \ . \tag{2.32}$$

Comparing to equation (2.27), $F[n(\mathbf{r})]$ corresponds to the kinetic and electron-electron interaction energy, whilst $V[n(\mathbf{r})] = \int d\mathbf{r} V_{\text{ext}}(\mathbf{r}) n(\mathbf{r})$ corresponds to the energy contribution due to the external potential $V_{\text{ext}}(\mathbf{r})$. It should be noted that $F[n(\mathbf{r})]$ is universal – it remains the same for any number of particles and any external potential.

To prove the second HK theorem, we need to show that the density that minimises the functional $E[n(\mathbf{r})]$ is the ground state density. We can express $E[n(\mathbf{r})]$ in terms of the wavefunction $\Psi = \Psi(\mathbf{r}_1, \ldots, \mathbf{r}_N)$ as

$$\mathcal{E}[\Psi] = \int \prod_i d\mathbf{r}_i \Psi^* \hat{\mathrm{H}} \Psi = F[n(\mathbf{r})] + \int d\mathbf{r} V_{\text{ext}}(\mathbf{r}) n(\mathbf{r}) = E[n(\mathbf{r})] \ , \tag{2.33}$$

where $\hat{\mathrm{H}}$ is the general Hamiltonian defined in equation (2.27). By the variational principle, this is minimised when the wavefunction is the ground state wavefunction of the Hamiltonian corresponding to $V_{\text{ext}}(\mathbf{r})$, Ψ_0. In particular, we can consider the ground state associated with a different external potential $V'_{\text{ext}}(\mathbf{r})$, Ψ'_0. Taking the ground state densities corresponding to $V_{\text{ext}}(\mathbf{r})$ and $V'_{\text{ext}}(\mathbf{r})$ as $n_0(\mathbf{r})$ and $n'_0(\mathbf{r})$ respectively, we can use the variational principle to write

$$E[n'_0(\mathbf{r})] = \mathcal{E}[\Psi'_0] > \mathcal{E}[\Psi_0] = E[n_0(\mathbf{r})] \ . \tag{2.34}$$

This shows that the functional $E[n(\mathbf{r})]$ is minimised by the true ground state density, as required.

The original proof of the second HK theorem by Hohenberg and Kohn, as outlined above [25], is restricted to densities that are *V-representable* – that is, the only densities included are those that correspond to the ground state of a Hamiltonian with a particular external potential $V_{\text{ext}}(\mathbf{r})$. Densities that are not V-representable can exist, for example in systems that have more than two degenerate ground states [34], and so it is desirable to extend the theorem to include *N-representable* densities - those that can be obtained directly from an antisymmetric N-body wavefunction. It has been proved that all mathematically well-behaved non-negative functions are N-representable, so any physical ground state density is also N-representable [27, 35]. Levy generalised the second HK theorem to N-representable densities by using a *constrained search* formulation [33].

Using bra-ket notation, the constrained search formulation of DFT redefines the

functional $E[n(\mathbf{r})]$ as

$$E_{\text{Levy}}[n(\mathbf{r})] = \min_{\Psi \to n(\mathbf{r})} \left[\langle \Psi | \, \hat{\text{H}} \, | \Psi \rangle \right] = \min_{\Psi \to n(\mathbf{r})} \left[\langle \Psi | \, (\hat{\text{T}}_e + \hat{\text{V}}_{\text{e-e}}) \, | \Psi \rangle \right] + \int d\mathbf{r} V_{\text{ext}}(\mathbf{r}) n(\mathbf{r}) = F_{\text{Levy}}[n(\mathbf{r})] + \int d\mathbf{r} V_{\text{ext}}(\mathbf{r}) n(\mathbf{r}) \ . \tag{2.35}$$

$\hat{\text{T}}_e$ is the electronic kinetic energy operator and $\hat{\text{V}}_{\text{e-e}}$ is the electron-electron interaction operator. The notation $\Psi \to n(\mathbf{r})$ here means that the expectation value of the operator is minimised over all antisymmetric wavefunctions, Ψ, that give the density $n(\mathbf{r})$. $E_{\text{Levy}}[n(\mathbf{r})]$ is then minimised with respect to $n(\mathbf{r})$ to obtain the ground state energy and density. Taking the functional derivative of equation (2.35) and setting it equal to zero to find the minimum gives the equation

$$\frac{\delta F_{\text{Levy}}[n(\mathbf{r})]}{\delta n(\mathbf{r})} = -V_{\text{ext}}(\mathbf{r}) \ . \tag{2.36}$$

The two HK theorems are exact, but two significant issues remain. Firstly, despite our assertion that the wavefunction and all other properties of the system are uniquely determined by the density, we have no method of actually obtaining the wavefunction from the density. Secondly, the functional $F[n(\mathbf{r})]$, which depends solely on the density and is universal to all systems, has not been found, and its form is unknown. Before we can make full use of DFT, these problems must be addressed.

2.2.3 The Kohn-Sham equations

In order to completely solve for the behaviour of the system defined by the general Hamiltonian in equation (2.27), we must find a way to deal with this many-body interacting problem. The method originally proposed by Kohn and Sham in 1965 [26] involved simplifying the problem by assuming that the complicated exact system can be replaced by a simpler non-interacting auxiliary system, with the same ground state density as the exact system [36]. This is called *non-interacting V-representability*. This non-interacting system is defined by the auxiliary Hamiltonian

$$\hat{\text{H}}_{\text{aux}} = -\frac{1}{2} \sum_i \nabla_i^2 + \sum_i V_{\text{aux}}(\mathbf{r}_i, \sigma_i) \ , \tag{2.37}$$

with $V_{\text{aux}}(\mathbf{r}_i, \sigma_i)$ the effective potential of the auxiliary system, the form of which is unknown at present. This potential is local as it only depends on the position and spin of the ith particle, $\mathbf{r}_i$ and σ_i. If we write the eigenfunctions and eigenvalues of $\hat{\text{H}}_{\text{aux}}$ as

$\psi_i(\mathbf{r},\sigma)$ and ϵ_i respectively, the ground state density (of both the auxiliary and the exact system) is

$$n(\mathbf{r}) = \sum_{\sigma}\sum_{i} |\psi_i(\mathbf{r},\sigma)|^2 \ . \tag{2.38}$$

This implies that solving the non-interacting system can lead us directly to the ground state density, which can then be used to solve the exact problem. The ψ_i are known as the *Kohn-Sham (KS) states*.

We now have a method for calculating the ground state density, given a form for V_{aux}. Let us now return to the exact interacting problem, and more specifically to the energy functional $E[n(\mathbf{r})]$ defined in equation (2.32). A second important part of the Kohn-Sham method now comes into play – a simple but powerful rewriting of $E[n(\mathbf{r})]$ [36]. $F[n(\mathbf{r})]$ is written as a sum of several terms, giving [28]

$$\begin{aligned} E[n(\mathbf{r})] &= T_0[n(\mathbf{r})] + E_{\text{Hartree}}[n(\mathbf{r})] + E_{\text{xc}}[n(\mathbf{r})] + V[n(\mathbf{r})] \\ &= \sum_{\sigma,i}\int d\mathbf{r}|\nabla\psi_i(\mathbf{r},\sigma)|^2 + \int d\mathbf{r}d\mathbf{r}'\frac{n(\mathbf{r})n(\mathbf{r}')}{2|\mathbf{r}-\mathbf{r}'|} + E_{\text{xc}}[n(\mathbf{r})] + \int d\mathbf{r}V_{\text{ext}}(\mathbf{r})n(\mathbf{r}) \ . \end{aligned} \tag{2.39}$$

$T_0[n(\mathbf{r})]$ is the kinetic energy of the non-interacting auxiliary system, which can be calculated directly from the KS states, as shown. This is clearly an approximation to the true kinetic energy, but is of comparable magnitude, and has the advantage that it can be calculated exactly [12]. Any corrections to the kinetic energy are absorbed into the unknown $E_{\text{xc}}[n(\mathbf{r})]$ term. $E_{\text{Hartree}}[n(\mathbf{r})]$ is the *Hartree energy*, which is simply the Coulomb energy due to the electron density interacting with itself.

The only term we do not have an exact form for is $E_{\text{xc}}[n(\mathbf{r})]$, known as the *exchange-correlation functional*. $E_{\text{xc}}[n(\mathbf{r})]$ is defined by equation (2.39), and contains everything not included in the three other exact terms, including exchange-correlation effects, thus making equation (2.39) formally exact.

Other than finding a suitable form for $E_{\text{xc}}[n(\mathbf{r})]$, the last remaining piece of the puzzle is finding $V_{\text{aux}}(\mathbf{r})$, the effective potential of the Kohn-Sham auxiliary system. We can approach this by minimising equation (2.39) with respect to the KS states, which gives [36]

$$\frac{\delta T_0[n(\mathbf{r})]}{\delta\psi_i^*(\mathbf{r})} + \left[\frac{\delta V[n(\mathbf{r})]}{\delta n(\mathbf{r})} + \frac{\delta E_{\text{Hartree}}[n(\mathbf{r})]}{\delta n(\mathbf{r})} + \frac{\delta E_{\text{xc}}[n(\mathbf{r})]}{\delta n(\mathbf{r})}\right]\frac{\delta n(\mathbf{r})}{\delta\psi_i^*(\mathbf{r})} = 0 \ , \tag{2.40}$$

subject to enforcing orthonormalisation of the $\psi_i(\mathbf{r})$. If we then use the results

$$\frac{\delta T_0[n(\mathbf{r})]}{\delta\psi_i^*(\mathbf{r})} = -\frac{1}{2}\nabla^2\psi_i(\mathbf{r}) \text{ and } \frac{\delta n(\mathbf{r})}{\delta\psi_i^*(\mathbf{r})} = \psi_i(\mathbf{r}) \ , \tag{2.41}$$

as well as using the method of Lagrange multipliers to enforce orthonormalisation, we obtain the Kohn-Sham equations [12, 14]:

$$\left[-\frac{1}{2}\nabla^2 + V_{\text{Hartree}}(\mathbf{r}) + V_{\text{ext}}(\mathbf{r}) + V_{\text{xc}}(\mathbf{r})\right]\psi_i(\mathbf{r}) = \epsilon_i\psi_i(\mathbf{r}) \ , \tag{2.42}$$

$$V_{\text{Hartree}}(\mathbf{r}) = \int d\mathbf{r}' \frac{n(\mathbf{r}')}{|\mathbf{r}-\mathbf{r}'|} \ , \ V_{\text{xc}}(\mathbf{r}) = \frac{\delta E_{\text{xc}}[n(\mathbf{r})]}{\delta n(\mathbf{r})} \ . \tag{2.43}$$

Comparing this to the non-interacting auxiliary Hamiltonian of equation (2.37), we obtain an expression for V_{aux}:

$$V_{\text{aux}}(\mathbf{r}) = V_{\text{Hartree}}(\mathbf{r}) + V_{\text{ext}}(\mathbf{r}) + V_{\text{xc}}(\mathbf{r}) \ . \tag{2.44}$$

With this expression for the auxiliary effective potential, the Kohn-Sham auxiliary system can be solved if we have an appropriate form for $V_{\text{xc}}(\mathbf{r})$ [26, 28]. It is clear that $V_{\text{aux}}(\mathbf{r})$ depends on $n(\mathbf{r})$, but $n(\mathbf{r})$ depends on the KS states $\psi_i(\mathbf{r})$, which are found using V_{aux}. This means a self-consistent procedure is required to solve this system of equations, which, at its simplest, involves four steps [14]:

1. Take an initial trial guess for the electron density $n_{\text{in}}(\mathbf{r})$.
2. Use the trial density to solve the KS equations for the KS states $\psi_i(\mathbf{r})$.
3. Calculate a new electron density $n_{\text{out}}(\mathbf{r})$ from the KS wavefunctions.
4. Compare $n_{\text{in}}(\mathbf{r})$ and $n_{\text{out}}(\mathbf{r})$. If they are the same to within some tolerance, the procedure is complete. If not, we must update the trial density in some way using $n_{\text{out}}(\mathbf{r})$, and then repeat from step 2.

There are several possible schemes for updating the density in the last step. The simplest is linear mixing, which gives the new density as $n_{\text{new}}(\mathbf{r}) = n_{\text{in}}(\mathbf{r}) + \alpha(n_{\text{out}}(\mathbf{r}) - n_{\text{in}}(\mathbf{r}))$, where α is an appropriate mixing parameter. However, this results in quite slow convergence, requiring many iterations of the steps shown above. More complicated schemes exist such as the Broyden and Pulay methods, both of which utilise information from previous steps in the self-consistency procedure to decide on n_{new}, resulting in much faster convergence [37]. Throughout this work, the Broyden method is used. Once a self-consistent solution has been successfully found, the final energy is given by the expression [28]:

$$E = \sum_i \epsilon_i + E_{\text{xc}}[n(\mathbf{r})] - \int \mathrm{d}\mathbf{r} V_{\text{xc}}(\mathbf{r}) n(\mathbf{r}) - \int \mathrm{d}\mathbf{r}\mathrm{d}\mathbf{r}' \frac{n(\mathbf{r})n(\mathbf{r}')}{2|\mathbf{r}-\mathbf{r}'|} \ . \tag{2.45}$$

Although in the above discussion the KS energy eigenvalues ϵ_i are simply a mathematical construct allowing us to solve our problem, they can in fact be shown to have some physical meaning. The eigenvalue of the highest energy occupied KS state is precisely equal to the first ionisation energy in atoms and molecules, and the Fermi energy in metals [27, 38]. The eigenvalues are often used to calculate the electronic band structure [27]. This is not strictly correct, and leads to some issues with the accuracy of the band structures calculated, although it is usually a good approximation.

2.2.4 The exchange-correlation functional

So far, everything in the Kohn-Sham formulation of DFT has been exact. This is because we have still not dealt with the exchange-correlation functional $E_{\text{xc}}[n(\mathbf{r})]$, which contains all the corrections to the other exact terms, including exchange-correlation effects. Although the true form of this functional is unknown, we can treat it approximately, allowing us to complete the theory. The form chosen for $E_{\text{xc}}[n(\mathbf{r})]$ is the key approximation, and thus the key limitation, of DFT. Because the long range Hartree term and the non-interacting kinetic energy have been separated out from $E_{\text{xc}}[n(\mathbf{r})]$ and treated exactly, we might expect that E_{xc} will be well approximated by a local or semi-local functional of the density. Examples of such approximate functionals are discussed below.

The local density approximation

In their initial paper, Kohn and Sham made what is now known as the *local density approximation* (LDA) – they took

$$E_{\text{xc}}[n(\mathbf{r})] = \int \mathrm{d}\mathbf{r}\; n(\mathbf{r})\epsilon_{\text{xc}}[n(\mathbf{r})]\;, \tag{2.46}$$

where $\epsilon_{\text{xc}}[n(\mathbf{r})]]$ is the exchange-correlation energy per electron in a uniform interacting electron gas of density $n(\mathbf{r})$ [26]. This quantity can be obtained by parametrising extremely accurate quantum Monte Carlo calculations [39, 40], allowing $E_{\text{xc}}[n(\mathbf{r})]$ to be computed to a high accuracy as well [28]. The most commonly used parametrisation for the LDA is due to Perdew and Zunger [41]. This is the parametrisation used wherever the LDA is applied in this work.

The LDA might be expected to work best for systems most like a homogeneous electron gas, where the approximation becomes exact, and less well in other systems.

However, despite its apparent crudeness, the LDA works surprisingly well in many situations, mainly when bonding is strong [12, 14, 28]. This is mostly due to the fact that, as it is exact for the homogeneous electron gas, the LDA obeys the exchange-correlation hole sum rules, as in equation (2.21) [12].

Generalised gradient approximations

To improve on and go beyond the LDA, other possible semi-local approximations for $E_{\mathrm{xc}}[n(\mathbf{r})]$ have been introduced, generally involving an expansion in terms of the gradient of the local electron density. The simplest possible approximation to the exchange-correlation functional using an expansion in terms of the gradient of the density is known as the *gradient expansion approximation* (GEA) [42]. This expansion does not obey the exchange-correlation hole sum rules though, unlike the LDA, and often gives worse results than the LDA [43]. However, the expansion in terms of the gradient of the density can be cut off in such a way that enforces the exchange-correlation hole sum rules, giving rise to the *generalised gradient approximation* (GGA) [44]. Mathematically, we can express this as

$$E_{\mathrm{xc}}[n(\mathbf{r})] = \int \mathrm{d}\mathbf{r}\; n(\mathbf{r})\epsilon_{\mathrm{xc}}[n(\mathbf{r})]F_{\mathrm{xc}}[n(\mathbf{r}, \nabla n(\mathbf{r}))]\;, \tag{2.47}$$

where the definition of ϵ_{xc} is the same as in the LDA. Different forms for the enhancement factor F_{xc} can be used, leading to several different GGA functionals [40, 45–47]. The PBE functional [45], named after the initials of its three creators, is one of the most commonly used GGA exchange-correlation functionals, and both it and the closely related PBEsol functional [46] are used in this work.

Beyond local exchange-correlation functionals

As mentioned above, the KS eigenvalues are often used to calculate the electronic band structure for the system in question. Whilst the shape of such DFT band structures is usually a good approximation to the experimentally measured band structure, the calculated band gap is often seriously underestimated, by up to 100%, when local or semi-local functionals are used [38]. It can be shown that this is due to the fact that the functional derivatives of the true exchange-correlation functional must have discontinuities at integer numbers of electrons [38, 48, 49], which LDA and GGA functionals do not possess. The difference between the true band gap and the DFT band gap is given

by [38]

$$\Delta = E_g^{(\text{true})} - E_g^{\text{DFT}} = V_{\text{xc}}^{(N+1)}(\mathbf{r}) - V_{\text{xc}}^{(N)}(\mathbf{r}) \ , \tag{2.48}$$

where $V_{\text{xc}}^{(N)}$ is the true exchange-correlation potential for a system with N electrons. The middle of the band gap, however, is correctly predicted by DFT [49].

The band gap problem can be dealt with by simply applying a scissor operator to move the bottom of the conduction band uniformly to match experimental band gap data, although this is clearly no longer a fully first-principles approach [50]. This is generally quite successful. Another method for obtaining more accurate band gaps is by introducing non-locality into the exchange-correlation functional, which can be done in a variety of ways. As the Hartree-Fock method includes the exact exchange term, it can be used to provide a non-local exchange-correlation functional, sometimes in combination with the LDA in order to include the correlation which is missing from the Hartree-Fock method. Various GGA functionals, the LDA functional and the exact exchange term can also be mixed together in ratios that provide a good fit to experimental data [51–54]. In this work, however, we are more interested in the shape of the electronic band structure than the size of the band gap. The increased accuracy of these more complex functionals comes at the price of a significant increase in computational cost, and therefore such functionals are not used in the rest of this work.

The size of the band gap is also renormalised by electron-phonon interactions. Changes to the band gap due to this effect can be calculated using DFT, and are generally thought to be accurate [55].

2.2.5 Pseudopotential plane-wave density functional theory

Now we possess all the machinery necessary to conduct DFT calculations, we simply need to devise a method for solving the KS equations. The DFT calculations in this work were performed using the `CASTEP` code [56], which is a plane-wave pseudopotential DFT code.

Plane waves

To begin solving the KS equations, we must choose a basis set to express our wavefunctions in terms of. One possible way of doing this is by using atomic orbitals, centred on the nuclei in the system. This is a popular method in quantum chemistry calculations [36]. However, condensed matter systems such as the crystalline solids we are

primarily interested in are periodic in nature, with a unit cell repeated many times. This suggests that we can describe the system using this unit cell and applying periodic boundary conditions, which in turn suggests a different basis set – plane waves.

In a system with periodic boundary conditions, Bloch's theorem states that we can write the KS states as [15]

$$\psi_{i\mathbf{k}}(\mathbf{r}) = \frac{1}{\sqrt{\mathcal{N}}} e^{i\mathbf{k}\cdot\mathbf{r}} u_{i\mathbf{k}}(\mathbf{r}) \ . \tag{2.49}$$

Here $\mathcal{N}$ is the number of unit cells in the simulated system, i enumerates the bands and $\mathbf{k}$ is the wave vector, the values of which are constrained by the boundary conditions used. $u_{i\mathbf{k}}(\mathbf{r})$ is a function with the same periodicity as the crystal itself. Mathematically, this can be written as

$$u_{i\mathbf{k}}(\mathbf{r}) = \frac{1}{\sqrt{\Omega}} \sum_n c_{in}(\mathbf{k}) e^{i\mathbf{G}_n\cdot\mathbf{r}} \ , \tag{2.50}$$

where $\mathbf{G}_n$ are reciprocal lattice vectors of the periodic crystal, Ω is the volume of the unit cell, and c_{in} are expansion coefficients. If we now apply the KS Hamiltonian of equation (2.37) to the wavefunction of equation (2.49) and substitute in (2.50), we obtain

$$\frac{1}{\sqrt{\Omega}} \sum_n c_{in}(\mathbf{k}) \left[\frac{|\mathbf{k}+\mathbf{G}_n|^2}{2} + V_{\text{aux}}(\mathbf{r}) \right] \xi_{\mathbf{k}+\mathbf{G}_n}(\mathbf{r}) = \epsilon_i(\mathbf{k}) \frac{1}{\sqrt{\Omega}} \sum_n c_{in}(\mathbf{k}) \xi_{\mathbf{k}+\mathbf{G}_n}(\mathbf{r}) \ , \tag{2.51}$$

$$\xi_{\mathbf{k}}(\mathbf{r}) = \frac{1}{\sqrt{\mathcal{N}}} e^{i\mathbf{k}\cdot\mathbf{r}} \ . \tag{2.52}$$

The $\xi_{\mathbf{k}}(\mathbf{r})$ are plane wave wavefunctions with wave number $\mathbf{k}$. If we now multiply (2.51) by $\xi^*_{\mathbf{k}+\mathbf{G}_m}(\mathbf{r})$ and integrate over the unit cell, we can take advantage of the orthogonality of the $\xi_{\mathbf{k}}(\mathbf{r})$ to obtain

$$\sum_n H_{mn} c_{in}(\mathbf{k}) = \sum_n \left[\frac{|\mathbf{k}+\mathbf{G}_n|^2}{2} \delta_{nm} + \tilde{V}_{\text{aux}}(\mathbf{G}_n - \mathbf{G}_m) \right] c_{in}(\mathbf{k}) = \epsilon_i(\mathbf{k}) c_{im}(\mathbf{k}) \ . \tag{2.53}$$

$\tilde{V}_{\text{aux}}(\mathbf{G})$ is the Fourier transform of the KS auxiliary potential, given by

$$\tilde{V}_{\text{aux}}(\mathbf{G}) = \frac{1}{\Omega} \int_\Omega \mathrm{d}\mathbf{r} \ V_{\text{aux}}(\mathbf{r}) e^{-i\mathbf{G}\cdot\mathbf{r}} \ . \tag{2.54}$$

The matrix equation (2.53) can now be solved to obtain the KS eigenvalues ϵ_i and the coefficients c_{in}, which lead directly to the KS states ψ_i. By construction, these KS states have the periodicity of the reciprocal lattice, so we can restrict $\mathbf{k}$ to the first Brillouin zone (BZ) of the reciprocal lattice.

The plane wave $\xi_{\mathbf{k}+\mathbf{G}}(\mathbf{r})$ has a momentum $\mathbf{k}+\mathbf{G}$ and a kinetic energy $E = \frac{|\mathbf{k}+\mathbf{G}|^2}{2}$, and therefore an associated length scale $\lambda \propto \frac{1}{|\mathbf{k}+\mathbf{G}|} \propto \frac{1}{\sqrt{E}}$. This tells us that to properly describe variations in the wavefunction, and hence the density, over increasingly small length scales, we need to include plane waves of increasingly high energy, increasing the cost of our calculations. Conversely, however, this also means that, if we only require our calculations to be accurate to within a certain tolerance, we need only to include plane waves up to a certain cut-off energy E_{cut}. Shorter scale variations in the wavefunction will not change the results of the calculation within the given tolerance. This tells us that a plane wave basis is systematically improvable, by increasing the cut-off energy E_{cut} until the properties in question remain constant to within the desired tolerance. E_{cut} is an example of a parameter that results must be converged with respect to, a topic which will be discussed further below.

Pseudopotentials

Thus far, we have been considering all the electrons present in the system, including ones bound very close to their nuclei, in our calculations. However, in order to ensure orthogonality with the core electrons' wavefunctions, the valence electrons' wavefunctions oscillate rapidly within the core region, meaning a very high cut-off energy is required to describe them correctly. This issue can be tackled through the use of pseudopotentials.

Intuitively, we know that by far the largest contribution to bonding and various other properties of the system comes from the valence electrons, and we would expect the 'core' electrons to be largely inactive – this is known as the *frozen-core approximation* [57, 58]. Additionally, the rapid oscillation of the valence electrons' wavefunctions within the core region leads to a high kinetic energy that almost exactly cancels the potential energy from the electron-nucleus interaction in the same region [59]. These facts taken together imply that we need only include the valence electrons in our calculations, replacing the potential due to the nuclei, V_{ext}, with an effective pseudopotential that includes the effect of the core electrons. This produces pseudo-wavefunctions, which have no nodes inside the core region, reducing the cut-off energy required substantially and thus making the calculation less computationally intensive [57, 60].

Two common types of pseudopotentials are used, each with slightly different properties. Norm-conserving pseudopotentials (NCPs) are constructed to possess four main properties for a certain chosen 'prototype' configuration [60]:

1. Pseudopotential KS single-particle valence energies match those of the all-electron atom.

2. KS pseudo-wavefunctions match the all-electron wavefunctions for $r > r_c$, where r_c is a chosen core radius.

3. The integral of the pseudopotential KS charge density from 0 to r matches the all-electron value for $r > r_c$ for each valence orbital.

4. The logarithmic derivative and the energy derivative of the KS pseudo-wavefunctions match the all-electron values for $r > r_c$.

Condition 3 is known as the norm-conserving condition, and ensures the electrostatic potential is correct for $r > r_c$, whilst condition 4 tries to minimise the error in the scattering properties of the cores [60], and is in fact implied by norm-conservation. However, NCPs can lead to problems – for many different orbitals, demanding norm conservation results in a pseudo-wavefunction that is not much smoother than the exact wavefunction, causing very little change in the computational cost of the calculation [61]. NCPs are generally 'hard' pseudopotentials – pseudopotentials that generate a large or small amount of oscillation in the pseudo-wavefunctions are termed 'hard' and 'soft' respectively. To deal with this problem, the norm-conserving condition can be relaxed, with condition 4 imposed separately, leading to an ultrasoft pseudopotential (USP). USPs allow higher values of r_c and smaller basis sets, reducing the computational cost [61], and are also much more transferable than NCPs – well-constructed USPs generated for a neutral atom tend to work well for ions of the same atom, which is usually not the case with NCPs [62]. The USP approach works by separating out the density into a smooth part and a rapidly oscillating part localised in the core region, with calculations done using the smooth part. Due to the relaxation of the norm-conserving condition, the density found in these calculations is not actually the full charge density, but must be added to the charge density derived from the part localised in the core, known as the augmentation charge. In this work, unless otherwise stated, USPs are used.

Calculating forces and geometry optimisation

One set of properties of potential interest in a condensed matter system are the forces acting on the constituent atoms for a given atomic configuration. These forces are

extremely useful in vibrational calculations, a topic discussed further below in Section 2.3 as well as Chapter 3. They can also be used in the process of geometry optimisation, i.e. obtaining an appropriate atomic configuration for further calculations. This is done by constructing an initial guess at the correct structure, and then allowing it to 'relax', or find the minimum energy configuration with respect to the positions of the constituent atoms.

The forces on each atom can be calculated using the Hellmann-Feynman theorem [63, 64], which states that, under steady-state conditions and for any quantity λ,

$$\frac{\partial E}{\partial \lambda} = \left\langle \frac{\partial \hat{\mathrm{H}}}{\partial \lambda} \right\rangle \ , \tag{2.55}$$

where $\left\langle \hat{\mathrm{A}} \right\rangle$ is the expectation value of the operator $\hat{\mathrm{A}}$. Taking $\lambda = \mathbf{R}_\alpha$, the position of the αth atom, and using $|\psi\rangle$ to represent the wavefunction in bra-ket notation, we can calculate the force on the αth atom as [65]:

$$\mathbf{f}_\alpha = -\frac{\partial E}{\partial \mathbf{R}_\alpha} = -\left\langle \psi \middle| \frac{\partial \hat{\mathrm{H}}}{\partial \mathbf{R}_\alpha} \middle| \psi \right\rangle - \left\langle \frac{\partial \psi}{\partial \mathbf{R}_\alpha} \middle| \hat{\mathrm{H}} \middle| \psi \right\rangle - \left\langle \psi \middle| \hat{\mathrm{H}} \middle| \frac{\partial \psi}{\partial \mathbf{R}_\alpha} \right\rangle \ . \tag{2.56}$$

Assuming that $|\psi\rangle$ is an exact eigenstate of $\hat{\mathrm{H}}$, it follows that the last two terms are equal to $-E\left(\left\langle \frac{\partial \psi}{\partial \mathbf{R}_\alpha} | \psi \right\rangle + \left\langle \psi | \frac{\partial \psi}{\partial \mathbf{R}_\alpha} \right\rangle\right) = -E \frac{\partial}{\partial \mathbf{R}_\alpha} \langle \psi | \psi \rangle = 0$, simplifying the expression significantly. If the basis for our wavefunctions depended on the positions of the atoms (for example, atomic centred Gaussians), further contributions to the forces would also appear, known as Pulay forces [64]. However, using a plane wave basis for our wavefunctions, which is independent of the atomic positions, makes these Pulay forces disappear. Finally, before applying the Hellmann-Feynman theorem, we must first add a nucleus-nucleus interaction to the energy, $E_{\text{n-n}} = \sum_\alpha \sum_{\beta \neq \alpha} E_{\alpha\beta} = \sum_\alpha \sum_{\beta \neq \alpha} \frac{Z_\alpha Z_\beta}{2|\mathbf{R}_\alpha - \mathbf{R}_\beta|}$ [63]. Adding this into equation (2.32) and applying the Hellmann-Feynman theorem, we obtain

$$\mathbf{f}_\alpha = -\int \mathrm{d}^3\mathbf{r} \ \frac{\partial V_{\text{ext}}(\mathbf{r})}{\partial \mathbf{R}_\alpha} - \sum_\beta \frac{\partial E_{\alpha\beta}}{\partial \mathbf{R}_\alpha} \ . \tag{2.57}$$

Equation (2.57) allows us to calculate the forces on each of the nuclei for a given configuration.

During a geometry optimisation procedure, we transform our initial atomic configuration into one that is hopefully closer to the energy minimum by displacing the nuclei along the direction of the force acting on them. We then iterate this procedure until

the forces on the nuclei are all below a defined value. The Broyden-Fletcher-Goldfarb-Shanno (BFGS) algorithm [66] is used to implement this process in this work. Symmetry constraints can also be imposed by symmetrising the forces, ensuring that the symmetry of the initial structure is conserved [67].

One potential problem with this relaxation procedure arises if we are searching for the *global* energy minimum, but the initial structure is close to a *local* minimum in the potential energy surface. In this case, it is likely that the structure will fall into this local minimum, corresponding to a metastable state, and remain there, instead of relaxing to the global minimum [68]. Care must be taken to ensure this state of affairs does not occur. Additionally, it can be shown that, whilst the error in the energy in DFT is merely quadratic in the charge density error, the error in the forces is linear in the charge density error, meaning that calculations must be converged to within a strict tolerance to obtain accurate forces [64]. This must be taken into account when deciding on the convergence tolerances used.

Convergence considerations

When conducting DFT calculations, it is important to ensure that the values used for calculational parameters are appropriate – the property of interest should be converged with respect to changes in these parameters. As mentioned above, the cut-off energy E_{cut} that determines the size of the plane wave basis set is one such parameter. There are two other main parameters that must be converged with respect to in `CASTEP`: the size of the Monkhorst-Pack **k**-point grid and the fine grid scale.

Electronic structure calculations often require integrations in reciprocal space to be performed over the first BZ. In practice, these integrals are approximated by summing up the values of the integrand at a set of **k**-points in the first BZ. The results of the integrals, and therefore the properties of interest, should be converged with respect to the density of this mesh of **k**-points, to ensure this approximation is good. Several different ways of generating these **k**-points exist, but in this work we use the Monkhorst-Pack grid method [69].

Some parts of the solution of the KS equations in a plane-wave basis are conducted in real space, whilst others are conducted in reciprocal space, to make the calculation as efficient as possible. This is only possible through the use of the fast Fourier transform (FFT), which allows rapid conversion between real and reciprocal space. A FFT

algorithm calculates the Fourier transform using a grid of **k**-points, here given by the allowed **k** values within the sphere defined by the cut-off energy. For a large portion of a DFT calculation, the KS states are the objects of interest being Fourier transformed, but inevitably the electron density must also be calculated. Because the density is proportional to the square of the wavefunction, the FFT grid for the density should be at least twice as dense as that for the KS states, corresponding to a cut-off sphere with twice the radius. In some situations an acceptable value for the density can be obtained with a grid less than twice as dense, by neglecting short length scale components, but this should always be checked. The grid scale in `CASTEP` sets the ratio between the spacings of the coarse grid, used for the wavefunctions, and the standard grid, used for the density. The results of the calculation should be converged with respect to this parameter to ensure that the FFT of the density has been performed accurately.

When DFT calculations are used to find the electronic energy of the system, it is often the case that the property of interest is actually the difference in energy between two systems, instead of the absolute value of the energy. This is extremely useful when converging with respect to the various parameters mentioned above, as differences in energy converge much faster than absolute energies. This is due to the cancellation of errors present in the calculated energy of each system.

2.3 Calculation of vibrational properties

As described above, DFT provides a method for solving the electronic Hamiltonian accurately and at reasonable computational cost. This is only half of the story, however – we still have not found the complete solution of the overall Hamiltonian expressed in equation (2.3). Although the Born-Oppenheimer approximation has allowed us to separate the problem into two parts – the motion of the electrons and of the nuclei – DFT only provides us with a method to solve the electronic problem. What must now be found is a way to solve the nuclear Schrödinger equation shown in equation (2.9), also known as the vibrational Schrödinger equation. As it will be of importance in the following discussion, the nuclear equation is reproduced here for convenience:

$$\hat{\mathrm{H}}_{\mathrm{vib}}\chi(\{\mathbf{R}\}) = \left[-\sum_{p\alpha} \frac{1}{2m_\alpha}\nabla^2_{p\alpha} + E_{\mathrm{elec}}(\{\mathbf{R}\}) \right]\chi(\{\mathbf{R}\}) = E_{\mathrm{vib}}\chi(\{\mathbf{R}\}) \ . \tag{2.58}$$

Equation (2.58) allows for the use of supercells, simulation cells made up of more than one unit cell. This allows for the possibility of atoms in adjacent unit cells moving differently, corresponding to a vibration with non-zero wave number. Here p runs over all unit cells in the simulated supercell, α runs over all nuclei within a unit cell, and $\{\mathbf{R}\}$ represents the set of nuclear positions.

An appropriate form for the BO surface $E_{\text{elec}}(\{\mathbf{R}\})$ must be found if equation (2.58) is to be solved, as it acts as the potential in the nuclear Hamiltonian. However, the BO surface is $3N$-dimensional, where N is the number of atoms in the system. This extremely high dimensionality, coupled with the fact that a calculation of E_{elec} for a given nuclear configuration using DFT will typically scale as $\mathcal{O}(N_{\text{elec}}^3)$ [70], where N_{elec} is the number of electrons, tells us that it is computationally impossible to fully sample the BO surface for all but the very smallest systems. Instead, a variety of approximations for the BO surface are used that vastly simplify this problem and allow for the solution of equation (2.58).

2.3.1 The harmonic approximation

The simplest and most common approach to simplifying the nuclear Hamiltonian is to use what is known as the harmonic approximation. Because the nuclei are relatively heavy, we expect that, in general, they will not move far away from their equilibrium positions. This suggests that we can expand E_{elec} as a Taylor series around the equilibrium positions, i.e. in $\mathbf{X}_{p\alpha} = \mathbf{R}_{p\alpha} - \mathbf{R}^0_{p\alpha}$, where $\mathbf{R}_{p\alpha}$ and $\mathbf{R}^0_{p\alpha}$ are the current and equilibrium positions of the αth nucleus in the pth unit cell, to obtain

$$E_{\text{elec}}(\{\mathbf{R}\}) = E_{\text{elec}}(\{\mathbf{R}^0\}) + \frac{1}{2}\sum_{p\alpha i;p'\alpha' j} \left.\frac{\partial^2 E_{\text{elec}}(\{\mathbf{R}\})}{\partial X_{p\alpha i}\partial X_{p'\alpha' j}}\right|_{\{\mathbf{R}^0\}} X_{p\alpha i}X_{p'\alpha' j} + \mathcal{O}(X^3)\ . \quad (2.59)$$

The harmonic approximation simply involves assuming that the $\mathbf{X}_{p\alpha}$ are small enough to allow us to neglect the $\mathcal{O}(X^3)$ terms in (2.59), which produces a quadratic potential [9, 71]. Neglecting the constant term in the Taylor expansion, the harmonic vibrational potential is

$$V_{\text{har}}(\{\mathbf{R}\}) = \frac{1}{2}\sum_{p\alpha i;p'\alpha' j} \left.\frac{\partial^2 E_{\text{elec}}(\{\mathbf{R}\})}{\partial X_{p\alpha i}\partial X_{p'\alpha' j}}\right|_{\{\mathbf{R}^0\}} X_{p\alpha i}X_{p'\alpha' j}\ . \quad (2.60)$$

Obtaining $V_{\text{har}}(\{\mathbf{R}\})$ requires calculation of the matrix of force constants, which is defined as

$$C_{p\alpha i;p'\alpha' j} = \left.\frac{\partial^2 E_{\text{elec}}(\{\mathbf{R}\})}{\partial X_{p\alpha i}\partial X_{p'\alpha' j}}\right|_{\{\mathbf{R}^0\}}\ . \quad (2.61)$$

The elements of this matrix can be calculated using one of two different methods: density functional perturbation theory (DFPT) [72] or the finite displacement method and its relations [73, 74]. In this work, the finite displacement method is used. This approach makes use of the fact that the nuclear forces calculated with the Hellmann-Feynman theorem give the first derivatives of the energy with respect to atomic displacements. To obtain the second derivatives that constitute the matrix of force constants, the forces are calculated for both the equilibrium nuclear configuration and one with an atom slightly displaced from equilibrium. The derivative of the forces with respect to the atomic displacement can then be found numerically. If the system possesses some symmetry, some elements of the matrix of force constants will be identical to others, potentially significantly reducing the number of calculations necessary.

Now we have the matrix of force constants, and thus the harmonic potential $V_{\text{har}}(\{\mathbf{R}\})$, we can simplify the problem further by rewriting the harmonic Hamiltonian in a new set of co-ordinates – phonon normal co-ordinates $u_{n\mathbf{q}}$. These are linked to the atomic displacements $\mathbf{X}_{p\alpha}$ through the expressions [75]

$$u_{n\mathbf{q}} = \frac{1}{\sqrt{N_p}} \sum_{p\alpha i} \sqrt{m_\alpha} X_{p\alpha i} e^{-i\mathbf{q}\cdot\mathbf{R}_p} w_{-\mathbf{q}ni\alpha} \ , \tag{2.62}$$

$$X_{p\alpha i} = \frac{1}{\sqrt{N_p m_\alpha}} \sum_{n\mathbf{q}} u_{n\mathbf{q}} e^{i\mathbf{q}\cdot\mathbf{R}_p} w_{\mathbf{q}ni\alpha} \ . \tag{2.63}$$

Here N_p is the number of unit cells, $\mathbf{R}_p$ is the real space lattice vector corresponding to the pth unit cell, and the $w_{\mathbf{q}ni\alpha}$ are the eigenvectors of the dynamical matrix $D_{i\alpha;j\alpha'}(\mathbf{q})$, discussed further below. $\mathbf{q}$ represents a point in the first vibrational BZ in reciprocal space. Although the definition of equation (2.62) implies that the normal co-ordinates $u_{n\mathbf{q}}$ can be complex, real normal co-ordinates can always be constructed, using the fact that $w_{-\mathbf{q}ni\alpha} = w^*_{\mathbf{q}ni\alpha}$, as [71]

$$u'_{n\mathbf{q}} = \frac{1}{\sqrt{2}}(u_{n\mathbf{q}} + u_{n-\mathbf{q}}) \ , \tag{2.64}$$

$$u'_{n-\mathbf{q}} = \frac{i}{\sqrt{2}}(u_{n\mathbf{q}} - u_{n-\mathbf{q}}) \ . \tag{2.65}$$

Real normal co-ordinates will be assumed from here on.

The dynamical matrix mentioned above is defined as the mass-reduced Fourier transform of the matrix of force constants:

$$D_{i\alpha;j\alpha'}(\mathbf{q}) = \frac{1}{N_p\sqrt{m_\alpha m_{\alpha'}}} \sum_{pp'} C_{p\alpha i;p'\alpha' j} e^{i\mathbf{q}\cdot(\mathbf{R}_p - \mathbf{R}_{p'})} \ . \tag{2.66}$$

This matrix appears if a plane wave is used as an ansatz to the harmonic vibrational Schrödinger equation, as this results in the characteristic eigenvalue equation

$$|D_{i\alpha;j\alpha'}(\mathbf{q}) - \omega^2_{n\mathbf{q}}\delta_{ij}\delta_{\alpha\alpha'}| = 0 \ , \tag{2.67}$$

where $\omega^2_{n\mathbf{q}}$ are the eigenvalues of the dynamical matrix [9].

With these definitions in hand, we can rewrite the harmonic vibrational Hamiltonian in a simple harmonic form [75]:

$$\hat{\mathrm{H}}_{\mathrm{vib}} = \sum_{n\mathbf{q}} -\frac{1}{2}\frac{\partial^2}{\partial u^2_{n\mathbf{q}}} + \frac{1}{2}\omega^2_{n\mathbf{q}}u^2_{n\mathbf{q}} \ . \tag{2.68}$$

This Hamiltonian is just a sum of non-interacting simple harmonic oscillators with frequencies $\omega_{n\mathbf{q}}$. These can each be solved analytically to give the energy eigenvalues

$$\varepsilon_{s_{n\mathbf{q}}} = \left(s_{n\mathbf{q}} + \frac{1}{2}\right)\omega_{n\mathbf{q}} \ , \tag{2.69}$$

and the corresponding wavefunctions

$$\phi_{n\mathbf{q};s_{n\mathbf{q}}}(u_{n\mathbf{q}}) = \frac{1}{\sqrt{2^{s_{n\mathbf{q}}}s_{n\mathbf{q}}!}}\left(\frac{\omega_{n\mathbf{q}}}{\pi}\right)^{\frac{1}{4}} e^{-\frac{1}{2}\omega_{n\mathbf{q}}u^2_{n\mathbf{q}}} H_{s_{n\mathbf{q}}}\left(\sqrt{\omega_{n\mathbf{q}}}q_{n\mathbf{q}}\right) \ . \tag{2.70}$$

$s_{n\mathbf{q}}$ is the occupation number of the vibrational mode labelled by $(n, \mathbf{q})$, which can be any non-negative integer, and $H_n(x)$ is the nth order Hermite polynomial, with leading coefficient 2^n. The associated quasiparticles are known as *phonons*. Phonons are bosons, as increasing $s_{n\mathbf{q}}$ corresponds to creating more and more identical phonons in the same state, which would be forbidden by the Pauli exclusion principle if they were fermions. This means we can write the overall vibrational wavefunction in phonon normal co-ordinates as a Hartree product of single-oscillator wavefunctions, using $\mathbf{s}$ and $\mathbf{u}$ to represent collective vectors of $s_{n\mathbf{q}}$ and $u_{n\mathbf{q}}$ respectively:

$$\Phi_{\mathbf{s}}(\mathbf{u}) = \prod_{n\mathbf{q}} \phi_{n\mathbf{q};s_{n\mathbf{q}}}(u_{n\mathbf{q}}) \ . \tag{2.71}$$

The harmonic vibrational energy is then simply

$$E_{\mathrm{har}} = \sum_{n\mathbf{q}} \varepsilon_{s_{n\mathbf{q}}} \ . \tag{2.72}$$

The use of the harmonic approximation has clearly significantly decreased the complexity of the vibrational problem, by reducing it from a $3N$-dimensional problem, requiring significant sampling of the entire BO surface, to $3N$ one-dimensional problems,

each requiring only one or two calculations. This, along with the fact that the harmonic approximation works very well in many situations, makes it the most popular method with which to solve the vibrational problem [71].

2.3.2 Including anharmonicity: the vibrational self-consistent field approximation

The principal axes approximation

The harmonic approximation is often very good, but it is clear that the true vibrational properties of the system cannot be obtained exactly using the harmonic approximation, as we neglect $\mathcal{O}(u^3)$ terms in the expansion of $E_{\text{el}}(\{\mathbf{R}\})$ in equation (2.59). These terms give rise to anharmonic effects in the properties of the system. Anharmonicity can be particularly important in systems with light atoms, with weak bonding, or at high temperatures [75]. Any one of these conditions can result in large amplitudes of the nuclear vibrations, meaning the nuclei explore the BO surface out beyond the region where the harmonic approximation is good. This tells us that it is important to include anharmonic effects in systems of interest where one or more of these conditions applies. To do this, we use a vibrational self-consistent field method outlined by Monserrat, Drummond and Needs [75], and used successfully several times since [76–83].

The first step in this method is to expand out the BO surface within what is known as the *principal axes approximation (PAA)*. This assumes that the harmonic approximation is a good first approximation to the dynamics of the system, and therefore the harmonic phonon normal co-ordinates of equation (2.62) are an appropriate set of co-ordinates to expand the BO surface in. The expansion is then performed in terms of increasing coupling between these phonon modes [75, 84], leading to the expression

$$E_{\text{PAA}}(\mathbf{u}) = E_{\text{elec}}(\mathbf{0}) + \sum_{n\mathbf{q}} V_{n\mathbf{q}}(u_{n\mathbf{q}}) + \frac{1}{2}\sum_{n\mathbf{q}}\sum_{n'\mathbf{q}'\neq n\mathbf{q}} V_{n\mathbf{q};n'\mathbf{q}'}(u_{n\mathbf{q}}, u_{n'\mathbf{q}'}) + \cdots \ . \quad (2.73)$$

The factor of $\frac{1}{2}$ accounts for double counting.

The single-body term $V_{n\mathbf{q}}(u_{n\mathbf{q}})$ is given by

$$V_{n\mathbf{q}}(u_{n\mathbf{q}}) = E_{\text{elec}}(0, \ldots, 0, u_{n\mathbf{q}}, 0, \ldots, 0) - E_{\text{elec}}(\mathbf{0}) \ . \quad (2.74)$$

This corresponds to exploring the BO surface along the direction defined by a single mode, and does *not* assume the harmonic approximation, as it is not necessarily

quadratic. Because of this, anharmonicity is already included in the single-body term. The two-body term is then defined as

$$V_{n\mathbf{q};n'\mathbf{q}'}(u_{n\mathbf{q}}, u_{n'\mathbf{q}'}) = E_{\text{elec}}(0,\ldots,0,u_{n\mathbf{q}},0,\ldots,0,u_{n'\mathbf{q}'},0,\ldots,0) - V_{n\mathbf{q}}(u_{n\mathbf{q}}) - V_{n'\mathbf{q}'}(u_{n'\mathbf{q}'}) - E_{\text{elec}}(\mathbf{0}) \ . \tag{2.75}$$

This corresponds to exploring the BO surface in two directions simultaneously to see the effect of one phonon mode on the other. Higher order terms can then be defined similarly, including coupling between three or more modes.

To use the expansion of equation (2.73) practically, we truncate it, most often to only include the single-body term. The harmonic modes, which are typically a good first approximation themselves, are independent, so we would expect the lower order terms in the expansion with little or no coupling to dominate, making such a truncation a good approximation. Previous work has found that only the single-body term is required to understand the most important effects in a variety of materials [79, 85, 86]. In this work, the expansion is truncated at both the single-body and the two-body levels as appropriate for different materials.

The vibrational self-consistent field approximation

Given the expression for the BO surface within the PAA from equation (2.73), suitably truncated, we must now solve the vibrational Schrödinger equation shown in equation (2.58). We again use a Hartree product for the overall vibrational wavefunction, as in equation (2.71):

$$\Phi_{\mathbf{s}}(\mathbf{u}) = \prod_{n\mathbf{q}} \phi_{n\mathbf{q};s_{n\mathbf{q}}}(u_{n\mathbf{q}}) \ . \tag{2.76}$$

Here, however, the single-mode wavefunctions $\phi_{n\mathbf{q};s_{n\mathbf{q}}}(u_{n\mathbf{q}})$ are no longer simple harmonic oscillator wavefunctions, but will depend on the form of the BO surface used. This wavefunction is then used to solve the vibrational equation in a mean field fashion. Solving this equation using a mean field, or self-consistent, approach is known as the *vibrational self-consistent field (VSCF)* method. Minimising the energy defined by the vibrational Hamiltonian of equation (2.58) with respect to the single-mode wavefunctions $\phi_{n\mathbf{q}}(u_{n\mathbf{q}})$ leads us to the VSCF equations [75, 87]

$$\left(-\frac{1}{2}\frac{\partial^2}{\partial u_{n\mathbf{q}}^2} + \overline{V}_{n\mathbf{q}}(u_{n\mathbf{q}})\right)\phi_{n\mathbf{q}}(u_{n\mathbf{q}}) = \lambda_{n\mathbf{q}}\phi_{n\mathbf{q}}(u_{n\mathbf{q}}) \ , \tag{2.77}$$

where the potential $\overline{V}_{n\mathbf{q}}(u_{n\mathbf{q}})$ is a mean-field potential, taking into account the average effect of the other phonon modes:

$$\overline{V}_{n\mathbf{q}}(u_{n\mathbf{q}}) = \int \prod_{n'\mathbf{q}' \neq n\mathbf{q}} du_{n'\mathbf{q}'} |\phi_{n'\mathbf{q}'}(u_{n\mathbf{q}})|^2 E_{\mathrm{PAA}}(\mathbf{u}) \ . \tag{2.78}$$

The total energy of the overall state $\mathbf{s}$ is given by

$$E_{\mathbf{s}}^{(\mathrm{vib})} = \sum_{n\mathbf{q}} \lambda_{n\mathbf{q}} + \int \prod_{n\mathbf{q}} du_{n\mathbf{q}} |\phi_{n\mathbf{q};s_{n\mathbf{q}}}(u_{n\mathbf{q}})|^2 \left(E_{\mathrm{PAA}}(\mathbf{u}) - \sum_{n\mathbf{q}} \overline{V}_{n\mathbf{q}}(u_{n\mathbf{q}}) \right) \ . \tag{2.79}$$

As the potential depends on the wavefunctions, which themselves depend on the potential, these equations must be solved self-consistently until the variation in the energy from one self-consistent cycle to the next is lower than a given tolerance.

Once the equations are solved, a perturbation theory can be constructed on the VSCF equations [88], with the second order correction given by

$$\Delta E_{\mathbf{s}}^{(\mathrm{vib},2)} = \sum_{\mathbf{s}' - \mathbf{s}} \frac{1}{E_{\mathbf{s}}^{(\mathrm{vib})} - E_{\mathbf{s}'}^{(\mathrm{vib})}} \left| \int \prod_{n\mathbf{q}} du_{n\mathbf{q}} \phi_{n\mathbf{q};s'_{n\mathbf{q}}} \left(E_{\mathrm{PAA}}(\mathbf{u}) - \sum_{n\mathbf{q}} \overline{V}_{n\mathbf{q}}(u_{n\mathbf{q}}) \right) \phi_{n\mathbf{q};s_{n\mathbf{q}}} \right|^2 \ . \tag{2.80}$$

Here, the difference between the 'true' PAA BO surface and the mean field potential acts as the small perturbation to the mean-field Hamiltonian. If the correction defined by equation (2.80) becomes large, this implies that the difference between these two quantities is not a small perturbation to the Hamiltonian, and therefore the VSCF approximation is not applicable.

Solving the VSCF equations theoretically provides the anharmonic energies and wavefunctions for all the vibrational states of the system. If we are interested in vibrational properties at zero temperature, i.e. we are looking at zero-point motion, we can directly find these by looking the ground state, as at zero temperature this is the state the system will be in. However, if we want to look at the effect of temperature on the anharmonic vibrational properties, we need to consider excited states as well. The partition function can be approximately calculated as

$$\mathcal{Z} = \sum_{\mathbf{s}} e^{-\beta E_{\mathbf{s}}^{(\mathrm{vib})}} \ , \tag{2.81}$$

where $\beta = \frac{1}{k_B T}$, which allows us to calculate the Helmholtz free energy

$$F = -\frac{1}{\beta} \ln \mathcal{Z} \ . \tag{2.82}$$

In metallic systems, i.e. those with no band gap, the shape of the BO surface will generally change with temperature, which should be taken into account when examining the vibrational properties of such a system at finite temperature. For systems with a band gap E_g, the BO surface at zero temperature remains a good approximation for temperatures significantly smaller than $\frac{E_g}{k_B}$.

Anharmonic vibrational expectation values

With the anharmonic vibrational wavefunction $\Phi(\mathbf{u})$ calculated within the VSCF approximation, we can theoretically obtain anharmonic vibrational expectation values of any operator we have an expression for. In general, the expectation value of an operator $\hat{\mathrm{O}}(\mathbf{u})$ can be expressed in bra-ket notation as [75]

$$\langle \hat{\mathrm{O}}(\mathbf{u}) \rangle = \langle \Phi(\mathbf{u}) | \, \hat{\mathrm{O}}(\mathbf{u}) \, | \Phi(\mathbf{u}) \rangle \ . \tag{2.83}$$

At finite temperature we can instead write

$$\langle \hat{\mathrm{O}}(\mathbf{u}) \rangle_\beta = \frac{1}{\mathcal{Z}} \sum_{\mathbf{s}} \langle \Phi_{\mathbf{s}}(\mathbf{u}) | \, \hat{\mathrm{O}}(\mathbf{u}) \, | \Phi_{\mathbf{s}}(\mathbf{u}) \rangle \, e^{-\beta E_{\mathbf{s}}^{(\mathrm{vib})}} \ . \tag{2.84}$$

In analogy to the expansion of the BO surface in equation (2.73), we can expand out the operator as

$$\hat{\mathrm{O}}(\mathbf{u}) = \hat{\mathrm{O}}(\mathbf{0}) + \sum_{n\mathbf{q}} \hat{\mathrm{O}}_{n\mathbf{q}}(u_{n\mathbf{q}}) + \sum_{n\mathbf{q}} \sum_{n'\mathbf{q}' \neq n\mathbf{q}} \hat{\mathrm{O}}_{n\mathbf{q};n'\mathbf{q}'}(u_{n\mathbf{q}}, u_{n'\mathbf{q}'}) + \cdots \ . \tag{2.85}$$

Such an expansion is useful because it allows data on the form of the operator to be collected at the same time as data on the shape of the BO surface. Examples of operators of interest that are investigated in this work are the electronic band structure, the stress tensor and the positions of the atoms.

2.3.3 Implementation of vibrational self-consistent field method

The first step in the calculation of the vibrational properties of a system using this VSCF method is to apply the harmonic approximation, as described in section 2.3.1. In this work, the finite displacement method is used, with the atomic forces required calculated using the `CASTEP` code. This method provides the harmonic phonon frequencies $\omega_{n\mathbf{q}}$ and eigenvectors $w_{\mathbf{q}ni\alpha}$. The eigenvectors describe the pattern of atomic displacements relating to the corresponding harmonic phonon. Having calculated these quantities, we

are now able to use the relations (2.62) and (2.63) to link atomic displacements to the harmonic phonon co-ordinates, $u_{n\mathbf{q}}$, that the BO surface is expanded in terms of in equation (2.73).

Mapping of the Born-Oppenheimer surface

The next step is to find a functional form for the terms in the PAA expansion of the BO surface. This mapping of the BO surface is done by running a series of DFT energy calculations, using `CASTEP`, for atomic configurations with different phonon mode amplitudes frozen in, known as mapping points. For the single-body terms in the expansion, only one mode at a time varies its amplitude from zero, giving a line of mapping points, whilst for two-body terms, the amplitudes of two modes are simultaneously varied, producing a grid of mapping points. The form for each of these terms in the expansion as a function of the harmonic phonon amplitudes, and thus the full BO surface within the PAA, is then found by fitting a functional form to these data points, typically a cubic spline.

There are several details of this mapping of the BO surface that require more detailed consideration: the range of amplitudes used, the distribution of mapping points within this range, and the number of these mapping points. A natural unit for the phonon amplitudes used in this mapping is the root mean square amplitude of the phonon within the harmonic approximation:

$$\sqrt{\langle u_{n\mathbf{q}}^2 \rangle} = \sqrt{\frac{1}{\omega_{n\mathbf{q}}} \left(\frac{1}{2} + \frac{1}{e^{\beta \omega_{n\mathbf{q}}} - 1} \right)} \,. \tag{2.86}$$

Typically, the maximum amplitude used to map the BO surface along a particular mode is 5 times this value, meaning the range of amplitudes is $-5\sqrt{\langle u_{n\mathbf{q}}^2 \rangle}$ to $5\sqrt{\langle u_{n\mathbf{q}}^2 \rangle}$, although this can be adjusted if a larger or smaller maximum amplitude is appropriate. The mapping points are generally distributed uniformly across this range, although this can be changed if a particular part of the BO surface requires a higher density of mapping points to get a good fit. Finally, the number of mapping points required for a good fit to the BO surface is another parameter that we must converge our results with respect to, which will be described in more detail below.

Conducting the mapping of the BO energy surface is almost always by far the most computationally expensive part of the whole VSCF method, as it requires the energy of many different atomic configurations to be calculated. Although it is only necessary to

map those modes within the irreducible vibrational BZ, since the mapping along other modes can be constructed using the symmetry of the system, the number of calculations required per mode is still N_p, where N_p is the number of mapping points. This is an order of magnitude larger than the cost of the harmonic approach. The calculations used to map the BO surface could be done in theory by any electronic structure code, but in this work we use DFT for its balance between accuracy and computational cost. To investigate larger systems or higher terms in the BO surface expansion, a cheaper method would need to be utilised, perhaps using force fields, whilst for extremely high accuracy results, methods such as quantum Monte Carlo could be applied.

Solving the VSCF equations

As shown in equation (2.76), we use a Hartree product of single-mode wavefunctions $\phi_{n\mathbf{q};s_{n\mathbf{q}}}(u_{n\mathbf{q}})$ as our overall wavefunction. Finding these single-mode wavefunctions by solving the VSCF equations of (2.77) requires that we express them in terms of a suitable set of basis functions. Typically, we use one-dimensional simple harmonic oscillator eigenstates, as they are simple to generate and should provide a good approximation to the anharmonic eigenstates of the system. The frequency used to calculate this set of basis functions is usually found by fitting a quadratic potential to the mapped BO surface along each mode, although it can be adjusted if required. This provides a better basis set than just simply using the harmonic frequency, as it accounts for modes with strong anharmonic character, such as soft modes with imaginary frequencies, much more accurately.

By re-expressing the VSCF equations like this, we are able to diagonalise them and find the coefficients of the simple harmonic oscillator eigenstates for each mode, and thus the overall wavefunction. This is true not just for the vibrational ground state of each mode, but also for the excited vibrational states that solving the VSCF equations gives. In practice, we set how many of these excited states we wish to describe beforehand, as this sets the size of the matrix to be diagonalised in the solution of the equations. Even if one is only interested in the properties of the vibrational ground state, these higher energy states can have an effect on the results through the perturbation theory correction applied in equation (2.80). The number of basis functions we use and the number of vibrational states described per mode are both computational parameters we must converge our results with respect to.

Non-diagonal supercells

In order to fully describe the vibrations of a material, it is necessary to include phonons from across the vibrational BZ, each with a different value of $\mathbf{q}$, and to integrate over $\mathbf{q}$ in the vibrational BZ to obtain vibrational properties. Vibrations with a non-zero value of $\mathbf{q}$ correspond to distortion patterns that vary as we move between unit cells, with a wavelength in the three dimensions of $\left(\frac{2\pi}{q_1}, \frac{2\pi}{q_2}, \frac{2\pi}{q_3}\right)$. However, if we were to consider only a single unit cell in our calculations, the frozen-phonon method that the VSCF method considered here relies on can only take into account phonons at the Γ-point – any distortion frozen into the single unit cell will be repeated in all other unit cells, making the wavelength of the phonon infinite and therefore $\mathbf{q} = 0$.

To sample phonons at non-zero values of $\mathbf{q}$, it is necessary to use a supercell for vibrational calculations, as including more unit cells within the repeated block allows for finer sampling of the vibrational BZ. Because we cannot do calculations with infinitely large supercells, in practice we replace integrals over the vibrational BZ with sums over a grid of $\mathbf{q}$-points. The resulting vibrational properties must be converged with respect to the size of this grid to ensure they are accurate.

We can describe the construction of a supercell using a supercell matrix S, which describes the transformation from the primitive lattice basis vectors $\mathbf{a}$ to the supercell lattice basis vectors $\mathbf{A}$ [89]:

$$\mathbf{A} = S\mathbf{a} \ . \tag{2.87}$$

Two supercell matrices describe the same supercell if they can be transformed into one another using elementary unimodular row operations [90], which allows all supercell matrices to be written in an upper-triangular Hermite normal form,

$$S = \begin{pmatrix} S_{11} & S_{12} & S_{13} \\ 0 & S_{22} & S_{23} \\ 0 & 0 & S_{33} \end{pmatrix} \ , \tag{2.88}$$

with all $S_{ij} \geq 0$, $S_{12} < S_{22}$ and $S_{13}, S_{23} < S_{33}$. The number of unit cells within the supercell is given by $|S| = S_{11}S_{22}S_{33}$.

Ordinarily, if an $n \times n \times n$ grid of $\mathbf{q}$-points is required to sample the vibrational BZ, an $n \times n \times n$ supercell is used for the calculations, containing n^3 unit cells. Such a supercell is commensurate with all the $\mathbf{q}$-points in the sampling grid, and is known as a *diagonal* supercell, as in this case the supercell matrix is diagonal, with $S_{11} = S_{22} = S_{33} = n$.

In most of this work, however, we utilise a method for sampling the vibrational BZ more efficiently using *non-diagonal* supercells, i.e. those where the supercell matrix is non-diagonal, proposed by Lloyd-Williams and Monserrat [89]. This method rests on the fact that in order to sample a **q**-point with reduced fractional co-ordinates $\left(\frac{m_1}{n_1}, \frac{m_2}{n_2}, \frac{m_3}{n_3}\right)$, it is only necessary to include l_{123} unit cells in the supercell, where l_{123} is the lowest common multiple of n_1, n_2 and n_3. Mathematically, it can be shown that [89]

$$\begin{aligned} S_{11} &= \frac{g_{123}n_1}{g_{12}g_{31}}, \; S_{12} = \frac{qg_{123}n_2}{g_{12}g_{23}}, \; S_{13} = \frac{rg_{123}n_3}{g_{31}g_{23}} \\ S_{22} &= \frac{n_2}{g_{23}}, \qquad S_{23} = \frac{pn_3}{g_{23}} \\ S_{33} &= n_3 \; . \end{aligned} \tag{2.89}$$

Here, g_{ij} is the greatest common factor of n_i and n_j, g_{123} is the greatest common factor of n_1, n_2 and n_3, and p, q and r are non-negative integers, chosen subject to the constraints $p < g_{23}$, $q < \frac{g_{12}}{g_{123}}$ and $r < \frac{g_{31}g_{23}}{g_{123}}$. This gives $|S| = \frac{g_{123}n_1n_2n_3}{g_{12}g_{23}g_{31}} = l_{123}$, as stated above.

The application of such non-diagonal supercells to vibrational calculations means that, if we only consider the sampled **q**-points one at a time, or in small groups, we can find a commensurate supercell that is much smaller than the one that is commensurate with all the **q**-points. In particular, if an $n \times n \times n$ sampling grid is required, the use of non-diagonal supercells instead of an $n \times n \times n$ diagonal supercell reduces the maximum supercell size required from n^3 to simply n. This massively reduces the computational cost of doing such calculations, and allows the vibrational BZ to be sampled much more finely than would previously have been possible. However, it does have the drawback that phonon modes at different **q**-points cannot be coupled unless the non-diagonal supercells they correspond to happen to be the same.

Convergence considerations

In the course of carrying out anharmonic vibrational calculations using the VSCF method outlined above, there are several computational parameters that must be assigned appropriate values, as previously mentioned. The two most important of these are the number of mapping points used per mode and the size of the **q**-point grid used to sample the vibrational BZ. Both of these directly affect the number and computational cost of the DFT calculations used to map the BO surface correctly – the most expensive part of the whole method – and so it is important to decide on an appropriate value for each.

Typically, the values of these parameters are increased until the anharmonic correction to the energy, $\Delta E_{\text{anh}} = E_{\text{anh}} - E_{\text{har}}$, is converged to within a given tolerance.

Additionally, the anharmonic correction should be converged with respect to the number of basis states used per mode when solving the VSCF equations, as well as the number of excited states described per mode. For calculations at zero temperature, as low as 20 basis functions can be used to obtain an accurate result. For calculations at finite temperature, more basis functions are required.

Part II

Method Development

Chapter 3

Improved Mapping of the Born-Oppenheimer Surface

In this chapter, we consider how the VSCF method detailed in Sections 2.3.2 and 2.3.3 can be improved. In particular, we look at how to reduce the computational cost of the method by reducing the number of calculations required to map the Born-Oppenheimer surface to a given accuracy. This can be done by utilising the forces on the atoms, which are easily calculated within a plane-wave DFT calculation, to additionally find the gradient of the BO surface at each mapping point. With this extra data, an accurate fit to the BO surface can be found using fewer mapping points, and thus for a lower computational cost. This 'VSCF+f' method is tested on a variety of systems – molecular hydrogen, solid hydrogen at 100 GPa, and the *bcc* phases of lithium and zirconium. The use of the forces in the fitting procedure is found to speed up the anharmonic calculations by up to 40%.

3.1 Improving the fitting of the Born-Oppenheimer surface

3.1.1 Motivation

As we have seen in Section 2.3.3, using the VSCF method to calculate the anharmonic properties of a material consists of two main tasks – mapping of the BO energy surface that the nuclei move through, and self-consistently solving the VSCF equations for the anharmonic vibrational wavefunction and energy. Of these two tasks, the former is typically by far the most expensive, as it is usually accomplished by performing a large number of DFT calculations and fitting a functional form to the calculated energies. The large number of calculations necessary to obtain a good fit to the true BO surface make the VSCF method significantly more expensive than just using the simpler harmonic approximation. Reducing this computational cost without losing accuracy is therefore a major aim. As the calculations mapping the BO surface constitute most of the computational cost of using the VSCF method, reducing the overall cost of the method can be done most effectively by reducing the cost of the mapping process, but in such a way as to not lose accuracy. To do this, there are two main options:

- reduce the cost of the individual mapping calculations, or
- reduce the number of mapping calculations required.

The only realistic way of implementing the first of these approaches is by using a cheaper method than DFT to conduct the mapping calculations, for example force fields [91, 92]. However, these methods do not provide sufficient accuracy for the high quality fit to the BO surface required by the VSCF method. Instead, we focus on the second approach – reducing the number of mapping calculations required for a given accuracy, or conversely, increasing the accuracy of the fit for a given number of mapping points.

The task of increasing the accuracy of the BO surface fit could be approached in two different ways – either by improving the method used to fit to the energies calculated at each mapping, or by making use of information that is already being calculated, but is currently discarded by the fitting process. The fitting method used in the standard VSCF method described in 2.3.3, that of cubic spline interpolation, is already among the most stable of the possible interpolation routines, and also guarantees that the resulting function has a continuous second derivative [93]. This implies that improving on the routine used for fitting the BO surface would be a difficult task. On the other hand, there is one glaringly obvious piece of data that can be obtained, basically for free, during the usual mapping DFT calculations – the forces on the atoms. Accurate atomic forces are easily calculated within plane-wave basis DFT, as seen in 2.2.5 [64], and in `CASTEP` they are calculated as a matter of course for any calculation of the total electronic energy. As we know that, in general, the force in a system at a given point is given by the negative of the derivative of the potential energy at that point, $\mathbf{F}(\mathbf{x}) = -\nabla U(\mathbf{x})$ [94], we would expect that we should be able to link the atomic forces to the gradient of the BO surface in a given direction. Using this data to improve the fitting of the BO surface, and thus reduce the calculational cost of the VSCF method, is the motivation behind the work presented in this chapter.

3.1.2 Fitting including calculated forces

The first step towards using the atomic forces to improve the fitting of the BO surface is to obtain an expression linking the gradient of the BO surface to the calculated forces on the atoms. To begin with, we consider exploring the BO surface as a function of one phonon normal co-ordinate at a time. Equations (2.62) and (2.63) tell us that we can express harmonic normal co-ordinates $u_{n\mathbf{q}}$ in terms of the atomic displacements $X_{p\alpha i}$,

and vice versa, through the expressions:

$$u_{n\mathbf{q}} = \frac{1}{\sqrt{N_p}} \sum_{p\alpha i} \sqrt{m_\alpha} X_{p\alpha i} e^{-i\mathbf{q}\cdot\mathbf{R}_p} w_{-\mathbf{q}ni\alpha} \ , \tag{3.1}$$

$$X_{p\alpha i} = \frac{1}{\sqrt{N_p m_\alpha}} \sum_{n\mathbf{q}} u_{n\mathbf{q}} e^{i\mathbf{q}\cdot\mathbf{R}_p} w_{\mathbf{q}ni\alpha} \ . \tag{3.2}$$

Here, N_p is the number of unit cells, $\mathbf{R}_p$ is the real space lattice vector corresponding to the pth unit cell, and the $w_{\mathbf{q}ni\alpha}$ are the eigenstates of the dynamical matrix. p runs over all unit cells in the supercell, α runs over atoms within the unit cell, and i runs over the three Cartesian directions. If we now consider the BO surface, E_{elec}, to be a function of the atomic displacements $X_{p\alpha i}$, we can express a small change in E_{elec}, dE_{elec}, as

$$dE_{\text{elec}} = \sum_{p\alpha i} \frac{\partial E_{\text{elec}}}{\partial X_{p\alpha i}} dX_{p\alpha i} = -\sum_{p\alpha i} f_{p\alpha i} dX_{p\alpha i} \ . \tag{3.3}$$

$f_{p\alpha i} = -\frac{\partial E_{\text{elec}}}{\partial X_{p\alpha i}}$ represents the force on the αth atom in the pth unit cell in the ith Cartesian direction, as typically calculated within plane-wave basis DFT. Dividing this equation through by $du_{n\mathbf{q}}$ and substituting in $\frac{\partial X_{p\alpha i}}{\partial u_{n\mathbf{q}}}$, obtained from equation (3.2), then gives

$$\begin{aligned} \frac{\partial E_{\text{elec}}}{\partial u_{n\mathbf{q}}} &= -\sum_{p\alpha i} f_{p\alpha i} \frac{\partial X_{p\alpha i}}{\partial u_{n\mathbf{q}}} \\ &= -\sum_{p\alpha;i} \frac{1}{\sqrt{N_p m_\alpha}} f_{p\alpha i} e^{i\mathbf{q}\cdot\mathbf{R}_p} w_{\mathbf{q}ni\alpha} \ . \end{aligned} \tag{3.4}$$

$\frac{\partial E_{\text{elec}}}{\partial u_{n\mathbf{q}}}$ is the gradient of the BO surface along the direction given by $u_{n\mathbf{q}}$. As the forces $f_{p\alpha i}$ and all of $\mathbf{q}$, N_p, m_α, $\mathbf{R}_p$ and $w_{\mathbf{q}ni\alpha}$ are known, this quantity can easily be calculated for each mapping point, and the result fed into the fitting, or interpolation, procedure. Using the atomic force data to help solve the VSCF equations more accurately will be referred to as the 'VSCF+f' method from here onwards, to differentiate this modified procedure from the standard VSCF method described in 2.3.3.

Cubic spline interpolation

The standard VSCF method uses cubic spline interpolation to obtain fits for the 1-D terms in the expansion of the BO surface given by equation (2.73). In general, given a set of points $\{x_1, \cdots, x_n\}$ and the values of a function at those points $\{y_1, \cdots, y_n\}$, cubic spline interpolation takes each interval (x_i, x_{i+1}) separately, and assumes that the

function in that interval can be described by a cubic polynomial. $(n-2)$ boundary conditions are then applied to ensure that the second derivative is continuous at the x_i, plus two further boundary conditions determining how the second derivative behaves at x_1 and x_n. Throughout this chapter, and indeed this thesis, we use what is called a 'natural' spline, where the second derivative is taken to be zero at x_1 and x_n. The system of equations that these boundary conditions imply has a particularly simple *tridiagonal* form - that is, the unknown coefficients of polynomial i only couple to the coefficients in polynomials $i \pm 1$. Solving such a system of equations can be done very easily to find the coefficients of the cubic polynomial in each interval, giving a smooth and well-fitted function overall [93].

A convenient way to express the cubic polynomials that make up a cubic spline is to use what is known as the Hermite form, in which the polynomials are written in terms of the function values and gradients at the end points of the interval in question. If we consider the interval (x_i, x_{i+1}) and define $t = \frac{x-x_i}{x_{i+1}-x_i} \in (0,1)$, we can write the polynomial in this interval as [95]

$$y(x) = h_0^{(3)}(t)y_i + h_1^{(3)}(t)(x_{i+1}-x_i)k_i + h_2^{(3)}(t)y_{i+1} + h_3^{(3)}(t)(x_{i+1}-x_i)k_{i+1} \ . \quad (3.5)$$

Here, k_i is the gradient of the fitted curve at x_i, and the $h_i^{(3)}(t)$ are Hermite basis functions. These are simple polynomials, defined as

$$h_0^{(3)}(t) = (1+2t)(1-t)^2 \qquad h_1^{(3)}(t) = t(1-t)^2 \quad (3.6)$$

$$h_2^{(3)}(t) = t^2(3-2t) \qquad h_3^{(3)}(t) = t^2(t-1) \ .$$

Without knowledge of the gradients k_i, the standard cubic spline interpolation procedure would impose the continuity of the second derivative to produce a set of tridiagonal equations, from which the k_i can be found. However, if the k_i are in fact known, they can be substituted directly into equation (3.5), obtaining a cubic spline fit for the function with no further work. This can all be very simply applied to the VSCF+f method, as we can easily obtain the gradient at each mapping point from the atomic forces, giving a form for the 1-D terms of the BO surface expansion immediately.

Quintic spline interpolation

If only the function values y_i at each of the points x_i are known, using a cubic polynomial as the functional form in each (x_i, x_{i+1}) interval gives two fittable parameters per

polynomial, the gradients at each point k_i. If we instead know both the function value and the gradients at each point *a priori*, using a cubic polynomial no longer provides any fittable parameters. This naturally leads to the idea that, if we now have more information, we should be able to use a higher order polynomial to describe the function in each (x_i, x_{i+1}) interval, still using no more than two fitting parameters per polynomial. Using a higher order polynomial like this could potentially provide a better fit to the true function, and so we consider quintic spline interpolation.

Quintic spline interpolation, as the name suggests, uses quintic polynomials to describe the function in each interval. The procedure is very similar to that of standard cubic spline interpolation, except now we enforce continuity of the third order derivative at the x_i, with a natural quintic spline corresponding to taking this derivative to be 0 at x_1 and x_n. The quintic polynomials used are of a similar form to equation (3.5) [95]:

$$\begin{aligned} y(x) = {} & h_0^{(5)}(t)y_i + h_1^{(5)}(t)(x_{i+1}-x_i)k_i + h_2^{(5)}(t)(x_{i+1}-x_i)^2 a_i \\ & + h_3^{(5)}(t)(x_{i+1}-x_i)^2 a_{i+1} + h_4^{(5)}(t)(x_{i+1}-x_i)k_{i+1} + h_5^{(5)}(t)y_{i+1} \ . \end{aligned} \tag{3.7}$$

Here, a_i is the second derivative of the fitted curve at x_i, and the $h_i^{(5)}(t)$ are quintic Hermite basis functions. They are defined as

$$\begin{aligned} h_0^{(5)}(t) &= (1-t)^3(6t^2+3t+1) \qquad & h_1^{(5)}(t) &= t(1-t)^3(3t+1) \\ h_2^{(5)}(t) &= \frac{1}{2}t^2(1-t)^3 \qquad & h_3^{(5)}(t) &= \frac{1}{2}t^3(t-1)^2 \\ h_4^{(5)}(t) &= t^3(1-t)(3t-4) \qquad & h_5^{(5)}(t) &= t^3(6t^2-15t+10) \ . \end{aligned} \tag{3.8}$$

By applying the boundary conditions on the third derivative noted above, a tridiagonal system of equations extremely similar to that found for the cubic spline can be obtained, allowing the unknown a_i to be found and the overall quintic spline fit to be found. This can again all be applied within the VSCF+f method, and its performance compared to that of the cubic spline.

Higher order spline interpolation

As we have been able to increase the order of the spline fit used from cubic to quintic with no extra computational effort, it is natural to ask if we can push this further, by using higher order spline interpolation methods. After the quintic spline, the next possible

order of the splines used is seventh order – known as either a heptic or septic spline. Such a spline interpolation procedure would write the polynomials in each interval as [95]

$$\begin{aligned} y(x) = {} & h_0^{(7)}(t)y_i + h_1^{(7)}(t)(x_{i+1}-x_i)k_i + h_2^{(7)}(t)(x_{i+1}-x_i)^2 a_i \\ & + h_3^{(7)}(t)(x_{i+1}-x_i)^3 j_i + h_4^{(7)}(t)(x_{i+1}-x_i)^3 j_{i+1} + h_5^{(7)}(t)(x_{i+1}-x_i)^2 a_{i+1} \\ & + h_6^{(7)}(t)(x_{i+1}-x_i)k_{i+1} + h_7^{(7)}(t)y_{i+1} \ . \end{aligned} \tag{3.9}$$

Here, j_i is the third derivative of the fitted curve at x_i. The heptic Hermite basis functions are defined as

$$\begin{aligned} h_0^{(7)}(t) &= (t-1)^4(20t^3+10t^2+4t+1) \qquad h_1^{(7)}(t) = t(t-1)^4(10t^2+4t+1) \\ h_2^{(7)}(t) &= \frac{1}{2}t^2(t-1)^4(4t+1) \qquad h_3^{(7)}(t) = \frac{1}{6}t^3(t-1)^4 \\ h_4^{(7)}(t) &= \frac{1}{6}t^4(t-1)^3 \qquad h_5^{(7)}(t) = \frac{1}{2}t^4(t-1)^2(5-4t) \ . \\ h_6^{(7)}(t) &= t^4(t-1)(10t^2-24t+15) \qquad h_7^{(7)}(t) = t^4(-20t^3+70t^2-84t+35) \ . \end{aligned} \tag{3.10}$$

By applying the usual boundary conditions on both the fourth and fifth order derivatives, we can obtain a set of equations that can be solved to obtain the unknown a_i and j_i, giving an overall form for the spline.

The use of a heptic spline to fit the 1-D terms in the expansion of the BO surface was tested as part of the work presented in this chapter, but this approach suffered from overfitting and performed significantly worse than the cubic and quintic splines. For this reason, heptic and higher order splines will not be discussed further.

Two-dimensional spline fitting

The previous sections have shown that utilising forces to improve the mapping of the 1-D terms in the expansion of the BO surface in equation (2.73) is a simple extension of the usual splining procedure. When we consider the higher dimensional terms, however, the task becomes more complex. In this thesis, the only higher dimensional terms considered are 2-D, as terms involving more than two dimensions are prohibitively computationally expensive, even for the smallest systems; therefore, we concentrate on the fitting of 2-D terms only. Given the values of the function on a grid of mapping points, a functional form for such terms can be found by fitting a series of 1-D splines along one direction (corresponding to the co-ordinate u_1), and then using the results to fit a spline along

the second direction (corresponding to the co-ordinate u_2). This means that in order to be able to conduct a fitting procedure that makes full use of the gradient information in both mapping directions, our procedure must give us the quantity $\frac{\partial E_{\mathrm{el}}(\mathbf{u})}{\partial u_2}\Big|_{x_2}(u_1)$. This represents the gradient along the u_2 direction as a function of u_1, for a fixed value of $u_2 = x_2$. This quantity gives the required gradient information for the fitting in the u_2 direction. However, fitting a functional form for this parameter using the same procedure as for the 1-D fittings of E_{el} requires knowledge of the cross derivative $\frac{\partial^2 E_{\mathrm{el}}(\mathbf{u})}{\partial u_1 \partial u_2}$ at each sampling point [93] – a quantity that is not easily available from DFT calculations. Instead, we are forced to use a simple cubic spline to obtain the form of $\frac{\partial E_{\mathrm{el}}(\mathbf{u})}{\partial u_2}\Big|_{x_2}(u_1)$, which may limit the accuracy of the fitting procedure. To examine the accuracy of the calculations including 2-D terms, we converge the correction to the anharmonic vibrational energy due to these terms, $\Delta E_{\text{2-D}} = E^{\mathrm{anh}}_{\text{2-D}} - E^{\mathrm{anh}}_{\text{1-D}}$, with respect to the number of mapping points used per direction.

Accuracy of forces

Although including the force data in the fitting process should reduce the number of calculations required to obtain convergence, the accuracy of the forces themselves must be considered. If a variational method is used to minimise the total energy in the DFT calculations, the energy itself will be correct to second order errors in the charge density. However, the error in the forces is instead linear with the error in the charge density [64], meaning that calculations must be converged to within a strict tolerance to obtain accurate forces. This requirement could potentially cancel out the reduction in computational cost gained by reducing the number of mapping points if the convergence tolerance is too strict, and our results include tests to determine whether this is true or not. These tests showed that this issue did not negatively affect the speed-up obtainable with the VSCF+f method, with both methods breaking down at the same level of energy convergence.

3.2 Fitting with and without forces: calculations on test systems

In order to test the performance of the VSCF+f method relative to the VSCF method, as well as the performance of the cubic spline against the quintic spline within the

VSCF+f method, test calculations on a variety of systems are required. To make sure that the methods are properly tested, the systems chosen should exhibit significant anharmonicity, so that differences in the performance of the two methods are easily visible. A range of different types of systems should also be used for testing, to check the generality of any conclusions made about the performance of the two methods.

To this end, six different test systems were chosen – molecular hydrogen, three different structures of solid hydrogen at 100 GPa, and the body centered cubic (*bcc*) high temperature phases of lithium and zirconium. Both the VSCF and VSCF+f methods were applied to all of these systems, and the convergence of the results with respect to the number of mapping points was compared. More detail on each system, its suitability as a test case, and the results for that system are presented below.

All DFT calculations were performed using version 8.0 of `CASTEP` [56] and ultrasoft pseudopotentials [61] generated 'on-the-fly' by `CASTEP`. In all calculations, a grid scale of 2.0 was used. The local density approximation (LDA) was used for the exchange-correlation functional in the hydrogen calculations [28], while the PBE functional was used for lithium and zirconium [45]. Previous work on solid hydrogen has shown that, while the exact quantitative results of DFT calculations are strongly dependent on the choice of functional, the qualitative results are similar for most functionals [96], and that the LDA is a reasonable choice for the purpose of tests on solid hydrogen. The PBE functional has been used successfully in several previous studies of lithium, zirconium and other similar materials [97, 98]. The preliminary harmonic calculations necessary before the full mapping of the BO surface begins were performed using the finite displacements method described in Section 2.3.3, with atomic displacements of 0.00529 Å (0.01 bohr) used.

3.2.1 Hydrogen

Background

As the lightest element, hydrogen is an excellent test case for the VSCF+f method, as its vibrations have strong anharmonic character, even at low temperatures. The most basic and common form of hydrogen, the hydrogen molecule H_2, is therefore a good system to use for initial comparisons between the VSCF and VSCF+f methods. The hydrogen molecule only has a single vibrational mode with a frequency of 0.5159 eV [99]. Because `CASTEP` uses periodic boundary conditions, however, it is necessary to be careful

that spurious interactions between the molecule and its periodic images do not affect the result; the unit cell must be large enough to sufficiently separate the molecule and its images.

Besides molecular hydrogen, solid hydrogen would also provide a suitable test case, as this should retain much of the anharmonic character of molecular hydrogen, but in a periodic system, much more like those typically considered using the VSCF method. Hydrogen becomes a solid at high pressure, and over the last few decades, much work has gone into determining how hydrogen behaves under these conditions, especially with regard to the crystal structure it takes. The high-pressure phase diagram of hydrogen is of interest due to the many different potential phenomena it is thought it may exhibit, such as high-temperature superconductivity [100, 101] and/or superfluidity [102]. Identifying the metallisation transition, i.e. the point at which hydrogen becomes metallic, is also of interest [103, 104]. Hydrogen exists under such extreme conditions inside gas giant planets, such as Jupiter and Saturn, so the high-pressure behaviour of hydrogen has significant implications for extra-terrestrial planetary science.

There are five experimentally known solid phases of hydrogen at room temperature, typically labelled as I, III, IV, IV′ and V in order of stability with increasing pressure [105, 106]. Phase II also exists at lower temperatures up to moderately high pressures [80, 107]. The phase diagram of hydrogen at high pressures and temperatures as it is currently understood is shown in Fig. 3.1 [106, 107]. Because these extreme conditions are difficult to reach experimentally, several *ab initio* studies of the high pressure phases of hydrogen, both with and without the inclusion of anharmonic effects, have been conducted to determine the structures of the high pressure phases [77, 80, 83, 96, 101, 108–111]. For the purposes of testing the VSCF+f method, we chose as test cases three structures that have been studied in previous work, labelled by their space group and number of atoms in the primitive unit cell: *Cmca*-4, *Cmca*-12 and *C2/c*-24 [77, 80, 96, 109, 110]. These are molecular phases arranged in layers; the *C2/c*-24 phase is a potential structure for phase III of hydrogen [109]. We consider these structures at a pressure of 100 GPa, at which all three phases are dynamically stable. Previous work has shown that anharmonicity has a significant effect on the vibrational energy of high pressure structures of solid hydrogen [83, 101], confirming that these systems are a suitable test case for the VSCF+f method.

The strongly anharmonic character of the nuclear vibrations in hydrogen also im-

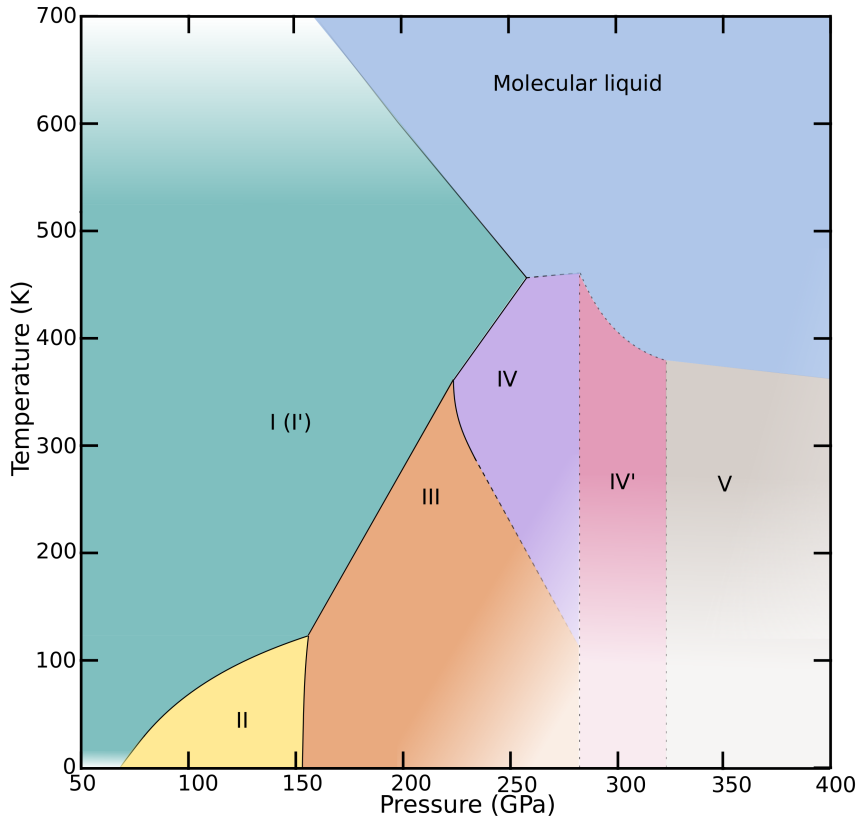

Figure 3.1: Currently accepted form of the phase diagram of solid hydrogen at high pressures and temperatures, adapted from Refs. 106 and 107. Data was not available for the region with pressures greater than around 200 GPa and temperatures less than around 300 K, so the boundaries between phases in this region are simply continuations of those at higher temperatures.

plies that anharmonic effects that cannot be described just using the 1-D terms in the expansion of the BO surface could be significant. This provides an opportunity to test the ability of the VSCF+f method to reduce the computational cost of calculations including the mapping of 2-D subspaces of the BO surface. Because conducting such a 2-D mapping is significantly more expensive than a simple 1-D mapping, we have only tested the mapping of such terms in the phase of solid hydrogen with the fewest atoms in its unit cell, *Cmca*-4.

Mapping of one-dimensional terms: molecular hydrogen

A plane-wave cut-off energy of 800 eV was used for the calculations on molecular hydrogen, with a $5 \times 5 \times 5$ Monkhorst-Pack **k**-point grid [69]. As previously mentioned, the periodic boundary conditions used in `CASTEP` make it necessary to have a unit cell large enough to prevent the molecule from interacting with its periodic images. The frequencies of the harmonic phonon modes were converged with respect to the size of the cubic unit cell, resulting in a converged 'lattice constant' of 8 Å. The distance between the atoms was allowed to relax, using the Broyden-Fletcher-Goldfarb-Shanno (BFGS) method [66] to converge the forces on the atoms to within 0.001 eV Å^{-1}, before single-point energy calculations were conducted.

Once the harmonic calculations were completed, a range of different numbers of mapping points per direction from 7 to 27 were used to map the BO surface of the hydrogen molecule. The performance of the basic VSCF method was compared to the VSCF+f method using both cubic and quintic splines in the fitting process. This was repeated with the energy convergence tolerance of the calculations set to $10^{-10}, 10^{-6}, 10^{-4}$ and 10^{-2} eV per SCF cycle, to test whether this affected the accuracy of the forces, and therefore the accuracy of the VSCF+f fitting relative to the normal fitting procedure. Fig. 3.2 shows the convergence of the anharmonic correction to the zero point energy, $\Delta E_{\text{anh}} = E_{\text{anh}} - E_{\text{har}}$, with respect to the number of mapping points for the three different methods. Here the energy convergence tolerance was set to 10^{-6} eV per SCF cycle. It can be seen that including the forces in the fitting process significantly speeds up the convergence of ΔE_{anh}, with the quintic spline fit performing even better than the cubic spline. This suggests that including forces in the fitting process can significantly improve the efficiency of the VSCF method, and that utilising a quintic spline allows fitting of the BO surface even more accurately for the same number of DFT calculations, especially

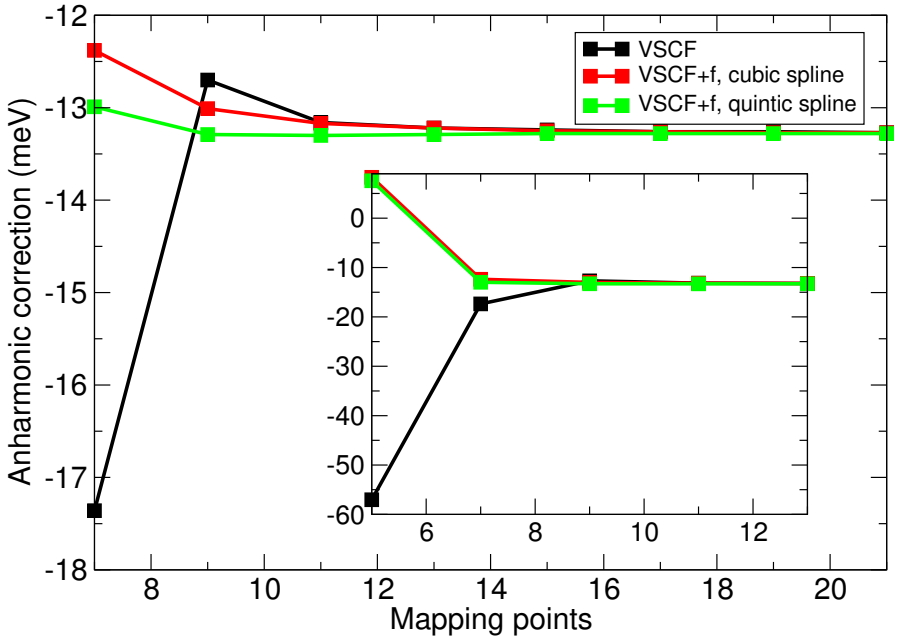

Figure 3.2: Convergence of anharmonic correction to the energy at 0 K for H_2, $\Delta E_{\mathrm{anh}} = E_{\mathrm{anh}} - E_{\mathrm{har}}$, with respect to the number of mapping points used per mapping direction, for the basic VSCF method, as well as the VSCF+f method, fitting with both cubic and quintic splines. The inset shows the results at low numbers of mapping points on a different energy scale.

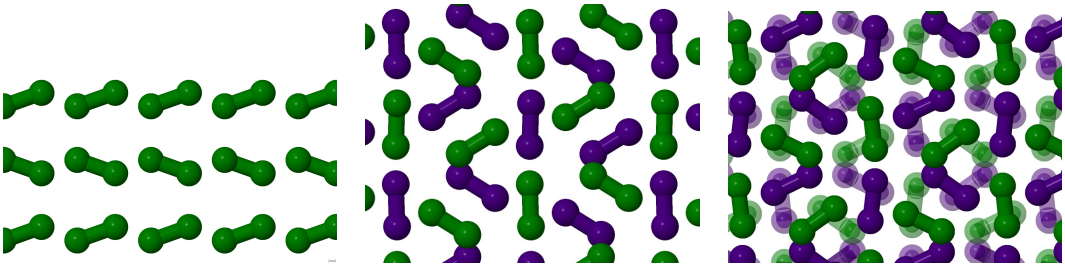

(a) *Cmca*-4 (b) *Cmca*-12 (c) *C2/c*-24

Figure 3.3: Views of the structures of solid hydrogen considered at 100 GPa. Both of the *Cmca* structures are shown looking along the x-axis, while the *C2/c*-24 structure is shown looking along the y-axis. As these are layered structures, atoms in inequivalent layers are denoted by different colours. Green, purple, translucent green and translucent purple denote the first, second, third and fourth inequivalent layers, respectively.

for low numbers of mapping points. An almost identical set of results was found for energy convergence tolerances from 10^{-4} eV up to 10^{-10} eV per SCF cycle, with the VSCF+f method converging more rapidly with the number of mapping points. For an energy convergence tolerance of 10^{-2} eV per SCF cycle, both the VSCF and VSCF+f methods failed to converge with 27 or fewer mapping points per direction. This shows that for a range of energy convergence tolerances, the VSCF+f fitting method is still able to outperform the basic VSCF method and map the BO surface accurately at a lower computational cost. Using a quintic spline improves the quality of the fit still further.

Mapping of one-dimensional terms: solid hydrogen at 100 GPa

With the results from the hydrogen molecule in mind, we turn our attention to the case of high pressure solid hydrogen. Three different structures of solid hydrogen were considered at a pressure of 100 GPa – *Cmca*-4, *Cmca*-12 and *C2/c*-24, as previously described. Fig. 3.3 gives a view of these three structures, showing that they are molecular in nature. These structures have all been studied previously with DFT over a range of pressures [110]. Again, once harmonic calculations were completed, the convergence of the anharmonic correction to the zero point energy per atom with respect to the number of mapping points was calculated for a single unit cell of each structure. A plane-wave cut-off energy of 1000 eV and an energy convergence tolerance of 10^{-6} eV per SCF cycle was used throughout, with Monkhorst-Pack grids of size $28 \times 28 \times 16$, $18 \times 18 \times 4$ and

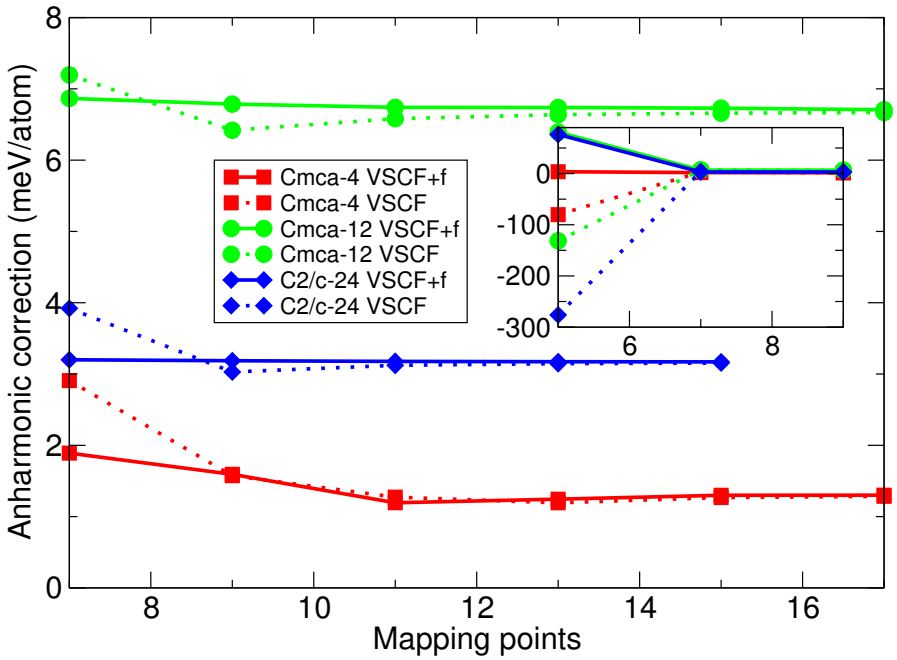

Figure 3.4: Convergence of the anharmonic correction to the energy at 0 K, ΔE_{anh}, of the *Cmca*-4, *Cmca*-12 and *C2/c*-24 phases of solid hydrogen at 100 GPa, with respect to the number of mapping points used per mapping direction. The convergence of the basic VSCF method as well as the VSCF+f method of fitting with a quintic spline are shown. The inset shows the results at low numbers of mapping points on a different energy scale.

$16 \times 8 \times 16$ for the *Cmca*-4, *Cmca*-12 and *C2/c*-24 structures respectively. Fig. 3.4 shows the convergence of ΔE_{anh} per atom for all three structures for the basic VSCF and the improved VSCF+f quintic spline methods. Again, convergence was reached with fewer numbers of mapping points per direction using the VSCF+f method than with the VSCF method, especially for the *Cmca*-12 and *C2/c*-24 structures. In the latter case, including forces in the fitting reduces the computational cost by around 40%. This further implies that the VSCF+f method is robust and improves on the efficiency of the basic VSCF method.

Mapping of two-dimensional terms

We now turn to applying the VSCF+f method to the mapping of 2-D subspaces of the BO surface. This poses a more significant challenge than the 1-D terms considered up to now, as interpolating data in two dimensions is required. As mentioned previously, we fo-

cus on a single unit cell of the *Cmca*-4 structure of solid hydrogen, which possesses twelve potential mapping directions, corresponding to the twelve harmonic phonon modes, labelled with numbers from 1 to 12. The first three of these modes are acoustic, meaning they have zero frequency, and are therefore not considered in the mapping process. To minimise the computational cost further, we consider only four of the many 2-D subspaces in this system – those corresponding to the directions described by the harmonic modes 4 and 5, 4 and 6, 4 and 7, and 4 and 9. The harmonic frequencies of modes 4, 5, 6, 7 and 9 are 69.4, 74.0, 77.3, 114 and 159 meV, respectively, and the displacement patterns corresponding to each of these mapping directions can be found in Appendix A. These subspaces were chosen by conducting a preliminary mapping of all 2-D subspaces with a low number of mapping points, and taking only those with significant corrections to the 1-D description of the BO surface. Subspaces where the mapping entered parts of energy minima in the BO surface corresponding to structures significantly lower in energy than the *Cmca*-4 structure were also neglected. The same cut-off energy and Monkhorst-Pack grid was used as for the calculations of the 1-D terms in the *Cmca*-4 structure, but an energy convergence tolerance of 10^{-10} eV was used to ensure accurate forces.

Figs. 3.5 and 3.6 shows the results of tests including the mapping of 2-D subspaces in the *Cmca*-4 solid hydrogen structure. The four rows of figures correspond to the four subspaces mapped. The left-hand column shows the BO surface mapped in the relevant subspace, and the right-hand column shows the convergence of the correction to the energy due to 2-D terms, $\Delta E_{\text{2-D}}$, with respect to the number of mapping points used per mapping direction. All energies were again calculated at zero temperature. The convergence graphs show that utilising forces in the mapping of the 2-D terms in the expansion of the BO surface brings the results closer to the converged final value, especially for small numbers of mapping points, although the improvement is not as pronounced as in the 1-D case. This could be due to the small size of the energy scales in question – the energies shown are all smaller than 1 meV per atom, which is around the finest energy scale that such anharmonic calculations can reasonably be assumed to be accurate to. The small size of the corrections due to 2-D terms compared to those seen for 1-D terms shows that the neglect of such higher-order terms in the BO surface expansion of equation (2.73) is justified. The ability of the VSCF+f method to show improvement even at such small energy scales again demonstrates its capabilities, even

in cases including mapping of 2-D subspaces of the BO surface.

3.2.2 Lithium and zirconium

Background

We now turn to the last two test cases for the VSCF+f method – the body-centred cubic (*bcc*) phases of lithium and zirconium. These two metals have significantly different properties, but share one important characteristic – both have a *bcc* phase that is unstable at 0 K, but is stabilised at finite temperatures. This property is shared with many other elements such as titanium and hafnium. The zero-temperature instability of the *bcc* phases is characterised by the presence of soft modes – modes with imaginary frequency. By their very nature, soft modes are highly anharmonic, as they must contain some quartic character for the BO energy surface to be bounded, so an accurate description of anharmonicity is required to understand the transition into the *bcc* phase in both cases. Several first-principles vibrational studies including anharmonicity have been reported for lithium, zirconium and other similar elements [85, 97, 98, 112–115]. The well-known presence of significant anharmonic effects in the *bcc* phase of these materials makes them suitable test cases for the VSCF+f method.

Zirconium has a relatively simple phase diagram, exhibiting three phases, typically labelled α, β and ω. α-Zr has a hexagonal close packed (*hcp*) structure, and β-Zr is the *bcc* phase of interest here. ω-Zr is a different hexagonal phase that is not close packed. The overall phase diagram as a function of temperature and pressure is shown in Fig. 3.7 [116, 117]. At ambient conditions, the stable phase is the *hcp* phase α-Zr, but upon heating this transitions to the *bcc* β-Zr phase at around 1136 K [112, 116]. It is this transition that we will use as a test for the VSCF+f method.

Lithium, on the other hand, has a much more complex phase diagram, some details of which are still not fully determined. Under ambient conditions, lithium forms a *bcc* structure, but there is then a phase transition at around 70 K to a different structure. This low-temperature phase was thought to be a close-packed structure with *hR*9 symmetry (using Pearson notation) [97, 118–120], but recent results have suggested that this is not the case [121], and indeed that this low-temperature phase is simply a continuation of the face-centred cubic (*fcc*) phase that appears at slightly higher temperatures and pressures [122]. The currently accepted overall phase diagram as a function of temperature and pressure is shown in Fig. 3.8 [118]. Here we are not concerned with the precise

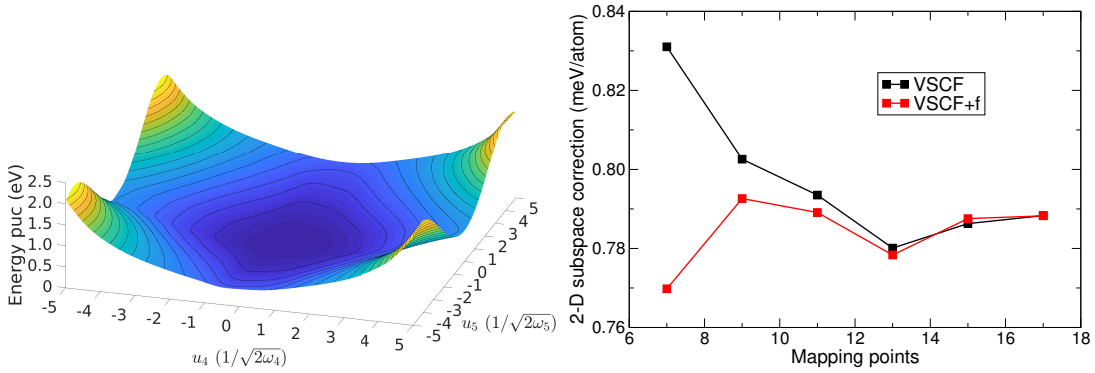

(a) Subspace corresponding to directions 4 and 5

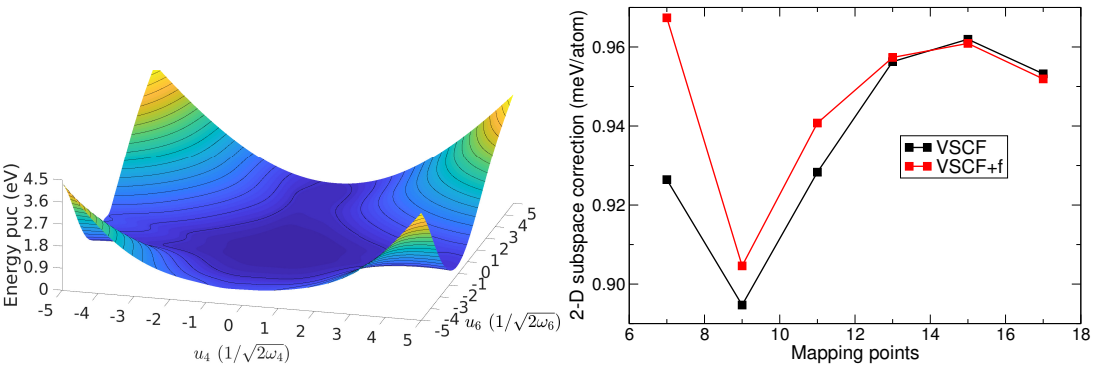

(b) Subspace corresponding to directions 4 and 6

Figure 3.5: Results of anharmonic vibrational calculations for the *Cmca*-4 structure of solid hydrogen including selected 2-D subspaces of the BO surface. The left-hand column shows BO surfaces mapped in the labelled subspace, where 'puc' stands for 'per unit cell', while the right-hand column shows the convergence of the correction to the vibrational energy due to the relevant 2-D term with respect to the number of mapping points used. Blue and yellow signify low and high energy parts of the BO surface respectively. Each contour line on the BO surface represents an energy increase of 0.115 and 0.235 eV in (a) and (b) respectively.

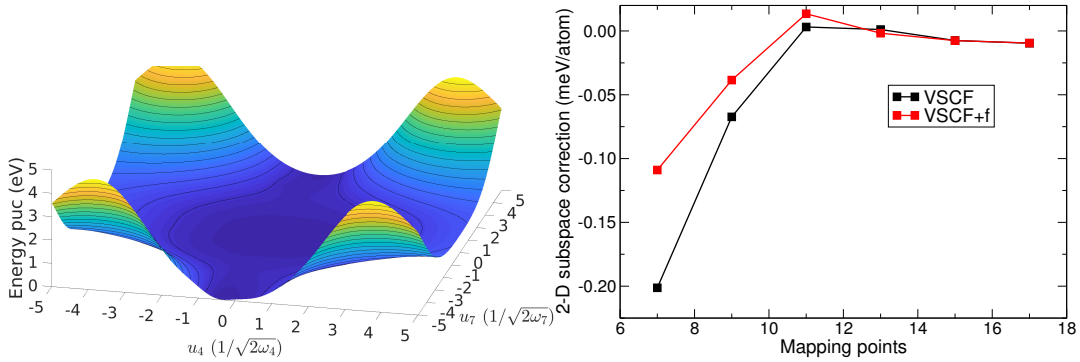

(a) Subspace corresponding to directions 4 and 7

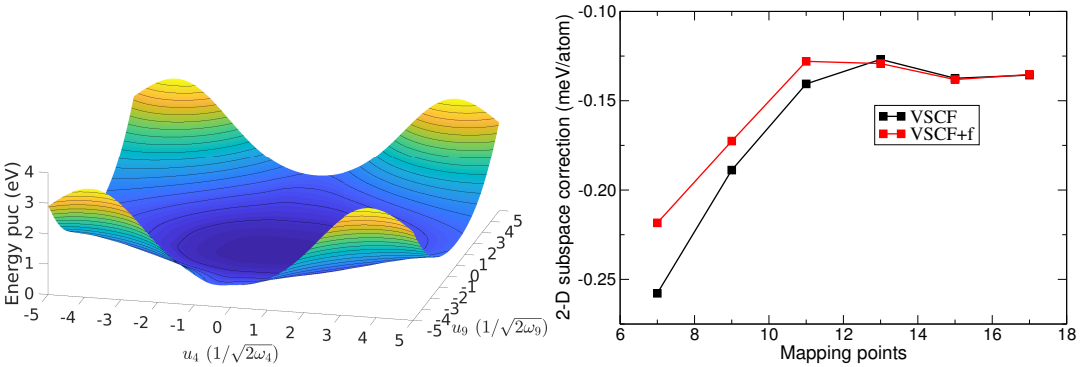

(b) Subspace corresponding to directions 4 and 9

Figure 3.6: Results of anharmonic vibrational calculations for the *Cmca*-4 structure of solid hydrogen including selected 2-D subspaces of the BO surface. The left-hand column shows BO surfaces mapped in the labelled subspace, where 'puc' stands for 'per unit cell', while the right-hand column shows the convergence of the correction to the vibrational energy due to the relevant 2-D term with respect to the number of mapping points used. Blue and yellow signify low and high energy parts of the BO surface respectively. Each contour line on the BO surface represents an energy increase of 0.249 and 0.190 eV in (a) and (b) respectively.

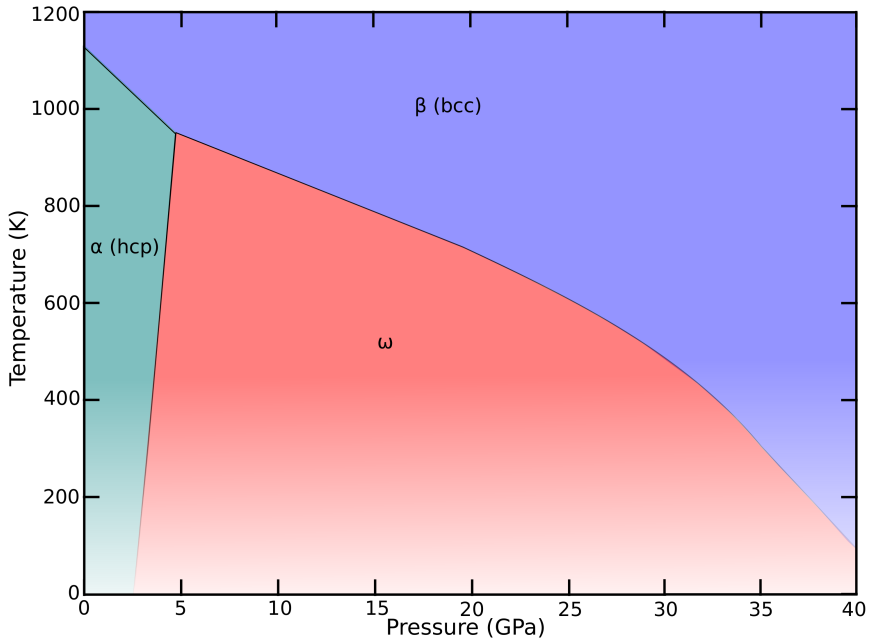

Figure 3.7: Phase diagram of zirconium over a range of pressures and temperatures, adapted from Refs. 116 and 117. Experimental data was not available at temperatures lower than 300 K for most of the pressure range, so the boundaries between phases in this region follow the trends predicted by first-principles DFT calculations.

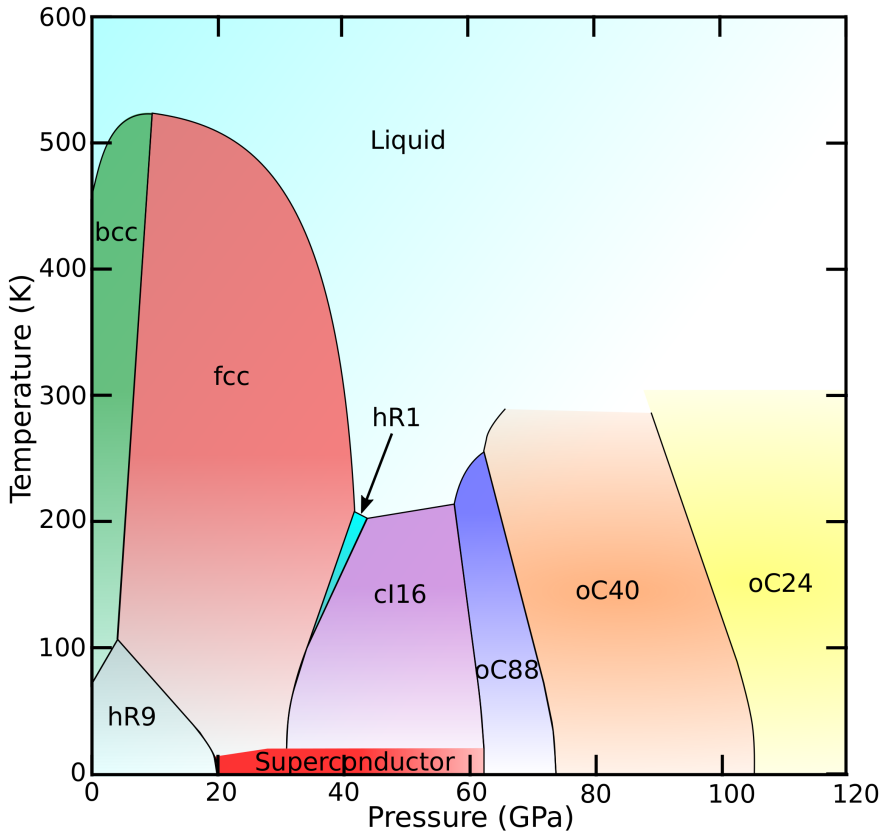

Figure 3.8: Currently accepted form of the phase diagram of lithium over a range of pressures and temperatures, adapted from Ref. 118. Little experimental data is available for the region with pressures greater than 70 GPa and temperatures greater than around 280 K, so no phase boundaries are shown in this region.

identity of the low-temperature phase of lithium, but only with the stabilisation of the *bcc* phase and how accurately the VSCF+f method describes this.

Results

For the calculations in lithium and zirconium, we also used the non-diagonal supercells method described in Section 2.3.3 to reduce the computational cost of sampling the vibrational Brillouin zone [89]. However, as the aim of the work presented in this chapter is to consider methods for improved fitting of the BO surface, rather than to conduct high-accuracy calculations on these well-studied materials, we did not attempt to completely converge our results with respect to the sampling of the vibrational BZ. Even with the non-diagonal supercell method, the computational cost increases rapidly with increasing sampling grid size. As a compromise between accuracy and speed, therefore, an $8 \times 8 \times 8$ sampling of the vibrational BZ was used. The Monkhorst-Pack grids in all supercells used had a spacing of 0.025 Å^{-1}, corresponding to a $16 \times 16 \times 16$ grid in the unit cell. An energy cut-off of 1500 eV was used in all calculations.

Fig. 3.9 and Figs. 3.10 and 3.11 present the results of the zero temperature calculations for Li and Zr respectively. Figs. 3.9(a) and 3.10(a) show how the sum of the calculated lowest energy eigenvalues for each mode, which would correspond to the anharmonic ground state energy if the *bcc* state was dynamically stable at 0 K, varies with the number of mapping points used. Similarly, Figs. 3.9(b) and 3.10(b) show how the contribution of the soft modes to this summation varies with the number of mapping points. Finally, Fig. 3.11 shows how the temperature at which the *bcc* phase in Zr is calculated to become dynamically stable varies with the number of mapping points used. In each case, the basic cubic spline fitting without using forces is compared to a cubic and a quintic spline fitting using the forces obtained in the mapping, as in the calculations on molecular hydrogen.

Our results for lithium, presented in Fig. 3.9, show that any differences in the anharmonic vibrational energy arising from the three different fitting methods are negligible, down to scales of 0.1 meV. The negligible difference between fitting methods arises from the fact that, apart from along the direction defined by the soft modes present, the vibrational properties of lithium are described well by the harmonic approximation, despite its low mass [123]. This means that a very good fit to the BO surface along most modes can be found with small numbers of mapping points (as in the standard finite

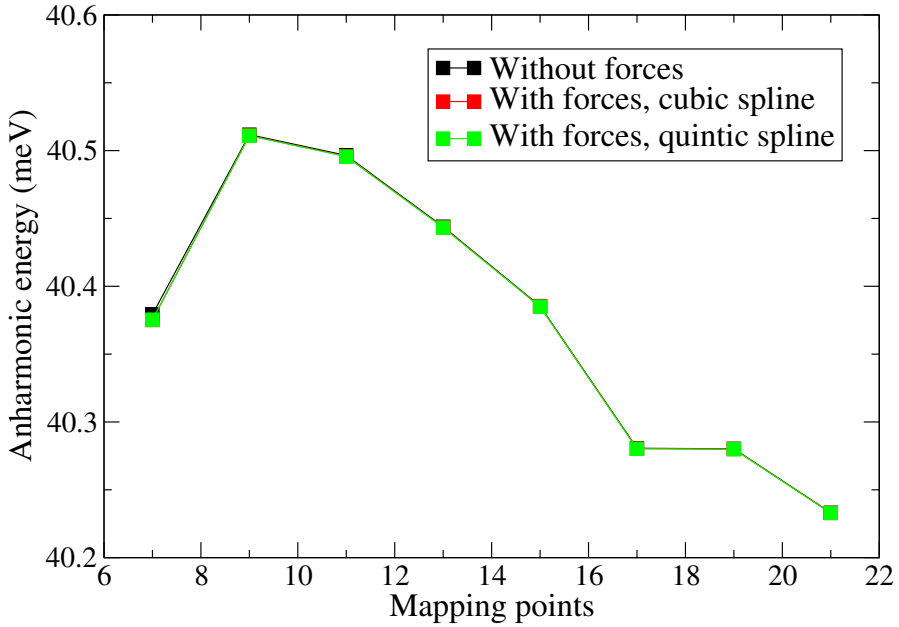

(a)

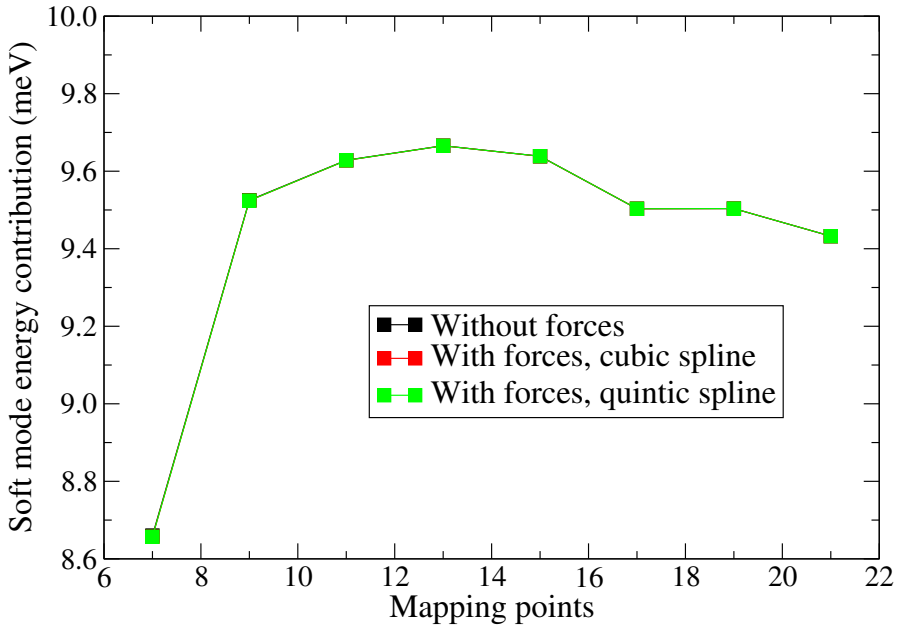

(b)

Figure 3.9: Convergence with respect to the number of mapping points used per mode of (a): the sum of the lowest energy eigenvalues for each mode, and (b): the sum of the lowest energy eigenvalues of just the soft modes, of the *bcc* phase of lithium. The convergence of the basic VSCF method as well as the VSCF+f method using both a cubic spline and a quintic spline are shown.

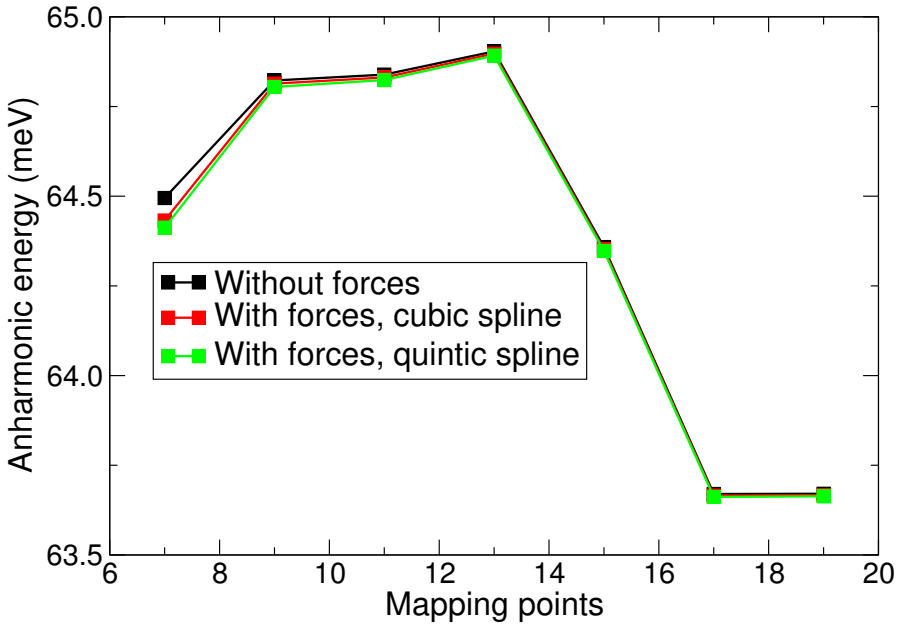

(a)

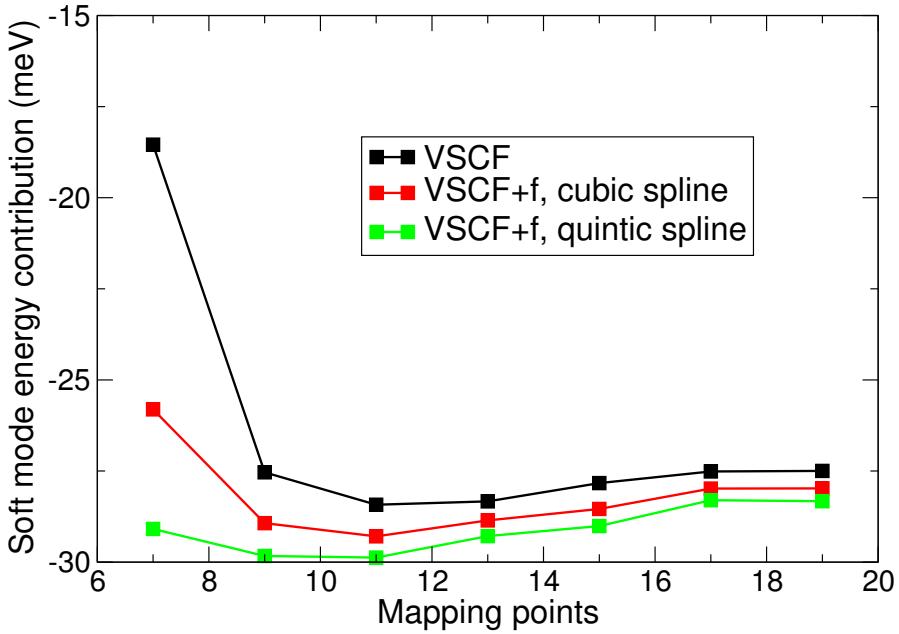

(b)

Figure 3.10: Convergence with respect to the number of mapping points used per mode of (a): the sum of the lowest energy eigenvalues for each mode, and (b): the sum of the lowest energy eigenvalues of just the soft modes, of the *bcc* phase of zirconium. The convergence of the basic VSCF method as well as the VSCF+f method using both a cubic spline and a quintic spline are shown.

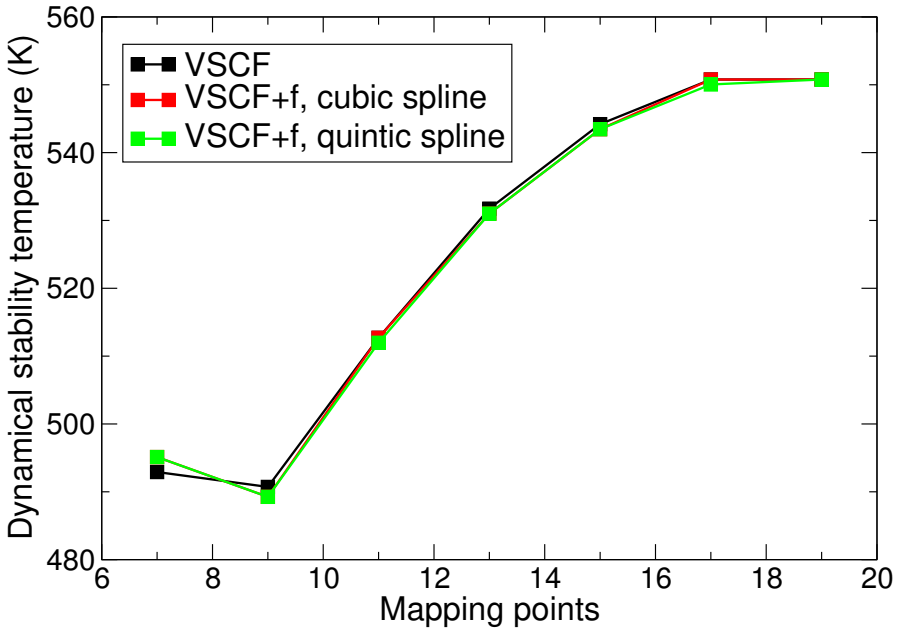

Figure 3.11: Convergence of the temperature at which the *bcc* phase of zirconium becomes dynamically stable with respect to the number of mapping points used per mapping direction. Results using the basic VSCF method and the VSCF+f method using both a cubic spline and a quintic spline are shown. The VSCF+f cubic spline results are hidden behind the VSCF+f quintic spline results.

displacement method for calculating harmonic frequencies), and so all three methods agree very well. Even in the case of the soft modes, which must necessarily contain some anharmonic character, the double-well structure is not very pronounced, with the overall BO surface appearing essentially quadratic. To see this double-well structure, where the two minima are very close to the central maximum, a finer than usual mapping of the BO surface proved necessary – maximum mapping amplitudes of $0.3\sqrt{\langle u^2_{n\mathbf{q}}\rangle}$ and $0.8\sqrt{\langle u^2_{n\mathbf{q}}\rangle}$ were used for the two soft modes present, instead of the maximum amplitude of $5\sqrt{\langle u^2_{n\mathbf{q}}\rangle}$ used throughout the rest of this work. Here, $\langle u^2_{n\mathbf{q}}\rangle = \frac{1}{2\omega_{n\mathbf{q}}}$ is the harmonic expectation value of the squared mode amplitude. Our calculations show these double wells are quite shallow, meaning that even at zero temperature the BO surface looks essentially harmonic. Our results imply that the *bcc* structure of lithium is dynamically stable at zero temperature, although experimental results show that the *bcc* phase becomes stable above 70 K. This disagreement could potentially be caused by incomplete convergence with respect to sampling of the vibrational BZ or by higher order terms in

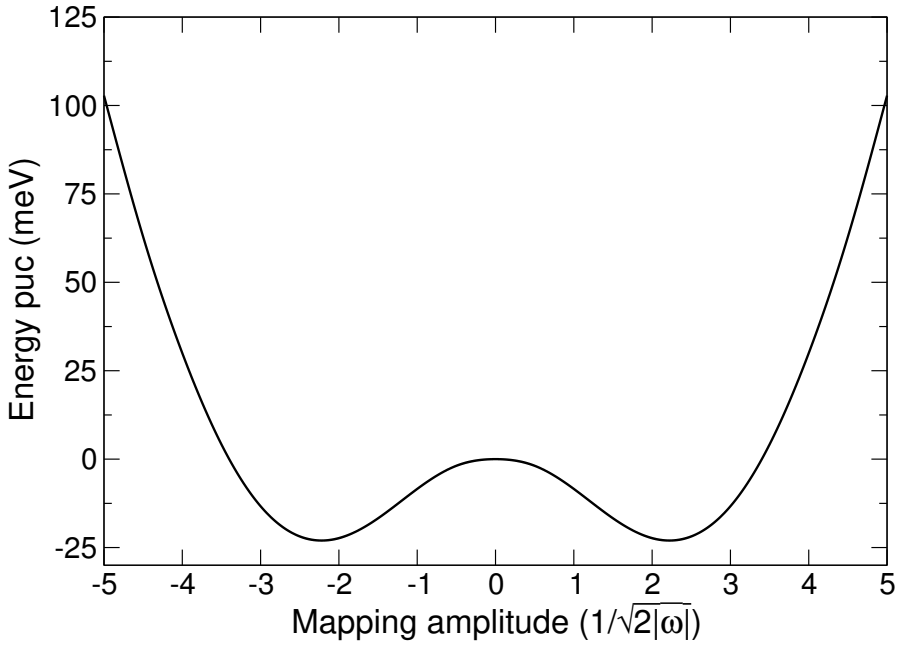

Figure 3.12: The shape of the BO surface as mapped along one of the soft modes of zirconium; 'puc' stands for 'per unit cell'.

the expansion of the BO surface of equation (2.73), as well as by the errors inherent in DFT. A different exchange-correlation functional could plausibly give results closer to experiment, but as we are primarily interested in the properties of the VSCF+f method here, and not matching experiment, we do not investigate this further.

The results for zirconium tell a different story to those of lithium. Fig. 3.10(a) shows that the differences between the values obtained by the different fitting methods for the sum of the lowest eigenvalues of all the different modes are small, as in lithium. However, there are much more significant differences in the contribution of the soft modes to this summation, as seen in Fig. 3.10(b). Although the effect is much less pronounced than that seen for hydrogen in Fig. 3.4, it is clear that, for low numbers of mapping points, including force data improves the fit to the BO surface. It is also evident that the quintic spline gives a better fit than the cubic spline when the forces are used. This demonstrates that the VSCF+f method can improve on the basic VSCF method in this type of system, as well as the hydrogen systems explored previously.

The soft modes in zirconium are more numerous, and mapping the BO surface along the directions defined by them gives much more pronounced double-well structures than

in lithium, meaning that the structure is not dynamically stable at zero temperature. An example of the pronounced double-well structure of the BO surface mapped along one of the soft modes in zirconium is shown in Fig. 3.12. Our results can be used to calculate the temperature at which the *bcc* phase is stabilised dynamically, by calculating the internal energy at a range of temperatures and finding where it becomes positive. The results are shown in Fig. 3.11 for a range of mapping points and the three fitting methods used. At these higher temperatures, it can be seen that the differences between the three fitting methods, visible at zero temperature in Fig. 3.10(b), are much less significant – the differences are mostly washed out by the overall vibrational energy increasing. Our calculations predict that the *bcc* structure of zirconium should become dynamically stable above about 520 K, which is significantly lower than the observed transition temperature of 1136 K. This disagreement could again potentially be caused by the incomplete convergence with respect to the vibrational BZ sampling, higher-order terms in the BO surface expansion, or errors inherent in DFT itself.

3.3 Summary

The results presented above show that the efficiency of the vibrational self-consistent field method described in Section 2.3.2 can be significantly improved by using both energy *and* force data from DFT calculations when mapping the BO energy surface. Testing of this 'VSCF+f' method on molecular and high-pressure solid hydrogen, including the contribution of 2-D subspaces of the BO surface to the energy, as well as on the *bcc* phases of lithium and zirconium, show that it agrees well with the basic VSCF method, but for systems with significant anharmonicity it can significantly reduce the computational cost involved, by a factor of up to 40%. Using this method routinely will make future anharmonic vibrational calculations both faster and more efficient. The next step is to apply the VSCF+f method to new systems of interest where anharmonicity is significant.

Part III

Applications

Chapter 4

The Neutral Vacancy in Diamond

In this chapter, we examine the electronic and vibrational properties of the neutral vacancy defect in diamond from first principles. This defect has been the subject of much work over many years, thanks to its ubiquity and possible technological applications. Despite this body of work, however, previous theoretical first-principles work and experiment still disagree on the structure of the vacancy itself. First-principles calculations predict that the vacancy should undergo a static Jahn-Teller distortion, whilst experimentally it is known that the system exhibits a dynamic Jahn-Teller effect. The work presented here applies the methods introduced in Chapter 2 in order to conduct first-principles calculations, including anharmonic vibrational effects, on this system, with the aim of resolving this discrepancy between theory and experiment. Our results show that anharmonic nuclear motion leads to a dynamic Jahn-Teller distortion of the vacancy in diamond very close to zero temperature, and we find that this remains true at least up to 400 K, in agreement with experimental results.

4.1 Background

4.1.1 Point defects in diamond

A defect in a crystalline material can most generally be defined as a flaw in the pristine periodic structure of the crystal. They can be extended in nature, such as grain boundaries or dislocations, or be effectively concentrated at a single point in the material. Such defects are known as point defects, and come in a wide variety of types. A substitutional defect occurs when an atom in the crystal is replaced by a different species of atom, an antisite defect occurs when two different species of atoms in the lattice swap positions, an interstitial defect is an atom that does not lie at a point where we would expect an atom, and a vacancy defect is the absence of an atom where we would expect one. Complexes containing two or more of these defects together are also possible. Point defects such as these can affect the properties of the material containing them substantially – they introduce electron energy levels within the electronic band gap, trap charge carriers, emit and absorb light, and phonon scattering from them limits thermal and electrical conductivities [124, 125].

This means that the presence of defects can influence many of the most desirable properties of diamond, an important material technologically due to its optical properties and high thermal conductivity. Because of this, point defects in diamond have been the

subject of much previous theoretical work [126, 127]. Some point defect complexes such as the Si-V [128, 129] and N-V^- centres [130] have been identified as potential 'qubits' in quantum computers [125, 131–136]. Both these defects include an interstitial atom, as well as a lattice vacancy, which is an important and very common defect in its own right.

Vacancies in diamond can act as either electron donors or acceptors, leading to three observed charge states – V^+, V^0 and V^- [137, 138], where V^q represents a vacancy with charge q. The neutral vacancy V^0 is particularly significant because it is known to be stable over a wide range of doping levels [137, 139], and plays a central role in defect diffusion [140]. It is associated with a series of lines in the absorption spectrum of diamond, including the strong and sharp GR1 line at 1.673 eV, as well as the weaker GR2-8 lines at higher energies, as seen in Fig. 4.1(a) [141]. The presence of significant numbers of vacancies also has a more easily visible effect on the optical properties of diamond – it gives the crystal a green colour, as in Fig. 4.1(b). The vacancy in diamond is also important for its applications in quantum information [142] and precision sensing [143].

An important aspect of the effect a vacancy defect has on the properties of diamond is its effect on the surrounding structure of the lattice. As might be expected, the defect results in the atoms nearby distorting from their pristine lattice positions, and how they do this will affect the resulting observable properties. In particular, the point group symmetry of the vacancy affects the polarisation of light emitted by the defect and the nature of the Stark effect on the defect [144, 146, 147]. Understanding this distortion from first principles is therefore central in obtaining a full understanding of the neutral vacancy defect in diamond.

4.1.2 The Jahn-Teller effect

As a starting point for investigating the structure of the neutral vacancy in diamond, we can consider the extensive work that has been done on the same defect in silicon [139, 148–150]. Drawing a parallel between the two systems is meaningful as carbon and silicon are isoelectronic, and silicon also crystallises into the same diamond lattice structure, meaning the pristine lattices of both elements have tetrahedral T_d point group symmetry, as depicted in Fig. 4.2(a). A very successful model that describes the physics of what happens at the neutral vacancy in silicon was developed by Watkins [148]. The model was based on a linear combination of atomic orbitals (LCAO) approach, but only including

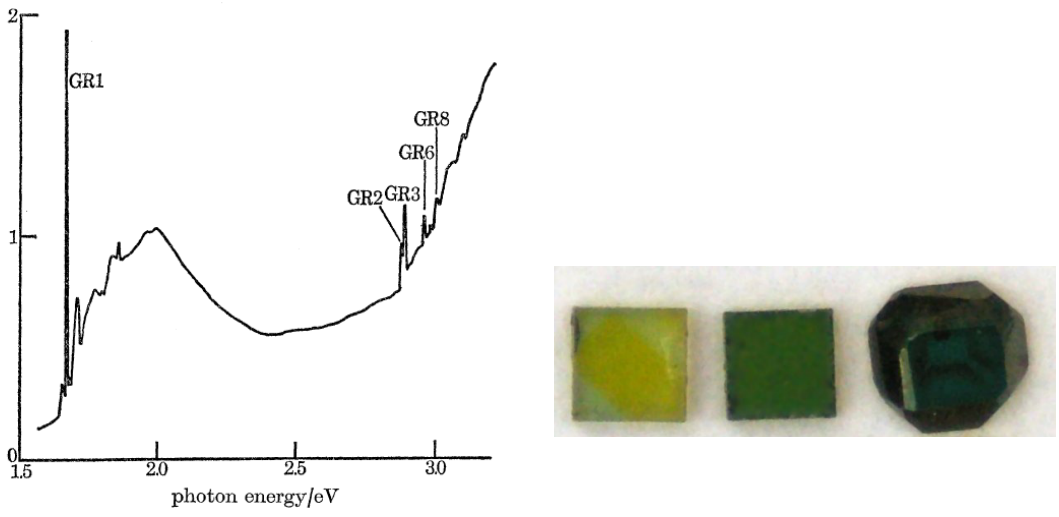

(a) (b)

Figure 4.1: Effects of the neutral vacancy on the optical properties of diamond. (a) shows the optical absorption spectrum of diamond with peaks associated with the neutral vacancy labelled. Note the very strong GR1 peak at 1.673 eV. Figure taken from Ref. 144. (b) shows three diamonds that have been subjected to ionising radiation, a process that creates vacancies. The radiation dose increases from left to right. Note the increasingly green colour of the crystals. Figure by Ref. 145.

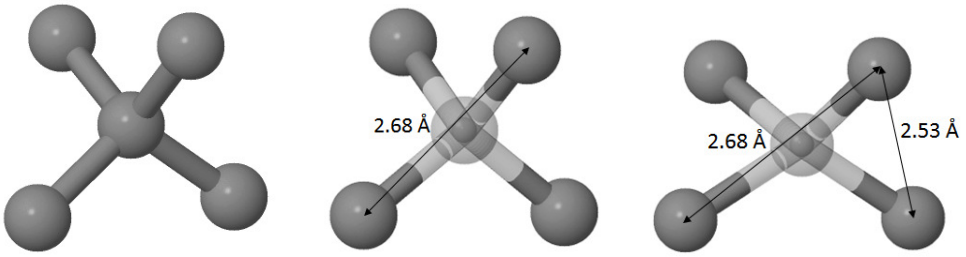

(a) (b) (c)

Figure 4.2: Structure of the pristine diamond lattice and possible distortions of the vacancy. (a) shows a site in the pristine lattice and its four nearest neighbours. (b) shows the nearest neighbours of the vacancy with a distortion of T_d symmetry, and (c) shows the vacancy structure with D_{2d} symmetry. The lengths indicate the distances between atoms in the relaxed LDA-DFT structures. The four atoms in (c) form two pairs.

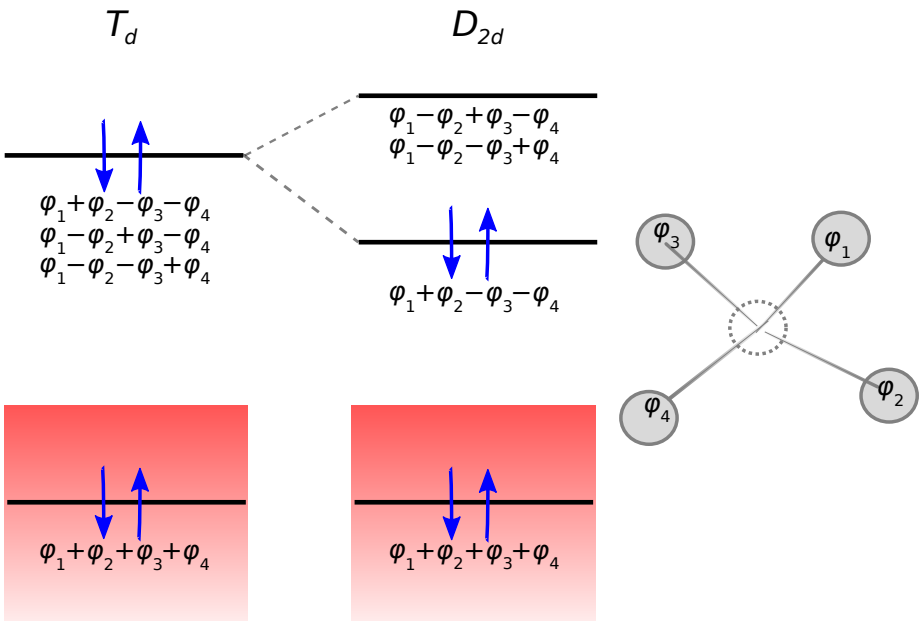

Figure 4.3: The Watkins model of the neutral vacancy in silicon. The orbitals associated with the four nearest neighbours of the vacancy are labelled ϕ_1 to ϕ_4, and combine to create the energy levels shown, which are occupied by four electrons, represented by blue arrows. The direction of the arrows represents the electrons' spin. One of the levels is within the valence band, shown here in red. On a distortion of tetragonal D_{2d} symmetry, the triply degenerate level in the gap splits into two, which lowers the energy of the system.

the four nearest neighbours of the vacancy. As can be seen in Fig. 4.3, the Watkins model predicts that there should be a singly degenerate defect state within the valence band, and a triply degenerate state in the band gap. Each of the four nearest neighbours has one electron associated with the dangling bond left by the presence of the vacancy, meaning that for a neutral vacancy we have four electrons to place into these energy levels. Two of these can occupy the state within the valence band, meaning two electrons are left to occupy the triply degenerate state in the band gap. A distortion that splits this degenerate state, such as a distortion from tetrahedral T_d to tetragonal D_{2d} point group symmetry, will therefore lower the energy of the system, as seen in Fig. 4.3 [139, 149, 150]. In the tetrahedral symmetry vacancy structure, shown in Fig. 4.2(b), all four of the nearest neighbours to the vacancy are equidistant from the defect. However, in the tetragonal structure, shown in Fig. 4.2(c), the four nearest neighbours form two pairs. There are three possible ways this pairing can occur, corresponding to the three Cartesian directions, which gives three possible Jahn-Teller distortions. The existence of an energy-lowering distortion in the presence of an occupied degenerate state is an example of the Jahn-Teller effect [151], a very important effect in the context of the vacancy in diamond.

The static Jahn-Teller effect

The Jahn-Teller effect follows from the Jahn-Teller theorem, which states that, except in the case of a linear molecule, it is not possible to have a stable state that contains degenerate occupied electronic orbitals [151]. Such a system will distort spontaneously away from its original structure towards a lower symmetry structure, breaking the degeneracy and lowering the energy of the system. When a system distorts in such a way, it is known as a *static* Jahn-Teller distortion. The possible distorted structures (as there may be more than one possible distortion) correspond to minima in the BO surface, whilst the original undistorted higher symmetry structure corresponds to a saddle point. Although the Jahn-Teller theorem was originally stated for molecules, it is also applicable to defects in crystals.

Theoretically, the presence of a Jahn-Teller distortion is revealed by the emergence in the undistorted structure of harmonic vibrational soft modes, that is, modes with imaginary frequencies; the displacement patterns corresponding to these modes then lead down to the minima corresponding to the Jahn-Teller distorted structure. In the

case of the vacancy in silicon, this approach and the Watkins model successfully predict the static tetragonal D_{2d} distortion seen in experiments.

Both the Watkins model and the presence of harmonic soft modes also suggest a static tetragonal D_{2d} distortion in the case of the vacancy in diamond. However, experimental observations show that the neutral diamond vacancy has tetrahedral T_d symmetry instead [138, 144, 146, 147]. This apparent contradiction between theory and experiment can be rationalised by the appearance of a *dynamic* Jahn-Teller effect [138, 150, 152, 153], due to strong anharmonic vibrational motion.

The dynamic Jahn-Teller effect

The dynamic Jahn-Teller effect is observed in a variety of systems, including doped manganites [154, 155], fullerides [156, 157], octahedral complexes of d^9 ions [158], and the excited states of the N-V^- centre in diamond [159]. It arises due to coupling of the electronic and vibrational degrees of freedom of the system, which taken together can exhibit very different behaviour to that of the electronic degrees of freedom alone [153]. In such systems, it is therefore important that the vibrational motion is treated accurately, including anharmonicity.

In a Jahn-Teller system, there are two or more minima in the Born-Oppenheimer (BO) energy surface, which are separated by energy barriers. In the static Jahn-Teller effect, the vibrational wavefunction is localised in one of these minima, meaning that the system has lowered its energy by permanently distorting into the structure corresponding to that minimum. However, if the energy barriers between the minima are low enough and the system possesses enough vibrational energy, the system is able to tunnel through the energy barriers, resulting in the vibrational wavefunction of the system being shared between the minima instead of localising in a single minimum. In other words, there is an equal probability of the system occupying any of the energy minima, meaning that on average the overall symmetry of the system remains the same as in the undistorted structure, although locally the structure may be distorted [153]. This is what is known as the dynamic Jahn-Teller effect. Whether a given system exhibits the static or the dynamic Jahn-Teller effect depends on its vibrational energy, making the cross-over between these two regimes temperature dependent.

In the vacancy in diamond, there are three minima, corresponding to tetragonal distortions in each of the Cartesian directions. Previous estimates, from experimental

data, of the energy barriers between minima and an Einstein-like frequency for the tetragonal defect modes of the vacancy in diamond show that the vibrational energy quantum is larger than or comparable to the barrier energy, implying that a dynamic Jahn-Teller effect exists close to 0 K [160]. Experiments have confirmed that the vacancy remains tetrahedral, and thus the system still exhibits a dynamic Jahn-Teller effect, down to liquid helium temperatures (4.2 K) [152].

The dynamic Jahn-Teller effect in the neutral vacancy in diamond is well-established experimentally, but from a first-principles standpoint the view is less clear. The commonly used harmonic approximation for lattice dynamics cannot account for the presence of a dynamic Jahn-Teller distortion, as this is an intrinsically anharmonic effect. To properly describe the dynamic Jahn-Teller effect, it is necessary to know the vibrational wavefunction, but first-principles calculations of the anharmonic vibrational wave function of the ground state of the neutral vacancy in diamond have not been reported previously. The focus of this work is therefore to determine for the first time an anharmonic wave function which accurately describes the dynamic Jahn-Teller distortion, and thus provide a theoretical description of the experimentally observed tetrahedral T_d symmetry of the neutral vacancy in diamond.

4.2 Computational details

4.2.1 Electronic calculations

As we are interested in the structure of the ground state of the neutral vacancy, the calculations were restricted to the electronic ground state. This is expected to be well-described within DFT, although some of the electronic excited states are not because they have many-body (multideterminant) character. The DFT calculations were performed using `CASTEP` version 7.0.3 [56] and the corresponding 'on-the-fly' ultrasoft carbon pseudopotential [61] generated by `CASTEP`. The local density approximation (LDA), as parametrised by Perdew and Zunger [41], was used for the exchange-correlation functional. The LDA has been widely used in previous calculations involving diamond and similar materials [73, 139, 149, 161, 162]. LDA-DFT calculations provide a lattice constant for diamond of 3.529 Å, compared to the experimental value of 3.567 Å [163]. In the calculations in this chapter, the LDA-DFT lattice constant is generally used, although some calculations were also carried out using the experimental lattice constant

to investigate the effect on the dynamic stability of the tetrahedral symmetry state.

Whenever a non-periodic feature, such as a point defect, is modelled with a code using periodic boundary conditions, such as `CASTEP`, care must be taken when designing the cell used for the calculations. The cell must be large enough to ensure that the defect and its periodic images are well separated, so the spurious interactions between them do not affect the results of the calculation. Such interactions can arise from electrostatic interactions in the case of charged defects, but here they mainly arise from overlapping of the wavefunctions of the defect and its periodic images [139]. In particular, in previous work a cell containing at least 255 atoms was found to be necessary to obtain a locally stable tetragonal state for the neutral vacancy in silicon [139, 149] – here 'locally stable' means that a structure with tetragonal symmetry will not relax back to a tetrahedral structure when geometry optimised. Calculations conducted using supercells with less than 255 atoms show the same is true for the vacancy in diamond. Because of this, a 255/256-atom supercell is used for all calculations in this chapter unless otherwise specified. This supercell is constructed by creating a $2 \times 2 \times 2$ supercell of a 32-atom *bcc* unit cell, followed by the removal of one atom.

To construct this cell for use in the calculations, several steps were followed. Firstly, both the lattice vectors and the internal atomic co-ordinates of the 2-atom *fcc* diamond unit cell were relaxed to obtain the LDA-DFT lattice constant. This relaxed cell was then used to construct a simple cubic conventional 8-atom unit cell. A $4 \times 4 \times 4$ supercell of this conventional unit cell, containing 512 atoms, was constructed, and from this the 256-atom *bcc* cell was created. A vacancy was formed by removing an atom, and the internal atomic co-ordinates were then allowed to relax. The relaxed tetrahedral symmetry structure was found by imposing the pristine lattice symmetry during the relaxation, whilst the tetragonal structure was found by creating a tetragonal distortion of the four nearest neighbours of the vacancy, before relaxing with no symmetry constraints. In all cases, the structural optimisation was allowed to continue until the root-mean-square of the forces on all the atoms was below 0.001 eV/Å. In both vacancy structures, the nearest neighbours relaxed away from the vacancy (by 0.11 Å in the tetrahedral case) in order to increase their sp^2-like bonding, as observed in previous work [150].

A plane-wave cut-off energy of 650 eV was used for relaxing the structures and for the harmonic vibrational calculations, with a $5 \times 5 \times 5$ Monkhorst-Pack **k**-point grid [69], as the energy differences between the structures were very well converged for

these parameters. A larger value of the cut-off energy was used for some calculations, corresponding to even stricter convergence criteria. The convergence tolerance for the results of the DFT calculations was taken to be 10^{-10} eV per atom per SCF cycle, to ensure a very accurate charge density, and thus accurate forces. In all calculations, a grid scale of 2.0 was used.

4.2.2 Vibrational calculations

The harmonic calculations were carried out using the finite displacement method described in Section 2.3.1, using atomic displacements of 0.00529 Å (0.01 bohr). The anharmonic calculation used the VSCF method described in Section 2.3.2, although the improved VSCF+f method described in Section 3 was not used. The large size of the cell used also precluded using the non-diagonal supercells method described in Section 2.3.3. 19 mapping points per mode were used to map the BO surface.

An important part of conducting anharmonic calculations using the VSCF method of Section 2.3.2 is deciding which terms to neglect in the expansion of the Born-Oppenheimer surface in equation (2.73). With such a large cell, and therefore such a large number of phonon modes, it is absolutely unfeasible to include all the two-body phonon coupling terms $V_{n\mathbf{q};n'\mathbf{q}'}(u_{n\mathbf{q}}, u_{n'\mathbf{q}'})$ in equation (2.73). Preliminary testing on the coupling between phonon modes also shows that almost all of these terms are small, as the harmonic model, which includes no interaction between phonon modes, works well for the nuclear motion in diamond [75]. For these reasons, the anharmonic vibrational calculations in this chapter neglect the contribution of almost all of the two-body $V_{n\mathbf{q};n'\mathbf{q}'}(u_{n\mathbf{q}}, u_{n'\mathbf{q}'})$ terms, focusing instead on the independent mode $V_{n\mathbf{q}}(u_{n\mathbf{q}})$ terms.

The only significant $V_{n\mathbf{q};n'\mathbf{q}'}$ term, and therefore the only one included, corresponds to the 2-dimensional BO subspace spanned by two soft modes, labelled as (u_1, u_2), that are present in the tetrahedral structure of the diamond vacancy. The BO surface described by this term has three equivalent minima, corresponding to a tetragonal distortion along each Cartesian direction. No matter how the orthogonal normal co-ordinates (u_1, u_2) are chosen, it is not possible for the axes to pass precisely through the centre of more than one of these minima at a time. This means that it is impossible to fully capture the behaviour of the system with 3 minima using only the independent $V_{n\mathbf{q}}$ terms for these soft modes – the associated coupled $V_{n\mathbf{q};n'\mathbf{q}'}$ term must therefore be included.

In a similar way, the vibrational wavefunction for this 2-dimensional subspace of the

BO surface cannot be described correctly as a product of two states labelled by the two corresponding normal modes (u_1, u_2), as is done in equation (2.76). Separating the wavefunction in this way breaks the rotational symmetry of the problem. Instead, for this subspace, we express the wavefunction using polar co-ordinates, $r_u = \sqrt{u_1^2 + u_2^2}$ and $\theta_u = \arctan(u_2/u_1)$, where the u_i are written in units of $1/\sqrt{2|\omega_{i,s}|}$, with $\omega_{i,s}$ the imaginary harmonic soft phonon frequencies. This preserves the correct symmetry of the problem and allows an accurate wavefunction to be determined. The usual wavefunction $|\phi_1(u_1)\rangle\,|\phi_2(u_2)\rangle$ is re-expressed as $|R(r_u)\rangle\,|T(\theta_u)\rangle$, where $|R(r_u)\rangle$ is written as a sum of isotropic harmonic oscillator radial basis states, and $|T(\theta_u)\rangle$ is a sum of sinusoids. A total of 80 angular basis functions and 20 radial basis functions are used for these calculations. As all of the other modes are almost harmonic and therefore well-described by the independent terms, the energy contribution from this particular 2-dimensional subspace can simply be added to the energy contributed by the rest of the modes of the tetrahedral defect.

Even if we neglect all phonon coupling terms in the tetragonal symmetry state and all but one in the tetrahedral state, it is still extremely computationally expensive to map all 762 anharmonic modes for both symmetry states of the vacancy. However, we can take advantage of the small anharmonicity in pristine diamond [75]. The fact that pristine diamond is well-described by the harmonic approximation implies that a necessary condition for modes to have significant anharmonic character is that they are strongly affected by the presence of the vacancy. We expect that these modes will generally have short wavelengths and high energies, as over longer length scales the effect of the vacancy will be averaged out. The effect of the vacancy on each mode can be calculated as the difference between the vacancy harmonic vibrational density of states (vDoS) and the pristine vDoS at the frequency of each mode, $\Delta g(\omega) = g_{\text{vib}}^{\text{vac}}(\omega) - g_{\text{vib}}^{\text{pris}}(\omega)$. We can then obtain an accurate value for the anharmonic correction to the energy without having to map all 762 modes by simply mapping the modes in descending order of $\Delta g(\omega)$, using the harmonic approximation for all unmapped modes, and converging the anharmonic correction with respect to the number of modes mapped. Converging the correction to within 0.1 meV requires 32 modes to be mapped for the tetrahedral state, but 350 for the tetragonal state, implying that the distortion away from tetrahedral symmetry leads to a significant increase in anharmonicity.

To further reduce the computational expense of the anharmonic calculations, an

energy cut-off of 350 eV was used, with a $5 \times 5 \times 5$ Monkhorst-Pack **k**-point grid [69], as the shape of the BO surface is well converged for these parameters. In some calculations, larger values of these parameters were used, corresponding to even stricter convergence criteria. The energy differences between structures were converged to within 0.5 meV per atom, with the self-consistency energy threshold for the DFT calculations set to 10^{-6} eV per atom. The anharmonic correction to the energy in the pristine 256-atom supercell was calculated from the anharmonic correction for a 16-atom *fcc* supercell, again to reduce the computational cost of the calculations.

4.3 Results

4.3.1 The Jahn-Teller effect and dynamical stability

Fig. 4.4 shows the calculated electronic density of states (eDoS) for the pristine, tetrahedral and tetragonal vacancy structures. There is little difference between the eDoS of the pristine and vacancy states, apart from the appearance of a peak in the band gap almost exactly at the Fermi level in the two vacancy structures. This is the defect state predicted by the Watkins model that arises from the combination of the four 'dangling bonds' around the vacancy. The inset to Fig. 4.4 shows that the peak splits into two upon introduction of the tetragonal distortion, as would be expected for a static Jahn-Teller distortion. These peaks correspond to the singly- and doubly-degenerate levels predicted by the Watkins model (see Fig. 4.3) [148].

Harmonic vibrational calculations show that the tetrahedral state exhibits two soft modes, with imaginary frequencies $\omega_{1,s}$ and $\omega_{2,s}$, that correspond to tetragonal distortions. The presence of soft modes means that, at the harmonic level, the tetrahedral state is dynamically unstable. The tetragonal configuration, however, exhibits no soft modes, and is therefore dynamically stable at the harmonic level. This leads to the conclusion that at the harmonic level of theory, a static Jahn-Teller distortion of tetragonal symmetry is favoured, as expected.

Including anharmonicity in the treatment of the tetrahedral configuration provides a very different picture. Fig. 4.5 shows the BO surface mapped along one of the soft mode directions, split into its symmetric (even) and antisymmetric (odd) parts. The antisymmetric part mostly arises due to the fact that any given direction cannot pass through two minima *and* the origin, meaning that both minima cannot be well mapped

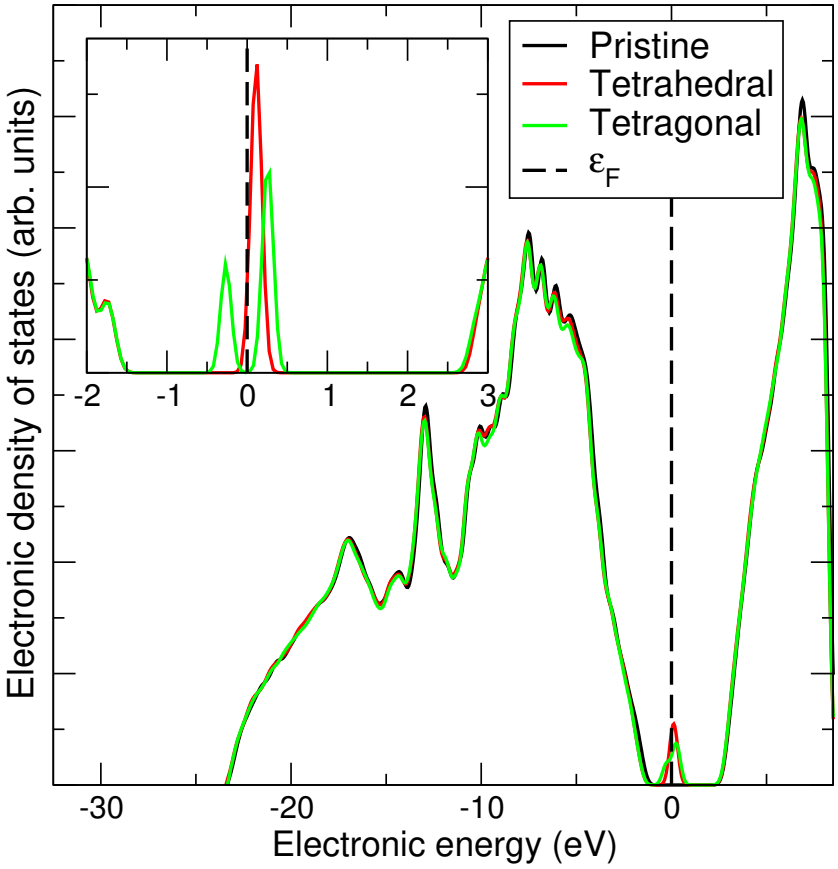

Figure 4.4: Electronic density of states of diamond. The dotted line marks the Fermi energy, ε_{F}. The inset contains the eDoS of the vacancy gap state, showing that the tetragonal distortion splits the state into a singlet at around -0.3 eV and a doublet at around 0.3 eV.

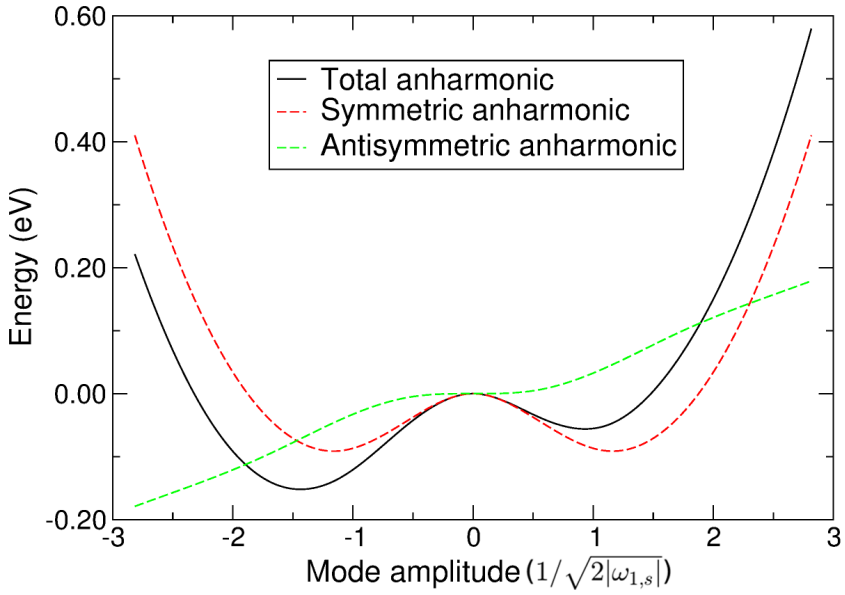

Figure 4.5: Anharmonic Born-Oppenheimer energy surface mapped along the direction of one of the two soft modes of the tetrahedral structure, as well as its decomposition into symmetric and antisymmetric parts. The symmetric part of the anharmonic energy surface is clearly quartic, giving two minima.

by a one-dimensional slice, as discussed in Section 4.2.2. However, the symmetric contribution clearly shows that quartic anharmonicity is present, as would be expected for a soft mode.

To map all three tetragonal minima correctly, it is necessary to include coupling between the soft modes by mapping the 2-dimensional subspace spanned by the two soft modes, as discussed in Section 4.2.2. Fig. 4.6(a) shows the BO surface mapped on this 2-dimensional subspace, and Fig. 4.6(b) shows the anharmonic ground state nuclear density in the same subspace. In addition to the slice shown in Fig. 4.5, further slices through the BO surface in Fig. 4.6(a) can be found in Appendix B. The anharmonic ground state vibrational density of the tetrahedral structure has peaks in each of the three minima of the BO surface, which lowers the overall energy of the system. The fact that the wavefunction is shared between the minima shows that, when anharmonic vibrational effects are included, the Jahn-Teller effect in this system becomes dynamic rather than static, with the system maintaining the full T_d point symmetry of the pristine lattice.

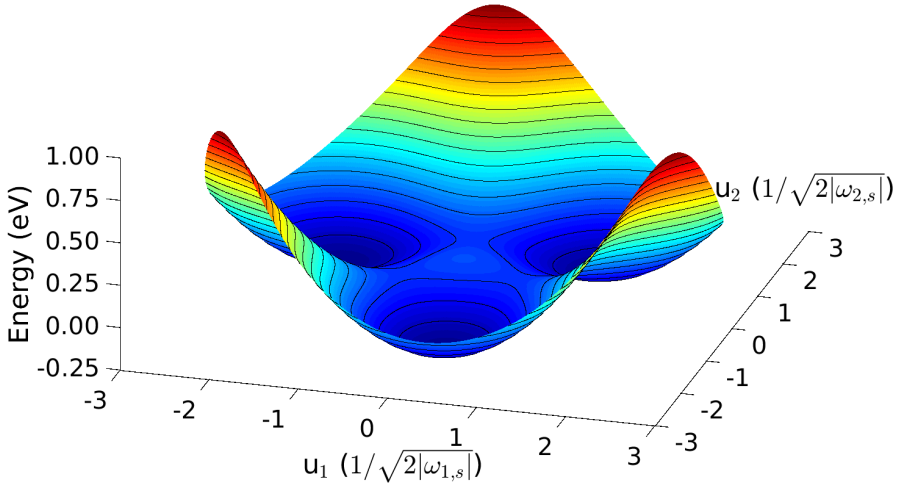

(a)

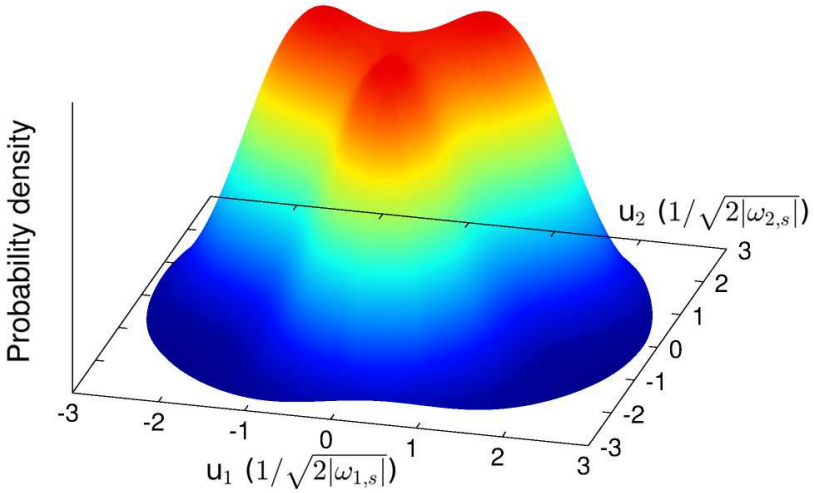

(b)

Figure 4.6: (a) Born-Oppenheimer energy surface in the plane spanned by the two soft modes of the tetrahedral structure. The static tetrahedral structure lies on the local maximum at the origin. Three equivalent minima corresponding to the three possible tetragonal distortions are arranged symmetrically around the tetrahedral structure. Blue and red signify low and high energies respectively. Each contour line represents an energy increase of 0.0615 eV.
(b) Anharmonic vibrational ground state probability density as a function of the amplitudes of the soft modes of the tetrahedral structure. The density has three peaks that correspond to the minima of the BO surface in (a).

The dynamical stability of the tetrahedral state is somewhat sensitive to the exact form of the BO surface found in the DFT calculations. If the relaxed LDA lattice constant (3.529 Å) is used when mapping the 2-dimensional subspace of the BO surface spanned by the soft modes, the tetrahedral state is dynamically unstable at 0 K, becoming stable at 16.9 K. However, using the experimental lattice constant of 3.567 Å [163] reduces the size of the dynamical instability significantly, decreasing the absolute value of the already small ground state energy associated with the coupled soft modes' subspace by an order of magnitude. Using the experimental lattice constant results in the tetrahedral state becoming dynamically stable at 8.6 K in the calculations. Given the errors inherent in DFT calculations, our results are consistent with the tetrahedral state being dynamically stable down to liquid helium temperatures, as implied by experiment [152], and even to absolute zero.

The minima in the BO surface are, in the polar co-ordinates defined in Section 4.2.2, at $r_u = 1.64/\sqrt{2|\omega_s|}$, $\theta_u = 39°, 159°, 279°$, which correspond to tetragonal distortions along the x, z and y directions, respectively. $\omega_s = (\omega_{1,s} + \omega_{2,s})/2 \simeq \omega_{1,s} \simeq \omega_{2,s}$. The values of θ_u depend on the precise choice of the axes defined by the two soft modes. The displacement patterns corresponding to the modes u_1 and u_2 in this work are presented in Appendix B, allowing these minima to be unambiguously identified. At these minima, the four nearest neighbours of the vacancy are displaced from their tetrahedral equilibrium positions; they are displaced by 0.074 Å *away* from the vacancy along the distortion direction, but by half this distance *towards* the vacancy in the other two directions. This forms the two pairs of atoms seen in Fig. 4.2(c). The tetrahedral structure is at a maximum of the BO surface along the direction of the soft modes, but a minimum along all of the other modes, placing the tetrahedral structure at a saddle point of the BO surface.

4.3.2 Thermodynamics of the neutral vacancy

The tetragonal and pristine structures are dynamically stable at the harmonic level, and the previous section shows that the tetrahedral structure is also dynamically stable at low temperatures when anharmonicity is accounted for. Having therefore established that all three structures – tetrahedral, tetragonal and pristine – are dynamically stable at low temperature at the anharmonic level, we turn to their thermodynamics. The static lattice and vibrational energies at 20 K for all three structures are reported in

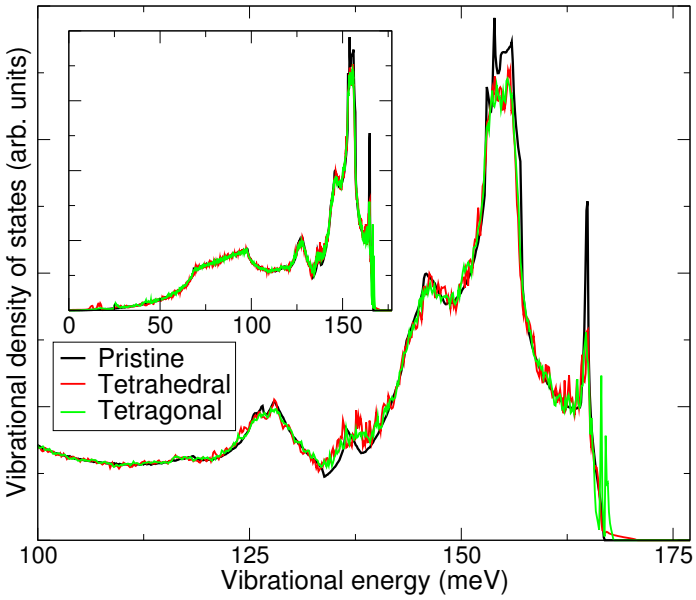

(a)

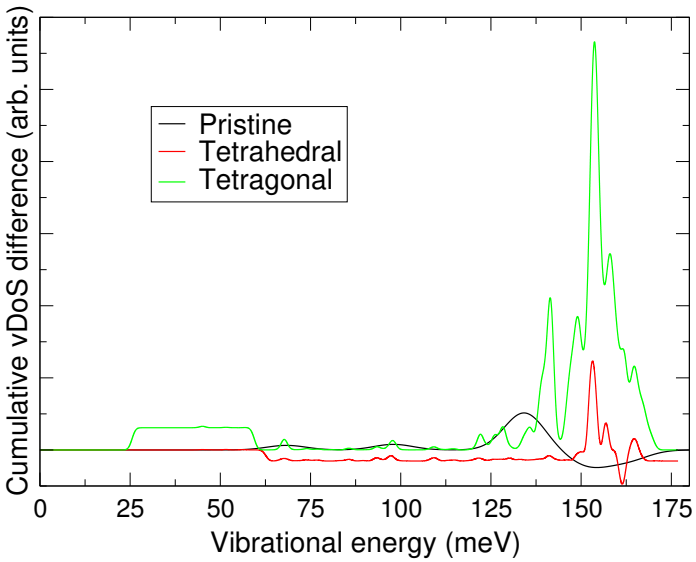

(b)

Figure 4.7: (a) shows the harmonic vibrational density of states for the pristine, tetrahedral vacancy and tetragonal vacancy structures in diamond, shown at high energies above 0.1 eV in the main plot, and in full in the inset. Note the main differences between the vacancy states and the pristine structure occur at high energies.
(b) shows the difference between the harmonic and anharmonic cumulative vDoS, $\Delta G(\varepsilon) = \int_0^{\varepsilon} d\varepsilon' g_{\mathrm{har}}(\varepsilon') - g_{\mathrm{anh}}(\varepsilon')$, of the vacancy and pristine structures, constructed using Gaussian smearing of the frequencies.

	Static energies	Vibrational energies	
Structure	E_{static} (eV/atom)	E_{har} (eV/atom)	ΔE_{anh} (meV/atom)
Tetrahedral	0.0292	*(0.1826)*	0.190
Tetragonal	0.0281	0.1831	0.821
Pristine	0.0000	0.1791	0.071

Table 4.1: DFT static lattice energies and vibrational energies for each structure at 20 K. The second column shows the electronic static lattice energy E_{static} per atom for the pristine, tetrahedral and tetragonal structures relative to the pristine structure. The third and fourth columns show the harmonic vibrational energy E_{har} and anharmonic energy correction $\Delta E_{\text{anh}} = E_{\text{anh}} - E_{\text{har}}$ per atom for the three structures. The tetrahedral structure is dynamically unstable at the harmonic level, as marked by *(italicised brackets)*.

Table 4.1, whilst formation energies at the same temperature are reported in Table 4.2, as at this temperature all three structures are dynamically stable. The harmonic energy E_{har} and the anharmonic correction $\Delta E_{\text{anh}} = E_{\text{anh}} - E_{\text{har}}$, per atom, are given, as well as the vacancy formation energy, which is calculated as: [139]

$$E_f = E_{\text{vac}} - \frac{N-1}{N} E_{\text{pris}},$$

where E_{vac} and E_{pris} are the total energies of the system with and without the vacancy, respectively, and N is the number of atoms in the pristine supercell. The values of E_f for the two different symmetry states of the vacancy are presented in Table 4.2, at three levels of theory – static (electronic), harmonic vibrational, and anharmonic vibrational.

Because the tetrahedral state is dynamically unstable at the harmonic level (although not at the anharmonic level), due to the presence of the two soft modes, a harmonic vibrational energy cannot strictly be defined for this structure. Despite this, an estimated value for the tetrahedral harmonic energy is included, calculated by simply cutting out the contribution of the two soft modes, to enable comparisons between the two symmetry states. The unphysical nature of such a procedure is highlighted by writing the results within italicised brackets in Tables 4.1 and 4.2.

With this caveat in mind, we can look at the thermodynamic stability of the two symmetry states at 20 K. When only electronic and harmonic effects are included in the formation energy, the state with tetragonal symmetry is the most stable, although the inclusion of harmonic vibrational effects reduces the Jahn-Teller relaxation energy – the energy difference between the tetrahedral and tetragonal structures – from 0.275 eV to

	Vacancy formation energies		
Structure	E_f^{static} (eV)	E_f^{har} (eV)	E_f^{anh} (eV)
Tetrahedral	7.451	*(8.343)*	8.373
Tetragonal	7.176	8.185	8.376

Table 4.2: DFT formation energies at each level of theory for each structure at 20 K. The last three columns show the formation energy at the static, harmonic, and anharmonic levels of theory, E_f^{static}, E_f^{har} and E_f^{anh}, respectively. The tetrahedral structure is dynamically unstable at the harmonic level, as marked by *(italicised brackets)*.

0.158 eV. Upon inclusion of anharmonic effects, the tetrahedral state becomes the most stable, as observed experimentally, by 3 meV. The predicted final formation energy for the neutral vacancy, including anharmonic effects, is therefore 8.373 eV, which is close to the estimates from experiments of 9–15 eV [164]. The formation energy of the unrelaxed vacancy at the static level is calculated to be 8.166 eV, implying a total relaxation energy of 0.989 eV at this level of theory. (This result is not included in Table 4.1).

Comparing the vDoS of the vacancy structures to that of pristine diamond gives further insight into the effect of the vacancy on the vibrational properties. Fig. 4.7(a) shows the harmonic vDoS for all three structures at high energies, with the full vDoS as an inset, and Fig. 4.7(b) shows the difference between the harmonic and anharmonic cumulative vDoS, $\Delta G(\omega) = \int_0^\omega d\omega' g_{\text{har}}(\omega') - g_{\text{anh}}(\omega')$, for both symmetry states of the vacancy as well as the pristine lattice. The cumulative densities of states were formed by broadening the mode frequencies with Gaussians (of width 8.163×10^{-4} eV for the vacancy states and 5.442×10^{-3} eV for the pristine lattice) and cumulatively summing them. This allows us to see how the presence of anharmonicity changes the frequencies themselves. Fig. 4.7(a) confirms that the presence of the vacancy only has a significant effect on high energy vibrations. This justifies our approach of including only the highest energy vibrational modes in the anharmonic calculations. The atoms neighbouring the vacancy tend to have larger vibrational amplitudes than the other atoms in the very highest energy modes for both symmetry configurations, while for lower energy modes the amplitudes are comparable.

Fig. 4.7(b) shows that the effect of anharmonicity is much more pronounced in the tetragonal configuration than in the tetrahedral or pristine structures. In the tetrahedral and pristine structures, the changes in the vDoS are of a similar size, and are

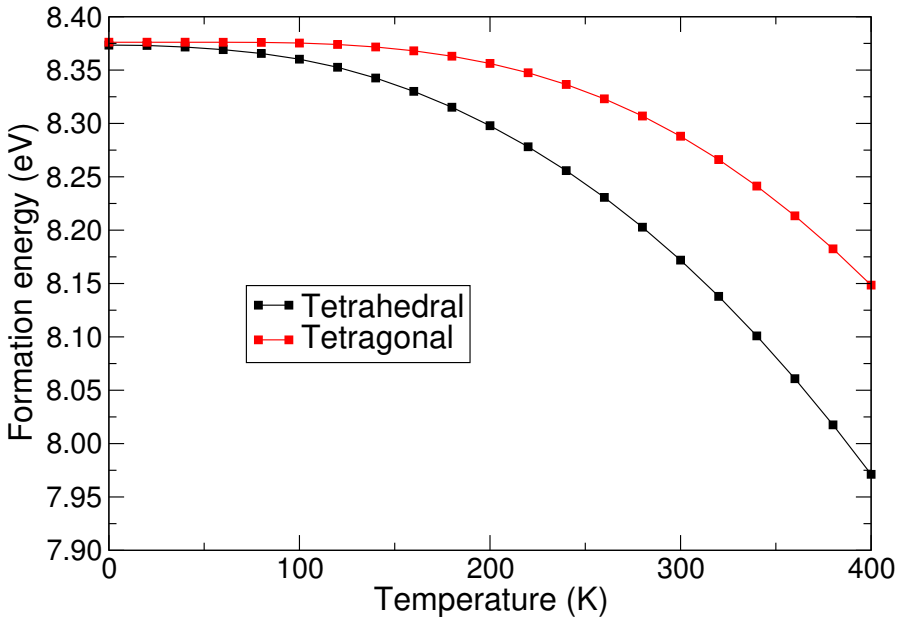

Figure 4.8: Temperature dependence of the formation energies of the tetrahedral and tetragonal symmetry configurations of the neutral vacancy, including anharmonic effects but neglecting the small thermal expansion.

much smaller than the changes seen in the tetragonal case. This demonstrates that distortions away from the tetrahedral symmetry of the pristine lattice strongly increase the anharmonicity of the phonon modes, with the tetrahedral vacancy retaining the weak anharmonic character of pristine diamond. The optical modes at high energies are clearly more affected by the inclusion of anharmonicity than the low energy acoustic modes. In the pristine and tetrahedral structures, anharmonicity raises the frequency of some modes whilst lowering those of others, leading to both positive and negative values of ΔG. In the tetragonal configuration, however, it generally raises the frequency of the modes by a small amount, showing that the leading anharmonic term is quartic in character, as cubic anharmonicity always acts to lower the energy in one dimension [75].

Given the above results at 20 K, we can finally examine the temperature dependence of the formation energies of the tetrahedral and tetragonal structures. Neglecting the effect of thermal expansion, which is very small for diamond over the range of temperatures considered [165], we can calculate the anharmonic vibrational contribution to the free energy at a set of finite temperatures, as detailed in Section 2.3.2. For these calculations, 80 basis functions were used to obtain accurate excited vibrational states. Fig.

4.8 shows the anharmonic formation energy of each symmetry state of the vacancy for a range of temperatures up to 400 K. It is clear that the tetrahedral structure remains the most stable over this temperature range – indeed, the difference in the formation energies of the two symmetry states increases from 0.003 to 0.177 eV at 400 K. The calculated value of the vacancy formation energy at room temperature (300 K) is 8.172 eV, again in reasonable agreement with experimental estimates of 9–15 eV [164].

4.4 Summary

The results presented above show that the tetrahedral symmetry structure of the neutral vacancy in diamond is stabilised down to almost zero temperature by anharmonic vibrations, resolving an old discrepancy between first-principles calculations and experimental work. The vacancy undergoes a dynamic Jahn-Teller distortion which has the full T_d point group symmetry of the pristine system, as observed experimentally. The anharmonic vibrational wavefunction of the tetrahedral defect has been calculated, and shown to be shared evenly among the three minima in the Born-Oppenheimer surface, which correspond to the three tetragonal distortions. We have also calculated the temperature dependence of the vacancy formation energy up to 400 K. The value obtained for the formation energy of the neutral vacancy agrees well with experimental estimates of 9–15 eV [164].

The work presented here provides the first demonstration that this method can be used to study materials where a higher symmetry structure is stabilised by anharmonic vibrations, whether at zero or finite temperature. This idea is pursued in the next chapter of this thesis, applying the same methods to a system extremely different from the case of the neutral vacancy in diamond.

Chapter 5

Ferroelectric Phase Transitions in $BaTiO_3$

In this chapter, we examine the phase transitions of the ferroelectric material barium titanate from first principles. Barium titanate is the prototypical ferroelectric ceramic, but the nature of the transitions between the various ferroelectric phases and the cubic non-ferroelectric phase is still under significant debate in the literature, with several different models proposed. The work presented here applies the VSCF method used throughout this thesis to obtain a description of the phase transitions of this material directly from first principles for the first time. As part of this work, improvements to the efficiency of the solution of the VSCF equations are made, and the effect of the coupling between Γ-point phonons and macroscopic polarisation, which leads to the well-known LO-TO splitting effect, is included in an anharmonic calculation for the first time. Our results are in qualitative agreement with the order-disorder description of phase transitions in barium titanate, with 8 equal regions of probability density at high temperature, which gives way to a lower symmetry configuration at lower temperatures. However, the results also demonstrate that the level of theory used here is insufficient to describe all three phase transitions quantitatively, and that further effects should be included to improve the accuracy of this description.

5.1 Background

5.1.1 Ferroelectricity

In 1920, it was discovered that the compound potassium sodium tartrate tetrahydrate ($KNaC_4H_4O_6{\cdot}4H_2O$), usually known as Rochelle salt, possessed an unusual property [166, 167]. A graduate student, Joseph Valasek, found that the electric polarisation of Rochelle salt exhibited a hysteresis loop as an applied electric field was varied, analogous to that of the magnetisation in a ferromagnet as an applied magnetic field is varied. Due to the striking similarity between these behaviours, the effect became known as ferroelectricity, despite the fact that few ferroelectric materials actually contain iron (the source of the '*ferro*' prefix).

Nowadays, it is recognised that the classification of 'ferroelectric' is just one of several different ways that insulating materials can be categorised, depending on how their electric polarisation $\mathbf{P}$ changes in response to external factors. The changes in polarisation in response to the relevant external factors for each of these classes – dielectrics, paraelectrics, piezoelectrics, pyroelectrics and ferroelectrics – are shown in Fig. 5.1 [168].

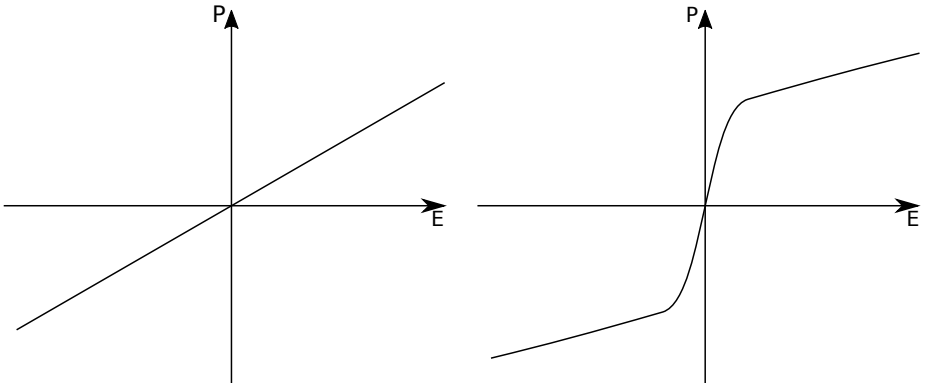

(a) Dielectric

(b) Paraelectric

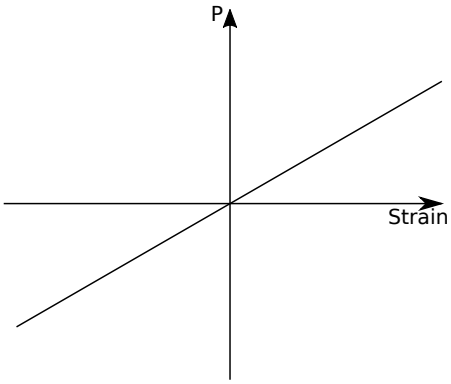

(c) Piezoelectric

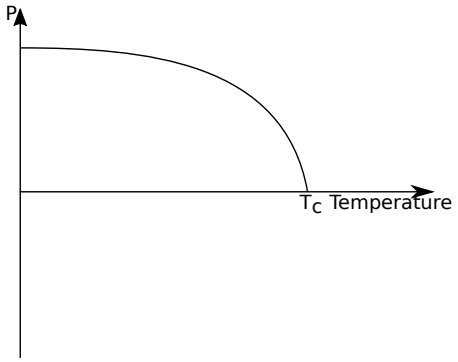

(d) Pyroelectric

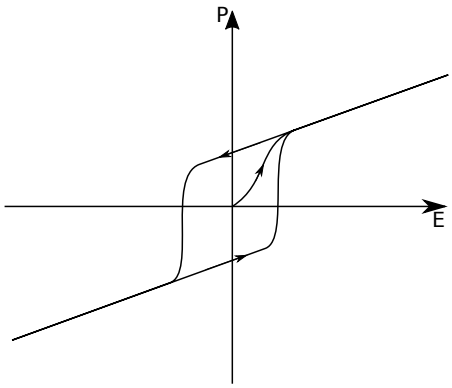

(e) Ferroelectric

Figure 5.1: Typical responses of the polarisation of different classes of materials when subjected to various external factors [168]. P is the polarisation and E the electric field throughout. In (d), T_C is the Curie temperature.

All insulators that do not belong to one of the other categories are dielectrics, which have no inherent polarisation, but become polarised in response to an external electric field **E**. A normal dielectric will typically have $\mathbf{P} \propto \mathbf{E}$ (Fig. 5.1(a)). The behaviour of paraelectric materials is similar, but the relationship between **P** and **E** is instead non-linear, with **P** often increasing rapidly for low values of **E** before levelling off (Fig. 5.1(b)). In piezoelectric materials, polarisation and mechanical stress are coupled, with the application of one resulting in the other appearing (Fig. 5.1(c)) [169, 170]. Similarly, in pyroelectric materials polarisation and temperature are linked – changing the temperature results in a change in polarisation, and such materials have a spontaneous polarisation (Fig. 5.1(d)) [170, 171]. Finally, ferroelectrics are defined as those materials that possess a spontaneous polarisation which can be reoriented by the application of a sufficiently strong electric field (Fig. 5.1(e)) [170, 172].

These last three classes – piezoelectrics, pyroelectrics and ferroelectrics – form a hierarchy: all pyroelectrics are piezoelectric (although not vice versa), and all ferroelectrics are pyroelectric, and thus also piezoelectric (although not vice versa) [170]. Rochelle salt itself was known for its piezoelectric and pyroelectric properties before its ferroelectric behaviour was discovered [173]. Ferroelectric materials are also typically only ferroelectric below what is known as the Curie temperature T_C, which varies from material to material. Above this temperature, the ferroelectric properties disappear and the material becomes paraelectric [170].

Thanks to their unique properties, ferroelectric materials have many technological applications. Some applications make use of the fact that all ferroelectrics are piezoelectric, employing them to produce and sense sound or ignite fuel in lighters, whilst other applications make use of their pyroelectric properties, allowing them to be used as heat sensors, for example [173]. The possibility of switching the polarisation direction can also be utilised, which allows for the production of ferroelectric memory for computers, instead of the more usual magnetic memory [174]. The extreme sensitivity of ferroelectric materials to external electric fields, especially near T_C, allows tunable capacitors to be produced as well [173]. A further possibility that is an active area of current research is that of multiferroics – materials where the phenomena of ferroelectricity and magnetism are coupled, allowing applied electric fields to affect the magnetisation of such a material, or vice versa [175, 176]. These applications, both established and novel, make ferroelectrics an extremely important research topic, and makes understanding the

phenomenon in common ferroelectric materials vital.

5.1.2 Barium titanate

After the discovery of ferroelectricity in Rochelle salt in 1920, ferroelectricity was regarded largely as an academic curiosity for the next twenty-five years. Only one further ferroelectric, potassium dihydrogen phosphate (KH_2PO_4), often known as KDP, was found in 1935 [173, 177]. With only two ferroelectric materials known, both simple salts, it was assumed that the phenomenon was rare, and was caused by the ordering of protons within the molecules [178, 179]. This state of affairs was completely overturned with the discovery of ferroelectricity in a crystalline oxide – barium titanate ($BaTiO_3$) [180–183].

Barium titanate is a member of the extremely well-studied perovskite class of materials. As shown in Fig. 5.2, the fundamental structure of a perovskite is cubic. In a general perovskite with chemical formula ABO_3, the oxygen ions form corner-sharing octahedra around the B ions, whilst the A ions sit in the spaces in between, resulting in a space group of $Pm\bar{3}m$. Many materials with perovskite or perovskite-like structures are technologically important, including materials with colossal magnetoresistance [184, 185], photovoltaics [186, 187], and high-temperature superconductors [188]. However, this perfect cubic structure can be unstable with respect to various symmetry-breaking distortions, depending on the identities of the A and B ions, giving rise to lower symmetry phases. These instabilities will reveal themselves as soft modes present in the cubic structure, often involving rotations or distortions of the octahedra.

The phase diagram of barium titanate perovskite exhibits several different phases of varying symmetry: hexagonal (space group $C6_3/mmc$) [189], cubic ($Pm\bar{3}m$), tetragonal ($P4/mmm$), orthorhombic ($Amm2$), and rhombohedral ($R3m$) symmetry [190, 191]. At zero pressure, the phase transition temperatures are 183 K (rhombohedral-orthorhombic), 278 K (orthorhombic-tetragonal), 393 K (tetragonal-cubic), and finally 1733 K (cubic-hexagonal) [190, 191]. The transition between the cubic and hexagonal phases is slow, and a stable polymorph with hexagonal symmetry has been observed well below 1733 K [190, 192, 193]. The cubic phase is non-ferroelectric, whilst the tetragonal, orthorhombic and rhombohedral phases are ferroelectric. Weak ferroelectric behaviour has also been observed in the hexagonal phase at low temperatures [192]. An approximate phase diagram for barium titanate is shown in Fig. 5.3 [194, 195].

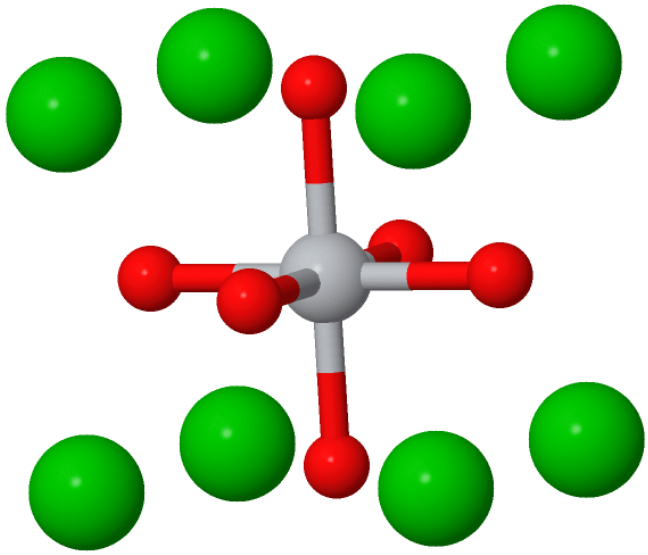

Figure 5.2: The cubic perovskite crystal structure of materials with the general formula ABO_3. Species A is green, B grey, and O red. The oxygen ions form an octahedral 'cage' around the B ions, with each O being shared between two octahedra. The A ions lie in the spaces between these octahedra.

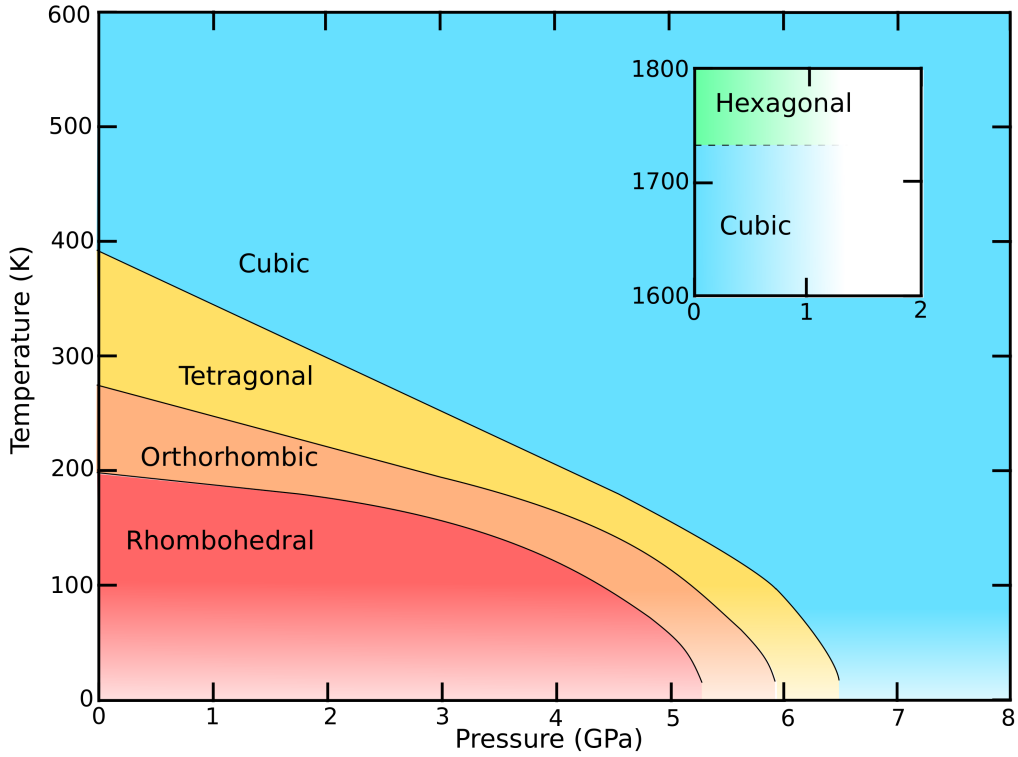

Figure 5.3: Phase diagram of barium titanate over a range of temperatures and pressures, adapted from Refs. 194 and 195. The main plot shows the low-temperature ferroelectric phases of barium titanate. The inset shows the high-temperature transition between the cubic and hexagonal phases. As the cubic-hexagonal phase transition is somewhat more complicated than the others, this is only shown at zero pressure.

Thanks to its status as the first crystalline oxide ferroelectric to be discovered, barium titanate is often seen as the archetype of this class of ferroelectrics, of which many examples have now been found [196–200]. However, the nature of the phase transitions between the ferroelectric rhombohedral, orthorhombic and tetragonal phases, and the non-ferroelectric cubic phase in $BaTiO_3$ is still under some debate. Obtaining an understanding of these phase transitions in the prototypical material for an extremely important class of ferroelectrics is key to furthering our knowledge of these materials, and is the focus of this work.

5.1.3 Ferroelectric phase transitions in $BaTiO_3$

Ferroelectric phase transitions are conventionally thought to fall into one of two groups: *order-disorder* transitions, or *displacive* transitions [178]. Displacive transitions, perhaps the simpler of the two, occur when a polar soft mode present in the high-temperature, non-ferroelectric phase condenses out below a certain temperature, resulting in a polar distortion of the high-temperature unit cell and a macroscopic dipole moment. Order-disorder transitions, however, are different – each unit cell is already distorted, and therefore possesses a dipole moment, but this moment can be pointing along any one of several different possible directions. In the high-temperature phase, the number of moments pointing along each direction is evenly distributed, leading to an average dipole moment of zero. Below the Curie temperature, however, the individual moments order along a given direction to give a non-zero average dipole moment. Applying a sufficiently strong electric field can then make a different ordering direction more favourable, changing the direction of the average dipole moment and resulting in a hysteresis loop – the signature of ferroelectric behaviour.

The ferroelectric behaviour of Rochelle salt, KDP and other similar materials has been conventionally explained using the order-disorder model, with the various orderings of the protons corresponding to the different distortions [178, 179]. $BaTiO_3$ and other similar perovskites were traditionally thought to instead exhibit displacive phase transitions, due to the condensation of polar soft modes [201–204]. Recent work has shown, however, that this traditional view may not be justified, and in fact the division of ferroelectrics into either displacive and order-disorder materials may not be correct in general [178, 205, 206]. There has been some significant support for $BaTiO_3$ to be viewed as an order-disorder ferroelectric [207–211], whilst other work has suggested it

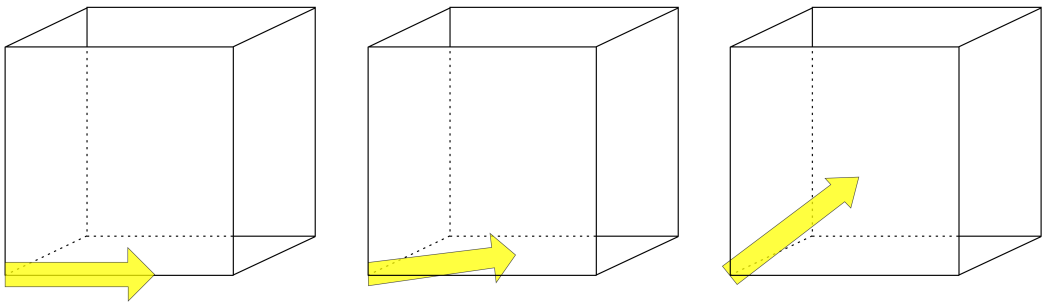

(a) Tetragonal (b) Orthorhombic (c) Rhombohedral

Figure 5.4: Direction of the macroscopic polarisation in each of the three ferroelectric phases of barium titanate. Relative to the cubic lattice vectors, the polarisation lies along the directions [1 0 0], [1 1 0], and [1 1 1] in the tetragonal (a), orthorhombic (b) and rhombohedral (c) phases respectively.

is in fact a mixture of both classes [178, 205, 212–215]. A ferroelectric-antiferroelectric model has also been suggested [216].

The ferroelectric distortions in $BaTiO_3$ can be described as being due to the motion of the Ti^{4+} ions relative to the octahedra formed by the O^{2-} ions [207, 208]. These distortions manifest themselves as three degenerate soft modes at the Γ-point, which together span the 3 possible Cartesian directions of the Ti^{4+} motion. The ferroelectric phases of $BaTiO_3$ are differentiated by the different directions of the polarisation in each phase – P lies along [1 0 0] in the tetragonal phase, [1 1 0] in the orthorhombic phase, and [1 1 1] in the rhombohedral phase, as shown in Fig. 5.4 [216]. In the displacive model for the phase transitions, this is thought to be due to a series of soft modes condensing, moving the Ti^{4+} ions so they are distorted first along the [1 0 0] direction, then the [1 1 0] direction, and finally the [1 1 1] direction.

However, the order-disorder model sees this differently. Taking the high-temperature cubic phase as the reference structure, the model rests on the existence of eight equivalent minima in the BO surface, corresponding to the body diagonals of the cubic unit cell – [1 1 1], [$\bar{1}$ 1 1], [$\bar{1}$ $\bar{1}$ 1], etc. [207] At high temperature in the cubic phase, all eight of these minima are 'occupied' – that is, the vibrational wavefunction has an equal peak in each minimum, corresponding to there being an equal probability for the Ti^{4+} ion to be distorted along each diagonal. On average, therefore, the displacement of the Ti^{4+} ion

is zero, giving the cubic phase. As the temperature is reduced, the number of occupied minima (or peaks in the wavefunction) is cut in half every time a phase transition occurs. In the tetragonal phase, only the four minima corresponding to the four diagonals with a positive x-component are occupied, namely $[1\,1\,1]$, $[1\,1\,\bar{1}]$, $[1\,\bar{1}\,1]$ and $[1\,\bar{1}\,\bar{1}]$, resulting in an average Ti^{4+} displacement, and thus a polarisation, along the $[1\,0\,0]$ direction. Similarly, in the orthorhombic phase, only the $[1\,1\,1]$ and $[1\,1\,\bar{1}]$ minima are occupied, giving a polarisation along the $[1\,1\,0]$ direction, and in the rhombohedral phase only the $[1\,1\,1]$ minimum is occupied, resulting in a polarisation along $[1\,1\,1]$. The VSCF method is extremely well suited to examining this order-disorder picture for $BaTiO_3$, thanks to the ability to calculate the vibrational wavefunction, a key quantity. The aim of this work is to apply the VSCF method to this system, using the high-temperature cubic structure as a reference, to see whether the order-disorder model provides an accurate description of the ferroelectric phase transitions from first principles.

5.1.4 The modern theory of polarisation

As we have already seen, one of the key quantities in the study of ferroelectrics, as well as several other classes of materials, is the macroscopic electric polarisation $\mathbf{P}$. As we are able to calculate the electronic density using DFT, it might seem that obtaining the polarisation should be trivial: a simple matter of integrating $\mathbf{r}n_{\text{elec}}(\mathbf{r})$ over all space, or just over in the unit cell in periodic boundary conditions, before adding in the ionic contribution. However, reality is not so simple – the resulting polarisation will depend on the shape and size of the unit cell chosen [217]. In fact, it can be shown that polarisation is a multi-valued quantity, with its values forming a lattice known as the *polarisation lattice*. The macroscopic polarisation is therefore not a bulk quantity, but can take any one of an infinite array of values dependent on the precise shape of the block of the material in question.

The solution to this problem is through the realisation that, although the absolute value of the polarisation is multi-valued, in experiment we actually measure differences in polarisation. From a theoretical point of view, working with polarisation differences also solves the problem of polarisation being multi-valued, as such differences are single-valued and well-defined [217]. If the shape and size of the unit cell is maintained throughout some change that affects the value of the polarisation, the polarisation will change smoothly and continuously from its equilibrium value; the system will remain on the

same 'branch' of the polarisation lattice, where each branch corresponds to a different choice of unit cell and thus different equilibrium value. No matter which branch the system is on, the polarisation changes by the same amount, meaning we can meaningfully assign the polarisation a value relative to its value at equilibrium. This is the basis of the well-established and successful *modern theory of polarisation* [218–220].

In this chapter, we use a cubic unit cell, like that shown in Fig. 5.2. The highly symmetric structure forces the polarisation to be $\mathbf{0}$ at equilibrium [220], and any value given for the polarisation should be understood as a difference from this equilibrium value.

5.2 Computational methods

5.2.1 Γ-point phonons and electric fields

In polar materials like $BaTiO_3$, the distortion associated with a phonon excitation can result in a dipole moment. In particular, if the phonon in question is at the Γ-point, i.e., $(0\,0\,0)$, the dipole moments in all the unit cells will be aligned, resulting in a macroscopic electric field, which the dipole moments will then in turn interact with. This can result in quite sizeable effects, such as the well known LO-TO splitting, where the degeneracy of the longitudinal optical (LO) and transverse optical (TO) modes at Γ is lifted [221]. As we are interested in polar distortions of $BaTiO_3$ at the Γ-point, including this effect will be very important to ensure all the relevant physics is captured.

The theory of how to include this interaction between the macroscopic electric field and the Γ-point phonons is well understood in the harmonic approximation [221, 222], and can easily be calculated within common DFT codes like `CASTEP` [223]. A point of particular interest is that the results of the calculation change depending on the direction along which $\mathbf{q} \to \mathbf{0}$. However, to the best of our knowledge, this interaction has not been implemented in a VSCF calculation, or indeed any anharmonic vibrational calculation to date. In view of this, the theory required to include this effect in VSCF calculations is described below, with $\mathbf{q} \to \mathbf{0}$ along the x-axis initially, before generalising this result to an arbitrary direction.

Two quantities that feature heavily in the derivations below are the Born effective charges $Z^*_{\alpha;ij} = -\frac{\partial^2 E}{\partial X_{\alpha;i}\partial \mathcal{E}_j} = \frac{\partial f_{\alpha;i}}{\partial \mathcal{E}_j} = \Omega_0 \frac{\partial P_j}{\partial X_{\alpha;i}}$, and the electric susceptibility $\chi_{ij} = \varepsilon^{\infty}_{ij} - \delta_{ij}$ [221]. Here, E represents the electronic energy, $\mathcal{E}_i$ a macroscopic electric field,

Ω_0 the unit cell volume, P_i the polarisation, $\varepsilon_{ij}^{\infty}$ the dielectric permittivity, and $X_{\alpha;i}$ a displacement of the αth atom. As the Born effective charges represent the difference in polarisation resulting from a change in the positions of the atoms, they can only be used to calculate differences in polarisation, making them an excellent example of the modern theory of polarisation at work [220]. Both $Z^*_{\alpha;ij}$ and χ_{ij} can be calculated within `CASTEP` [223], and the values obtained are used as input for the anharmonic calculations.

We start with the basic vibrational Hamiltonian of equation (2.9), reproduced here again for convenience:

$$H_{\text{vib}} = \sum_{p\alpha} -\frac{1}{2m_\alpha}\nabla^2_{p\alpha} + E_{\text{elec}}(\mathbf{R}) \ . \tag{5.1}$$

With the addition of a macroscopic electric field, two more terms appear [222]:

$$H_{\text{vib}} = \sum_{p\alpha} -\frac{1}{2m_\alpha}\nabla^2_{p\alpha} + E_{\text{elec}}(\mathbf{R}) - \sum_{p\alpha}\sum_{ij} X_{p\alpha;i} Z^*_{\alpha;ij}\mathcal{E}_j - \sum_{ij}\frac{1}{2}\chi_{ij}\mathcal{E}_i\mathcal{E}_j \ . \tag{5.2}$$

As we are only interested in $\mathbf{q} = 0$, we only need to consider a single unit cell, so the summation over p can be neglected.

We can write the polarisation (in reality the change in polarisation relative to the equilibrium configuration) as [222]

$$\begin{aligned} P_i &= \sum_{\alpha j} Z^*_{\alpha;ij} X_{\alpha;j} + \sum_j \chi_{ij}\mathcal{E}_j \\ &= \sum_{\alpha j} Z^*_{\alpha;ij}\frac{1}{\sqrt{m_\alpha}}\sum_n u_n w_{n;\alpha j} + \sum_j \chi_{ij}\mathcal{E}_j \\ &= \sum_{\alpha j}\sum_n Z^*_{\alpha;ij} u_n w'_{n;\alpha j} + \sum_j \chi_{ij}\mathcal{E}_j \ . \end{aligned} \tag{5.3}$$

Here we have substituted in the expression for $X_{\alpha;i}$ from equation (2.63), taken $\mathbf{q} = 0$ (and therefore removed it as a label), and finally defined $w'_{n;\alpha j} = \frac{1}{\sqrt{m_\alpha}} w_{n;\alpha j}$, the phonon eigenvectors normalised by the square root of the atomic mass, for convenience.

The electric field is then given by [222]

$$\mathcal{E}_i = -\frac{q_i}{q^2}\sum_j q_j P_j \tag{5.4}$$

$$= -\frac{q_i}{q^2}\left\{\sum_{jk}\sum_\alpha\sum_n q_j Z^*_{\alpha;jk} u_n w'_{n;\alpha k} + \sum_{jk} q_j \chi_{jk}\mathcal{E}_k\right\} \ , \tag{5.5}$$

where we have substituted in for P_i from equation (5.3).

We now take $\mathbf{q}$ to be approaching Γ along the x-axis. This means that $q_i = E_i = 0$ for $i \neq 1$, as $\mathcal{E}$ is parallel to $\mathbf{q}$, and $q_1 = q$. The remaining component of $\mathcal{E}$ is therefore given by

$$\mathcal{E}_1 = -\left\{ \sum_k \sum_\alpha \sum_n Z^*_{\alpha;1k} u_n w'_{n;\alpha k} + \sum_k \chi_{1k} \mathcal{E}_k \right\} . \tag{5.6}$$

Rearranging the equation gives

$$-\sum_k \sum_\alpha \sum_n Z^*_{\alpha;1k} u_n w'_{n;\alpha k} = \mathcal{E}_1 + \sum_k \chi_{1k} \mathcal{E}_k = (1 + \chi_{11}) \mathcal{E}_1 = \varepsilon^\infty_{11} \mathcal{E}_1 , \tag{5.7}$$

where we have again used the fact that $E_i = 0$ for $i \neq 1$. This finally gives us

$$\mathcal{E}_i = \begin{cases} -\frac{1}{\varepsilon^\infty_{11}} \sum_k \sum_\alpha \sum_n Z^*_{\alpha;1k} u_n w'_{n;\alpha k} & \text{for } i = 1 \\ 0 & \text{otherwise} \end{cases} . \tag{5.8}$$

If we substitute equation (5.8) back into the Hamiltonian of equation (5.2) and transform to phonon normal co-ordinates, we obtain

$$\begin{aligned} H_{\text{vib}} = & \sum_n -\frac{1}{2} \frac{\partial^2}{\partial u_n^2} + V_{\text{el}}(\mathbf{u}) \\ & + \frac{1}{\varepsilon^\infty_{11}} \sum_{\alpha i} \sum_{\beta k} \sum_{nm} u_n u_m w'_{n;\alpha i} w'_{m;\beta k} Z^*_{\alpha;1i} Z^*_{\beta;1k} \\ & - \frac{\chi_{11}}{2 \left(\varepsilon^\infty_{11}\right)^2} \sum_{\alpha i} \sum_{\beta k} \sum_{nm} u_n u_m w'_{n;\alpha i} w'_{m;\beta k} Z^*_{\alpha;1i} Z^*_{\beta;1k} . \end{aligned} \tag{5.9}$$

The summations in the last two terms are identical, meaning they can be combined. The resulting constant in front of the summations can be simplified by using the fact that, in $BaTiO_3$, $\varepsilon^\infty_{ii} \gg 1$, giving

$$\frac{1}{\varepsilon^\infty_{11}} - \frac{\chi_{11}}{2 \left(\varepsilon^\infty_{11}\right)^2} = \frac{2\varepsilon^\infty_{11} - \chi_{11}}{2 \left(\varepsilon^\infty_{11}\right)^2} = \frac{\varepsilon^\infty_{11} + 1}{2 \left(\varepsilon^\infty_{11}\right)^2} \approx \frac{1}{2\varepsilon^\infty_{11}} . \tag{5.10}$$

Equation (5.9) therefore becomes

$$\begin{aligned} H_{\text{vib}} &= \sum_n -\frac{1}{2} \frac{\partial^2}{\partial u_n^2} + V_{\text{el}}(\mathbf{u}) \\ &\quad + \frac{1}{2\varepsilon^\infty_{11}} \sum_{\alpha i} \sum_{\beta k} \sum_{nm} u_n u_m w'_{n;\alpha i} w'_{m;\beta k} Z^*_{\alpha;1i} Z^*_{\beta;1k} \\ &= \sum_n -\frac{1}{2} \frac{\partial^2}{\partial u_n^2} + V_{\text{el}}(\mathbf{u}) + V_{q=0}(\mathbf{u}) . \end{aligned} \tag{5.11}$$

This makes the VSCF equations become

$$\left(-\frac{1}{2}\frac{\partial^2}{\partial u_n^2} + \bar{V}_n(u_n)\right)|\phi_n(u_n)\rangle = \lambda_n |\phi_n(u_n)\rangle \ , \tag{5.12}$$

where

$$\bar{V}_n(u_n) = \left\langle \prod_{n'}{}' \phi_{n'}(u_{n'}) \middle| V_{\mathrm{el}}(\mathbf{u}) + V_{q=0}(\mathbf{u}) \middle| \prod_{n'}{}' \phi_{n'}(u_{n'}) \right\rangle \ . \tag{5.13}$$

If $\mathbf{q} \to \mathbf{0}$ along a direction other than the x-axis, it is a simple matter to transform the problem into the one described above, by rotating the Cartesian axes so that the direction along which $\mathbf{q} \to \mathbf{0}$ becomes the new x-axis. This can be achieved by using the rotation matrix U to transform the phonon eigenvectors, Born effective charges, and dielectric permittivity matrix – $\tilde{w}'_{n;\alpha i} = \sum_j U_{ij} w'_{n;\alpha j}$, $\tilde{Z}^*_{\alpha;ij} = \sum_{kl} U_{ki} Z^*_{\alpha;kl} U_{lj}$, and $\tilde{\varepsilon}^\infty_{ij} = \sum_{kl} U_{ki} \varepsilon^\infty_{ij} U_{lj}$. U can be computed using Rodrigues's rotation formula [224, 225]. If the direction along which $\mathbf{q} \to \mathbf{0}$ is defined by the unit vector $\hat{\mathbf{n}} = (n_1, n_2, n_3)$, an axis and angle of rotation can easily be computed and substituted into the formula, giving the result

$$U = \begin{pmatrix} 1 - \frac{n_2^2+n_3^2}{1+n_1} & n_2 & n_3 \\ -n_2 & 1 - \frac{n_2^2}{1+n_1} & -\frac{n_2 n_3}{1+n_1} \\ -n_3 & -\frac{n_2 n_3}{1+n_1} & 1 - \frac{n_3^2}{1+n_1} \end{pmatrix} \ . \tag{5.14}$$

Once the relevant quantities have been transformed using U, in analogy to equation (5.11), the correction to the vibrational Hamiltonian, $V_{q=0}$, can be expressed as

$$V_{q=0}(\mathbf{u}) = \frac{1}{2\tilde{\varepsilon}^\infty_{ii}} \sum_{\alpha i} \sum_{\beta k} \sum_{nm} u_n u_m \tilde{w}'_{n;\alpha i} \tilde{w}'_{m;\beta k} \tilde{Z}^*_{\alpha;1i} \tilde{Z}^*_{\beta;1k} \ . \tag{5.15}$$

All of the above assumes that the Born effective charges remain constant as the atoms are displaced. This is not in general a good assumption, and previous studies have shown that in $BaTiO_3$ and similar compounds the Born effective charges vary with atomic position [226–228]. However, this can easily be included in the final result of equation (5.11) by replacing the constant $Z^*_{\alpha;ij}$ with $Z^*_{\alpha;ij}(\mathbf{u})$. One practical consideration is that to calculate the Born effective charges at a given configuration of nuclei requires a full phonon calculation, which becomes too computationally expensive to do at every point when mapping two-dimensional terms. Instead, we can expand $Z^*_{\alpha;ij}(\mathbf{u})$ in a similar way to the BO surface, but truncate at the one-dimensional terms, so that $Z^*_{\alpha;ij}(\mathbf{u}) = Z^*_{\alpha;ij}(\mathbf{0}) + \sum_n Z^*_{n\alpha;ij}(u_n)$, which is analogous to equation (2.73). There are then few enough mapping points that these one-dimensional terms can be easily mapped.

Comparisons to previous results [226] show that this is a good approximation, and therefore this method is used for the calculations in this chapter.

Equation (5.11) shows that $V_{q=0}(\mathbf{u})$ is quadratic in the mode amplitudes u_n, so the expansion of the BO surface needs to include at least two-dimensional terms including all the modes involved. Dealing with all these coupled terms requires significant computational effort, and ideally a more efficient way of calculating the integrals needed to construct and diagonalise the vibrational Hamiltonian.

5.2.2 Clenshaw-Curtis quadrature

As described in Section 2.3.3, in order to solve the VSCF equation we first need to express the Hamiltonian in our chosen basis: typically the one-dimensional simple harmonic oscillator eigenstates. Doing this involves computing many integrals – for each n-dimensional term in the Hamiltonian, we will have a $2n$-dimensional integral, which can be decomposed into a number of one-dimensional integrals which scales as $\mathcal{O}(N_{\text{basis}}^{2n})$, where N_{basis} is the size of the basis set. When coupling between several modes is important, as is the case in $BaTiO_3$, this rapidly becomes expensive, and a method of reducing this cost becomes especially desirable.

One way to address this problem is to simply increase the speed of each integration. The VSCF method used in this thesis typically uses the extremely well-established and simple trapezoid rule [229], where the interval of integration is divided up into many small parts of width dx, the integrand $f(x)$ is evaluated at a point in each of these parts x_i, and the result is summed, giving the result $I = \sum_i f(x_i)dx$. A typical number of evaluation points is around 5000 for each one-dimensional integral, meaning that for an n-body term we have $(5000N_{\text{basis}})^{2n}$ evaluation points. We could simply reduce the number of evaluation points per one-dimensional integral to reduce the cost of the trapezoid rule, but accuracy is rapidly lost for numbers of evaluation points less than 5000. Instead, we can turn to other methods of integration that can provide similar accuracy to the trapezoid rule with fewer evaluation points – quadrature methods.

The most famous quadrature method for evaluating integrals is that of Gaussian quadrature. This method assumes our integrand can be written as $f(x) = g(x)w(x)$, where $w(x)$ is a weight function, which should contain any singularities present in $f(x)$. Gaussian quadrature then rests upon finding a set of polynomials $\{p_n(x)\}$ that are orthogonal under $w(x)$ over the integration interval $[a, b]$, and evaluating $g(x)$ at the

zeroes of these polynomials $\{x_{i;n}\}$ [230–232]. These values are then summed with appropriate weights to give the final result $I = \sum_i w_{i;n} g(x_{i;n})$; these weights are given by $w_{i;n} = \frac{a_n}{a_{n-1}} \frac{\int_a^b w(x) p_{n-1}^2(x) dx}{p_n'(x_{i;n}) p_{n-1}(x_{i;n})}$, where a_n is the coefficient of x^n in $p_n(x)$ [93]. If N evaluation points are used, which corresponds to evaluating $g(x)$ at the zeros of $p_N(x)$, the result will be exact if $g(x)$ is a polynomial of order less than or equal to $2N - 1$. Gaussian quadrature is an extremely well studied method, and much theory and many computational routines are available for specific weight functions and integration intervals. Examples of these different flavours of Gaussian quadrature include Gauss-Legendre ($w(x) = 1$, $a = -1$, $b = 1$), Gauss-Jacobi ($w(x) = (1-x)^\alpha (1+x)^\beta$, $a = -1$, $b = 1$), Gauss-Hermite ($w(x) = e^{-x^2}$, $a = -\infty$, $b = \infty$) and Gauss-Laguerre ($w(x) = x^\alpha e^{-x}$, $a = 0$, $b = \infty$). Outside of these well-studied cases, some routines are also available for the general case [93, 233]. However, Gaussian quadrature does have several drawbacks. Firstly, because the evaluation points for different values of N are the zeroes of different polynomials, in general they cannot be reused for different orders, which results in many more function evaluations than would otherwise be required. In addition, the pairing of the weight function and integration interval required here is non-standard – the most sensible choice of weight function is $w(x) = e^{-x^2}$, as this forms part of all the basis functions, but $a \neq -\infty$ and $b \neq \infty$, unlike in Gauss-Hermite quadrature. Tests conducted as part of this work showed that the routines used to determine the appropriate orthogonal polynomials for this weight function and interval proved to be unstable, as they depended strongly on small differences between increasingly large numbers. Because of these failings, we instead turn to a different way to evaluate the integrals – Clenshaw-Curtis quadrature.

Clenshaw-Curtis quadrature relies on expanding the integrand $f(x)$ in terms of Chebyshev polynomials $\{T_k(x)\}$ [234]. As $T_k(\cos\theta) = \cos(k\theta)$, this is precisely equivalent to changing variables from x to θ via the transformation $x = \cos\theta$, and then expanding the resulting function as a cosine series. This means that the integral I can be calculated as:

$$I = \int_{-1}^{1} f(x) dx = \int_0^\pi f(\cos\theta) \sin\theta d\theta = a_0 + \sum_{k=1}^{\infty} \frac{2a_{2k}}{1 - (2k)^2} \ , \tag{5.16}$$

where $a_k = \frac{2}{\pi} \int_0^\pi f(\cos\theta) \cos(k\theta) d\theta$ are the coefficients of the cosine series. Although here we use the interval $[-1, 1]$, any interval can easily be considered by changing variables to map it onto $[-1, 1]$. If we truncate our Chebyshev expansion of $f(x)$ at order N, or

equivalently only want to conduct $N+1$ function evaluations, we only require a_{2k} with $k \leq \frac{N}{2}$, giving [234]

$$I = \int_{-1}^{1} f(x)dx = \int_{0}^{\pi} f(\cos\theta)\sin\theta d\theta = a_0 + \sum_{k=1}^{\frac{N}{2}-1} \frac{2a_{2k}}{1-(2k)^2} + \frac{a_N}{1-N^2} \ . \tag{5.17}$$

The a_N and a_0 terms have only half the weight of the others, to avoid aliasing. These coefficients can then be calculated by approximating them using a discrete cosine transform [235]:

$$a_{2k} = \frac{2}{N}\left[\frac{f(1)+f(-1)}{2} + f(0)(-1)^k + \sum_{n=1}^{\frac{N}{2}-1}(f(\cos\frac{n\pi}{N}) + f(-\cos\frac{n\pi}{N}))\cos\frac{2nk\pi}{N}\right] \ . \tag{5.18}$$

As can be seen from equation (5.18), $f(x)$ is evaluated at the extrema of the highest order Chebyshev polynomial $T_N(x)$, $x_n = \cos\left(\frac{n\pi}{N}\right)$. If we substitute equation (5.18) into equation (5.17) and rearrange, using $-\cos\frac{n\pi}{N} = \cos\frac{(N-n)\pi}{N}$, we can find an expression for I similar to that for Gaussian quadrature, with a sum over $N+1$ function evaluations multiplied by weights:

$$\begin{aligned}
I = \frac{2}{N}\Bigg[& f(1)\left(\frac{1}{2} + \frac{1}{2(1-N^2)} + \sum_{k=1}^{\frac{N}{2}-1}\frac{1}{1-(2k)^2}\right) \\
& + f(-1)\left(\frac{1}{2} + \frac{1}{2(1-N^2)} + \sum_{k=1}^{\frac{N}{2}-1}\frac{1}{1-(2k)^2}\right) \\
& + f(0)\left(1 + \frac{1}{1-N^2} + \sum_{k=1}^{\frac{N}{2}-1}\frac{2(-1)^k}{1-(2k)^2}\right) \\
& + \sum_{n=1}^{\frac{N}{2}-1} f\left(\cos\frac{n\pi}{N}\right)\left(1 + \frac{\cos n\pi}{1-N^2} + \sum_{k=1}^{\frac{N}{2}-1}\frac{2}{1-(2k)^2}\cos\frac{2nk\pi}{N}\right) \\
& + \sum_{n=\frac{N}{2}+1}^{N-1} f\left(\cos\frac{n\pi}{N}\right)\left(1 + \frac{\cos(N-n)\pi}{1-N^{\,2}} + \sum_{k=1}^{\frac{N}{2}-1}\frac{2}{1-(2k)^2}\cos\frac{2(N-n)k\pi}{N}\right)\Bigg] \ .
\end{aligned} \tag{5.19}$$

Although in theory Clenshaw-Curtis quadrature with N points is only exact for polynomial integrands of order less than or equal to $N-1$, in many practical situations Clenshaw-Curtis quadrature is as accurate as Gaussian quadrature [236]. This is due

to the fact that an expansion of many functions in terms of Chebyshev polynomials converges very quickly. In particular, the Gaussian function e^{-x^2}, which forms the only non-polynomial factor in the integrands here, can be well described using a Chebyshev expansion with order around 15 [237]. This, combined with the fact that the evaluation points can be re-used for lower order integrands, makes Clenshaw-Curtis quadrature an appropriate choice for our purposes here.

5.2.3 Density functional theory calculations

In addition to the terms arising from the interaction between Γ-point phonons and the macroscopic electric field described above, it is of course necessary to first obtain a geometry optimised structure, before mapping the BO surface as usual. The DFT calculations used to do this were performed using `CASTEP` version 16.1 and the corresponding 'on-the-fly' norm-conserving pseudopotentials generated by `CASTEP` [60]. In all calculations, a grid scale of 2.0 was used. The ferroelectric properties of $BaTiO_3$ and other similar materials are known to be extremely sensitive to the volume of the cell used [212, 238, 239], so it is very important to get the lattice constant correct when optimising the cell geometry. In order to fulfil this requirement, we used the PBEsol exchange-correlation functional [46], which was designed to give accurate lattice constants and volumes. Of the most common (semi-)local functionals available, the PBEsol functional was found to give a cubic lattice constant of 3.981 Å, the closest to the experimental value of 4.012 Å [240, 241] of the most common (semi-)local functionals available. The lattice constant was then made to match the experimental lattice constant by applying a external pressure of -0.4 GPa. The plane-wave cut-off energy was taken to be 700 eV, and an $11 \times 11 \times 11$ Monkhorst-Pack grid was used.

As noted above, the ferroelectric distortions we are interested in are associated with three degenerate soft modes at the Γ-point. As we are only interested in Γ, we only need to consider the normal modes of a single unit cell, and as we are only interested in the soft modes, we only need to anharmonically map the BO surface in the subspace spanned by those modes. All modes other than the soft modes are therefore described within the harmonic approximation. In addition to simply mapping the one-dimensional terms associated with the soft modes in the BO surface expansion of equation 2.73, the inclusion of the interaction described in Section 5.2.1 means that we also need to include coupling between these soft modes. This means three two-dimensional terms,

one for each possible pairing of the soft modes, need to be mapped as well. Since the three soft modes are degenerate, we can select appropriate displacement patterns for the three modes to make the calculations simpler – here we use displacement patterns that correspond to Ti^{4+} ions distorting along the $[0\,1\,\bar{1}]$, $[0\,1\,1]$ and $[1\,0\,0]$ directions. This ensures that the three two-dimensional terms include the minima along the $[1\,1\,1]$, $[\bar{1}\,1\,1]$, $[\bar{1}\,\bar{1}\,1]$, etc. directions, which would not be included if we chose displacement patterns aligned with the Cartesian axes. The chosen displacement patterns can be found in Appendix C.

The harmonic calculations were carried out using the finite displacement method of Section 2.3.1 with atomic displacements of 0.00529 Å (0.01 bohr), whilst the anharmonic calculations were conducted using the VSCF method of Section 2.3.2. As the most important terms in the expansion of the BO surface in $BaTiO_3$ are the two-dimensional terms, the VSCF+f method of Section 3 was not used, as it provides only minimal improvement for two-body terms. The three-dimensional term coupling all three soft modes together was also mapped, but due to the rapid increase in the number of integrals required for higher dimensional terms, solving the VSCF equations becomes prohibitively expensive, even with the improvements outlined in Section 5.2.2. For this reason the three-dimensional and higher terms in the BO surface expansion are neglected. 21 mapping points are used per mode for the mapping of the BO surface, with further details of the mapping process described in Section 5.3.1. The variation of the Born effective charges is also mapped along each mode, as noted above, using 21 points per mode, whilst the dielectric permittivity, and thus the electric susceptibility, is assumed to remain constant at the value calculated for the cubic structure, 6.3636. When solving the VSCF equations, 40 simple harmonic oscillator basis functions are used per mode as a basis in which to diagonalise the Hamiltonian. For the three soft modes, a frequency of 0.218 eV (8×10^{-3} a.u.) is used to create these basis functions. The required integrals are evaluated using a 110-point Clenshaw-Curtis quadrature method.

5.3 Results

5.3.1 Mapping the Born-Oppenheimer surface and Born effective charges

Obtaining a solution to the modified VSCF equations (equation (5.12)) relies on the input of several calculated quantities – the BO surface itself, the variation of the Born effective

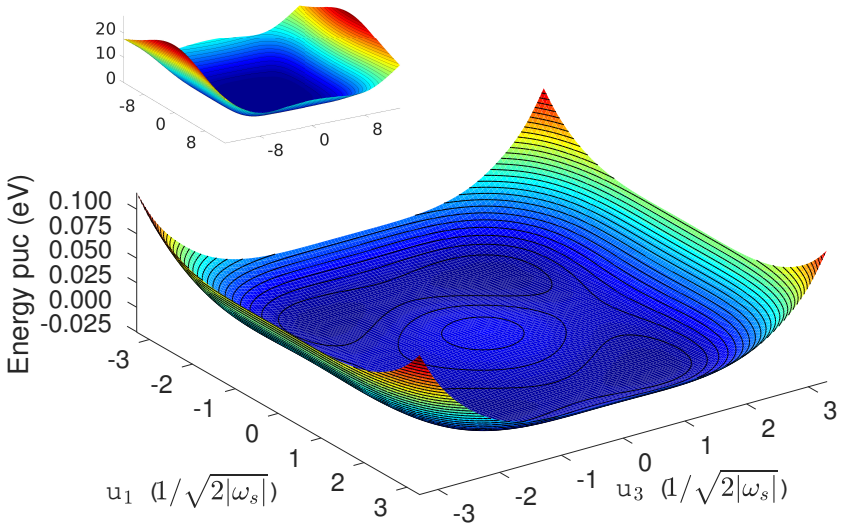

(a)

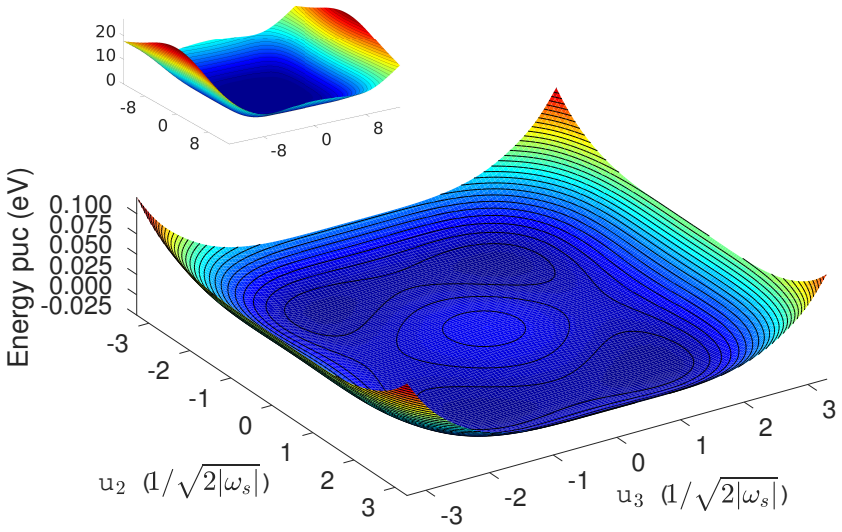

(b)

Figure 5.5: Two 2-D subspaces of the Born-Oppenheimer surface spanned by the three soft modes of cubic $BaTiO_3$. u_1, u_2, and u_3 relate to soft modes corresponding to distortions along the $[0\,1\,\bar{1}]$, $[0\,1\,1]$, and $[1\,0\,0]$ directions. 'puc' stands for 'per unit cell'. The main figures show the subspaces mapped out to low amplitudes, whilst the insets show them mapped out to much higher amplitudes. Blue and red signify low and high energy parts of the BO surface respectively. Each contour line represents an energy increase of 0.865 eV in the insets, and 4.24 and 4.37 meV in the main figures of (a) and (b) respectively.

charges, and the dielectric permittivity. Fig. 5.5 presents two of the two-dimensional subspaces of the BO surface mapped as part of this work, with Figs. 5.5(a) and 5.5(b) corresponding to the coupling between the u_1 and u_3 soft modes, and the u_2 and u_3 soft modes, respectively. Here, and indeed in the rest of this section, u_1, u_2, and u_3 will be used as shorthand for the soft modes with the Ti^{4+} ions moving along the $[0\,1\,\bar{1}]$, $[0\,1\,1]$, and $[1\,0\,0]$ directions, respectively. All three of these soft modes are degenerate, as noted previously, with a frequency of $\omega_s = 23.8i$ meV. In both figures, four minima in the BO surface are visible, which together correspond to the eight possible directions of Ti^{4+} distortion discussed in Section 5.1.3. This agrees with the picture behind the order-disorder theory of the transitions of $BaTiO_3$ [207], lending support to this description of the ferroelectric transitions.

The main parts of Figs. 5.5(a) and 5.5(b) show the BO surface mapped out to relatively small amplitudes of displacement away from the cubic structure, up to around $3\sqrt{\langle u_s^2 \rangle}$, where $\sqrt{\langle u_s^2 \rangle}$ is the harmonic expectation value of the squared mode amplitude of an oscillator with frequency $|\omega_s|$. The insets, however, show the BO surface mapped out to much larger amplitudes, around $13\sqrt{\langle u_s^2 \rangle}$, to ensure that basis functions which are non-zero at large amplitudes can still be dealt with accurately. To obtain both a detailed picture of the BO surface around the cubic structure, and a mapping out to very large amplitudes, 17 mapping points per mode were used to map the BO surface up to amplitudes of $5\sqrt{\langle u_s^2 \rangle}$. 4 more mapping points per mode were then used to complete the mapping out to large amplitudes, with a much larger spacing between them. This allowed for both fine detail of the central region of interest, and a broad picture of the overall BO surface.

The Born effective charges were also mapped using the same scheme as the BO surface itself, with a fine mapping using 17 points at small amplitudes, followed by a coarser mapping using 4 more points out to larger amplitudes. An example of the resulting form of the Born effective charges is shown in Fig. 5.6. This shows the variation in the xx component of the Born effective charges as the amplitude of the u_3 soft mode (which corresponds to distortion along the x direction) changes. If we take the Ti^{4+} ion to be at the origin at equilibrium, we can see that the charge on the O^{2-} ion that lies along the x-axis and the charge on the Ti^{4+} ion itself are heavily affected by the distortion, whilst the charges on the other two O^{2-} ions and the Ba^{2+} ion is barely affected. Both the Ti^{4+} and x-axis O^{2-} ions have charges significantly higher than their formal charges

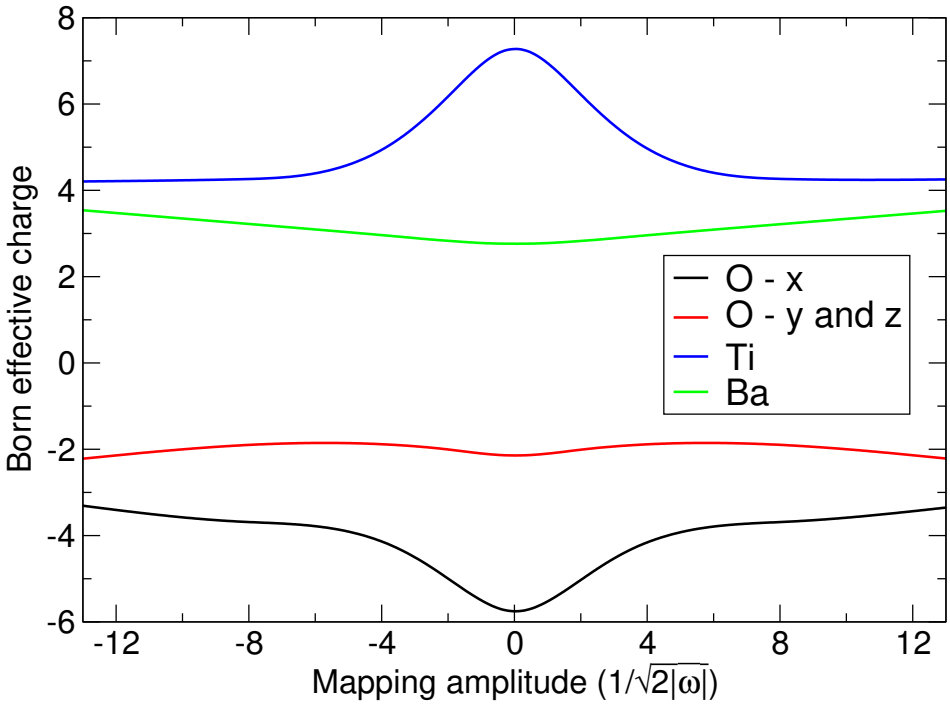

Figure 5.6: Variation of the xx component of the Born effective charges of the five ions in $BaTiO_3$ as a function of u_3, the amplitude of the soft mode corresponding to distortion in the x direction. If we take the Ti ion to lie at the origin, there are three O ions lying on the three Cartesian axes, which are referred to on the graph as O-x, O-y, and O-z. The behaviour of the Born effective charge of O-x as a function of u_3 is significantly different to that of O-y and O-z, both of which exhibit identical behaviour.

at equilibrium, although they reduce as the amplitude increases; Ti^{4+} essentially tends to its formal charge, while the x-axis O^{2-} remains somewhat higher. The other O^{2-} ions have a charge that is essentially equal to their formal charge, whilst the Ba^{2+} ion has a charge that is somewhat higher than its formal charge.

With the Born effective charges mapped as shown above, and a value for the dielectric permittivity calculated, we can examine the effect of the interaction between the macroscopic polarisation and Γ-point phonons on the BO surface. Figs. 5.7(a) and (b) show the correction to the BO surface, $V_{q=0}$, in the u_1-u_3 and u_2-u_3 two-dimensional subspaces respectively, with $\mathbf{q} \to \mathbf{0}$ along the x-axis. The magnitude of this correction shows that the interaction between the macroscopic polarisation and Γ-point phonons is significant, on the order of several meV in the region of the minima of the BO surface. However, despite this correction to the BO surface, it is clear that this interaction alone will not lead to a full first-principles explanation of the phase transitions in $BaTiO_3$. Fig. 5.7 shows that the inclusion of this effect favours areas where the product of mode amplitudes $u_i u_j$ is positive, and penalises areas where $u_i u_j$ is negative – a feature that makes sense, given the form of $V_{q=0}(\mathbf{u})$ in equation (5.11). This is true no matter which direction $\mathbf{q}$ approaches Γ from, with the same minima of the BO surface simply favoured by differing amounts depending on the direction. This means that any predicted phase transitions will be largely unaffected by the direction $\mathbf{q}$ approaches Γ from.

5.3.2 The nuclear probability density

Figs. 5.8 and 5.9 present the calculated nuclear probability density in the two-dimensional subspaces previously shown in Fig. 5.5, at 5 K and 6000 K respectively. The reasoning behind choosing such a high temperature in Fig. 5.9 is addressed below, but first we make some important observations about the features of the two figures. In both figures, there are 8 clear regions of significant probability density (each containing several subsidiary peaks), which directly correspond to the 8 wells in the BO surface shown in Fig. 5.5. This provides further support for the order-disorder picture, as we can see the system localising in the minima of the BO surface. Fig. 5.8 shows that the nuclear probability density is more localised in certain minima at low temperatures, whilst Fig. 5.9 shows that at higher temperatures the probability density is shared much more evenly across all 8 minima. This demonstrates that calculations using the VSCF method predict that, as temperature is increased, a transition from an ordered state, where a particular

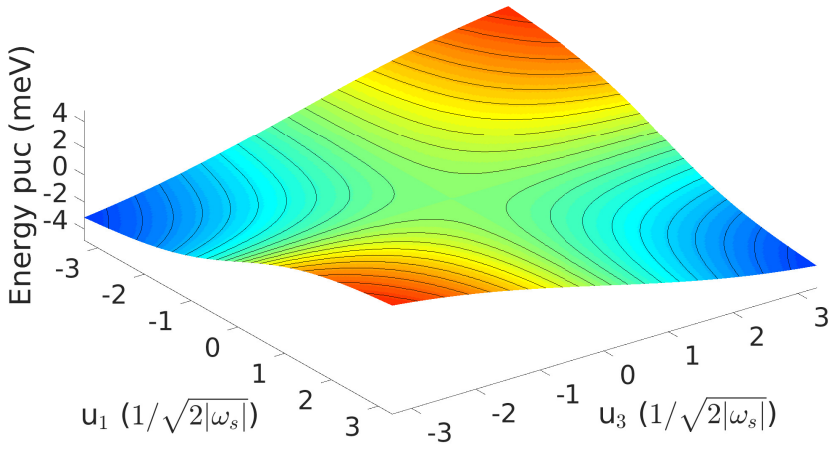

(a)

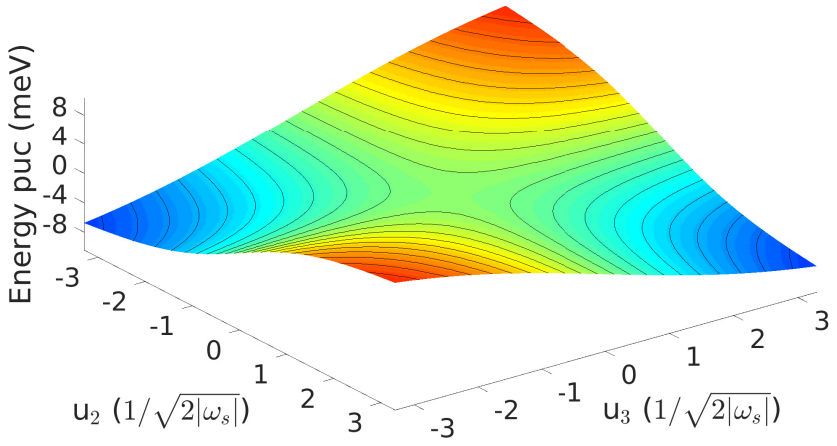

(b)

Figure 5.7: The correction to the Born-Oppenheimer surface due to the interaction between Γ-point phonons and the macroscopic polarisation, with $\mathbf{q}$ approaching Γ along the x-axis. (a) shows this correction in the two-dimensional subspace spanned by the u_1 and u_3 soft modes, whilst (b) shows the same in the subspace spanned by the u_2 and u_3 soft modes. u_1, u_2, and u_3 relate to soft modes corresponding to distortions along the $[0\,1\,\bar{1}]$, $[0\,1\,1]$, and $[1\,0\,0]$ directions. 'puc' stands for 'per unit cell'. Blue and red signify low and high energy parts of the correction respectively. Each contour line represents an increase of 0.311 and 0.670 meV in (a) and (b) respectively. Note the strong similarities between (a) and (b) – both favour areas where $u_i u_j$ is positive, and penalise areas where $u_i u_j$ is negative.

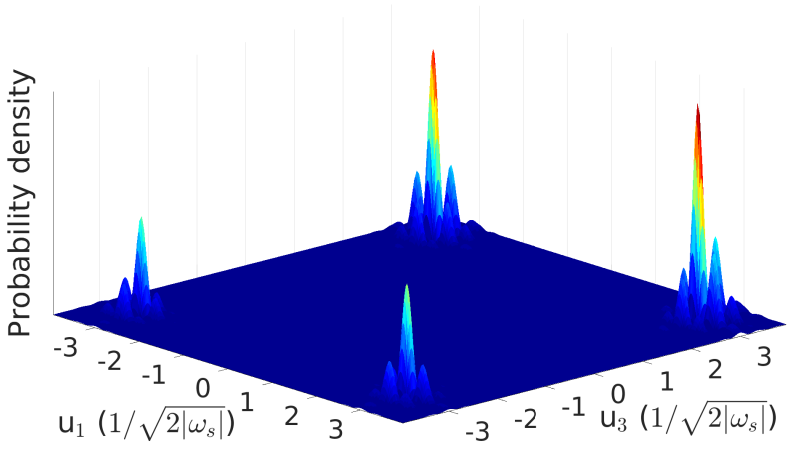

(a)

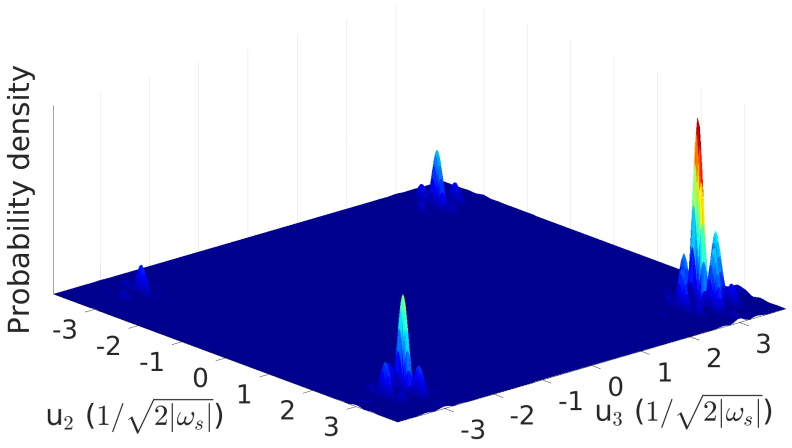

(b)

Figure 5.8: The calculated nuclear probability density at 5 K, shown in the two 2-D subspaces spanned by the three soft modes of cubic $BaTiO_3$. $\mathbf{q} \to \mathbf{0}$ along the x-axis. u_1, u_2, and u_3 relate to soft modes corresponding to distortions along the $[0\,1\,\bar{1}]$, $[0\,1\,1]$, and $[1\,0\,0]$ directions. Blue and red signify low and high probability density respectively. Note the significant differences between the 8 peaks visible in (a) and (b), resulting in a low symmetry state on average.

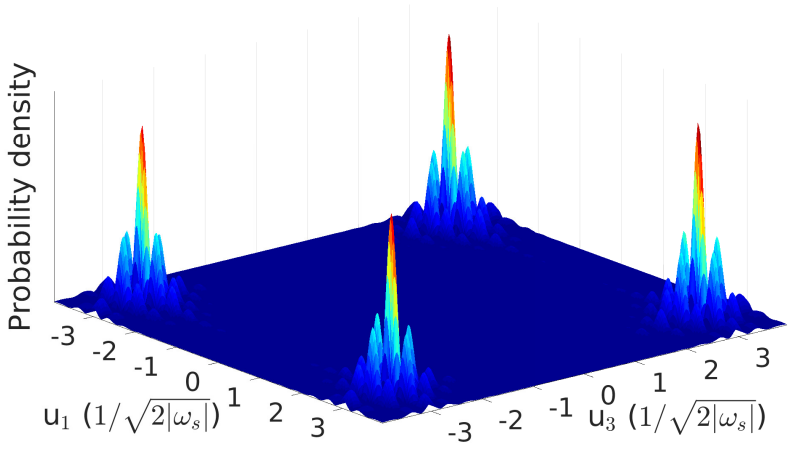

(a)

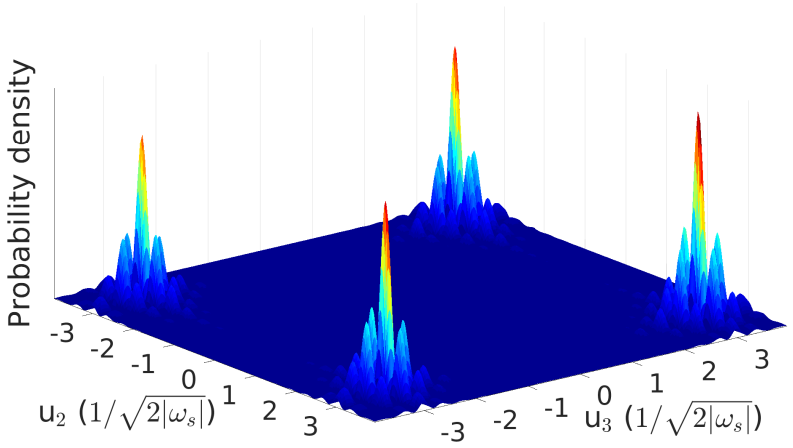

(b)

Figure 5.9: The calculated nuclear probability density at 6000 K, shown in the two 2-D subspaces spanned by the three soft modes of cubic $BaTiO_3$. $\mathbf{q} \to \mathbf{0}$ along the x-axis. u_1, u_2, and u_3 relate to soft modes corresponding to distortions along the $[0\,1\,\bar{1}]$, $[0\,1\,1]$, and $[1\,0\,0]$ directions. Blue and red signify low and high probability density respectively. Note the strong similarity of all 8 peaks visible in (a) and (b) – this results in a high symmetry state on average.

minimum or set of minima is preferred, to a disordered state, where all directions are equally likely, occurs. This is precisely as the order-disorder model of the ferroelectric phase transitions in $BaTiO_3$ predicts, and lends support to this picture of the material.

The high temperature calculations are performed at 6000 K, a much higher temperature than might be expected for seeing the transition from a low symmetry wavefunction to a higher symmetry one. This is because of the large energy spacing between the calculated anharmonic vibrational states of each of the soft modes, which is on the order of 0.1 eV. Up to around 300 K, this large energy spacing means that only the ground state is appreciably occupied, meaning that the probability density at 400 K is effectively identical to that at 5 K. Above this temperature, however, higher energy vibrational states begin to become excited, resulting in a rapid phase transition to the disordered state. This is shown clearly in Fig. 5.10, which shows how the vibrational average of the displacement of the Ti^{4+} ion in each of the Cartesian directions changes with temperature. Up to around 300 K, the displacement is essentially constant, but above this it rapidly decreases in magnitude, levelling off at a small value (around -0.002 Å) in each direction. This describes a continuous phase transition of the kind expected by the order-disorder picture. The transition temperature predicted by the calculations in this work is clearly significantly larger than that measured experimentally – this could be due to the errors inherent in DFT, the neglect of phonons not at the Γ-point, or other effects. The model also does not predict a series of phase transitions, as seen experimentally, instead only predicting a single transition from a low symmetry to a high symmetry state. However, the underlying physics described by these calculations is *qualitatively* in line with that of the order-disorder model, meaning this work constitutes the first fully first-principles description of the physics of phase transitions in $BaTiO_3$.

Although the nuclear probability density at low temperatures is clearly shared less evenly between the 8 minima than at high temperatures, it is not completely localised in one particular minimum, as might be expected in a description of the experimental rhombohedral phase. In Fig. 5.8, several different minima have corresponding regions of significant probability density, although some are more pronounced than others. This favouring of certain minima can be traced back to the original mapping of the BO surface, which resulted in some minima being slightly deeper than others. This asymmetry is unlikely to have arisen from the procedure used to fit the BO surface itself, as each direction is treated equivalently. This implies that the source of the asymmetry must

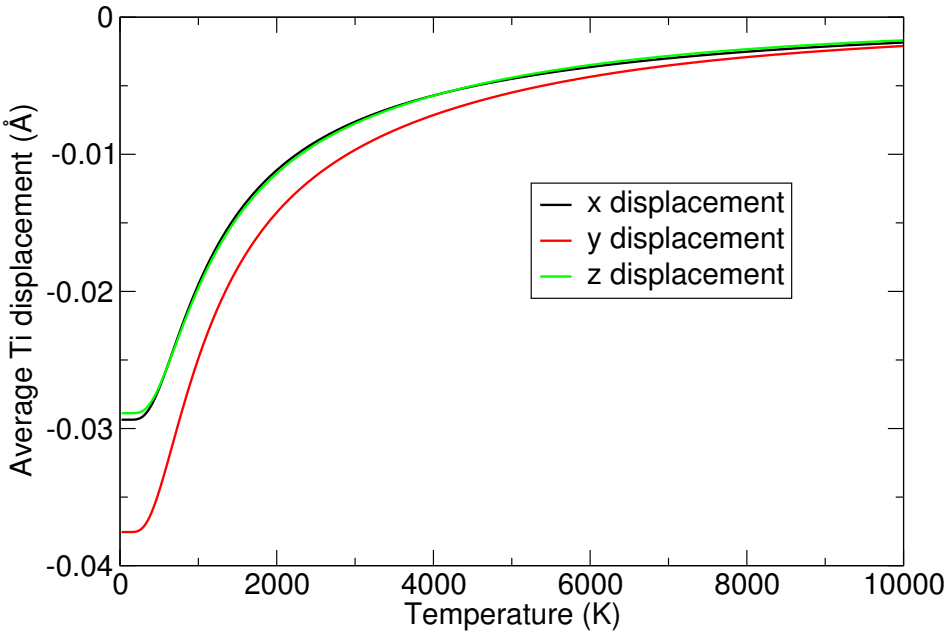

Figure 5.10: Vibrationally averaged displacement of the Ti^{4+} ion as a function of temperature. This displacement acts as an order parameter for the phase transition between the low and high symmetry states described by the order-disorder model. The three curves correspond to the x-,y-, and z-components of the displacement vector. Note the continuity and differentiability of the order parameter as a function of temperature, implying that this is a continuous phase transition.

be the mapping calculations themselves. As the unit cell used for the DFT calculations is also highly symmetrical, the source of this asymmetry in the BO surface requires further investigation – one possible source is small errors in the displacement patterns used for the soft modes. Small differences in the depth of the wells affect the shape of the wavefunction considerably, demonstrating that extremely accurate mapping calculations are necessary.

The results presented here show that the VSCF method can provide a qualitative first-principles description of the order-disorder model of phase transitions in $BaTiO_3$. To improve on this qualitative picture, we need a model that can describe not one, but all three phase transitions present experimentally, and that can bring the transition temperatures more into line with experimental values. To do this, it will be necessary to go beyond the level of theory included here, such as the interaction between Γ-point phonons and macroscopic polarisation. This could take the form of explicitly including (anti-)ferroelectric coupling between dipole moments in neighbouring unit cells, as previously explored in Ref. 216. This could be done by considering coupling between modes in a diagonal $2 \times 2 \times 2$ supercell, or the equivalent set of non-diagonal supercells. This would be a more expensive process than the calculations presented in this chapter, but should provide a more accurate description of the phase transitions in $BaTiO_3$. Including a three-dimensional term in the expansion of the BO surface corresponding to the coupling of all three Γ-point soft modes together would also provide a more accurate description of the phase transitions, but doing so becomes extremely expensive. Besides the much larger cost of mapping such a three-dimensional term, for small systems such as $BaTiO_3$ solving the VSCF equations becomes the more expensive part of the process, thanks to the large number of integrals that must be computed. Without further improvements in the efficiency of the VSCF method, this strategy is computationally unfeasible.

5.4 Summary

In this chapter, we have examined the problem of the ferroelectric phase transitions in barium titanate from first principles, using the VSCF method. As part of this work, we have introduced a more efficient method of computing the integrals required to solve the VSCF equations, using Clenshaw-Curtis quadrature. We have also included the effects of the interaction between Γ-point phonons and the macroscopic polarisation in this po-

lar material, a well-known effect that has never before been included in an anharmonic vibrational calculation. The mapped BO surface contains 8 different minima, giving support for the order-disorder picture of these phase transitions. The inclusion of the interaction between Γ-point phonons and macroscopic polarisation is found to lead to small but significant corrections to the BO surface. The calculated vibrational wavefunction demonstrates that we can qualitatively describe phase transitions in barium titanate from first principles. Each of the 8 minima corresponds to 8 equal regions of probability density at high temperature, which then become unequal at lower temperatures, leading to a phase transition. However, the level of theory used in this study is insufficient to obtain quantitative agreement with experimental data on the phase transitions of $BaTiO_3$. Further work is therefore required to obtain a full first-principles description of these phase transitions, but the first qualitative steps towards procuring this description have been taken here.

Part IV

Conclusions and Outlook

Chapter 6

Conclusions

6.1 Summary

In this thesis, several problems of significant interest within condensed matter physics have been studied, with the intention of better understanding the role of nuclear motion within these systems. We have moved beyond the typical harmonic approximation used to describe the motion of the nuclei by using a vibrational self-consistent field (VSCF) method, allowing anharmonic effects such as coupling between vibrational modes to be considered. The work presented here includes both development and application of this method to the systems of interest. The applications in particular focus on the effect of anharmonic vibrations on the structure of the material in question.

In Chapter 3, we demonstrated one method of improving the efficiency of the VSCF method, by making use of force data already readily available from DFT calculations. This means that less calculations are required to obtain the same accuracy of fit to the Born-Oppenheimer (BO) surface that the nuclei move in, reducing the computational cost of the method. This VSCF+f method was tested on a variety of different systems – molecular hydrogen, three structures of solid hydrogen under pressure, and the *bcc* phases of lithium and zirconium – and was found to give significant improvements over the basic VSCF method. The effect of the use of forces on the mapping of two-dimensional subspaces of the Born-Oppenheimer surface was also investigated, and was found to give a much smaller increase in efficiency.

In Chapter 4, we applied the VSCF method to the neutral vacancy in diamond, a system of technological interest. This point defect has long been known experimentally to exhibit a dynamic Jahn-Teller effect, maintaining the pristine tetrahedral point group, but first-principles calculations had thus far been unable to replicate this, predicting instead a tetragonal static Jahn-Teller distortion. By using the VSCF method to include anharmonic effects, in particular the coupling between the two soft modes present in the tetrahedral configuration, we were able to obtain the vibrational wavefunction and describe the dynamic Jahn-Teller effect from first principles, resulting in the resolution of this long-standing discrepancy between theory and experiment.

In Chapter 5, we applied the VSCF method to the well-known ferroelectric material barium titanate ($BaTiO_3$), in order to understand the series of phase transitions it undergoes from 400 K downwards. The nature of these phase transitions is still a matter of debate, with research supporting a displacive description, an order-disorder description, or a mixture of the two. The VSCF method was modified to include the

interaction between macroscopic polarisation and Γ-point phonons, and used to obtain the anharmonic nuclear probability density of the system at several temperatures, providing a qualitative description of phase transitions in barium titanate. The analysis of the results of these calculations moves the field towards the first truly first-principles description of the phase transitions of this important ferroelectric.

6.2 Outlook and Future Work

Using the work presented in this thesis as a starting point, several avenues of possible future research present themselves. To conclude, we will briefly explore these possibilities, concerning both the development of the VSCF method and its application to new and physically interesting systems.

Although the work presented in Chapter 3 constitutes a significant improvement in the efficiency of the VSCF method, more can still be done to reduce the computational cost of the mapping of the BO surface, and thus the overall method. One possible way of doing this would be to devise a procedure by which the most anharmonic phonon modes can be identified, before mapping commences. If only these modes were then mapped, this would constitute a significant decrease in the computational cost of the VSCF method. Such a procedure was defined in Chapter 4, but was based on physical intuition and the ability to compare the defect system in question to an extremely harmonic pristine structure. A more general method that does not rely on knowing the properties of the system in advance would be desirable.

Similarly, a procedure that would allow important couplings between modes to be identified before mapping the associated two-dimensional or higher subspaces would be extremely useful, especially in systems where the higher dimensional terms in the expansion of the BO surface are significant. In both Chapters 4 and 5, making such an identification was relatively easy, as it was clear that, physically, the soft modes present in both cases and the coupling between them must be the most important. In systems more like the solid hydrogen investigated in Chapter 3, however, a more general method would again be desirable. The computational expense of including higher dimensional terms in the BO surface expansion could also possibly be further reduced by extending the non-diagonal supercells method to include two-dimensional terms – in other words, using a smaller non-diagonal supercell that is commensurate with the $\mathbf{q}$ values of both vibrations, instead of a larger diagonal supercell.

Besides improving the efficiency of the VSCF method, it is important to apply the method to systems of physical interest where anharmonic effects are potentially important. This thesis has focused particularly on the effects of anharmonic vibrations on structure, and there are many other examples of systems where this may prove to be an important effect. Two examples are calcium silicate ($CaSiO_3$) and methylammonium lead iodide ($CH_3NH_3PbI_3$), both of which exhibit the perovskite structure, like barium titanate.

Calcium silicate is important in the Earth's lower mantle, where it is the third most common mineral by volume [242], but its structure under the high pressures and temperatures present deep within the Earth is unknown [243–250]. Different structures could potentially transmit seismic waves differently, having a knock-on effect in our understanding of earthquakes; understanding this material is therefore extremely important [243, 251–253]. Previous work has suggested that soft modes and anharmonicity have a potentially important role to play in determining whether the structure remains cubic or undergoes a distortion under lower mantle conditions [246, 254] – an excellent reason to apply the VSCF+f method to this system.

Methylammonium lead iodide is slightly different to most perovskite materials, in that the A cation is a molecular ion, methylammonium $CH_3NH_3^+$, which breaks the cubic symmetry and is able to rotate [255]. $CH_3NH_3PbI_3$ is the archetype of a recently discovered and very promising class of solar cell materials, organic-inorganic hybrid perovskites [186, 256]. Experiments have found these materials to provide solar cell efficiencies of over 20% [186, 257, 258], although they are somewhat unstable and contain lead, which is toxic [259–262]. The photovoltaic properties of $CH_3NH_3PbI_3$ rely on it being in its high-temperature, high-symmetry pseudo-cubic phase [263], in which the motion of the molecular ion averages out to give the usual cubic symmetry [264]. Applying the VSCF+f method to this system may therefore be able to shed some light on the importance of the molecular motion to the photovoltaic properties of methylammonium lead iodide.

Finally, and more generally, with the improvements in the efficiency of the method discussed above, it may become possible to include anharmonic vibrational effects more routinely. In particular, the calculation of anharmonic effects could be included as part of structure searching methods, such as *ab initio* random structure searching (AIRSS) [68]. From the work presented in Chapters 4 and 5, as well as the literature [76, 79, 83],

it can be seen that structures at saddle points in the BO surface can be stabilised by vibrational motion, and that if this is not included, structure searching methods may miss stable structures. This is particularly important when considering searching for stable structures at finite temperature, where the effect of vibrational motion is larger.

Part V

Appendices

Appendix A

Supplementary Material for Chapter 3

A.1 Pseudopotentials

All density functional theory calculations in Chapter 3 were performed using `CASTEP` version 8.0, and its own 'on-the-fly' ultrasoft pseudopotentials. The definition strings for the pseudopotentials were:

- H:

  ```
  1|0.6|1|6|10|10(qc=8)
  ```

- Li:

  ```
  1|1.0|14|16|18|10U:20(qc=7)
  ```

- Zr:

  ```
  3|2.1|7|8|9|40U:50:41:42
  ```

A.2 Equilibrium unit cell configurations

The unit cells for the structures used in this work, containing the atoms at their equilibrium positions, are given below in `.cif` file format.

- H_2

```
data_global

_cell_length_a      8.0000000
_cell_length_b      8.0000000
_cell_length_c      8.0000000
_cell_angle_alpha   90.0000000
_cell_angle_beta    90.0000000
_cell_angle_gamma   90.0000000

loop_
_atom_site_type_symbol
_atom_site_fract_x
_atom_site_fract_y
_atom_site_fract_z
```

```
_atom_site_U_iso_or_equiv
_atom_site_occupancy
H -0.0478791775 0.0000000000 0.0000000000 0.01 1.00
H 0.0478791775 0.0000000000 0.0000000000 0.01 1.00
```

- Solid hydrogen – *Cmca*-4 structure

```
data_global

_cell_length_a      1.6583232
_cell_length_b      1.6583232
_cell_length_c      2.5864026
_cell_angle_alpha   90.0000000
_cell_angle_beta    90.0000000
_cell_angle_gamma   119.1895730

loop_
_atom_site_type_symbol
_atom_site_fract_x
_atom_site_fract_y
_atom_site_fract_z
_atom_site_U_iso_or_equiv
_atom_site_occupancy
H 0.6288586141 0.3711413859 0.4499201931 0.01 1.00
H 0.8711413859 0.1288586141 0.9499201931 0.01 1.00
H 0.3711413859 0.6288586141 0.5500798069 0.01 1.00
H 0.1288586141 0.8711413859 0.0500798069 0.01 1.00
```

- Solid hydrogen – *Cmca*-12 structure

```
data_global

_cell_length_a      2.7673679
_cell_length_b      2.7673679
_cell_length_c      2.9356678
_cell_angle_alpha   90.0000000
_cell_angle_beta    90.0000000
_cell_angle_gamma   123.3367702

loop_
_atom_site_type_symbol
_atom_site_fract_x
```

```
_atom_site_fract_y
_atom_site_fract_z
_atom_site_U_iso_or_equiv
_atom_site_occupancy
H 0.9975714678 0.0024285322 0.1316877460 0.01 1.00
H 0.5024285322 0.4975714678 0.6316877460 0.01 1.00
H 0.0024285322 0.9975714678 0.8683122540 0.01 1.00
H 0.4975714678 0.5024285322 0.3683122540 0.01 1.00
H 0.8677974354 0.1322025646 0.4543868237 0.01 1.00
H 0.6322025646 0.3677974354 0.9543868237 0.01 1.00
H 0.1322025646 0.8677974354 0.5456131763 0.01 1.00
H 0.3677974354 0.6322025646 0.0456131763 0.01 1.00
H 0.7355833946 0.2644166054 0.3184257716 0.01 1.00
H 0.7644166054 0.2355833946 0.8184257716 0.01 1.00
H 0.2644166054 0.7355833946 0.6815742284 0.01 1.00
H 0.2355833946 0.7644166054 0.1815742284 0.01 1.00
```

- Solid hydrogen – *C2/c*-24 structure

```
data_global

_cell_length_a      2.9043932
_cell_length_b      5.1545051
_cell_length_c      2.9043932
_cell_angle_alpha   90.0818617
_cell_angle_beta    119.9030440
_cell_angle_gamma   90.0818617

loop_
_atom_site_type_symbol
_atom_site_fract_x
_atom_site_fract_y
_atom_site_fract_z
_atom_site_U_iso_or_equiv
_atom_site_occupancy
H 0.8643624666 0.1214632279 0.5001462745 0.01 1.00
H 0.1356375334 0.8785367721 0.4998537255 0.01 1.00
H -0.0001462745 0.3785367721 0.6356375334 0.01 1.00
H 1.0001462745 0.6214632279 0.3643624666 0.01 1.00
H 0.6165805121 0.1104506812 0.5217179301 0.01 1.00
H 0.3834194879 0.8895493188 0.4782820699 0.01 1.00
H 0.9782820699 0.3895493188 0.8834194879 0.01 1.00
```

```
H 0.0217179301 0.6104506812 0.1165805121 0.01 1.00
H 0.3099253065 0.1259861930 0.7571913283 0.01 1.00
H 0.6900746935 0.8740138070 0.2428086717 0.01 1.00
H 0.7428086717 0.3740138070 0.1900746935 0.01 1.00
H 0.2571913283 0.6259861930 0.8099253065 0.01 1.00
H 0.3386779374 0.1246038210 0.0289324391 0.01 1.00
H 0.6613220626 0.8753961790 0.9710675609 0.01 1.00
H 0.4710675609 0.3753961790 0.1613220626 0.01 1.00
H 0.5289324391 0.6246038210 0.8386779374 0.01 1.00
H 0.7978012899 0.1281915022 0.9726160204 0.01 1.00
H 0.2021987101 0.8718084978 0.0273839796 0.01 1.00
H 0.5273839796 0.3718084978 0.7021987101 0.01 1.00
H 0.4726160204 0.6281915022 0.2978012899 0.01 1.00
H 0.0717024691 0.1393502158 0.2130702123 0.01 1.00
H 0.9282975309 0.8606497842 0.7869297877 0.01 1.00
H 0.2869297877 0.3606497842 0.4282975309 0.01 1.00
H 0.7130702123 0.6393502158 0.5717024691 0.01 1.00
```

- Lithium – *bcc* structure

```
data_global

_cell_length_a      2.9760772
_cell_length_b      2.9760772
_cell_length_c      2.9760772
_cell_angle_alpha   109.4712206
_cell_angle_beta    109.4712206
_cell_angle_gamma   109.4712206

loop_
_atom_site_type_symbol
_atom_site_fract_x
_atom_site_fract_y
_atom_site_fract_z
_atom_site_U_iso_or_equiv
_atom_site_occupancy
Li 0.0000000000 0.0000000000 0.0000000000 0.01 1.00
```

- Zirconium – *bcc* structure

```
data_global
```

```
_cell_length_a      3.0959890
_cell_length_b      3.0959890
_cell_length_c      3.0959890
_cell_angle_alpha   109.4712206
_cell_angle_beta    109.4712206
_cell_angle_gamma   109.4712206

loop_
_atom_site_type_symbol
_atom_site_fract_x
_atom_site_fract_y
_atom_site_fract_z
_atom_site_U_iso_or_equiv
_atom_site_occupancy
Zr 0.0000000000 0.0000000000 0.0000000000 0.01 1.00
```

A.3 Harmonic mode displacement patterns

The displacement patterns corresponding to the mapping directions used in the mapping of 2-D subspaces of the BO surface of the *Cmca*-4 structure of solid hydrogen are given below. They correspond to the displacement patterns of harmonic modes with frequencies of 69.4, 74.0 and 114 meV, labelled as 4, 5 and 7 respectively. Each row shows the displacement of a H atom in the three Cartesian directions, in the same order as the atoms are listed in their equilibrium configuration above.

- Direction 4:

```
x     y     z
0.00  0.75 -1.00
0.00  0.75  1.00
0.00 -0.75  1.00
0.00 -0.75 -1.00
```

- Direction 5:

```
x  y  z
0  1  0
0 -1  0
0  1  0
0 -1  0
```

- Direction 6:

```
x     y     z
0.00  0.33 -1.00
0.00 -0.33 -1.00
0.00 -0.33  1.00
0.00  0.33  1.00
```

- Direction 7:

```
 x  y  z
 1  0  0
-1  0  0
-1  0  0
 1  0  0
```

- Direction 9:

```
 x  y  z
-1  0  0
-1  0  0
 1  0  0
 1  0  0
```

Appendix B

Supplementary Material for Chapter 4

B.1 Pseudopotentials

All density functional theory calculations performed in Chapter 4 used `CASTEP` version 7.0.3, and its own 'on-the-fly' ultrasoft pseudopotential for carbon. The definition string for the pseudopotential was

```
2|1.4|1.4|1.3|6|10|12|20:21(qc=6).
```

B.2 Equilibrium positions

The equilibrium positions of the 255 atoms in the tetrahedral symmetry structure with the experimental lattice constant are given below in atomic units. Each line corresponds to the position of a different atom. The 4 nearest neighbours of the vacancy are the 1st, 37th, 41st and 69th atoms listed.

x	y	z
-0.125046099000000	-0.125046099000000	-0.125046099000000
-5.05730941300000	5.05680823200000	5.05680823200000
-6.74434100100000	6.74353252700000	6.74353252700000
-11.7996474160000	11.8169519130000	11.8169519130000
-1.66435433200000	1.68866773300000	5.03468089300000
-3.38383346800000	3.37602318100000	6.75416002900000
-8.43031378000000	8.43182053100000	11.8006403410000
-10.1177808130000	10.1173547230000	13.4881073740000
1.68866773300000	-1.66435433200000	5.03468089300000
6.801117000000000E-003	6.801117000000000E-003	6.73427809500000
-5.05757258200000	5.05667219300000	11.7977613810000
-6.74234342200000	6.74218005500000	13.4829899650000
5.05680823200000	-5.05730941300000	5.05680823200000
3.37602318100000	-3.38383346800000	6.75416002900000
-1.68474223200000	1.68597040600000	11.7953777110000
-3.37050123800000	3.37061378000000	13.4816107730000
6.74353252700000	-6.74434100100000	6.74353252700000
1.68597040600000	-1.68474223200000	11.7953777110000
7.285570000000000E-004	7.285570000000000E-004	13.4809798620000
-5.05340710100000	5.05387142400000	18.5379784370000
5.05667219300000	-5.05757258200000	11.7977613810000
3.37061378000000	-3.37050123800000	13.4816107730000
-1.68474223200000	1.68435615500000	18.5375613390000
-3.36863626100000	3.36864284000000	20.2234862990000

```
  8.43182053100000        -8.43031378000000         11.8006403410000
  6.74218005500000        -6.74234342200000         13.4829899650000
  1.68435615500000        -1.68474223200000         18.5375613390000
 1.632600000000000E-005  1.632600000000000E-005    20.2221360660000
  11.8169519130000        -11.7996474160000         11.8169519130000
  10.1173547230000        -10.1177808130000         13.4881073740000
  5.05387142400000        -5.05340710100000         18.5379784370000
  3.36864284000000        -3.36863626100000         20.2234862990000
 -1.66435433200000         5.03468089300000         1.68866773300000
 -3.38383346800000         6.75416002900000         3.37602318100000
 -8.43031378000000         11.8006403410000         8.43182053100000
 -10.1177808130000         13.4881073740000         10.1173547230000
-0.125046099000000         3.49537266000000         3.49537266000000
 -5.05773654200000         8.42806310300000         8.42806310300000
 -6.74471634700000         10.1150429080000         10.1150429080000
  5.03468089300000        -1.66435433200000         1.68866773300000
  3.49537266000000       -0.125046099000000         3.49537266000000
 -1.68648167100000         5.05680823200000         8.42763597400000
 -3.37320596600000         6.74353252700000         10.1146675620000
  6.75416002900000        -3.38383346800000         3.37602318100000
  1.68516328100000         1.68516328100000         8.42088731300000
 1.632600000000000E-005    3.37031023500000         10.1108029840000
 -5.05193076300000         8.42225732400000         15.1666373530000
  5.05680823200000        -1.68648167100000         8.42763597400000
  3.37031023500000        1.632600000000000E-005    10.1108029840000
 -1.68381866900000         5.05414523000000         15.1667797970000
 -3.36700653300000         6.73733309400000         16.8531206430000
  8.42806310300000        -5.05773654200000         8.42806310300000
  6.74353252700000        -3.37320596600000         10.1146675620000
  1.68516328100000         1.68516328100000         15.1664695250000
 7.285430000000000E-004    3.36959801800000         16.8519591740000
  11.8006403410000        -8.43031378000000         8.43182053100000
  10.1150429080000        -6.74471634700000         10.1150429080000
  5.05414523000000        -1.68381866900000         15.1667797970000
  3.36959801800000        7.285430000000000E-004    16.8519591740000
  13.4881073740000        -10.1177808130000         10.1173547230000
  8.42225732400000        -5.05193076300000         15.1666373530000
  6.73733309400000        -3.36700653300000         16.8531206430000
  1.68516328100000         1.68516328100000         21.9120517360000
  1.68866773300000         5.03468089300000        -1.66435433200000
 6.801117000000000E-003    6.73427809500000        6.801117000000000E-003
```

```
 -5.05757258200000        11.7977613810000        5.05667219300000
 -6.74234342200000        13.4829899650000        6.74218005500000
  5.03468089300000         1.68866773300000       -1.66435433200000
  3.49537266000000         3.49537266000000      -0.125046099000000
 -1.68648167100000         8.42763597400000        5.05680823200000
 -3.37320596600000        10.1146675620000         6.74353252700000
  6.73427809500000       6.801117000000000E-003  6.801117000000000E-003
  1.68165882800000         5.03468089300000        5.03468089300000
-5.696607000000000E-003    6.75416001600000        6.75416001600000
 -5.06149397000000        11.8006403410000        11.8006403410000
  5.03468089300000         1.68165882800000        5.03468089300000
  3.36352544400000         3.36352544400000        6.73427806800000
 -1.68634564500000         8.42789915700000        11.7977613940000
 -3.37185349400000        10.1126699830000         13.4829899650000
  8.42763597400000        -1.68648167100000        5.05680823200000
  6.75416001600000       -5.696607000000000E-003   6.75416001600000
  1.68435615500000         5.05506879300000        11.7953777110000
-2.872060000000000E-004    6.74082778600000        13.4816107870000
  11.7977613810000        -5.05757258200000        5.05667219300000
  10.1146675620000        -3.37320596600000        6.74353252700000
  5.05506879300000         1.68435615500000        11.7953777110000
  3.36959800400000         3.36959800400000        13.4809798890000
  13.4829899650000        -6.74234342200000        6.74218005500000
  8.42789915700000        -1.68634564500000        11.7977613940000
  6.74082778600000       -2.872060000000000E-004   13.4816107870000
  1.68597040600000         5.05506879300000        18.5375613390000
  11.8006403410000        -5.06149397000000        11.8006403410000
  10.1126699830000        -3.37185349400000        13.4829899650000
  5.05506879300000         1.68597040600000        18.5375613390000
  3.37031023500000         3.37031023500000        20.2221360660000
  5.05680823200000         5.05680823200000       -5.05730941300000
  3.37602318100000         6.75416002900000       -3.38383346800000
 -1.68474223200000         11.7953777110000        1.68597040600000
 -3.37050123800000         13.4816107730000        3.37061378000000
  6.75416002900000         3.37602318100000       -3.38383346800000
  1.68516328100000         8.42088731300000        1.68516328100000
 1.632600000000000E-005    10.1108029840000        3.37031023500000
 -5.05193076300000         15.1666373530000        8.42225732400000
  5.03468089300000         5.03468089300000        1.68165882800000
  3.36352544400000         6.73427806800000        3.36352544400000
 -1.68634564500000         11.7977613940000        8.42789915700000
```

```
 -3.37185349400000         13.4829899650000         10.1126699830000
  8.42088731300000         1.68516328100000         1.68516328100000
  6.73427806800000         3.36352544400000         3.36352544400000
  1.68499545200000         8.42937548100000         8.42937548100000
-1.487824000000000E-003    10.1142996970000         10.1142996970000
  11.7953777110000        -1.68474223200000         1.68597040600000
  10.1108029840000         1.632600000000000E-005   3.37031023500000
  5.05099246400000         5.05099246400000         8.41981227400000
  3.36864284000000         6.73896282200000         10.1094527500000
  13.4816107730000        -3.37050123800000         3.37061378000000
  8.42937548100000         1.68499545200000         8.42937548100000
  6.73896282200000         3.36864284000000         10.1094527500000
  1.68516328100000         8.42581640300000         15.1664695250000
  11.7977613940000        -1.68634564500000         8.42789915700000
  10.1142996970000        -1.487824000000000E-003   10.1142996970000
  5.05414523000000         5.05414523000000         15.1661592520000
  3.37061375300000         6.74082779900000         16.8513282760000
  15.1666373530000        -5.05193076300000         8.42225732400000
  13.4829899650000        -3.37185349400000         10.1126699830000
  8.42581640300000         1.68516328100000         15.1664695250000
  6.74082779900000         3.37061375300000         16.8513282760000
  6.74353252700000         6.74353252700000        -6.74434100100000
  1.68597040600000         11.7953777110000        -1.68474223200000
 7.285570000000000E-004    13.4809798620000        7.285570000000000E-004
 -5.05340710100000         18.5379784370000         5.05387142400000
  5.05680823200000         8.42763597400000        -1.68648167100000
  3.37031023500000         10.1108029840000        1.632600000000000E-005
 -1.68381866900000         15.1667797970000         5.05414523000000
 -3.36700653300000         16.8531206430000         6.73733309400000
  8.42763597400000         5.05680823200000        -1.68648167100000
  6.75416001600000         6.75416001600000       -5.696607000000000E-003
  1.68435615500000         11.7953777110000         5.05506879300000
-2.872060000000000E-004    13.4816107870000         6.74082778600000
  11.7953777110000         1.68597040600000        -1.68474223200000
  10.1108029840000         3.37031023500000        1.632600000000000E-005
  5.05099246400000         8.41981227400000         5.05099246400000
  3.36864284000000         10.1094527500000         6.73896282200000
  13.4809798620000        7.285570000000000E-004   7.285570000000000E-004
  8.41981227400000         5.05099246400000         5.05099246400000
  6.73658989700000         6.73658989700000         6.73658989700000
  1.68485300800000         11.7974875760000         11.7974875760000
```

```
 11.7953777110000        1.68435615500000        5.05506879300000
 10.1094527500000        3.36864284000000        6.73896282200000
 5.05387141100000        8.42373364900000        11.7949606260000
 3.37002201800000        10.1108050190000        13.4810190380000
 15.1667797970000       -1.68381866900000        5.05414523000000
 13.4816107870000      -2.872060000000000E-004   6.74082778600000
 8.42373364900000        5.05387141100000        11.7949606260000
 6.73733310800000        6.73733310800000        13.4798183930000
 18.5379784370000       -5.05340710100000        5.05387142400000
 16.8531206430000       -3.36700653300000        6.73733309400000
 11.7974875760000        1.68485300800000        11.7974875760000
 10.1108050190000        3.37002201800000        13.4810190380000
 5.05667219300000        11.7977613810000       -5.05757258200000
 3.37061378000000        13.4816107730000       -3.37050123800000
-1.68474223200000        18.5375613390000        1.68435615500000
-3.36863626100000        20.2234862990000        3.36864284000000
 8.42806310300000        8.42806310300000       -5.05773654200000
 6.74353252700000        10.1146675620000       -3.37320596600000
 1.68516328100000        15.1664695250000        1.68516328100000
7.285430000000000E-004   16.8519591740000        3.36959801800000
 11.7977613810000        5.05667219300000       -5.05757258200000
 10.1146675620000        6.74353252700000       -3.37320596600000
 5.05506879300000        11.7953777110000        1.68435615500000
 3.36959800400000        13.4809798890000        3.36959800400000
 13.4816107730000        3.37061378000000       -3.37050123800000
 8.42937548100000        8.42937548100000        1.68499545200000
 6.73896282200000        10.1094527500000        3.36864284000000
 1.68516328100000        15.1664695250000        8.42581640300000
 11.7953777110000        5.05506879300000        1.68435615500000
 10.1094527500000        6.73896282200000        3.36864284000000
 5.05387141100000        11.7949606260000        8.42373364900000
 3.37002201800000        13.4810190380000        10.1108050190000
 15.1664695250000        1.68516328100000        1.68516328100000
 13.4809798890000        3.36959800400000        3.36959800400000
 8.42356970200000        8.42356970200000        8.42356970200000
 6.73696524300000        10.1081002780000        10.1081002780000
 18.5375613390000       -1.68474223200000        1.68435615500000
 16.8519591740000       7.285430000000000E-004   3.36959801800000
 11.7949606260000        5.05387141100000        8.42373364900000
 10.1081002780000        6.73696524300000        10.1081002780000
 20.2234862990000       -3.36863626100000        3.36864284000000
```

15.1664695250000	1.68516328100000	8.42581640300000
13.4810190380000	3.37002201800000	10.1108050190000
8.42225732400000	8.42225732400000	15.1663016960000
8.43182053100000	11.8006403410000	-8.43031378000000
6.74218005500000	13.4829899650000	-6.74234342200000
1.68435615500000	18.5375613390000	-1.68474223200000
1.632600000000000E-005	20.2221360660000	1.632600000000000E-005
11.8006403410000	8.43182053100000	-8.43031378000000
10.1150429080000	10.1150429080000	-6.74471634700000
5.05414523000000	15.1667797970000	-1.68381866900000
3.36959801800000	16.8519591740000	7.285430000000000E-004
13.4829899650000	6.74218005500000	-6.74234342200000
8.42789915700000	11.7977613940000	-1.68634564500000
6.74082778600000	13.4816107870000	-2.872060000000000E-004
1.68597040600000	18.5375613390000	5.05506879300000
11.7977613940000	8.42789915700000	-1.68634564500000
10.1142996970000	10.1142996970000	-1.487824000000000E-003
5.05414523000000	15.1661592520000	5.05414523000000
3.37061375300000	16.8513282760000	6.74082779900000
15.1667797970000	5.05414523000000	-1.68381866900000
13.4816107870000	6.74082778600000	-2.872060000000000E-004
8.42373364900000	11.7949606260000	5.05387141100000
6.73733310800000	13.4798183930000	6.73733310800000
18.5375613390000	1.68435615500000	-1.68474223200000
16.8519591740000	3.36959801800000	7.285430000000000E-004
11.7949606260000	8.42373364900000	5.05387141100000
10.1081002780000	10.1081002780000	6.73696524300000
20.2221360660000	1.632600000000000E-005	1.632600000000000E-005
15.1661592520000	5.05414523000000	5.05414523000000
13.4798183930000	6.73733310800000	6.73733310800000
8.42399683100000	11.7948245730000	11.7948245730000
18.5375613390000	1.68597040600000	5.05506879300000
16.8513282760000	3.37061375300000	6.74082779900000
11.7948245730000	8.42399683100000	11.7948245730000
10.0974727890000	10.0974727890000	13.4756096100000
11.8169519130000	11.8169519130000	-11.7996474160000
10.1173547230000	13.4881073740000	-10.1177808130000
5.05387142400000	18.5379784370000	-5.05340710100000
3.36864284000000	20.2234862990000	-3.36863626100000
13.4881073740000	10.1173547230000	-10.1177808130000
8.42225732400000	15.1666373530000	-5.05193076300000

6.73733309400000	16.8531206430000	-3.36700653300000
1.68516328100000	21.9120517360000	1.68516328100000
11.8006403410000	11.8006403410000	-5.06149397000000
10.1126699830000	13.4829899650000	-3.37185349400000
5.05506879300000	18.5375613390000	1.68597040600000
3.37031023500000	20.2221360660000	3.37031023500000
15.1666373530000	8.42225732400000	-5.05193076300000
13.4829899650000	10.1126699830000	-3.37185349400000
8.42581640300000	15.1664695250000	1.68516328100000
6.74082779900000	16.8513282760000	3.37061375300000
18.5379784370000	5.05387142400000	-5.05340710100000
16.8531206430000	6.73733309400000	-3.36700653300000
11.7974875760000	11.7974875760000	1.68485300800000
10.1108050190000	13.4810190380000	3.37002201800000
20.2234862990000	3.36864284000000	-3.36863626100000
15.1664695250000	8.42581640300000	1.68516328100000
13.4810190380000	10.1108050190000	3.37002201800000
8.42225732400000	15.1663016960000	8.42225732400000
18.5375613390000	5.05506879300000	1.68597040600000
16.8513282760000	6.74082779900000	3.37061375300000
11.7948245730000	11.7948245730000	8.42399683100000
10.0974727890000	13.4756096100000	10.0974727890000
21.9120517360000	1.68516328100000	1.68516328100000
20.2221360660000	3.37031023500000	3.37031023500000
15.1663016960000	8.42225732400000	8.42225732400000
13.4756096100000	10.0974727890000	10.0974727890000

B.3 Soft mode displacement patterns

The displacement patterns of the two soft modes, labelled by u_1 and u_2 in the main text, are given below in atomic units. Each line corresponds to the displacement of a different atom. The 4 nearest neighbours of the vacancy are the 1st, 37th, 41st and 69th atoms listed.

- u_1

x	y	z
-1.286412451253704E-003	-2.386261164627135E-004	1.555073843168644E-003
-2.576362541502554E-004	1.203718177984954E-004	-8.023499603283071E-005
-1.089750370697337E-004	6.710079083857408E-005	1.628040504329516E-005

```
-1.043379114630177E-004  3.490527602037540E-004  1.008377882770519E-003
-3.898809657141529E-004  2.103833543211643E-005 -6.538257553567O8E-004
-1.635748563537825E-004  2.365073173755346E-005 -3.090555346817120E-004
 5.898208014207576E-005 -6.046371808333979E-005  2.963528565771877E-005
 1.726928121517416E-004 -1.207492715461922E-004  1.222220957548132E-004
 1.101412532144252E-004  3.415463862441808E-004 -1.001828756921255E-003
 1.056464447464681E-004  2.108200106668805E-004 -7.571655719767719E-004
 6.012072967183886E-005 -5.629843966177005E-005 -7.510025035681626E-005
 1.172469705511506E-004 -9.080252542085448E-005 -1.376481467794462E-005
 1.681322661267275E-004 -5.213959465478351E-005 -1.478822874411587E-004
 1.171653173210187E-004  2.178275139931153E-004 -5.173455397459988E-004
 5.635978131948092E-005  7.987911845093600E-006 -1.757559640526633E-004
 7.981468818574673E-005 -4.106276589436978E-005 -6.868713427010986E-005
 5.081778120430244E-005 -2.514098879975399E-005 -2.824494116917624E-005
 7.892344537098551E-006  1.003544996810327E-004 -1.875237890625604E-004
 5.046613184416915E-005  6.773376995105335E-005 -9.257884910033286E-005
 1.118422519110848E-004 -6.581025897890245E-005  7.719759641323916E-005
-1.027704354464536E-004  1.295892376485903E-004 -1.102223448171852E-004
-5.601725717391492E-005  1.285970524375329E-004 -8.154937234513330E-005
 5.677768155372575E-005 -8.625697509332229E-006  1.725414913412176E-004
 7.786234729880981E-005 -5.732579787315664E-005  2.189314690258018E-004
-3.243437642788936E-004  1.045409433515147E-004 -4.841993973977878E-005
-2.329744392929114E-004  1.578564715480133E-004 -4.987316957576347E-005
-8.688928094945433E-006  1.009054614264414E-004  1.845738531699109E-004
 1.159133164137295E-005  3.893560541238735E-005  3.103586333591639E-004
-3.901403617696795E-004 -1.885096938720741E-005  6.540765205259165E-004
-6.322926723176578E-004  2.253876543256137E-004 -3.912837639412729E-005
-1.088241314058121E-004  1.413953228757839E-004  1.095394461478105E-004
-6.073686339517340E-005  1.510221192065414E-004  2.584782978996776E-004
-9.987398408224776E-004  6.154293821872280E-004 -1.253611210907542E-004
-5.312698628257785E-004  3.581330241601140E-004 -1.326112828738835E-004
-7.625610062608931E-005  1.091783329386158E-004  3.888914552905971E-004
-1.042825485172728E-004  2.112979179721830E-004  7.556913679625830E-004
-1.296261019201879E-003  2.522130469679143E-004 -1.546329266250995E-003
-2.039399881520675E-005  6.045786143896394E-006 -2.325224474146879E-005
 6.619982921494930E-005 -1.145737443886275E-005  8.011177168830330E-005
 1.002055612092973E-003 -6.182144677513459E-004 -1.221236314908345E-004
 1.310751336547820E-003 -2.659578018917467E-004 -1.531232228676602E-003
-3.601055781285230E-005 -7.958310169389229E-005 -3.094033055741213E-004
 3.269940512343447E-005 -6.043779088253969E-005 -1.337500328896154E-004
 5.348323798452762E-004 -3.609915006169821E-004 -1.298738224950781E-004
```

```
 1.038475232491444E-006 -1.064287664996301E-006 -4.938803727396052E-004
 1.295386530194087E-005 -3.997149916257939E-005 -3.123873788152929E-004
 3.328718534537105E-004 -2.590897825164345E-004 -2.280857207168678E-005
 4.229433767910622E-005  7.351829141647400E-005 -3.076024180811569E-004
-1.090532690822112E-005  3.770429397172370E-005 -3.123527098850976E-004
 1.139337117857592E-004 -1.234793935002850E-004  1.612580531324560E-006
 1.985003819429232E-004 -1.818471337556229E-004  2.928306978528667E-005
 2.365801665173875E-005 -7.398349160916385E-006 -2.256913784812341E-005
-2.954202207323713E-005  5.809475482384339E-005 -1.352258660025058E-004
-5.095538554608004E-007  3.678893986466484E-007 -2.260228888314870E-006
 5.128704673076641E-005 -6.803816776601236E-005  8.891966807475224E-005
 7.586459104251779E-005 -1.088330457084633E-004  3.890648791712031E-004
-6.565552210106771E-005  1.143302419493383E-005  8.089885350188295E-005
-1.142746799690792E-004  1.239513436914022E-004  1.626869535465444E-006
-5.215547373383090E-005  6.867629854889015E-005  8.880475526528701E-005
 1.031576453990382E-004 -2.111318141247637E-004  7.554238922418739E-004
-3.317294263544916E-004  2.585316248726696E-004 -2.307892295079628E-005
-1.979981486339747E-004  1.819520890786670E-004  2.909306431538532E-005
-6.385116830445827E-007  1.285842648347446E-007  4.920451473353678E-004
 1.040622888865675E-004 -3.479053450545002E-004  1.007027642060124E-003
-1.722659335641350E-004  1.216162714250822E-004  1.206682506584732E-004
-1.117826527333342E-004  6.589292136085923E-005  7.708337029653354E-005
-7.864557357658975E-005  5.772846221729218E-005  2.188424620322675E-004
 3.874508914138350E-004  1.808221994777262E-005  6.558197688065563E-004
 1.282439408852158E-003  2.378935138712563E-004  1.556532658550539E-003
-1.648211590108647E-004  5.116633607978165E-005 -1.514680372371430E-004
-4.884157473450774E-005  2.404323170366711E-005 -2.986564326142321E-005
 6.315825784576862E-004 -2.255691801868544E-004 -3.769697982119952E-005
-1.065917891979717E-004 -3.456897855273656E-004 -1.006083156841695E-003
-1.147627416310400E-004 -2.218027479783858E-004 -5.213785575897489E-004
 3.236866087299138E-004 -1.040967776828459E-004 -4.848896517197000E-005
 3.946785770787769E-004 -2.467503441547198E-005 -6.490016163140253E-004
-1.037733956612838E-004 -2.127006198384219E-004 -7.570305776848674E-004
 1.030224467168084E-004 -1.294729398336533E-004 -1.104646356544120E-004
 2.326349187857914E-004 -1.574079647741322E-004 -5.004991696345027E-005
 2.602807307884299E-004 -1.242525522592861E-004 -7.560075382756650E-005
 1.683801575312831E-004 -2.629922591188523E-005 -3.046218850530436E-004
-8.311263290937311E-006 -1.000975602904336E-004 -1.877300182078511E-004
 5.562609767455566E-005 -1.278844896948050E-004 -8.166497240911216E-005
 1.104369283329648E-004 -1.413874561545387E-004  1.095029846821069E-004
 1.153395918117432E-004 -6.847740135982651E-005  1.822032055912195E-005
```

```
-5.686645229332732E-005 -8.003273035886819E-006 -1.756410400675502E-004
-5.140781109130770E-005 -6.718840553285841E-005 -9.273182679948228E-005
 6.090958706311901E-005 -1.506427964396857E-004  2.585481431316146E-004
-5.966064739040702E-005  5.646702283392159E-005 -7.483967075046352E-005
-8.029699654394837E-005  4.142495227863124E-005 -6.874672994991835E-005
 7.948494379447947E-006 -1.002729256358147E-004  1.845077761121462E-004
-5.878960402958443E-005  6.158804713101860E-005  2.967417072733932E-005
-1.171155532572907E-004  9.163816488236429E-005 -1.358148122205538E-005
-5.779061649316588E-005  9.153535042030734E-006  1.722949230900014E-004
-1.285408895886495E-005 -3.880178583338430E-005  3.100922528789925E-004
 3.704290551736255E-005 -7.857467469819882E-005  3.092073890367121E-004
 1.121294297402082E-004 -2.244746588215456E-004  5.229438706674951E-004
-7.221378622389351E-005  4.579900488906460E-005 -7.020606092782308E-007
-8.305115756967205E-005  3.180221902789514E-005  2.779676701006577E-005
 1.614643101936553E-004  2.164064495874218E-005  3.115078458543914E-004
-1.537684814784771E-006  7.878664749452080E-005 -9.029395898394565E-009
-4.238826398320875E-005  4.998602981126339E-005 -3.226098639947483E-005
 5.040430243455879E-005  7.163685884496015E-006  1.478036699504104E-004
 9.921235947116954E-004  6.082365562097712E-004  1.289169781251660E-004
 1.696970731427836E-004  1.212367510794209E-004 -1.204694012163065E-004
 4.692610827758800E-005 -3.066462151251772E-005 -8.010403332200027E-005
 1.635842918059729E-004 -4.178674219032844E-005 -3.328385625712016E-005
 4.105335819730518E-004 -2.140965581809313E-006  1.648801559166906E-006
 6.311818158156748E-004  2.215619983068457E-004  4.071330046993373E-005
-2.425531788132279E-005 -1.821807621141921E-004 -3.110301133296938E-004
 2.020145323852914E-005 -1.410691827948693E-004 -1.721858731553067E-004
 1.598366295754351E-004 -1.028207222690974E-004 -5.147292872664138E-006
 2.587016078180407E-004 -4.696555162895721E-005  4.510986231777770E-007
-7.617351580424169E-005 -1.083853778629291E-004 -3.914252682710417E-004
-6.149758741707195E-005 -1.497807381640635E-004 -2.611881884540112E-004
 7.425272860123648E-005 -1.282219313028588E-004  5.418091005539714E-005
 5.413851367234896E-005 -6.983076100592807E-006 -1.468619995499069E-004
-7.737804362048704E-005 -5.619318582140021E-005 -2.211459410942124E-004
-3.441816034376304E-007 -1.322620703430083E-004 -9.406088669658218E-007
 4.937682499782067E-005 -3.081299440963646E-005  2.032406808937680E-005
-5.655488075460430E-006  2.276056623133101E-006 -5.216321398290832E-005
-1.136246319995628E-004 -1.217769389322771E-004 -4.847763884287406E-006
-5.542368945150065E-005 -1.276495130211776E-004  7.929857834324736E-005
 2.345090086879608E-005 -1.839759938239647E-004  3.095419490307761E-004
-1.871404858224091E-006 -1.632762014580108E-005  8.004557109571871E-005
-8.463125036437791E-005  9.459374231502460E-007 -1.300782433414331E-006
```

```
-8.064147212525300E-005 -3.959236674919432E-005  6.585178911147143E-005
-3.185750382114971E-005 -6.091747060049762E-005  1.382164122136761E-004
-7.158538839368807E-007  1.275011588537668E-005  4.570738160537129E-005
-3.150712832099464E-005  1.485710156619580E-005  1.274933067833526E-005
-6.095658742599635E-005 -5.551884913874064E-005  7.395515471458681E-005
 1.585389533952024E-004  4.798716974540764E-005  1.557884373416241E-004
 3.929047254274189E-005  4.950333662874269E-005  3.219029473612297E-005
-3.298074488160446E-005  2.437606338864720E-006  4.919275846648698E-006
-8.043187317469581E-006 -1.357000354108721E-006  5.171309320356445E-005
 2.571921513520415E-004  1.123885314974725E-004  8.647863214969862E-005
 5.259001426133223E-004  3.515473205285839E-004  1.344774902987829E-004
-6.516635217506886E-007  1.329089499693042E-005 -4.820824570997250E-005
 9.834309182941222E-006 -3.944839282356804E-006 -5.055494247673398E-005
 1.389003554315575E-004 -4.957424612523177E-006 -2.881077765144652E-005
 2.586442651135270E-004  4.268972168150719E-005  3.123588262138124E-006
 5.791641880809136E-005  6.201668777201368E-005 -3.082149489227022E-005
 8.684510729781292E-007 -1.534724698212460E-005 -8.213777897433681E-005
 7.415783055169281E-005 -6.225721890440095E-005 -3.524203748117816E-005
 3.234036004608903E-004  1.042296607535445E-004  4.800835732590079E-005
 6.595779403656964E-005  1.286145555233803E-005 -8.100698783074184E-005
-1.263554788744180E-006 -1.061732738124712E-004 -9.204804025731880E-005
 1.393454740266877E-004  5.172164641670958E-006  2.757981348399807E-005
 1.646518950035909E-004  4.285335756105436E-005  3.222380446260784E-005
-1.117438420872346E-004 -1.396851854508349E-004 -1.105754213034190E-004
-7.584539496835074E-005 -1.274886888734596E-004 -5.593146120948325E-005
-8.262210241947488E-008 -1.068003694308508E-004  8.981976280966277E-005
 5.188002629769452E-005 -2.951360185132357E-005  4.445841848059342E-005
-1.108382123178778E-004 -6.391818578175668E-005 -7.834990545431442E-005
-1.969933613967619E-004 -1.786112677249891E-004 -3.152606798613379E-005
-1.026088532128614E-004 -1.299137724939296E-004  1.098769639874082E-004
-2.123670939751862E-005 -1.422667794799518E-004  1.702083101766321E-004
-3.167145972415333E-005 -5.792918163970306E-007 -6.862450182219162E-006
-8.243845833377897E-005 -2.994347389509089E-005 -2.986534408412891E-005
-4.800090389892971E-005 -3.278294008086127E-005  7.843019879669771E-005
-1.089380918594185E-005 -4.766510428440621E-006  4.775023371086334E-005
-7.164563963604206E-005 -4.398703781066242E-005 -9.304204175364138E-007
-1.171825131630087E-004 -8.983326599518758E-005  1.227446171344320E-005
 2.253359870473654E-005  3.112102542458828E-006  2.575372838056337E-005
 4.682922080895648E-005  1.974849889238045E-005  3.113028285475277E-005
-3.715428831697712E-007  1.041333614750830E-006 -1.488350005773475E-006
-3.173241235596331E-005 -1.307238344439824E-005 -1.497535453315485E-005
```

```
 4.913274998780670E-005  2.995272371539097E-005 -2.117638676101578E-005
 1.193196072661328E-004  6.294017176922644E-005 -1.398528708465536E-005
 7.096575829859156E-005  4.544418497330511E-005 -1.230280850325240E-006
 3.068955763978255E-005  1.487877626968194E-005 -1.535823431145920E-005
 5.168797069255254E-005  2.974532664595987E-005 -4.647474341180609E-005
 3.284475939301688E-004  2.557293122736928E-004  2.235443898680267E-005
 1.162589714656379E-004  9.110244250855391E-005  1.254507733498644E-005
-6.550414743970433E-007  6.195823336168356E-007 -5.041062666593795E-005
 1.596703997234965E-004  1.031875943993383E-004  4.651385517596555E-006
 2.312891036625733E-004  1.578172272183952E-004  4.953452799090737E-005
-5.047018207287256E-005 -2.938820489847041E-005 -2.154239543509314E-005
-5.309221823182204E-005 -2.885680673122401E-005 -4.676723398323858E-005
-8.040687476837934E-007  6.613366799076912E-007 -1.066907256587930E-006
 7.451383492230467E-005  6.345897886927573E-005  3.357938649427372E-005
-2.315258409585861E-005 -4.508253831692363E-006  2.707147205826213E-005
-1.199191493737118E-004 -6.398566236474510E-005 -1.477771378982343E-005
-1.610995061471673E-004 -1.019936469829452E-004  3.903446067876206E-006
-7.575558849741464E-005 -6.201218287602831E-005  3.315717924655673E-005
 4.780043311169651E-005  3.293452478980977E-005  7.880271373625889E-005
-4.675061885924172E-005 -2.337688278110618E-005  3.256141578527409E-005
-2.328408072993351E-004 -1.566087703183470E-004  4.882597141648904E-005
 1.388495930114922E-007  8.266895242941213E-007  4.769103500776709E-005
 1.101396960465747E-005  5.906336788057702E-006  4.801856972109206E-005
-3.299252960762464E-004 -2.548546666138986E-004  2.220774156714682E-005
-3.245906465088643E-004 -1.037395426436136E-004  4.754865910072339E-005
-1.651852891028176E-004 -4.223890975967755E-005  3.162085944093269E-005
 9.522368834870175E-007 -1.126090374344074E-005  4.550321088007488E-005
-3.861282510388579E-005 -4.856698404744149E-005  3.327074460901439E-005
-5.856855999219469E-005 -6.089849311626460E-005 -3.070626603639155E-005
-6.686217666020681E-005 -1.243000930173205E-005 -8.121370622226187E-005
 3.176657397759598E-005  1.925298948591955E-006 -7.696724997024447E-006
 3.132833330647013E-005 -1.320877693033275E-005  1.237780378588393E-005
-1.940464728765963E-006  1.630847910353214E-005 -8.147003638582967E-005
 1.098552765588094E-004  6.377095192884590E-005 -7.935052641981752E-005
 8.167834505389168E-005  3.080200625733799E-005 -3.067488268824902E-005
-1.663700184029446E-007 -1.172821557480144E-005 -4.766228476403776E-005
 1.103494466362712E-004  1.402153641052825E-004 -1.101227911906095E-004
 1.956023196661159E-004  1.793990389375534E-004 -3.147487158524380E-005
 3.161641548720634E-005 -9.483029645017380E-007  4.737547008844589E-006
-1.097831509954679E-005  5.358245352044990E-006 -5.026770564185250E-005
-1.081630170577971E-007  1.068888494395468E-004 -9.129096991561451E-005
```

```
 7.452620913891097E-005  1.285318274409183E-004 -5.524661724970602E-005
 5.983286700286620E-005  5.610912824269320E-005  7.520377568125856E-005
 6.205930315931459E-006  2.455762285657819E-006  5.145948324085859E-005
-1.402901979727174E-004  5.640955045054247E-006 -2.895578180725770E-005
-7.556784427307401E-005  6.314374029588505E-005 -3.501334710300154E-005
 1.011185783149677E-004  1.310342195048797E-004  1.111147165733462E-004
 3.067273672266281E-005  6.071151291921031E-005  1.424259995194344E-004
-2.597289174898306E-004 -4.310082721005205E-005  1.546281565163910E-006
-6.211447021542805E-007  1.083320466686192E-004  9.011661036433322E-005
 2.045029550300388E-005  1.435513571613114E-004  1.707644452451283E-004
-2.588863850194140E-004 -1.151490576253818E-004  8.331337967349324E-005
-1.401391700555622E-004 -4.228225080597795E-006  2.705501761676470E-005
-5.177700099468163E-005  3.129532728668842E-005  4.415944481427859E-005
-1.570517385117494E-004 -4.784600969074622E-005  1.581379009700681E-004
-5.269080398010804E-004 -3.520990699812354E-004  1.340736930684990E-004
-9.932808302937864E-004 -6.085852553483991E-004  1.286654343438908E-004
-6.317579178923554E-004 -2.225052819721737E-004  3.961770058954999E-005
-4.753783944733416E-005  3.211583966031902E-005  1.910834977539590E-005
 2.561452895386362E-006  1.775606367141094E-005  7.945258614302806E-005
-1.689705856580535E-004 -1.207124955639077E-004 -1.197397079723399E-004
-5.275672713163481E-005  7.063748440459922E-006 -1.491241838485930E-004
 6.670199935779282E-006 -1.366046965847157E-006 -5.360729890820396E-005
 2.152396427908318E-006 -7.795182714742824E-005  1.240439343887306E-006
 7.581862727288626E-005  1.084255459296074E-004 -3.915763612997925E-004
 7.688762461531943E-005  5.634732175409661E-005 -2.218774174591230E-004
 7.191226823321811E-005 -4.445249992794317E-005 -6.629007592376658E-007
 4.307512707822344E-005 -4.892312016598391E-005 -3.086349504624672E-005
 2.391287966001984E-005  1.813301257657469E-004 -3.089545042165223E-004
 6.063885436884086E-005  1.500236317164263E-004 -2.606320352319516E-004
 8.370117090394175E-005 -3.237045394828584E-007 -1.397270224353641E-006
 8.228009060512334E-005 -3.077853582465272E-005  2.763238255066818E-005
-4.747513901387904E-005  3.113264342538887E-005 -7.922597235172167E-005
-2.098423216709731E-005  1.410120988657988E-004 -1.708047961968818E-004
 1.122846250508065E-004  1.225945327833090E-004 -4.548472230117181E-006
 7.939974429213642E-005  4.022709565186046E-005  6.642220252146170E-005
-1.648170768820632E-004  4.235457243496752E-005 -3.300907232707483E-005
-4.844677354308442E-007  1.333593288481890E-004 -4.165335167642119E-007
 5.404553797398561E-005  1.287035007287008E-004  7.987109729963578E-005
-5.225539680879097E-005 -6.721376212752777E-006  1.473489825748549E-004
-1.606843540293420E-004  1.035464239411465E-004 -5.266917089932960E-006
-7.449890518015619E-005  1.292583695371356E-004  5.457154243951419E-005
```

```
-3.847425705580973E-005  7.828787761917852E-005  3.100531005635068E-004
-1.638056330102249E-004 -2.184285790313907E-005  3.101650959025538E-004
-4.112310265415339E-004  1.623751833696926E-006  1.064534349173637E-007
-2.591792673088629E-004  4.636755264017321E-005 -1.203886749014720E-006
-2.350628423376248E-005  1.851749389284525E-004  3.097782312456366E-004
-1.123414221079336E-004  2.251152571421197E-004  5.242229337964993E-004
```

- u_2

```
 x                       y                       z
-1.041184821833900E-003  1.637107745166548E-003 -6.046937675633113E-004
-2.051978261477660E-004 -1.173087437431191E-004  1.318974072799559E-004
-9.147238773737234E-005 -2.786122340358557E-006  5.940044216365037E-005
-8.510030108242575E-005  9.531597200463947E-004  1.297079538094370E-004
-9.288430934640068E-004 -1.394391411762581E-004  7.692997140905918E-004
-5.010045931216402E-004 -1.468350788501986E-004  4.284502562228111E-004
-9.073819392694878E-005  4.124137941086784E-004  1.043356759973663E-004
-1.451487023758395E-004  8.017903686434247E-004  1.904823548063941E-004
 8.670426738717946E-005  9.499832546356273E-004 -1.249072677955838E-004
-1.978227388996553E-004  7.376487815325731E-005  2.956042580230873E-004
-1.266577567692024E-004  9.049250273880833E-005  8.131887059362448E-005
-1.060058552119730E-004  2.452437435327211E-004  5.940962684513597E-005
 2.323001974022481E-006  3.286049946113079E-004 -4.472198034533529E-005
 9.064401654966429E-005  4.821620893050949E-004 -1.076490422015087E-004
-8.711516087151532E-005 -2.750307945028381E-006  8.677250312274502E-005
-1.035905451238485E-004  3.825071483213176E-005  4.679932111170883E-005
-4.365209950722518E-005  1.497063797930516E-004 -5.512979394034499E-005
-3.834711356332604E-006  2.531541363901257E-005  5.630676710358759E-005
-4.532351856283299E-005 -1.180455341163167E-006  3.701968239489868E-005
-8.820307482707876E-005  9.393049516171072E-005 -7.591604613910610E-005
-2.785700951727610E-005  5.247867576928107E-005 -8.623003433138517E-006
-2.975320835771124E-007  2.152882187403374E-005  1.327029076779802E-005
-8.803531671616765E-005  3.961789427608362E-006 -8.400803582062416E-005
-1.391633675921622E-004  2.914235221158007E-005 -1.425666694464223E-004
-2.620358777499217E-004  2.666685714831976E-005 -9.634984069646264E-005
-1.185598853959588E-004 -1.995022958202251E-006 -3.367687193605828E-005
 2.414650167261184E-006  2.566306079580422E-005 -5.345577526305525E-005
-4.495363344881266E-005  2.561336846099821E-005 -1.202789992624736E-004
-9.362419019915716E-004  1.330199183733855E-004 -7.763586716673761E-004
-5.072890899965863E-004 -1.084127319859047E-005 -2.227511613043004E-004
-2.451607921740593E-005 -1.183112641019699E-005  4.790173131490733E-006
 1.689970947651754E-005  4.871430477453763E-005 -4.183777148486112E-005
```

```
-1.711346714475833E-004 -8.123357075706664E-004  4.400117852523567E-005
-4.404397173923987E-005 -4.020102227627053E-004  4.813625025646295E-005
 7.720611847770565E-005  5.973573259077649E-006 -1.513514261810361E-004
 1.982924388094449E-004  7.703471215843155E-005 -2.942299359973515E-004
-1.014295799968142E-003 -1.662986534947625E-003  5.807442657926331E-004
-1.487636199363795E-005 -2.968853071309538E-005  6.977604205181463E-006
 5.412624002298994E-005  8.391761561559281E-005 -3.207382742585371E-005
 1.773975451150540E-004  8.068240978673221E-004  5.022565078763818E-005
 1.042245763771501E-003  1.635810581179730E-003  6.104139767095900E-004
-1.499978063320178E-004 -1.478474456203144E-004  1.179746084479062E-004
-5.254863912677689E-005 -2.219823605617795E-005  5.118881250500267E-005
 5.050933018849861E-005  3.964426225177136E-004  5.319233606358388E-005
 1.726428248815076E-006 -2.266301998793697E-006  1.929821898051157E-004
-4.262163564897348E-005 -2.685432989576596E-005  1.221163055498790E-004
-2.113118985575118E-005  2.096828729114643E-004  9.314854495488079E-006
 1.617235670931973E-004  1.356831576638213E-004  1.222994211347438E-004
 4.590846801201024E-005  2.214064635989542E-005  1.223966404553422E-004
-5.972917469520119E-005  3.478199855495447E-005  1.136124099903171E-007
-5.301071436221774E-005  9.617307430037216E-005 -1.046509120785358E-005
 1.960164809338298E-005  2.812996949598632E-005  9.809026235093662E-006
 5.756920596529825E-005  1.756844664613066E-005  5.162607644505180E-005
-1.372153691115571E-006  5.505312454000921E-007  1.852876885322385E-006
-4.597353102770276E-005  2.809510454104105E-006 -3.376593367013814E-005
-7.835695461511612E-005 -5.147302293464836E-006 -1.508447045231500E-004
-5.392247962402058E-005 -8.423925577321884E-005 -3.044766166791351E-005
 5.797334568904755E-005 -3.444298804292171E-005  3.637558761946102E-007
 4.355602865198300E-005 -1.728429254317976E-006 -3.387664066943864E-005
-1.988644585950542E-004 -7.514871878065192E-005 -2.946398054830893E-004
 2.231151304675319E-005 -2.115975265929718E-004  8.952949773839174E-006
 5.278632720957819E-005 -9.663332892650866E-005 -1.077287165567205E-005
-4.027752271052436E-007  1.214745750660096E-006 -1.915804585145530E-004
 8.755984717975412E-005 -9.477551782395299E-004  1.237459481069993E-004
 1.466346614891993E-004 -8.005456986283247E-004  1.868187023314344E-004
 8.722875111101853E-005 -9.312590750863368E-005 -7.710281229206439E-005
 1.370566966594567E-004 -2.816000246697603E-005 -1.433549744107854E-004
 9.351429102401607E-004 -1.320476453570155E-004 -7.766382321032389E-004
 1.045942015120060E-003 -1.628086591050416E-003 -6.138111710160055E-004
 5.413399328232745E-006 -3.303922755754699E-004 -5.371561388716264E-005
 4.716378033051994E-005 -1.472762890081576E-004 -5.958596207528739E-005
 5.059499568231910E-004  1.097448910232424E-005 -2.206717068980815E-004
-7.921090160160371E-005 -9.590565096757045E-004 -1.345305175057258E-004
```

```
-8.588661103867622E-005 -4.905848411553717E-004 -1.167418010126543E-004
 2.600046939065434E-004 -2.629411095689312E-005 -9.678281928716737E-005
 9.371335350266147E-004  1.328280220614756E-004  7.779705243719986E-004
 2.011782899539093E-004 -7.772015763290785E-005  2.956986898020662E-004
 2.711140989826096E-005 -5.320273448677047E-005 -1.023094521867553E-005
 1.167888494526810E-004  1.828769253967714E-006 -3.459368554795441E-005
 2.083064644085818E-004  1.118837041237677E-004  1.384704017993445E-004
 5.091442841287933E-004  1.416892076931115E-004  4.366889602739483E-004
 2.514577579151559E-006 -2.528766956002639E-005  5.583475548142789E-005
-1.607863856301206E-006 -2.096284852117710E-005  1.258883485636234E-005
 2.519555416830609E-005  1.178901386947910E-005  4.817094350107574E-006
 9.840575286111719E-005  8.820087730414285E-007  6.277237498524636E-005
 8.540028825968884E-005  2.286857312793724E-006  8.717449589027752E-005
 4.293889644611316E-005  1.906821793380285E-006  3.680006795924296E-005
-1.771702861387148E-005 -4.773170247641010E-005 -4.201213361380439E-005
 1.266231339244015E-004 -9.066746139917457E-005  8.285640638255180E-005
 1.016785389327315E-004 -3.800250510627910E-005  4.715327485144010E-005
-4.369186133676033E-006 -2.420386201610338E-005 -5.370297271915924E-005
 9.053960114926051E-005 -4.111057744249044E-004  1.042046286792816E-004
 1.055229720224681E-004 -2.446375896210209E-004  5.993602638741968E-005
 8.556779950451801E-005 -2.535807773609510E-006 -8.458004060065423E-005
 4.404857965770383E-005 -2.321883683046675E-005 -1.207875465553956E-004
 1.580119778132419E-004 -1.379936063402960E-004 -1.223522699579283E-004
 9.189318377287983E-005 -4.801511014118739E-004  1.062142586576702E-004
 7.387273529248795E-005 -1.874545756853375E-004  7.960397580673441E-006
 9.940491856869918E-005 -7.654815058687146E-005 -4.853186696586522E-005
 5.073226780785263E-004 -1.407809184681051E-004 -4.360547737176646E-004
 2.348743705027089E-006 -5.211678993243580E-004 -2.182506197689003E-006
 2.416194593493401E-005 -3.287004492976749E-004 -3.514255740529196E-005
 3.268443908100489E-004 -2.702696226031818E-005 -2.969480316690787E-004
 1.808986516957928E-004 -8.020060352197988E-004 -5.221236702051966E-005
-1.423541981150148E-004 -8.008511591466631E-004 -1.909795000922149E-004
 9.596962651439522E-005 -1.077043835890033E-004 -1.166969102373864E-004
 2.016266681031865E-004 -4.311565518858481E-005 -1.544749499527560E-004
 3.293959650220474E-004  1.216713197089760E-006  1.325573245544868E-007
 5.065009897021008E-004 -8.858874843647348E-006  2.207121546422665E-004
-1.641325951597726E-005 -2.789659526845758E-004 -1.203341341965877E-004
 1.825112702574074E-005 -1.458105896448011E-004 -1.095981734941599E-004
 1.063529785425649E-004 -5.414408506328326E-006 -5.162442829459757E-006
 2.076785022534476E-004  1.272112984273031E-005  4.615495499974554E-005
 7.739049082018335E-005 -6.322579098424414E-006  1.533348285688565E-004
```

```
 1.670401299337400E-005 -4.910341960324322E-005  4.330759814079373E-005
 3.507608893570240E-005 -1.688285984191531E-005  1.706535911553999E-005
 3.272429582075371E-004  2.740912908752076E-005  2.990288961629123E-004
 1.364784680464363E-004  2.748268646877564E-005  1.459083584285440E-004
-1.436165576964900E-006 -1.956816123644555E-005  3.393682603337359E-009
 1.019332170430659E-004 -1.019876801265957E-004  1.406080556585837E-004
 2.025770331226226E-004 -2.827782070313672E-005  1.976299545983500E-004
 5.651900922547655E-005  3.415980074708302E-005  1.992838756853783E-006
-1.753900501915363E-006 -2.037164391240079E-005 -1.179989955069705E-005
 1.638927135666864E-005 -2.737081542853484E-004  1.174265730072083E-004
 6.132578371886025E-005 -2.594857157673430E-004  1.366508302864948E-004
 1.038324803655791E-004 -9.425272821248423E-008  1.220262404903159E-006
 1.012044792390726E-004  3.769343796840941E-005 -4.531783574683015E-005
 5.529501579841916E-005 -1.773465440517584E-005 -5.909292144567481E-005
 7.535230500632683E-006 -1.919209176861950E-004  9.315270524319099E-005
 5.827582328071220E-005 -9.468554770155001E-005  6.703813524797634E-005
 1.260647263250155E-004  9.082023463821584E-005 -8.286555454918660E-005
 8.281035865771432E-006 -3.259130191912284E-004  3.967066410974671E-005
-1.931290639040653E-005 -3.284894239005292E-004  3.080277225102304E-005
 1.222960270936466E-004  1.910254630397124E-006 -1.264518668223912E-004
 2.016328354487579E-004  2.964891734555723E-005 -1.953811767340019E-004
 2.069556188179127E-004 -1.088998428936682E-004 -1.394187825981333E-004
 5.312139003999563E-005 -3.923577070530135E-004 -5.377324675519550E-005
-7.661059385806668E-006 -1.922838778779375E-004 -9.175374800147685E-005
 5.457962418028661E-005 -8.168153892659493E-005 -1.196720327509413E-004
 1.319467658538854E-004 -4.362570934220158E-006 -9.897770738188946E-005
 2.071886555697753E-004 -1.032846512080022E-005 -4.591734957652604E-005
-9.059628345450711E-005 -4.114869763256476E-004 -1.035319883682524E-004
-6.149088494829358E-005 -2.611743733720276E-004 -1.353752025993929E-004
 5.890020816062948E-005 -2.154804862178476E-005 -5.728488408827255E-005
 2.598730895441231E-004  2.707884764809589E-005  9.747833782987966E-005
 5.304790304534043E-005 -8.477295639878370E-005  3.216187435520065E-005
-1.443849568523911E-007 -6.944272039973371E-005 -8.978849154807513E-005
 1.321816402821029E-004  5.753393215810291E-006  1.004167662108456E-004
 2.016100634202463E-004  4.329988362868568E-005  1.555657075634788E-004
-2.481409004472738E-005  1.095496021215624E-005 -4.525092099064691E-006
-3.705008540856036E-005 -1.757655685368558E-005 -1.725268020303145E-005
-2.572768375968327E-006 -6.750213230750072E-005  8.971143412932950E-005
 6.366026942525217E-005 -4.672284472488628E-005  1.227507295113153E-004
 8.558192913904350E-005  9.133357314463931E-005  7.908110587862736E-005
 5.025789374961631E-005  9.487714195948713E-005  1.247719596736118E-005
```

```
-2.959983426967984E-005 -5.087566218407956E-005  8.117050824936452E-006
-2.020459432481295E-005 -1.423277927284672E-004  1.077488048197282E-004
 1.227868391583390E-004 -5.804796013500774E-007  1.291940862529145E-004
 9.902065433761131E-005  7.691177660333569E-005  5.133830068517658E-005
-9.640932442936050E-005 -1.066927359457880E-004  1.159911695789677E-004
-5.556033083089656E-005 -8.160121934493313E-005  1.210531246700258E-004
 7.303715641125168E-005  1.888271473611742E-004 -6.193610376103987E-006
 1.045265646029402E-004  2.454229727604605E-004 -5.885189099410454E-005
 1.744818463254225E-005 -2.729384051457444E-005 -1.256120356933344E-005
-4.202692476745821E-005 -1.493787032559243E-004  5.319725493544128E-005
-1.048307020612616E-006  1.280701157881776E-006  1.301558461791166E-006
 5.758020056691293E-005  9.674768275827844E-005 -6.429894781460850E-005
 9.976499427382899E-005  1.044390922736148E-004 -1.385133425075535E-004
 9.135886965846445E-005  1.264901374412998E-006 -6.330192096030602E-005
-7.474740035014900E-005 -1.868846353767131E-004 -6.950458789488185E-006
-5.984655715753321E-005 -9.438546094062527E-005 -6.475437438436902E-005
 6.261544209981490E-005  4.901529068919937E-005 -1.206548523316651E-004
-2.019299952447442E-005 -2.066609792161586E-004 -8.642908280615632E-006
-1.062570823968874E-004 -2.433331364442509E-004 -5.838965476233543E-005
-1.187580783350673E-006  6.492680715711490E-007 -1.242870216018965E-004
 1.059781709318308E-004  7.080923878408429E-006  6.233784107230350E-006
 1.167539120757397E-004 -5.313197920534704E-007  3.534981166092206E-005
-1.011253306408600E-004 -1.043009921200459E-004 -1.384309520892393E-004
-6.531631085183622E-005 -4.858265359524233E-005 -1.210152830771561E-004
-2.155548267843863E-006  7.506400980019253E-007  7.388469231400186E-007
 5.878913097297235E-005  2.286623527945095E-005  5.856577611379739E-005
-1.608706878469633E-005  2.531152948985265E-005 -9.652584082137192E-006
-8.842559375924503E-005 -2.428589455998528E-006 -6.351749672936476E-005
-1.093179138390834E-004 -5.285056289549124E-006  4.934980995582161E-006
-6.228487268179407E-005 -2.081668927981205E-005  5.766203704493870E-005
 9.581627181802361E-005  1.061831401753655E-004  1.171467606784608E-004
 4.383808750293861E-005  1.413205329427138E-004  5.712216488575834E-005
-1.198193196764068E-004  2.678049917001684E-006  3.393698675887986E-005
-3.505255960223145E-007  8.413617032159423E-007  1.264666604667245E-004
 5.499882631582642E-005  8.250862119918063E-005  1.217572630449941E-004
 1.837968738479103E-005  2.090356388423142E-004 -8.740001891999147E-006
-2.624067576508934E-004 -2.633659570546408E-005  9.661316338542725E-005
-2.033933418997668E-004 -4.266395716218657E-005  1.543275138822007E-004
-7.947398736329547E-006  1.936679647110770E-004  9.333071320091345E-005
 2.113412329614266E-005  3.295343294654805E-004  3.419036967470477E-005
 8.962546955837253E-005  4.129818649770472E-004 -1.031962066417173E-004
```

```
-5.428275208109978E-005  8.566289592816429E-005  3.130799468936113E-005
-1.236086254519955E-004  2.090199131662074E-006  1.275985644884316E-004
-5.948488947023546E-005  9.658008552980284E-005  6.657197439896766E-005
 5.991820949301744E-005  2.619863272192528E-004 -1.343693146905997E-004
-8.749337091111406E-005 -9.202260868792729E-005  7.695731563745467E-005
-1.011327447012894E-004 -7.603487124421036E-005  4.977154060038949E-005
 6.166585592887208E-006  1.942156073350956E-004 -9.079089989929574E-005
 2.312178369052398E-005 -9.933549471921784E-006 -3.680700959196070E-006
-5.247306877908826E-005 -9.322299610222643E-005  1.247526908453434E-005
-1.249480078188435E-004  5.040017875823740E-008 -1.261424899964933E-004
-5.673865112841369E-005  8.370225743322248E-005 -1.189279184360081E-004
-3.119109066308173E-006  6.964334953346990E-005 -8.807588632114531E-005
 3.411533125814106E-005  1.886880577800656E-005 -1.581059393778568E-005
-1.279982918783728E-004 -8.953651160294660E-005 -8.055237249598626E-005
-2.044060810323761E-004 -2.813424699180927E-005 -1.947726816647287E-004
-1.351639034576110E-004  5.013284000376710E-006 -9.894320509281516E-005
-6.255274256557337E-005  2.214293385921012E-005 -5.654923866375490E-005
 2.702565030659535E-005  5.310204261592470E-005  1.042854924345979E-005
-5.518119789855555E-005  1.920494617807454E-005 -5.309010718745659E-005
-2.094309636346623E-004  9.918584706404400E-006 -4.784924096675649E-005
-2.264601964278487E-008  6.980637447454785E-005  9.070490675273650E-005
 1.805430246244403E-005  1.448676161084555E-004  1.097490683965422E-004
-2.082067048305712E-004  1.062064755664377E-004 -1.423908550753411E-004
-1.347531560711945E-004 -4.621857125469964E-006  9.957974081410932E-005
-6.504831406965112E-005  4.904066608613454E-005  1.223927352285944E-004
-2.577124528172077E-006  3.266691533983914E-004  4.706909139062900E-005
-5.192246005758514E-005  3.935870382767872E-004 -5.256738931035616E-005
-1.800557432359653E-004  8.034982643989111E-004 -5.025476653127312E-005
-5.076739768279839E-004  7.261951506143709E-006  2.196160321656746E-004
-1.007279624805824E-004  1.037519360729879E-004  1.388027484170908E-004
-6.130738902009462E-005  2.615301225044334E-004  1.363223289295537E-004
 1.444396167155308E-004  8.013622994551431E-004 -1.882955253669678E-004
-3.255988049539444E-004 -2.757566457628069E-005  2.946834946588007E-004
-2.019705086708286E-004  2.927039338579358E-005  1.947462493279463E-004
-6.077203043750350E-007  5.222060210574534E-004  1.340013841596725E-006
-7.817364453317112E-005  6.102560465799594E-006  1.529223427372517E-004
-1.379829137228847E-004 -2.759162329659459E-005  1.443730397842202E-004
-7.510476980860317E-005  1.890278826052200E-004  8.318102443449771E-006
-2.229118374405526E-005  3.301019750496201E-004 -3.143583145640377E-005
 1.583220093457968E-005  2.762509338398054E-004 -1.159039948856705E-004
-1.821621923794563E-005  4.924885715533568E-005  4.436948958701113E-005
```

```
-1.064121688230527E-004  1.012255253326762E-006  1.085105200829455E-006
-1.016650193733421E-004  7.812927955677654E-005 -4.811648455351104E-005
-9.724088545811686E-005  1.088083792699548E-004 -1.148328277956829E-004
-2.041340391160671E-005  1.446014736997556E-004 -1.063159836610601E-004
-5.936353144472908E-005 -3.262633809048953E-005  2.554406097650789E-006
-1.040139729705454E-004 -3.639314711165743E-005 -4.434004924202720E-005
-2.043495080944857E-004  4.382407678664722E-005 -1.536429469778012E-004
-1.246557520372200E-006  2.097484535181630E-005  1.135806422343458E-006
-1.259946282636534E-006  2.215797753312868E-005 -1.074540046639814E-005
-3.292874330878562E-004  2.783193010974153E-005 -2.960619672764758E-004
-1.091077278539531E-004  5.888550891478962E-006 -4.901524187139410E-006
-3.713968881637178E-005  1.818045960687907E-005  1.790096163183937E-005
-1.559183400092810E-004  1.422592713878085E-004 -1.196180393286312E-004
-5.079959585217721E-004  1.423511438396550E-004 -4.353420701633613E-004
-3.309575427556529E-004 -1.931021616219745E-006 -1.817411116002246E-006
-2.093550053870188E-004 -1.375184870209034E-005  4.401216499900147E-005
-1.688854064804159E-005  2.767457551835793E-004  1.193701927761663E-004
-9.063417058921109E-005  4.843281755835614E-004  1.115421378714973E-004
```

B.4 Born-Oppenheimer energy surface slices

Fig. B.1 shows two cross-sections of the BO surface in the subspace spanned by the two soft modes of the tetrahedral structure. Fig. B.1(a) shows a slice running from one of the three minima of the surface to the opposite high point. Fig. B.1(b) shows a slice that runs from one minimum to an adjacent minimum. In the atomic units used, $1/\sqrt{2|\omega|} = 52$ a.u. for both soft modes.

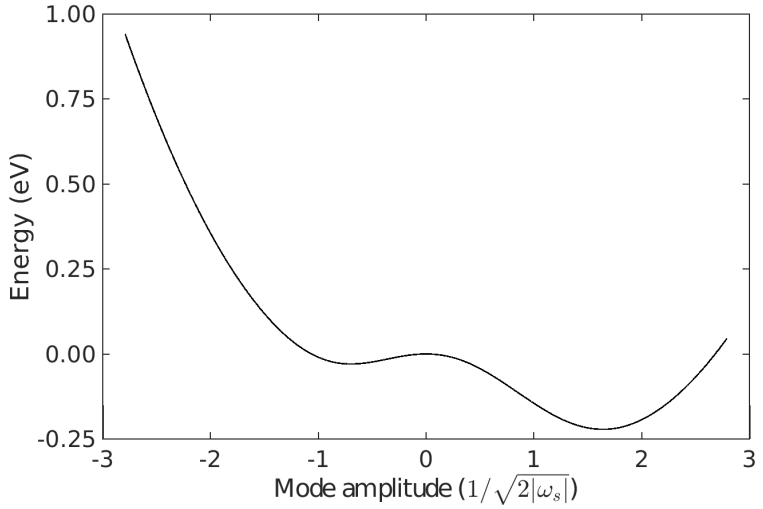

(a)

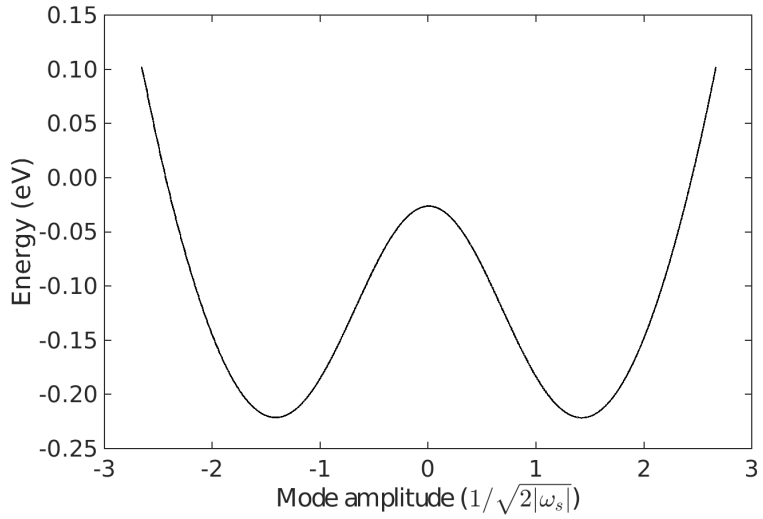

(b)

Figure B.1: Slices through the BO surface in the plane spanned by the two soft modes of the tetrahedral structure. The slice in (a) runs through one minimum and the origin, also passing through the high point of the graph opposite. The slice in (b) runs through two adjacent minima. In (b), the point midway between the two minima is taken as the zero point of the mode amplitude.

Appendix C

Supplementary Material for Chapter 5

C.1 Pseudopotentials

All density functional theory calculations in Chapter 5 were performed using `CASTEP` version 16.1, and its own 'on-the-fly' norm-conserving pseudopotentials. The definition strings for the pseudopotentials were:

- O:

  `1|1.2|23|26|31|20N:21L(qc=9)`

- Ti:

  `3|1.8|15|17|19|30N:40N:31N:32N(qc=7)`

- Ba:

  `2|2.0|8|10|11|50N:60N:51N(qc=5.5)`

C.2 Cubic unit cell configuration

The unit cell for the cubic perovskite structure of $BaTiO_3$ used as the reference structure in this work, containing the atoms at their equilibrium positions, is given below in `.cif` file format.

```
data_global

_cell_length_a      3.9843631
_cell_length_b      3.9843631
_cell_length_c      3.9843631
_cell_angle_alpha   90.0000000
_cell_angle_beta    90.0000000
_cell_angle_gamma   90.0000000

loop_
_atom_site_type_symbol
_atom_site_fract_x
_atom_site_fract_y
_atom_site_fract_z
_atom_site_U_iso_or_equiv
```

```
_atom_site_occupancy
O 0.4710178976 0.0036662051 0.0256155973 0.01 1.00
O -0.0143852900 0.0036646292 0.5489697542 0.01 1.00
O -0.0143859834 0.5064992423 0.0250311466 0.01 1.00
Ti 0.0180564465 -0.0044419248 -0.0312372643 0.01 1.00
Ba 0.4995839025 0.4993181123 0.4990175886 0.01 1.00
```

C.3 Soft mode displacement patterns

The displacement patterns corresponding to the three harmonic soft modes associated with the ferroelectric phase transitions considered in $BaTiO_3$ are given below. All three are degenerate, with a frequency of $23.5i$ meV, and correspond to the Ti^{4+} ions moving relative to the O^{2-} octahedra in the $[0\,1\,\bar{1}]$, $[0\,1\,1]$ and $[1\,0\,0]$ directions respectively. Each row shows the displacement of the ions in the three Cartesian directions, in the same order as they are listed in the equilibrium configuration above.

- Displacement along $[0\,1\,\bar{1}]$:

```
     x     y     z
O   0.00  0.50 -0.50
O   0.00  0.50 -1.00
O   0.00  1.00 -0.50
Ti  0.00 -0.63  0.63
Ba  0.00  0.00  0.00
```

- Displacement along $[0\,1\,1]$:

```
     x     y     z
O   0.00  0.50  0.50
O   0.00  0.50  1.00
O   0.00  1.00  0.50
Ti  0.00 -0.63 -0.63
Ba  0.00  0.00  0.00
```

- Displacement along $[1\,0\,0]$:

```
     x     y     z
O   1.00  0.00  0.00
O   0.50  0.00  0.00
```

```
O   0.50  0.00  0.00
Ti -0.63  0.00  0.00
Ba  0.00  0.00  0.00
```

Bibliography

[1] T.S. Kuhn, *The Structure of Scientific Revolutions*, 1st ed. (University of Chicago Press, Chicago, 1962).

[2] A. Einstein, *Über einen die Erzeugung und Verwandlung des Lichtes betreffenden heuristischen Gesichtspunkt*, Ann. Phys. (Berlin) **17**, 132 (1905).

[3] A. Einstein, *Über die von der molekularkinetischen Theorie der Wärme geforderte Bewegung von in ruhenden Flüssigkeiten suspendierten Teilchen*, Ann. Phys. (Berlin) **17**, 549 (1905).

[4] A. Einstein, *Zur Elektrodynamik bewegter Körper*, Ann. Phys. (Berlin) **17**, 891 (1905).

[5] A. Einstein, *Ist die Trägheit eines Körpers von seinem Energieinhalt abhängig?*, Ann. Phys. (Berlin) **18**, 639 (1905).

[6] P.A.M. Dirac, *The quantum theory of the electron*, Proc. R. Soc. A **117**, 610 (1928).

[7] P.W. Anderson, *More is different*, Science **177**, 393 (1972).

[8] M. Born and R. Oppenheimer, *Zur Quantentheorie der Molekeln*, Ann. Phys. **389**, 457 (1927).

[9] D.C. Wallace, *Thermodynamics of Crystals* (John Wiley & Sons, 1972).

[10] G.E. Moore, *Cramming more components onto integrated circuits*, Electronics **38**, 114 (1965).

[11] J. Binney and D. Skinner, *The Physics of Quantum Mechanics* (Cappella Archive, 2008).

[12] R.O. Jones and O. Gunnarsson, *The density functional formalism, its applications and prospects*, Rev. Mod. Phys. **61**, 689 (1989).

[13] P.A.M. Dirac, *Quantum mechanics of many-electron systems*, Proc. R. Soc. A **123**, 714 (1929).

[14] D.S. Sholl and J.A. Steckel, *Density Functional Theory: A Practical Introduction* (John Wiley & Sons, 2009).

[15] J.M. Ziman, *Principles of the Theory of Solids* (Cambridge University Press, 1964).

[16] M. Born and V.A. Fock, *Beweis des adiabatensatzes*, Z. Phys. **51**, 165 (1928).

[17] A. Szabo and N.S. Ostlund, *Modern Quantum Chemistry* (Macmillan, 1982).

[18] W. Pauli, *The connection between spin and statistics*, Phys. Rev. **58**, 716 (1940).

[19] J.C. Slater, *The theory of complex spectra*, Phys. Rev. **34**, 1293 (1929).

[20] C. Møller and M.S. Plesset, *Note on an approximation treatment for many-electron systems*, Phys. Rev. **46**, 618 (1934).

[21] G.H. Booth, A.J.W. Thom, and A. Alavi, *Fermion Monte Carlo without fixed nodes: a game of life, death, and annihilation in Slater determinant space*, J. Chem. Phys. **131**, 054106 (2009).

[22] C. Daday, S. Smart, G.H. Booth, A. Alavi, and C. Filippi, *Full configuration interaction excitations of ethene and butadiene: resolution of an ancient question*, J. Chem. Theory Comput. **8**, 4441 (2012).

[23] W.A. Vigor, J.S. Spencer, M.J. Bearpark, and A.J.W. Thom, *Understanding and improving the efficiency of full configuration interaction quantum Monte Carlo*, J. Chem. Phys. **144**, 094110 (2016).

[24] J. Čížek, *On the correlation problem in atomic and molecular systems. Calculation of wavefunction components in Ursell-type expansion using quantum-field theoretical methods*, J. Chem. Phys. **45**, 4256 (1966).

[25] P. Hohenberg and W. Kohn, *Inhomogeneous electron gas*, Phys. Rev. **136**, B864 (1964).

[26] W. Kohn and L.J. Sham, *Self-consistent equations including exchange and correlation effects*, Phys. Rev. **140**, A1133 (1965).

[27] R.O. Jones, *Density functional theory: its origins, rise to prominence, and future*, Rev. Mod. Phys. **87**, 897 (2015).

[28] W. Kohn, A.D. Becke, and R.G. Parr, *Density functional theory of electronic structure*, J. Phys. Chem. **100**, 12974 (1996).

[29] L.H. Thomas, *The calculation of atomic fields*, Math. Proc. Cambridge **23**, 542 (1927).

[30] E. Fermi, *Un metodo statistico per la determinazione di alcune prioprietà dell'atomo*, Rend. Accad. Naz. Lincei **6**, 602 (1927).

[31] E.H Lieb and B. Simon, *The Thomas-Fermi theory of atoms, molecules and solids*, Adv. Math. **23**, 22 (1977).

[32] E. Teller, *On the stability of molecules in the Thomas-Fermi theory*, Rev. Mod. Phys. **34**, 627 (1962).

[33] M. Levy, *Universal variational functionals of electron densities, first-order density matrices, and natural spin-orbitals and solution of the v-representability problem*, Proc. Natl. Acad. Sci. USA **76**, 6062 (1979).

[34] M. Levy, *Electron densities in search of Hamiltonians*, Phys. Rev. A **26**, 1200 (1982).

[35] J.E. Harriman, *Orthonormal orbitals for the representation of an arbitrary density*, Phys. Rev. A **24**, 680 (1981).

[36] R.M. Martin, *Electronic Structure: Basic Theory and Practical Methods* (Cambridge University Press, 2004).

[37] G. Kresse and J. Furthmüller, *Efficient iterative schemes for ab initio total-energy calculations using a plane-wave basis set*, Phys. Rev. B **54**, 11169 (1996).

[38] R.W. Godby, M. Schlüter, and L.J. Sham, *Accurate exchange-correlation potential for silicon and its discontinuity on addition of an electron*, Phys. Rev. Lett. **56**, 2415 (1986).

[39] D.M. Ceperley and B.J. Alder, *Ground state of the electron gas by a stochastic method*, Phys. Rev. Lett. **45**, 566 (1980).

[40] J.P. Perdew and Y. Wang, *Accurate and simple analytic representation of the electron-gas correlation energy*, Phys. Rev. B **45**, 13244 (1992).

[41] J.P. Perdew and A. Zunger, *Self-interaction correction to density-functional approximations for many-electron systems*, Phys. Rev. B **23**, 5048 (1981).

[42] F. Herman, J.P. Van Dyke, and I.B. Ortenburger, *Improved statistical exchange approximation for inhomogeneous many-electron systems*, Phys. Rev. Lett. **22**, 807 (1969).

[43] D.C. Langreth and J.P. Perdew, *Theory of nonuniform electronic systems. I. Analysis of the gradient approximation and a generalization that works*, Phys. Rev. B **21**, 5469 (1980).

[44] J.P. Perdew, *Accurate density functional for the energy: real-space cutoff of the gradient expansion for the exchange hole*, Phys. Rev. Lett. **55**, 1665 (1985).

[45] J.P. Perdew, K. Burke, and M. Ernzerhof, *Generalized gradient approximation made simple*, Phys. Rev. Lett. **77**, 3865 (1996).

[46] J.P. Perdew, A. Ruzsinsky, G.I. Csonka, O.A. Vydrov, G.E. Scuseria, L.A. Constantin, X. Zhou, and K. Burke, *Restoring the density-gradient expansion for exchange in solids and surfaces*, Phys. Rev. Lett. **100**, 136406 (2008).

[47] Z. Wu and R.E. Cohen, *More accurate generalized gradient approximation for solids*, Phys. Rev. B **73**, 235116 (2006).

[48] L.J. Sham and M. Schlüter, *Density-functional theory of the energy gap*, Phys. Rev. Lett. **51**, 1888 (1983).

[49] J.P. Perdew and M. Levy, *Physical content of the exact Kohn-Sham orbital energies: band gaps and derivative discontinuities*, Phys. Rev. Lett. **51**, 1884 (1983).

[50] F. Gygi and A. Baldereschi, *Quasiparticle energies in semiconductors: self-energy correction to the local-density approximation*, Phys. Rev. Lett. **62**, 2160 (1989).

[51] C. Adamo and V. Barone, *Toward reliable density functional methods without adjustable parameters: the PBE0 model*, J. Chem. Phys. **110**, 6158 (1999).

[52] A.D. Becke, *Density-functional thermochemistry. III. The role of exact exchange*, J. Chem. Phys. **98**, 5648 (1993).

[53] J. Heyd, G.E. Scuseria, and M. Ernzerhof, *Hybrid functionals based on a screened Coulomb potential*, J. Chem. Phys. **118**, 8207 (2003).

[54] A.V. Krukau, O.A. Vydrov, A.F. Izmaylov, and G.E. Scuseria, *Influence of the exchange screening parameter on the performance of screened hybrid functionals*, J. Chem. Phys. **125**, 224106 (2006).

[55] F. Giustino, S.G. Louie, and M.L. Cohen, *Electron-phonon renormalization of the direct band gap of diamond*, Phys. Rev. Lett. **105**, 265501 (2010).

[56] S.J. Clark, M.D. Segall, C.J. Pickard, P.J. Hasnip, M.I.J. Probert, K. Refson, and M.C. Payne, *First principles methods using CASTEP*, Z. Kristallogr. **220**, 567 (2005).

[57] P. Schwerdtfeger, *The pseudopotential approximation in electronic structure theory*, ChemPhysChem **12**, 3143 (2011).

[58] G.P. Srivastava and D. Weaire, *The theory of the cohesive energies of solids*, Adv. Phys. **36**, 463 (1987).

[59] W.H.E. Schwarz, E.M. van Wezenbeek, E.J. Baerends, and J.G. Snijders, *The origin of relativistic effects of atomic orbitals*, J. Phys. B **22**, 1515 (1989).

[60] D.R. Hamann, M. Schlüter, and C. Chiang, *Norm-conserving pseudopotentials*, Phys. Rev. Lett. **43**, 1494 (1979).

[61] D. Vanderbilt, *Soft self-consistent pseudopotentials in a generalized eigenvalue formalism*, Phys. Rev. B **41**, 7892 (1990).

[62] M.D. Segall, P.J.D. Lindan, M.J. Probert, C.J. Pickard, P.J. Hasnip, S.J. Clark, and M.C. Payne, *First-principles simulation: ideas, illustrations and the CASTEP code*, J. Phys.: Condens. Matter **14**, 2717 (2002).

[63] R.P. Feynman, *Forces in molecules*, Phys. Rev. **56**, 340 (1939).

[64] M.C. Payne, M.P. Teter, D.C. Allan, T.A. Arias, and J.D. Joannopoulos, *Iterative minimization techniques for ab initio total-energy calculations: molecular dynamics and conjugate gradients*, Rev. Mod. Phys. **64**, 1045 (1992).

[65] P. Pulay, *Ab initio calculation of force constants and equilibrium geometries in polyatomic molecules*, Mol. Phys. **17**, 197 (1969).

[66] J. Nocedal and S.J. Wright, *Numerical Optimization*, 2nd ed. (Springer-Verlag, Berlin, 2006).

[67] B.G. Pfrommer, M. Côté, S.G. Louie, and M.L. Cohen, *Relaxation of crystals with the quasi-Newton method*, J. Comput. Phys. **131**, 233 (1997).

[68] C.J. Pickard and R.J. Needs, *Ab initio random structure searching*, J. Phys.: Condens. Matter **23**, 053201 (2011).

[69] H.J. Monkhorst and J.D. Pack, *Special points for Brillouin-zone integrations*, Phys. Rev. B **13**, 5188 (1976).

[70] C.-K. Skylaris, P.D. Haynes, A.A. Mostofi, and M.C. Payne, *Introducing ONETEP: linear-scaling density functional simulations on parallel computers*, J. Chem. Phys. **122**, 084119 (2005).

[71] A.A. Maradudin, E.W. Montroll, G.H. Weiss, and I.P. Ipatova, *Theory of Lattice Dynamics in the Harmonic Approximation*, 2nd ed. (Academic Press, New York, 1971).

[72] S. Baroni, S. de Gironcoli, A. Dal Corso, and P. Giannozzi, *Phonons and related crystal properties from density-functional perturbation theory*, Rev. Mod. Phys. **73**, 515 (2001).

[73] K. Kunc, I. Loa, and K. Syassen, *Equation of state and phonon frequency calculations of diamond at high pressures*, Phys. Rev. B **68**, 094107 (2003).

[74] G.J. Ackland, M.C. Warren, and S.J. Clark, *Practical methods in ab initio lattice dynamics*, J. Phys.: Condens. Matter **9**, 7861 (1997).

[75] B. Monserrat, N.D. Drummond, and R.J. Needs, *Anharmonic vibrational properties in periodic systems: energy, electron-phonon coupling, and stress*, Phys. Rev. B **87**, 144302 (2013).

[76] B. Monserrat, N.D. Drummond, C.J. Pickard, and R.J. Needs, *Electron-phonon coupling and the metallization of solid helium at terapascal pressures*, Phys. Rev. Lett. **112**, 055504 (2014).

[77] S. Azadi, B. Monserrat, W.M.C. Foulkes, and R.J. Needs, *Dissociation of high-pressure solid molecular hydrogen: a quantum Monte Carlo and anharmonic vibrational study*, Phys. Rev. Lett. **112**, 165501 (2014).

[78] B. Monserrat, R.J. Needs, and C.J. Pickard, *Temperature effects in first-principles solid state calculations of the chemical shielding tensor made simple*, J. Chem. Phys. **141**, 134113 (2014).

[79] E.A. Engel, B. Monserrat, and R.J. Needs, *Anharmonic nuclear motion and the relative stability of hexagonal and cubic ice*, Phys. Rev. X **5**, 021033 (2015).

[80] N.D. Drummond, B. Monserrat, J.H. Lloyd-Williams, P. López Ríos, C.J. Pickard, and R.J. Needs, *Quantum Monte Carlo study of the phase diagram of solid molecular hydrogen at extreme pressures*, Nat. Commun. **6**, 7794 (2015).

[81] E.A. Engel, B. Monserrat, and R.J. Needs, *Vibrational renormalisation of the electronic band gap in hexagonal and cubic ice*, J. Chem. Phys. **143**, 244708 (2015).

[82] E.A. Engel, B. Monserrat, and R.J. Needs, *Vibrational effects on surface energies and band gaps in hexagonal and cubic ice*, J. Chem. Phys. **145**, 044703 (2016).

[83] B. Monserrat, R.J. Needs, E. Gregoryanz, and C.J. Pickard, *Hexagonal structure of phase III of solid hydrogen*, Phys. Rev. B **94**, 134101 (2016).

[84] J.O. Jung and R.B. Gerber, *Vibrational wave functions and spectroscopy of* $(H_2O)_n$*,* $n = 2, 3, 4, 5$*: vibrational self-consistent field with correlation corrections*, J. Chem. Phys. **105**, 10332 (1996).

[85] N. Antolin, O.D. Restrepo, and W. Windl, *Fast free energy calculations for unstable high-temperature phases*, Phys. Rev. B **86**, 054119 (2012).

[86] I.I. Naumov, R.E. Cohen, and R.J. Hemley, *Graphene physics and insulator-metal transition in compressed hydrogen*, Phys. Rev. B **88**, 045125 (2013).

[87] J.M. Bowman, *Selfconsistent field energies and wavefunctions for coupled oscillators*, J. Chem. Phys. **68**, 608 (1978).

[88] L.S. Norris, M.A. Ratner, A.E. Roitberg, and R.B. Gerber, *Møller-Plesset perturbation theory applied to vibrational problems*, J. Chem. Phys. **105**, 11261 (1996).

[89] J.H. Lloyd-Williams and B. Monserrat, *Lattice dynamics and electron-phonon coupling calculations using nondiagonal supercells*, Phys. Rev. B **92**, 184301 (2015).

[90] G.L.W. Hart and R.W. Forcade, *Algorithm for generating derivative structures*, Phys. Rev. B **77**, 224115 (2008).

[91] A.K. Rappe, C.J. Casewit, K.S. Colwell, W.A. Goddard III, and W.M. Skiff, *UFF, a full periodic table force field for molecular mechanics and molecular dynamics simulations*, J. Am. Chem. Soc. **114**, 10024 (1992).

[92] H. Sun, *COMPASS: an ab initio force-field optimized for condensed-phase applications – overview with details on alkane and benzene compounds*, J. Phys. Chem. B **102**, 7338 (1998).

[93] W.H. Press, S.A. Teukolsky, W.T. Vetterling, and B.P. Flannery, *Numerical Recipes in FORTRAN: The Art of Scientific Computing*, 2nd ed. (Cambridge University Press, Cambridge, 1992).

[94] G.R. Fowles and G. Cassiday, *Analytical Mechanics*, 7th ed. (Brooks Cole, Pacific Grove, CA, USA, 2004).

[95] C. Sprunk, B. Lau, and W. Burgard, *Improved non-linear spline fitting for teaching trajectories to mobile robots*, in Proc. of the IEEE International Conference on Robotics and Automation (2012), p. 2068.

[96] S. Azadi and W.M.C. Foulkes, *Fate of density functional theory in the study of high-pressure solid hydrogen*, Phys. Rev. B **88**, 014115 (2013).

[97] O. Hellman, I.A. Abrikosov, and S.I. Simak, *Lattice dynamics of anharmonic solids from first principles*, Phys. Rev. B **84**, 180301 (2011).

[98] P. Souvatzis, O. Eriksson, M.I. Katsnelson, and S.P. Rudin, *Entropy driven stabilization of energetically unstable crystal structures explained from first principles theory*, Phys. Rev. Lett. **100**, 095901 (2008).

[99] G.D. Dickenson, M.L. Niu, E.J. Salumbides, J. Komasa, K.S.E. Eikema, K. Pachucki, and W. Ubachs, *Fundamental vibration of molecular hydrogen*, Phys. Rev. Lett. **110**, 193601 (2013).

[100] N.W. Ashcroft, *Metallic hydrogen: a high-temperature superconductor?*, Phys. Rev. Lett. **21**, 1748 (1968).

[101] M. Borinaga, I. Errea, M. Calandra, F. Mauri, and A. Bergara, *Anharmonic effects in atomic hydrogen: superconductivity and lattice dynamical stability*, Phys. Rev. B **93**, 174308 (2016).

[102] E. Babaev, A. Sudbø, and N.W. Ashcroft, *A superconductor to superfluid phase transition in liquid metallic hydrogen*, Nature **431**, 666 (2004).

[103] E. Wigner and H.B. Huntington, *On the possibility of a metallic modification of hydrogen*, J. Chem. Phys. **3**, 764 (1935).

[104] S.T. Weir, A.C. Mitchell, and W.J. Nellis, *Metallization of fluid molecular hydrogen at* 140 *GPa (*1.4 *Mbar)*, Phys. Rev. Lett. **76**, 1860 (1996).

[105] R.T. Howie, P. Dalladay-Simpson, and E. Gregoryanz, *Raman spectroscopy of hot hydrogen above* 200 *GPa*, Nat. Mater. **14**, 495 (2015).

[106] P. Dalladay-Simpson, R.T. Howie, and E. Gregoryanz, *Evidence for a new phase of dense hydrogen above* 325 *gigapascals*, Nature **529**, 63 (2016).

[107] J.M. McMahon, M.A. Morales, C. Pierleoni, and D.M. Ceperley, *The properties of hydrogen and helium under extreme conditions*, Rev. Mod. Phys. **84**, 1607 (2012).

[108] K.A. Johnson and N.W. Ashcroft, *Structure and bandgap closure in dense hydrogen*, Nature **403**, 632 (2000).

[109] C.J. Pickard and R.J. Needs, *Structure of phase III of solid hydrogen*, Nat. Phys. **3**, 473 (2007).

[110] C.J. Pickard, M. Martinez-Canales, and R.J. Needs, *Density functional theory study of phase IV of solid hydrogen*, Phys. Rev. B **85**, 214114 (2012).

[111] J. Chen, X. Ren, X.-Z. Li, D. Alfè, and E. Wang, *On the room-temperature phase diagram of high pressure hydrogen: an ab initio molecular dynamics perspective and a diffusion Monte Carlo study*, J. Chem. Phys. **141**, 024501 (2014).

[112] G. Grimvall, B. Magyari-Köpe, V. Ozoliņš, and K.A. Persson, *Lattice instabilities in metallic elements*, Rev. Mod. Phys. **84**, 945 (2012).

[113] W. Petry, A. Heiming, J. Trampenau, M. Alba, C. Herzig, H.R. Schober, and G. Vogl, *Phonon dispersion of the bcc phase of group-IV metals. I. bcc titanium*, Phys. Rev. B **43**, 10933 (1991).

[114] A. Heiming, W. Petry, J. Trampenau, M. Alba, C. Herzig, H.R. Schober, and G. Vogl, *Phonon dispersion of the bcc phase of group-IV metals. II. bcc zirconium, a model case of dynamical precursors of martensitic transitions*, Phys. Rev. B **43**, 10948 (1991).

[115] J. Trampenau, A. Heiming, W. Petry, M. Alba, C. Herzig, W. Miekeley, and H.R. Schober, *Phonon dispersion of the bcc phase of group-IV metals. III. bcc hafnium*, Phys. Rev. B **43**, 10963 (1991).

[116] J. Zhang, Y. Zhao, C. Pantea, J. Qian, L.L. Daemen, P.A. Rigg, R.S. Hixson, C.W. Greeff, G.T. Gray III, Y. Yang, and L. Wang, *Experimental constraints on the phase diagram of elemental zirconium*, J. Chem. Phys. Solids **66**, 1213 (2005).

[117] C.-E. Hu, Z.-Y. Zeng, L. Zhang, X.-R. Chen, and L.-C. Cai, *Density functional study of the phase diagram and thermodynamic properties of Zr*, Comput. Mater. Sci. **50**, 835 (2011).

[118] C.L. Guillaume, E. Gregoryanz, O. Degtyareva, M.I. McMahon, M. Hanfland, S. Evans, M. Guthrie, S.V. Sinogeikin, and H-K. Mao, *Cold melting and solid structures of dense lithium*, Nat. Phys. **7**, 211 (2011).

[119] A.W. Overhauser, *Crystal structure of lithium at* 4.2 *K*, Phys. Rev. Lett. **53**, 64 (1984).

[120] A.M. Schaeffer, W. Cai, E. Olejnik, J.J. Molaison, S. Sinogeikin, A.M. dos Santos, and S. Deemyad, *Boundaries for martensitic transition of* ^{7}*Li under pressure*, Nat. Commun. **6**, 8030 (2015).

[121] S.F. Elatresh, W. Cai, N.W. Ashcroft, R. Hoffmann, S. Deemyad, and S.A. Bonev, *Evidence from Fermi surface analysis for the low-temperature structure of lithium*, Proc. Natl. Acad. Sci. U.S.A. **114**, 5389 (2017).

[122] G.J. Ackland, M. Dunuwille, M. Martinez-Canales, I. Loa, R. Zhang, S. Sinogeikin, W. Cai, and S. Deemyad, *Quantum and isotope effects in lithium metal*, Science **356**, 1254 (2017).

[123] S.H. Taole, H.R. Glyde, and R. Taylor, *Anharmonic properties of Li*, Phys. Rev. B **18**, 2643 (1978).

[124] A.M. Stoneham, *Theory of Defects in Solids: Electronic Structure of Defects in Insulators and Semiconductors* (Oxford University Press, 1975).

[125] T. Schröder, S.L. Mouradian, J. Zheng, M.E. Trusheim, M. Walsh, E.H. Chen, L. Li, I. Bayn, and D. Englund, *Quantum nanophotonics in diamond*, J. Opt. Soc. Am. B **33**, B65 (2016).

[126] C. Freysoldt, B. Grabowski, H. Tilmann, J. Neugebauer, G. Kresse, A. Janotti, and C.G. Van de Walle, *First-principles calculations for point defects in solids*, Rev. Mod. Phys. **86**, 253 (2014).

[127] D. Drabold and S. Estreicher, eds., *Theory of Defects in Semiconductors*, Vol. 104, Topics in Applied Physics (Springer-Verlag, 2007).

[128] L.J. Rogers, K.D. Jahnke, M.W. Doherty, A. Dietrich, L.P. McGuinness, C. Müller, T. Teraji, H. Sumiya, J. Isoya, N.B. Manson, and F. Jelezko, *Electronic structure of the negatively charged silicon-vacancy center in diamond*, Phys. Rev. B **89**, 235101 (2014).

[129] A. Gali and J.R. Maze, *Ab initio study of the split silicon-vacancy defect in diamond: electronic structure and related properties*, Phys. Rev. B **88**, 235205 (2013).

[130] P.C. Maurer, G. Kucsko, C. Latta, L. Jiang, N.Y. Yao, S.D. Bennett, F. Pastawski, D. Hunger, N. Chisholm, M. Markham, D.J. Twitchen, J.I. Cirac, and M.D. Lukin, *Room-temperature quantum bit memory exceeding one second*, Science **336**, 1283 (2012).

[131] L.J. Rogers, K.D. Jahnke, M.H. Metsch, A. Sipahigil, J.M. Binder, T. Teraji, H. Sumiya, J. Isoya, M.D. Lukin, P. Hemmer, and F. Jelezko, *All-optical initialization, readout, and coherent preparation of single silicon-vacancy spins in diamond*, Phys. Rev. Lett. **113**, 263602 (2014).

[132] A. Sipahigil, K.D. Jahnke, L.J. Rogers, T. Teraji, J. Isoya, A.S. Zibrov, F. Jelezko, and M.D. Lukin, *Indistinguishable photons from separated silicon-vacancy centers in diamond*, Phys. Rev. Lett. **113**, 113602 (2014).

[133] G. Balasubramanian, P. Neumann, D. Twitchen, M. Markham, R. Kolesov, N. Mizuochi, J. Isoya, J. Achard, J. Beck, J. Tissler, V. Jacques, P.R. Hemmer, F. Jelezko, and J. Wrachtrup, *Ultralong spin coherence time in isotopically engineered diamond*, Nat. Mater. **8**, 383 (2009).

[134] H. Bernien, B. Hensen, W. Pfaff, G. Koolstra, M.S. Blok, L. Robledo, T.H. Taminiau, M. Markham, D.J. Twitchen, L. Childress, and R. Hanson, *Heralded entanglement between solid-state qubits separated by three metres*, Nature **497**, 86 (2013).

[135] H.S. Knowles, D.M. Kara, and M. Atatüre, *Observing bulk diamond spin coherence in high-purity nanodiamonds*, Nat. Mater. **13**, 21 (2014).

[136] F. Dolde, I. Jakobi, B. Naydenov, N. Zhao, S. Pezzagna, C. Trautmann, J. Meijer, P. Neumann, F. Jelezko, and J. Wrachtrup, *Room-temperature entanglement between single defect spins in diamond*, Nat. Phys. **9**, 139 (2013).

[137] A. Mainwood and A.M. Stoneham, *Stability of electronic states of the vacancy in diamond*, J. Phys. Condens. Matter **9**, 2453 (1997).

[138] G. Davies, *The Jahn-Teller effect and vibronic coupling at deep levels in diamond*, Rep. Prog. Phys. **44**, 787 (1981).

[139] F. Corsetti and A.A. Mostofi, *System-size convergence of point defect properties: the case of the silicon vacancy*, Phys. Rev. B **84**, 035209 (2011).

[140] R.Q. Hood, P.R.C. Kent, R.J. Needs, and P.R. Briddon, *Quantum Monte Carlo study of the optical and diffusive properties of the vacancy defect in diamond*, Phys. Rev. Lett. **91**, 076403 (2003).

[141] J. Walker, *Optical absorption and luminescence in diamond*, Rep. Prog. Phys. **42**, 1605 (1979).

[142] J. Wrachtrup and F. Jelezko, *Processing quantum information in diamond*, J. Phys.: Condens. Matter **18**, S807 (2006).

[143] R. Schirhagl, K. Chang, M. Loretz, and C.L. Degen, *Nitrogen-vacancy centers in diamond: nanoscale sensors for physics and biology*, Ann. Rev. Phys. Chem. **65**, 83 (2014).

[144] C.D. Clark and J. Walker, *The neutral vacancy in diamond*, Proc. R. Soc. A **334**, 241 (1973).

[145] Materialscientist at English Wikipedia, `https://commons.wikimedia.org/w/index.php?curid=7963314`, CC BY-SA 3.0. Accessed 11/05/17.

[146] C.D. Clark and C.A. Norris, *Photoluminescence associated with the 1.673, 1.944 and 2.498 eV centres in diamond*, J. Phys. C: Solid State Phys. **4**, 2223 (1971).

[147] A.A. Kaplyanskii, V.I. Kolyshkin, V.N. Medvedev, and A.P. Skvortsov, *Inversion symmetry of optical centres in diamond*, Soviet Physics, Solid State **12**, 2867 (1971).

[148] G. D. Watkins, *The Lattice Vacancy in Silicon*, in *Deep centers in semiconductors*, edited by S. T. Pantelides (Gordon and Breach, 1986).

[149] M.I.J. Probert and M.C. Payne, *Improving the convergence of defect calculations in supercells: an ab initio study of the neutral silicon vacancy*, Phys. Rev. B **67**, 075204 (2003).

[150] S.J. Breuer and P.R. Briddon, *Ab initio investigation of the native defects in diamond and self-diffusion*, Phys. Rev. B **51**, 6984 (1995).

[151] H.A. Jahn and E. Teller, *Stability of polyatomic molecules in degenerate electronic states. I. Orbital degeneracy*, Proc. R. Soc. A **161**, 220 (1937).

[152] M. Lannoo and A.M. Stoneham, *The optical absorption of the neutral vacancy in diamond*, J. Phys. Chem. Solids **29**, 1987 (1968).

[153] F.S. Ham, *The Jahn-Teller effect*, Int. J. Quantum Chem. **5**, 191 (1971).

[154] A.J. Millis, B.I. Shraiman, and R. Mueller, *Dynamic Jahn-Teller effect and colossal magnetoresistance in* $La_{1-x}Sr_xMnO_3$, Phys. Rev. Lett. **77**, 175 (1996).

[155] V. Dediu, C. Ferdeghini, F.C. Matacotta, P. Nozar, and G. Ruani, *Jahn-Teller dynamics in charge-ordered manganites from Raman spectroscopy*, Phys. Rev. Lett. **84**, 4489 (2000).

[156] V. Brouet, H. Alloul, T. Le, S. Garaj, and L. Forro, *Role of dynamic Jahn-Teller distortions in* Na_2C_{60} *and* Na_2CsC_{60} *studied by NMR*, Phys. Rev. Lett. **86**, 4680 (2001).

[157] S.E. Canton, A.J. Yencha, E. Kukk, J.D. Bozek, M.C.A. Lopes, G. Snell, and N. Berrah, *Experimental evidence of a dynamic Jahn-Teller effect in* C_{60}^+, Phys. Rev. Lett. **89**, 045502 (2002).

[158] M.C.M. O'Brien, *The dynamic Jahn-Teller effect in octahedrally co-ordinated* d^9 *ions*, Proc. R. Soc. A **281**, 323 (1964).

[159] K.C. Fu, C. Santori, P.E. Barclay, L.J. Rogers, N.B. Manson, and R.G. Beausoleil, *Observation of the dynamic Jahn-Teller effect in the excited states of nitrogen-vacancy centers in diamond*, Phys. Rev. Lett. **103**, 256404 (2009).

[160] A.M. Stoneham, *The low-lying levels of the GR 1 centre in diamond*, Solid State Commun. **21**, 339 (1977).

[161] O.K. Al-Mushadani and R.J. Needs, *Free-energy calculations of intrinsic point defects in silicon*, Phys. Rev. B **68**, 235205 (2003).

[162] R. Maezono, A. Ma, M.D. Towler, and R.J. Needs, *Equation of state and Raman frequency of diamond from quantum Monte Carlo simulations*, Phys. Rev. Lett. **98**, 025701 (2007).

[163] O. Madelung, ed., *Semiconductors - Basic Data* (Springer, 1996).

[164] J.C. Bourgoin, *An experimental estimation of the vacancy formation energy in diamond*, Radiat. Eff. Defects Solids **79**, 235 (1983).

[165] S. Stoupin and Y.V. Shvyd'ko, *Thermal expansion of diamond at low temperatures*, Phys. Rev. Lett. **104**, 085901 (2010).

[166] J. Valasek, *Piezo-electric and allied phenomena in Rochelle salt*, in Minutes of the Washington Meeting, April 23 and 24, 1920 (1920), p. 537.

[167] J. Valasek, *Piezo-electric and allied phenomena in Rochelle salt*, Phys. Rev. **17**, 475 (1921).

[168] A.J. Moulson and J.M. Herbert, *Electroceramics*, 2nd ed. (John Wiley & Sons, Oxford, 2003).

[169] J. Curie and P. Curie, *Développement, par pression, de l'électricité polaire dans les cristaux hémièdres à faces inclinées*, Comptes rendus **91**, 294 (1880).

[170] N.W. Ashcroft and N.D. Mermin, *Solid State Physics*, 1st ed. (Brooks Cole, Pacific Grove, 1976).

[171] D. Brewster, *Observations on the pyro-electricity of minerals*, The Edinburgh Journal of Science **1**, 208 (1824).

[172] W. Kanzig, *Ferroelectrics and Antiferroelectrics*, 1st ed. (Academic Press, Cambridge, MA, 1957).

[173] R.E. Newnham and L.E. Cross, *Ferroelectricity: the foundation of a field from form to function*, MRS Bull. **30**, 845 (2005).

[174] J.F. Scott, *Ferroelectric Memories*, 1st ed. (Springer-Verlag, Berlin, 2000).

[175] R. Ramesh and N.A. Spaldin, *Multiferroics: progress and prospects in thin films*, Nat. Mater. **6**, 21 (2007).

[176] M.M. Vopson, *Fundamentals of multiferroic materials and their possible applications*, Crit. Rev. Solid State Mater. Sci. **40**, 223 (2015).

[177] G. Busch and P. Scherrer, *Eine neue seignette-elektrische Substanz*, Naturwiss. **23**, 737 (1935).

[178] R. Blinc, *Order and disorder in ferroelectrics*, Ferroelectrics **301**, 3 (2004).

[179] J.C. Slater, *Theory of the transition in KH_2PO_4*, J. Chem. Phys. **9**, 16 (1941).

[180] B.M. Wul and I.M. Goldman, *Dielectric constant of titanates of the metals of the second group*, Comptes rendus (Doklady) de l'Académie des sciences de l'URSS **46**, 139 (1945).

[181] B.M. Wul and I.M. Goldman, *Dielectric constant of barium titanate as a function of strength of an alternating field*, Comptes rendus (Doklady) de l'Académie des sciences de l'URSS **49**, 177 (1945).

[182] B.M. Wul and I.M. Goldman, *Dielectric hysteresis in barium titanate*, Comptes rendus (Doklady) de l'Académie des sciences de l'URSS **51**, 21 (1946).

[183] A. von Hippel, R.G. Breckenridge, F.G. Chesley, and L. Tisza, *High dielectric constant ceramics*, Ind. Eng. Chem. **38**, 1097 (1946).

[184] G.H. Jonker and J.H. van Santen, *Ferromagnetic compounds of manganese with perovskite structure*, Physica **16**, 337 (1950).

[185] B. Raveau, A. Maignan, C. Martin, and M. Hervieu, *Colossal magnetoresistance manganite perovskites: relations between crystal chemistry and properties*, Chem. Mater. **10**, 2641 (1998).

[186] M.M. Lee, J. Teuscher, T. Miyasaka, T. Murakami, and H.J. Snaith, *Efficient hybrid solar cells based on meso-superstructured organometal halide perovskites*, Science **338**, 643 (2012).

[187] L.M. Herz, *Charge-carrier dynamics in organic-inorganic metal halide perovskites*, Annu. Rev. Phys. Chem. **67**, 65 (2016).

[188] J.G. Bednorz and K.A. Müller, *Possible high T_c superconductivity in the Ba-La-Cu-O system*, Z. Physik B Con. Mat. **64**, 189 (1986).

[189] R.D. Burbank and H.T. Evans, *The crystal structure of hexagonal barium titanate*, Acta Cryst. **1**, 330 (1948).

[190] D.E. Rase and R. Roy, *Phase equilibria in the system BaO-TiO_2*, J. Amer. Ceram. Soc. **38**, 102 (1955).

[191] G.H. Kwei, A.C. Lawson, S.J.L. Billinge, and S.W. Cheong, *Structures of the ferroelectric phases of barium titanate*, J. Phys. Chem. **97**, 2368 (1993).

[192] E. Sawaguchi, Y. Akishige, and M. Kobayashi, *Ferroelectric behavior in hexagonal type barium titanate*, Jpn. J. Appl. Phys. **24**, 252 (1985).

[193] S. Hashemizadeh, A. Biancoli, and D. Damjanovic, *Symmetry breaking in hexagonal and cubic polymorphs of $BaTiO_3$*, J. Appl. Phys. **119**, 094105 (2016).

[194] T. Ishidate, S. Abe, H. Takahashi, and N. Môri, *Phase diagram of $BaTiO_3$*, Phys. Rev. Lett. **78**, 2397 (1997).

[195] S.A. Hayward and E.K.H. Salje, *The pressure-temperature phase diagram of $BaTiO_3$: a macroscopic description of the low-temperature behaviour*, J. Phys. Condens. Matter **14**, L599 (2002).

[196] I. Bhaumik, S. Ganesamoorthy, R. Bhatt, A.K. Karnal, V.K. Wadhawan, P.K. Gupta, K. Kitamura, S. Takekawa, and M. Nakamura, *The ferroelectric phase transition in lithium tantalate single crystals: a composition-dependence study*, J. Appl. Phys. **103**, 014108 (2008).

[197] B. Jaffe, R.S. Roth, and S. Marzullo, *Piezoelectric properties of lead zirconate-lead titanate solid-solution ceramics*, J. Appl. Phys. **25**, 809 (1954).

[198] G. Shirane, K. Suzuki, and A. Takeda, *Phase transitions in solid solutions of $PbZrO_3$ and $PbTiO_3$ (II) X-ray study*, J. Phys. Soc. Jpn. **7**, 12 (1952).

[199] L.G. Van Uitert and L. Egerton, *Bismuth titanate. A ferroelectric*, J. Appl. Phys. **32**, 959 (1961).

[200] H. Buhay, S. Sinharoy, W.H. Kasner, M. H. Francombe, D.R. Lampe, and E. Stepke, *Pulsed laser deposition and ferroelectric characterization of bismuth titanate films*, Appl. Phys. Lett. **58**, 1470 (1991).

[201] W. Cochran, *Crystal stability and the theory of ferroelectricity*, Phys. Rev. Lett. **3**, 412 (1959).

[202] W. Cochran, *Crystal stability and the theory of ferroelectricity*, Adv. Phys. **9**, 387 (1960).

[203] G. Shirane, J.D. Axe, J. Harada, and A. Linz, *Inelastic neutron scattering from single-domain $BaTiO_3$*, Phys. Rev. B **2**, 3651 (1970).

[204] J. Harada and G. Honjo, *X-ray studies of the lattice vibration in tetragonal barium titanate*, J. Phys. Soc. Jpn. **22**, 45 (1967).

[205] Y. Girshberg and Y. Yacoby, *Ferroelectric phase transitions in perovskites with off-center ion displacements*, Solid State Commun. **103**, 425 (1997).

[206] N. Dalal, A. Klymachyov, and A. Bussmann-Holder, *Coexistence of order-disorder and displacive features at the phase transitions of hydrogen-bonded solids: squaric acid and its analogs*, Phys. Rev. Lett. **81**, 5924 (1998).

[207] M.S. Senn, D.A. Keen, T.C.A. Lucas, J.A. Hriljac, and A.L. Goodwin, *Emergence of long-range order in $BaTiO_3$ from local symmetry-breaking distortions*, Phys. Rev. Lett. **116**, 207602 (2016).

[208] R. Pirc and R. Blinc, *Off-center Ti model of barium titanate*, Phys. Rev. B **70**, 134107 (2004).

[209] R. Comes, M. Lambert, and A. Guinier, *The chain structure of $BaTiO_3$ and $KNbO_3$*, Solid State Commun. **6**, 715 (1968).

[210] I.B. Bersuker, *On the origin of ferroelectricity in perovskite-type crystals*, Phys. Lett. **20**, 589 (1966).

[211] A.S. Chaves, F.C.S. Barreto, R.A. Nogueira, and B. Zẽks, *Thermodynamics of an eight-site order-disorder model for ferroelectrics*, Phys. Rev. B, 207 (1976).

[212] W. Zhong, D. Vanderbilt, and K.M. Rabe, *Phase transitions in $BaTiO_3$ from first principles*, Phys. Rev. Lett. **73**, 1861 (1994).

[213] W. Zhong, D. Vanderbilt, and K.M. Rabe, *First-principles theory of ferroelectric phase transitions for perovskites: the case of $BaTiO_3$*, Phys. Rev. B **52**, 6301 (1995).

[214] M. Sepliarsky, R.L. Migoni, and M.G. Stachiotti, *Ab initio supported model simulations of ferroelectric perovskites*, Computational Materials Science **10**, 51 (1998).

[215] Y. Qi, S. Liu, I. Grinberg, and A.M. Rappe, *Atomistic description for temperature-driven phase transitions in $BaTiO_3$*, Phys. Rev. B **94**, 134308 (2016).

[216] Q. Zhang, T. Cagin, and W.A. Goddard III, *The ferroelectric and cubic phases in $BaTiO_3$ ferroelectrics are also antiferroelectric*, Proc. Natl. Acad. Sci. USA **103**, 14695 (2006).

[217] N.A. Spaldin, *A beginner's guide to the modern theory of polarization*, J. Solid State Chem. **195**, 2 (2012).

[218] R. Resta, *Theory of the electric polarization in crystals*, Ferroelectrics **136**, 51 (1992).

[219] R.D. King-Smith and D. Vanderbilt, *Theory of polarization of crystalline solids*, Phys. Rev. B **47**, 1651 (1993).

[220] R. Resta, *Macroscopic polarization in crystalline dielectrics: the geometric phase approach*, Rev. Mod. Phys. **66**, 899 (1994).

[221] X. Gonze and C. Lee, *Dynamical matrices, Born effective charges, dielectric permittivity tensors, and interatomic force constants from density-functional perturbation theory*, Phys. Rev. B **55**, 10355 (1997).

[222] W. Cochran and R.A. Cowley, *Dielectric constants and lattice vibrations*, J. Phys. Chem. Solids **23**, 447 (1962).

[223] K. Refson, P.R. Tulip, and S.J. Clark, *Variational density-functional perturbation theory for dielectrics and lattice dynamics*, Phys. Rev. B **73**, 155114 (2006).

[224] O. Rodrigues, *Des lois géometriques qui regissent les déplacements d' un systéme solide dans l'espace, et de la variation des coordonnées provenant de ces déplacement considérées indépendant des causes qui peuvent les produire*, J. Math. Pures Appl. **5**, 380 (1840).

[225] S. Belongie, *Rodrigues' Rotation Formula*, `http://mathworld.wolfram.com/RodriguesRotationFormula.html`, From MathWorld – A Wolfram Web Resource, created by Eric W. Weisstein. Accessed 18/09/17.

[226] P. Ghosez, J.-P. Michenaud, and X. Gonze, *Dynamical atomic charges: the case of ABO_3 compounds*, Phys. Rev. B **58**, 6224 (1998).

[227] C.-Z. Wang, R. Yu, and H. Krakauer, *Born effective charges, dielectric constants, and lattice dynamics of $KNbO_3$*, Ferroelectrics **194**, 97 (1997).

[228] P. Ghosez and X. Gonze, *Band-by-band decompositions of the Born effective charges*, J. Phys. Condens. Matter **12**, 9179 (2000).

[229] J.F. Epperson, *An Introduction to Numerical Methods and Analysis*, 1st ed. (John Wiley & Sons, Oxford, 2013).

[230] C.F. Gauss, *Methodus nova integralium valores per approximationem inviendi* (Henricum Dieterich, Göttingen, 1815).

[231] C.G.J. Jacobi, *Ueber Gauß neue Methode, die Werthe der Integrale näherungsweise zu finden*, J. Reine Angew. Math. **1**, 301 (1826).

[232] C.G.J. Jacobi, *Ueber eine besondere Gattung algebraischer Functionen, die aus der Entwicklung der Function* $(1-2xz+z^2)^{\frac{1}{2}}$ *entstehen*, J. Reine Angew. Math. **2**, 223 (1827).

[233] E.B. Christoffel, *Sur une classe particulière de fonctions entières et de fractions continues*, Ann. Mat. Pura Appl. **8**, 1 (1877).

[234] C.W. Clenshaw and A.R. Curtis, *A method for numerical integration on an automatic computer*, Numer. Math. **2**, 197 (1960).

[235] S. Xiang, G. He, and H. Wang, *On fast and stable implementation of Clenshaw-Curtis and Fejér-type quadrature rules*, Abstr. Appl. Anal. **2014**, 436164 (2014).

[236] L. Trefethen, *Is Gauss quadrature better than Clenshaw-Curtis?*, SIAM Rev. **50**, 67 (2008).

[237] K.L. Lee, *High-precision Chebyshev approximation to the exponential integral*, tech. rep. (National Aeronautics and Space Administration, 1970).

[238] R. Wahl, D. Vogtenhuber, and G. Kresse, *$SrTiO_3$ and $BaTiO_3$ revisited using the projector augmented wave method: performance of hybrid and semilocal functionals*, Phys. Rev. B **78**, 104116 (2008).

[239] D.I. Bilc, R. Orlando, R. Shaltaf, G.-M. Rignanese, J. Íñiguez, and P. Ghosez, *Hybrid exchange-correlation functional for accurate prediction of the electrionic and structural properties of ferroelectric oxides*, Phys. Rev. B **77**, 165107 (2008).

[240] H.D. Megaw, *Crystal structure of barium titanate*, Nature **155**, 484 (1945).

[241] W.L. Bragg and E.A. Wood, *The conversion factor for kX units to Ångström units*, J. Am. Chem. Soc. **69**, 2919 (1949).

[242] R. Caracas and R.M. Wentzcovitch, *Theoretical determination of the structures of $CaSiO_3$ perovskites*, Acta Crystallogr. B **62**, 1025 (2006).

[243] T. Uchida, Y. Wang, N. Nishiyama, K. Funakoshi, H. Kaneko, A. Nozawa, R.B. Von Dreele, M.L. Rivers, S.R. Sutton, A. Yamada, T. Kunimoto, T. Irifune, T. Inoue, and B. Li, *Non-cubic crystal symmetry of $CaSiO_3$ perovskite up to 18 GPa and 1600 K*, Earth Planet. Sci. Lett. **282**, 268 (2009).

[244] L. Li, D.J. Weidner, J. Brodholt, D. Alfè, G.D. Price, R. Caracas, and R. Wentzcovitch, *Elasticity of $CaSiO_3$ perovskite at high pressure and high temperature*, Phys. Earth Planet. Int. **155**, 249 (2006).

[245] L. Li, D.J. Weidner, J. Brodholt, D. Alfè, G.D. Price, R. Caracas, and R. Wentzcovitch, *Phase stability of $CaSiO_3$ perovskite at high pressure and temperature: insights from ab initio molecular dynamics*, Phys. Earth Planet. Int. **155**, 260 (2006).

[246] T. Sun, D.-B. Zhang, and R.M. Wentzcovitch, *Dynamic stabilization of cubic $CaSiO_3$ perovskite at high temperatures and pressures from ab initio molecular dynamics*, Phys. Rev. B **89**, 094109 (2014).

[247] T. Komabayashi, K. Hirose, N. Sata, Y. Ohishi, and L.S. Dubrovinsky, *Phase transition in $CaSiO_3$ perovskite*, Earth Planet. Sci. Lett. **260**, 564 (2007).

[248] L. Stixrude, C. Lithgow-Bertelloni, B. Kiefer, and P. Fumagalli, *Phase stability and shear softening in $CaSiO_3$ perovskite at high pressure*, Phys. Rev. B **75**, 024108 (2007).

[249] D.J. Adams and A.R. Oganov, *Ab initio molecular dynamics study of $CaSiO_3$ perovskite at P-T conditions of Earth's lower mantle*, Phys. Rev. B **73**, 184106 (2006).

[250] M. Noguchi, T. Komabayashi, K. Hirose, and Y. Ohishi, *High-temperature compression experiments of $CaSiO_3$ perovskite to lowermost mantle conditions and its thermal equation of state*, Phys. Chem. Minerals **40**, 81 (2012).

[251] R. Caracas, R. Wentzcovitch, G.D. Price, and J. Brodholt, *$CaSiO_3$ perovskite at lower mantle pressures*, Geophys. Res. Lett. **32**, L06306 (2005).

[252] E. Mattern, J. Matas, Y. Ricard, and J. Bass, *Lower mantle composition and temperature from mineral physics and thermodynamic modelling*, Geophys. J. Int. **160**, 973 (2005).

[253] B.B. Karki and J. Crain, *First-principles determination of elastic properties of $CaSiO_3$ perovskite at lower mantle pressures*, Geophys. Res. Lett. **25**, 2741 (1998).

[254] R.J. Hemley, M.D. Jackson, and R.G. Gordon, *Theoretical study of the structure, lattice dynamics, and equations of state of perovskite-type $MgSiO_3$ and $CaSiO_3$*, Phys. Chem. Minerals **14**, 2 (1987).

[255] R.E. Wasylishen, O. Knop, and J.B. Macdonald, *Cation rotation in methylammonium lead halides*, Solid State Commun. **56**, 581 (1985).

[256] A. Kojima, K. Teshima, Y. Shirai, and T. Miyasaka, *Organometal halide perovskites as visible-light sensitizers for photovoltaic cells*, J. Am. Chem. Soc. **131**, 6050 (2009).

[257] W.S. Yang, J.H. Noh, N.J. Jeon, Y.C. Kim, S. Ryu, J. Seo, and S.I. Seok, *High-performance photovoltaic perovskite layers fabricated through intramolecular exchange*, Science **348**, 1234 (2015).

[258] E.H. Anaraki, A. Kermanpur, L. Steier, K. Domanski, T. Matsui, W. Tress, M. Saliba, A. Abate, M. Grätzel, A. Hagfeldt, and J.-P. Correa-Baena, *Highly efficient and stable planar perovskite solar cells by solution-processed tin oxide*, Energy Environ. Sci., 3128 (2016).

[259] B. Conings, J. Drijkoningen, N. Gauquelin, A. Babayigit, J. D'Haen, L. D'Olieslaeger, A. Ethirajan, J. Verbeeck, J. Manca, E. Mosconi, F. De Angelis, and H.-G. Boyen, *Intrinsic thermal instability of methylammonium lead trihalide perovskite*, Adv. Energy Mater. **5**, 1500477 (2015).

[260] T.A. Berhe, W.-N. Su, C.-H. Chen, C.-J. Pan, J.-H. Cheng, H.-M. Chen, M.-C. Tsai, L.-Y. Chen, A.A. Dubale, and B.-J. Hwang, *Organometal halide perovskite solar cells: degradation and stability*, Energy Environ. Sci. **9**, 323 (2016).

[261] Q. Chen, H. Liu, H.-S. Kim, Y. Liu, M. Yang, N. Yue, G. Ren, K. Zhu, S. Liu, N.-G. Park, and Y. Zhang, *Multiple-stage structure transformation of organic-inorganic hybrid perovskite $CH_3NH_3PbI_3$*, Phys. Rev. X **6**, 031042 (2016).

[262] P. Singh, P.J.S. Rana, P. Dhingra, and P. Kar, *Towards toxicity removal in lead based perovskite solar cells by compositional gradient using manganese chloride*, J. Mater. Chem. C **4**, 3101 (2016).

[263] F. Brivio, J.M. Frost, J.M. Skelton, A.J. Jackson, O.J. Weber, M.T. Weller, A.R. Goñi, A.M.A. Leguy, P.R.F. Barnes, and A. Walsh, *Lattice dynamics and vibrational spectra of the orthorhombic, tetragonal, and cubic phases of methylammonium lead iodide*, Phys. Rev. B **92**, 144308 (2015).

[264] J.M. Frost and A. Walsh, *What is moving in hybrid halide perovskite solar cells?*, Acc. Chem. Res. **49**, 528 (2016).